University of Rome "Tor Vergata"

PhD Thesis

ALTEA: Anomalous Long Term Effects on Astronauts on board the International Space Station.

PhD in Physics

XIX ciclo

A. A. 2006/2007

Tutor

Prof. Livio Narici

Candidate

Veronica Zaconte

PhD Coordinator

Prof. Piergiorgio Picozza

"...'til the end of time

'til the Earth stops turning…"

To Luca

Index

INTRODUCTION **9**

CHAPTER 1: SPACE ENVIRONMENT AND RADIATION RISKS **11**

1.1 Cosmic rays: introduction **11**

1.2 Cosmic rays: origin and composition **12**

1.3 Solar cycles, Solar Wind and Solar Particle Events (SEP) **20**

1.4 Geomagnetic field and magnetosphere **23**

1.5 Energy loss for heavy charged particles **28**

CHAPTER 2: THE ALTEA PROGRAM **37**

2.1 Background **37**

2.2 The ALTEA program **39**
2.2.1 ALTEA-survey 40
2.2.2 Alteino 41
2.2.3 ALTEA-MICE 42
2.2.4 ALTEA-HIT 43
2.2.5 ALTEA-Biophys 43

CHAPTER 3 THE ALTEA-SPACE FACILITY **45**

3.1 Operative Modes **46**
3.1.1 DOSI 47
3.1.2 CNSM 47

3.2 System description **48**
3.2.1 SDS 48
3.2.2 PBS 49
3.2.3 VSS 50
3.2.4 EEGS 50
3.2.5 DAU 51
3.2.6 LapTop Unit (LTU) 52
3.2.7 ALTEA block diagram 52

3.3 Particle detection system (SDS) **52**
3.3.1 SDU 52
3.3.2 Particles and energy intervals detectable 58

CHAPTER 4: EXPECTED PARTICLE SIMULATED WITH CREME **61**

CHAPTER 5: ALTEA-UHB ARCHITECTURE **69**

5.1 Mission support **69**

5.2 Real-time data **70**

5.3 Data on request **71**

5.4 UHB scheme **72**

CHAPTER 6: DETECTOR PERFORMANCES AND CHARACTERIZATION **73**

6.1 Pedestals and rms **73**

6.2 Big and Small response analysis **82**

6.3 Linearity in low range **83**

CHAPTER 7: DETECTOR TESTS AND CALIBRATION **87**

7.1 GSI, November 2003: beam test **87**

7.2 GSI, November 2003: results **88**
7.2.1 Software for data analysis 88
7.2.2 FM1, Strip 63, silicon plane X0: an example of malfunctioning 88
7.2.3 Anomalous energy loss distributions of plane X2 and Y2 90
7.2.5 Baseline movement 98
7.2.6 SDU FM1 preliminary calibration 101

7.3 GSI, November 2003: conclusions **108**

7.4 GSI, April 2004: beam tests **108**

7.5 GSI, April 2004: results **110**
7.5.1 Software for data analysis 110
7.5.2 GSI, April 2004: final calibration 110
7.5.3 GSI, April 2004: troubleshooting 116

CHAPTER 8: INTEGRATED FM TEST **119**

8.1 Data analysis software **119**

8.2 File 'X17FEBPROVA19_somma.bin.out' **120**

8.3 File AlteaLog_21032005_1921_000.log **126**

8.4 Integrated tests: conclusion **129**

CHAPTER 9: SIMULATIONS OF FLIGHT OPERATIONS **131**

9.1 Simulation #1 - 2006 February, 14th **131**

9.1.1 Simulation #1: comments **133**

9.2 Simulation #2 - 2006 March, 14th **133**

9.2.1 Simulation #2: comments **135**

CHAPTER 10: ALTEA OPERATIONS AND PRELIMINARY RESULTS **137**

10.1 ALTEA operation chronology **138**

10.2 ALTEA DOSI activation: first data 139

10.3 ALTEA operations: a summary 142

10.4 First analysis: particle rate 143

10.5 DOSI data analysis: filter setting 153

10.6 Preliminary analysis results 156

10.7 Work in progress 162

Table 10.4: Relative abundances for the six SDUs normalized to Carbon. 165

10.7.1 Track recognition: the Hough transform method 165

CONCLUSIONS 171

APPENDIX A: PEDESTAL AND RMS VALUES WITH AND WITHOUT SILICON BONDED 173

APPENDIX B: MIP DEFINITION 187

APPENDIX C: MIP→MV CONVERSION 188

REFERENCES 189

Introduction

This work presents the work I carried out last three years on ALTEA experiment.

ALTEA (*Anomalouos Long Term Effects on Astronauts*) is a project funded by ASI, the Italian Space Agency; it is a multidisciplinary experiment devoted to investigate the functional effects of radiation during man permanences in the space and concurrently to get a measure of radiation environment inside the International Space Station.

Investigation of effects of long time exposure to space radiation, during current permanence on board ISS or for a future mission to Mars, is crucial in order to define some risk factors and to look for possible countermeasures.

ALTEA includes several experiment both ground-based and in space.

I was involved in the ALTEA-space experiment and I followed the hardware functioning tests, the calibration and finally I began the analysis of flight data.

In the first chapter an overview of space environment and a brief description of the main effects of radiation exposure will be given.

In the second chapter the ALTEA program, its scientific goals and the experiments that involves will be described while in the third one the ALTEA-space facility will be deeply treated.

In the fourth chapter a simple simulation to calculate the expected particle flux inside the ISS will be presented.

In the following chapters the work performed in order to test and calibrate the device (chapters 6, 7 and 8) will be showed together with the preparation of the ALTEA User Home Base (chapter 5) and the NASA simulations carried out to reproduce the flight operations (chapter 9).

Finally, in the chapter 10 the actual flight operations will be described and results of analysis performed on the first scientific data gathered onboard ISS will be showed.

Chapter 1:

Space environment and radiation risks

In this chapter an overview of the space environment will be given; cosmic rays, their composition and all the mechanisms in which they are involved will be described. In particular, their interactions with the geomagnetic field will be treated. Finally, a very brief outline of what happens when humans are exposed to radiation will be described.
A deep knowledge of this scenario is crucial in assessing the risk parameters for humans in space.

1.1 Cosmic rays: introduction

The main source of the radiation absorbed by astronauts is constituted by cosmic rays, high energy charged particles that can have cosmological, galactic or solar origin. They travel the universe at the light speed and hit the Earth from all directions.

Cosmic rays were first discovered in 1912 by Austrian physics Victor Hess; he found that an electroscope inside an aerostatic balloon discharged faster and faster while going away from Earth surface; it demonstrated that the atmospheric ionization increases proportionally to the altitude. Hess interpreted this phenomenon as evidence of a radiation coming from a non terrestrial source. It was believed for a long time this radiation having electromagnetic nature and this is the reason for the name "cosmic rays".

During 30'cosmic rays were discovered having an electric charge because they undergo the effect of terrestrial magnetic field.

Between 1930 and 1950, before particle accelerators capable to produce high energy were realized, cosmic rays constituted the only source of energetic particles to investigate the high energy physics and they made possible the discovery of several subatomic particles, such us positron and muon.

The goal of today cosmic ray research is the comprehension of their origin and of acceleration mechanisms; also their compositions is studied to know the matter distribution outside the solar system.

Since the beginning of the space era, also the biological risk due to radiation exposition began an important fact to account for. In fact astronauts live in an environment with a radiation level, composition and intensity they do not experience on the Earth. It is then important to guarantee them protection from radiation risks, in particular during high solar activity period or in the future interplanetary journey. In this scenario it is crucial the definition of safety levels for men in the space and for this reason the acquisition of a lot of data is requested.

Cosmic rays were observed and studied since the beginning of the past century at different altitudes, inside deep underground caves, in laboratories at the top of the mountains, in aerostatic balloons above 40 km of altitude [1,2,3] and with detectors on satellites (SAMPEX, COSMOS, ULYSSES, ACE, GOES, NINA-1, NINA-2) [4,5].

1.2 Cosmic rays: origin and composition

There is a complex interconnection between our galaxy, the sun and the terrestrial environment from the point of view of cosmic rays and this complexity makes difficult the radiation risk evaluation in interplanetary flights, in long duration staying on board International Space Station and in intercontinental high altitude flights.

Cosmic rays are usually considered as a flux of particles coming prevalently from outside the Solar System, but generally from inside our galaxy (Galactic Cosmic Rays, GCR); there is then a solar component (Solar Energetic Particles, SEP) and an extragalactic component, constituted by high energy particles ($E>10^8 \div 10^{10}$ GeV). Each component has characteristics, origin and acceleration mechanisms well distinguishable [6].

Before arriving nearby the Earth, cosmic rays are accelerated almost at the light speed and they cross our Galaxy several times because they are trapped by the galactic magnetic field; they stay in the galaxy for about ten million years, interacting with the interstellar medium. Once they enter in the terrestrial magnetic field, some of these particles are trapped in the Van Allen belts. The ones penetrating the atmosphere undergo interactions with electrons and nuclei. Then the radiation composition changes as particles propagate inside the atmosphere and product secondary particle showers [7].

The study of cosmic ray composition and energetic spectrum provides information on their origin, on the matter evolution in our galaxy and on fundamental processes governing its dynamic. It is believed that most of galactic cosmic rays are produced by supernovae explosions (happening about once every 50 years in our galaxy); they are then accelerated by shock waves, by scattering with ionized gas clouds in the interstellar medium (mainly constituted by atomic Hydrogen with varying density and temperature) or by irregularity of interstellar magnetic field. An isotropic radiation covering a wide energetic range is then produced; it results constituted by stable particles and by nuclei with a lifetime of about 10^6 years or more.

Cosmic rays are constituted by all the elements of periodic table; about the 89 % of them is constituted by Hydrogen nuclei (protons), 10% by Helium and about 1 % by heavier element nuclei. In table 1.1 the cosmic ray elemental abundance (normalized to the Silicon) is reported in a comparison with the Solar System composition. The most common heavier elements (Carbon, Oxygen, Magnesium, Silicon and Iron) are almost equal abundant in the Solar System and in cosmic rays. In fig. 1.1 those relative abundances, normalized to Silicon, are plotted: even Z elements result more abundant than odd Z ones. Then, while C, N, O and Fe group elements have similar abundance in the Solar System and in cosmic rays, the two element groups Li, Be, B and Sc, Ti, V, Cr, Mn are few order of magnitudes more abundant in cosmic rays. The reason of this difference is found in the so called “spallation” phenomenon: it consists in the collision of cosmic rays with interstellar medium. The spallation involves abundant nuclei like Carbon and Oxygen (producing Li, Be, B) and Iron (producing Sc, Ti, V, Cr and Mn). If the spallation cross section is known, from cosmic ray abundance some information on the crossed matter between their production an observation can be evinced.

In spite of the highlighted differences, the elemental abundances in cosmic rays and in the Solar System are quite similar.

Also the spectrum of cosmic ray with energy higher than 1 GeV is similar despite different production mechanism and interaction processes they undergo. It can be described with a power law:

$$N(E)\,dE = KE^{-1}dE \qquad (1.1)$$

where $x = 2.5 \div 2.7$.

Elemento	Raggi cosmici			Sistema Solare	Galassia
	70-280	600-1000	Media a 1000-2000		
He	41700±3000	27030±580			$(0.27 \pm 0.06) \times 10^6$
Li	100±6	136±3		5.0×10^{-3}	
Be	45±5	67±2	69.4±10	8.1×10^{-5}	
B	210±9	233±4	212±10	3.5×10^{-3}	
C	851 ±29	760± 16	684±27	1110	1300±300
N	194±8	208± 5	188 ±6	231	230±100
0	777±28	707± 15	607±28	1840	2300±500
F	18.3±1.3	17.0±1.1	13.5±2.3	0,078	0.093 (1.6)
Ne	112±6	113±3	100±3	240	270(t.7)
Na	27.3±3.4	25.8±1.1	21.3±3.2	6	5.6±0.9
Mg	143±6	142±4	123±12	106	105±3
Al	25.2±3.0	28.2±1.2	22.2±3.2	8,5	8.4±0.4
Si	100	100	100	100	100±3
P	4.0±0.7	5.3±0.5	5.3±1.6	0,65	0.%±0.20
S	16.4±1.2	23.1 ±1.1	19.6±0.9	50	45± 13
Cl	3.6±0.5	6.4±0.5	4.7±0.4	0,47	0.47(l.6)
A	6.3±0.6	10.2±0.7	8.2±1.2	10,6	9.0(1.7)
K	5.1 ±0.6	7.2±0.5	6.3±0.4	0,35	0.36±0.12
Ca	13.5±1.0	16.1±0.9	13.1±1.2	6,25	6.2±0.8
Sc	2.9±0.5	4.5±0.5	3.3±1.1	0,003	0.0035±0.0005
Ti	10.7±0.9	10.2±0.7	9.1 ±0.9	0,24	0.27±0.04
V	5.7±0.6	6.7±0.5	4.6±0.3	0,025	0.026±0.005
Cr	10.9±1.0	11.8±0.8	9.1±0.8	1,27	1.30±0.12
Mn	7.2±1.2	8.2±0.7	6.3±0.4	0,93	0.79±0.17
Fe	60.2±3.2	69.8±2.0	60.5±7.6	90,0	88±6
Co	0.2±0.1		0.4±0.2	0,22	0.21 ±0.03
Ni	2.9±0.4	3.7±0.5	2.8±0.6	4,78	4.8±0.6
Cu			0.038±0.006		0.052(l.6)
Zn			0.035±0.005		0.135 (1.6)

Tabella 1.1 : Abbondanze degli elementi nei raggi cosmici ad 1 UA, normalizzate al Si = 100 e confrontate con le abbondanze nel Sistema Solare e nel mezzo interstellare locale (gli intervalli di energia per i raggi cosmici sono espressi in MeV/nucleone).

Simpson(1983), Cameron (1973) [8, 9]

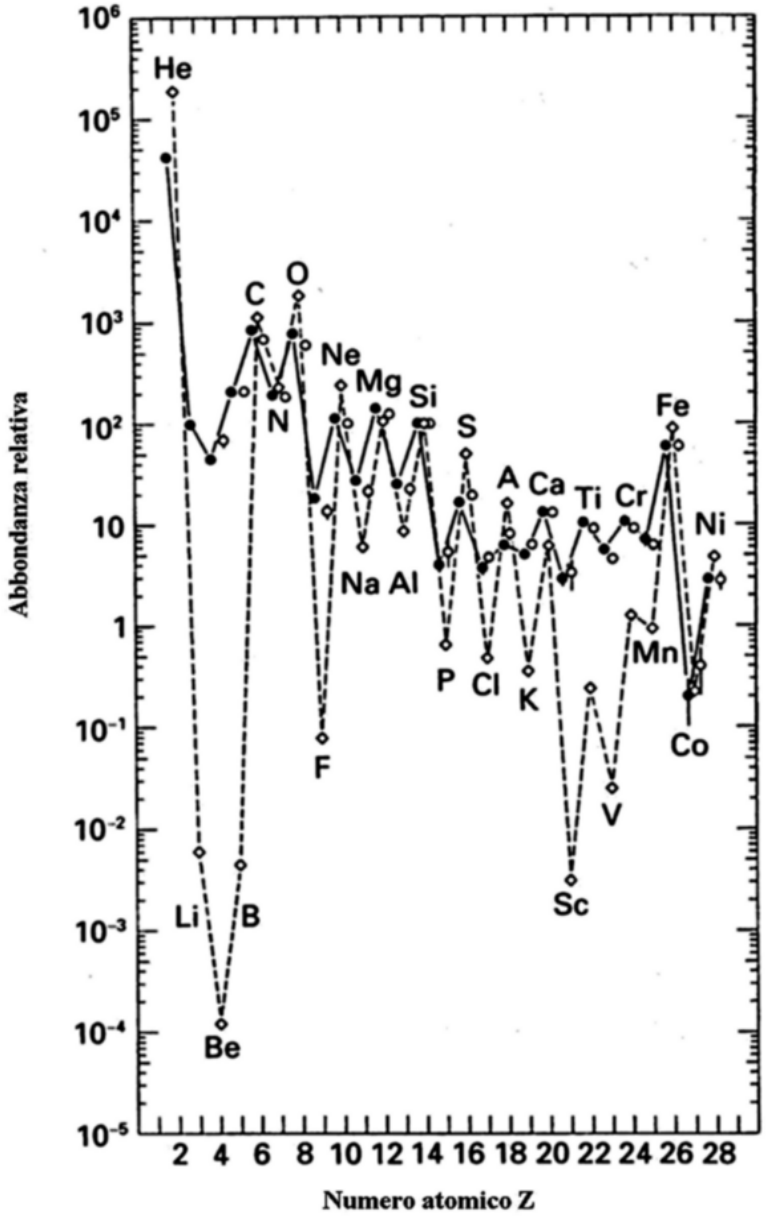

Fig. 1.1 : Elemental abundances in cosmic rays (continuous line) and in Solar System (dashed line). *Simpson (1983),* [8]

In fig. 1.2 differential spectrum for some nuclei [8] is showed; for energy less than 1 GeV the power law trend is attenuated. Energy and cut-off shape strongly depend on the solar cycle period, because low energy particle flux is inversely proportional to the solar activity intensity. In fact the cut-off is entirely produced by cosmic ray diffusion in the interstellar medium towards the Earth through the magnetic field created by the Solar Wind; it is constituted by charged low energy particles coming from the Sun. This phenomenon is known as solar modulation of cosmic ray flux. The solar

modulation becomes predominant when the solar activity increase and the interplanetary magnetic field prevents the low energy particles reaching the Earth. In the fig. 1.2 plot, continuous line is the proton expected spectrum in absence on solar modulation: in this case the cut-off disappears.

Dynamics of charged particles moving in a magnetic field depends on the particle magnetic rigidity, defined as:

$$R = \frac{pc}{Ze} \tag{1.2}$$

where p is the relativistic momentum of particle and Ze its charge.

Particles with different mass and charge but with the same rigidity have the same dynamics in a magnetic field. Considering particles with the same velocity v, their rigidity can be written as:

$$R = \left(\frac{A}{Z}\right)\left(\frac{m_n v c \gamma}{e}\right) \tag{1.3}$$

where γ is the Lorentz and $m_n = (m_p + m_N)/2$, with m_p the proton mass and m_N the neutron mass. In this way the rigidity dependence on the A/Z ratio of considered particles is highlighted, where A and Z are their mass and the atomic numbers. This ratio is about 2 for elements up to Fe, so if the cosmic ray fluxes are expressed in terms of kinetic energy (measure of velocity), the dynamics in magnetic field and the solar modulation effects are expected to be very similar for different elements.

Actually, a part the common characteristics, different element spectra show significant differences, as can be seen in fig. 1.3, where differential spectra of some elements are showed normalized to the Fe one [10,11]. Some elements have a spectrum similar to the Fe one, while others show a very dissimilar inclination, for example B or Ti. This is the consequence of the different origin of nuclei constituting cosmic rays: some nuclei, as C and Fe, are created with the stellar nucleosynthesis, others (as B, Ti, V, etc.) are produced by spallation. Difference in the spectrum inclination is just due to the different spallation cross sections.

Looking back at the fig. 1.2, it has to be noticed the Helium spectrum shows an ascent flux for energy lower than 60 MeV/nucleon. This component, known as the ^{4}He anomalous component, was discovered in 1972 during a minimal solar modulation period when an increment in ^{4}He, N e O abundances were found. A reliable model explains those increments with a certain number of neutral particles that are ionized and accelerated (with not completely known mechanisms) in regions outside the eliosphere.

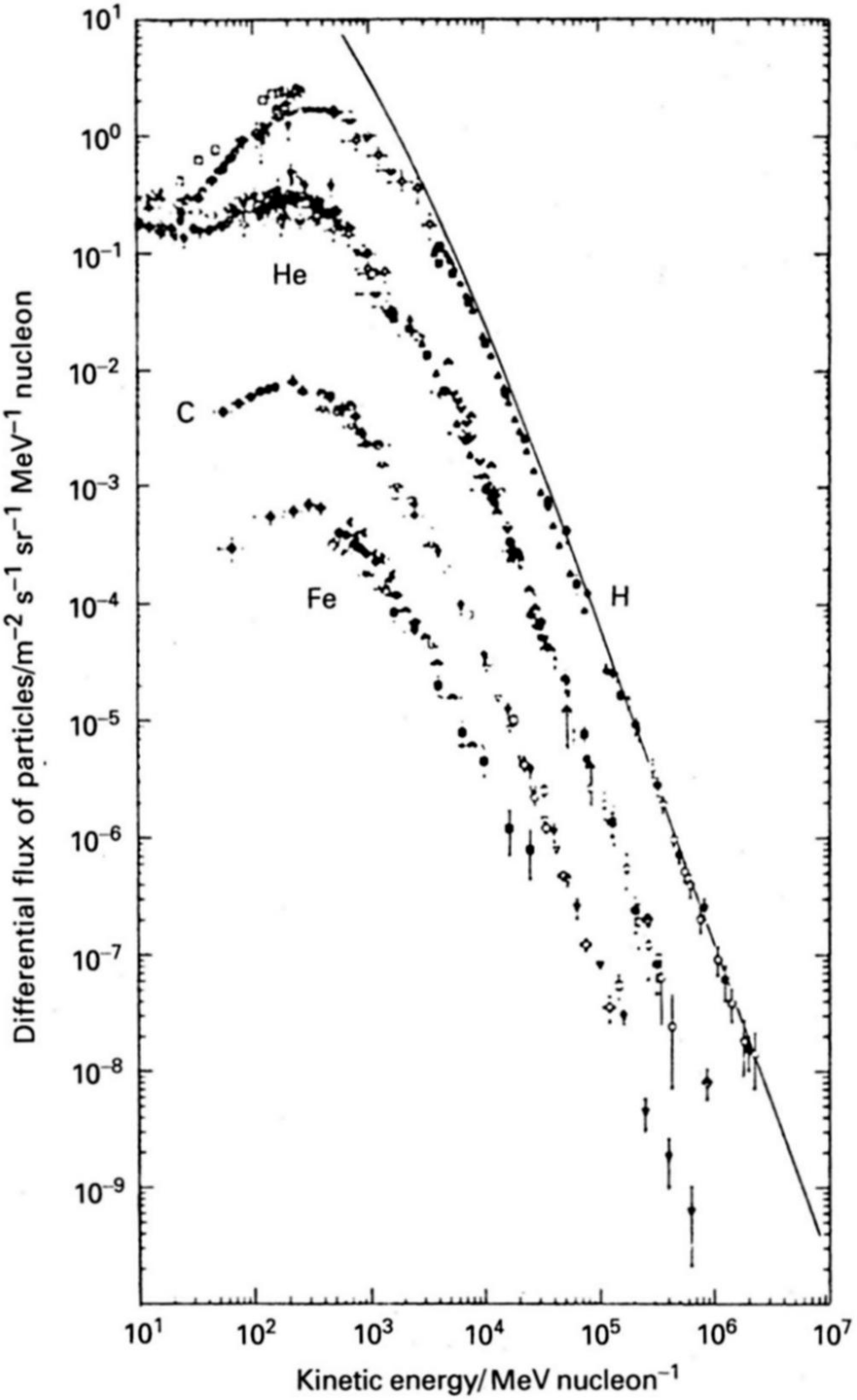

Fig. 1.2: Differential spectrum for different cosmic ray nuclei depending on kinetic energy.
Simpson (1983) [8]

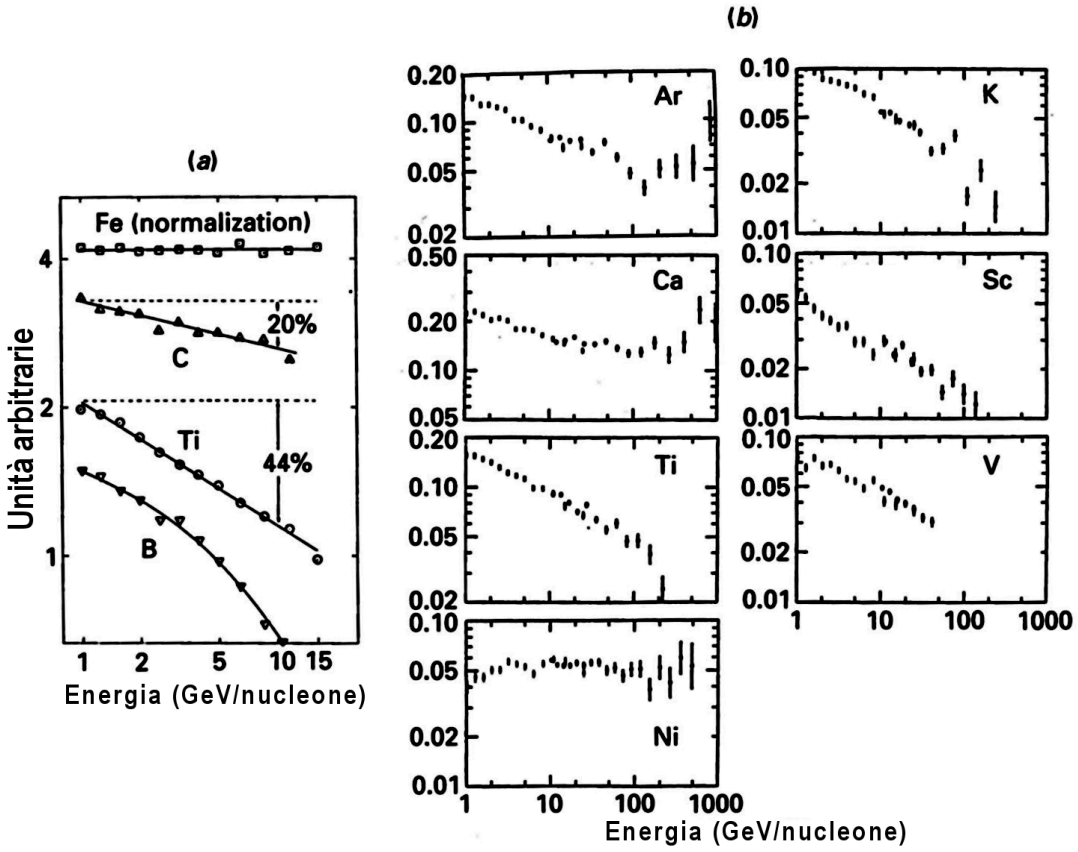

Fig. 1.3 : Some examples of differential spectrum variations for different elements in cosmic rays.
G. W. Cameron (1973) , M.D.Jones et al.,(1985) [9, 10]

In cosmic rays also electrons are present; their fluxes and energy are measured by satellites and balloons. A big high energy electron flux is originated by collisions between cosmic rays and nuclei in the higher layers of atmosphere. Data to study electrons were gathered by Webber (1983) [12]; those data were found consistent with the differential spectrum showed in fig. 1.4. Also electron spectra are strongly influenced by solar modulation effect for energy below 1 GeV.

When cosmic rays collide with terrestrial atmosphere nuclei, a secondary particle cascade going toward the Earth surface is produced. Secondary cosmic rays include pions (quickly decaying in muons, neutrinos, gamma ray) and electrons and positrons produced by the muon decay and by interaction with atmosphere nuclei.

Number of particles reaching the Earth surface depends on the energy of cosmic rays impinging the high atmosphere; cosmic rays with energy higher than 10^{14} eV are studied with large array detectors distributed on many square kilometer areas detecting particles produced in the showers.

Cosmic ray interactions produce also neutrinos, detected by big detector placed deeply underground or underwater.

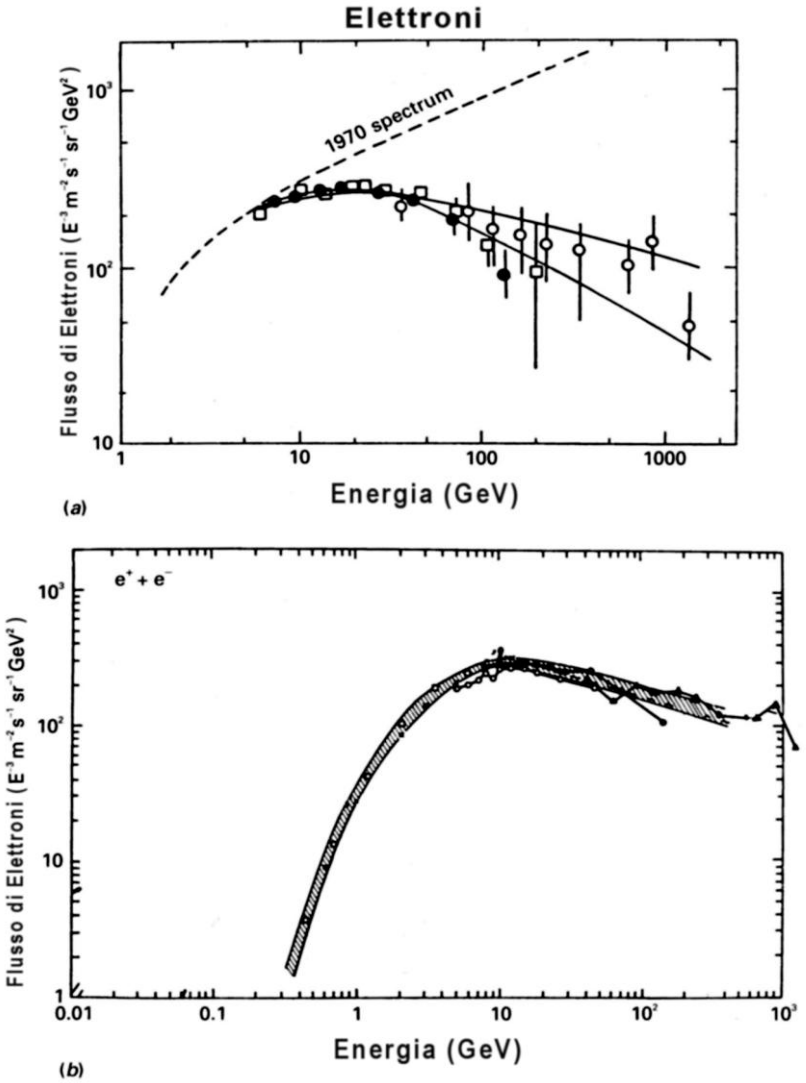

Fig. 1.4 : Cosmic ray electron spectrum. (*Webber, 1983* [12]).

Most of the cosmic rays arriving on the Earth surface is constituted by muons, with a mean intensity of about 100 particles per m^2 per second.

Also if thousand of cosmic rays cross our body every minute, resulting radiation levels are relatively low at the sea level, constituting only a little fraction of natural background radiation. Scenario is completely different talking about astronauts in space; they are continuously exposed to consistent radiation quantities, that become dangerous if the Sun is in a very active period. The electronic instrumentation suffers radiation damage, too, because highly ionizing nuclei can cause circuit breaking.

s1.3 Solar cycles, Solar Wind and Solar Particle Events (SEP)

The Sun is the dominant energy source of terrestrial environment (and of the entire Solar Sistem, of course), it provides electromagnetic radiation and charged cosmic rays from the low energies of the ones constituting the Solar Wind to the high energies of SEP. Solar particles have a direct influence on the man life, both for technologies and for health. In fact, plasma ejection from the solar corona or the ionization caused by particles coming from the Sun can interfere with the communication systems functioning and in general with all the electronic devices. Then, as already mentioned, solar events can be dangerous for astronauts in space. It is crucial the complete comprehension of the solar phenomena giving radiation and charged particles.

Many solar phenomena happen on precise time scale; the Solar Cycles, the ones occurring on the largest time scale, have a 11 years period. The Cycles are tightly correlated with the observation of solar maculae, regions of the Sun with a magnetic field ($B \approx 0.3$ T) very higher than the mean solar magnetic field ($B \approx 10^{-4}$ T); this high magnetic field inhibits plasma movement, so temperature decreases and there is a lower electromagnetic emission.

In each Solar Cycle a period of solar minimum, with a low number of maculae and an almost dipolar solar magnetic field, and one of solar maximum, with a big number of solar maculae and an irregular magnetic field, alternate. The following solar minimum period will have still a dipolar magnetic field, but with inverted polarities. This phenomenon is explained in terms of dynamo effect: the Sun is not a rigid body but it has a differential rotation speed depending on latitude. Ionized plasma is linked to the magnetic field lines that result distorted because of the different rotation speed, higher at the equator; the lines locally intertwine increasing the field itself intensity [13].

Before approaching the description of Solar Wind it is needed a deeper description of the solar structure. Its photosphere has a temperature about 5800 K. Outside the superficial layer of the Sun a high temperature ($T \approx 10^5$ K) gas is placed in the region called *solar corona*. Solar corona is visible during the total Sun eclipses; its high temperature is measured by the excitation lines of its emission spectrum. The solar corona is not gravitationally linked because of its great kinetic energy; it expands in the interplanetary medium. The corona expansion origins the Solar Wind, a totally ionized gas mainly constituted by protons and electrons that blows in the entire Solar System. Through the *flux freezing* phenomenon (considering as infinite the plasma conductivity, the magnetic field appears as frozen, so it cannot independently move in the plasma itself), the interplanetary magnetic field is linked to the particles of Solar Wind, that continues to expand until

it interacts with the galactic magnetic field. Characteristics of Solar Wind in the Earth proximity are summarized in table 1.2, where mean value for a low solar activity period are reported.

particle speed	~ 350 km/s
particle flux	~ 1.5 x 10^{12} $m^{-2}s^{-1}$
particle density	~ 10^{7} m^{-3}
proton energy	~ 500 eV
proton energy density	~ 4 x 10^{10} J/m^{3}
temperature	~ 10^{6} K

Table 1.2 : Typical parameters of Solar Wind. [6]

The Solar Particle Events (SEP) constitute most of the high energy component of cosmic rays. Those events consist of rapid increments of particle flux (until four orders of magnitude); the particles are emitted in the active regions of the solar surface due to increment of the electronic plasma density. Those energies are released in few seconds during *solar flares*, intense flares on the solar surface, usually nearby the solar maculae. Flares emit high radiation level with wave lengths ranging from tens of kilometres of radio emissions until 0.001 Å of X rays and γ rays, covering more than 17 orders of magnitude.

Typical energy released by a flare is around 10^{25} J, most of which is electromagnetic and mechanical energy and a significant fraction of it is emitted in the form of high energy particles. In fact flares, such as the corona magnetic rearrangements associated with the flares, cause emission of relativistic particles, among them electrons, protons, neutrons, heavy ions and probably neutrinos, too. Radio microwave bursts are then produced on millisecond scales, while *noise storms* with greater wave length last for several days.

In fig. 1.5 the appearance of a solar flare is showed in dependence of the electromagnetic wave length.

It has to be noticed that the flare intensity has a different trend depending on the considered wavelength. Those differences imply that flares can have different phases, probably because of different physical processes or different steps for the flare evolution. In the bottom part of the plot the flare phases are showed: in the first stage a little amount of energy is released as a prelude of the main event.

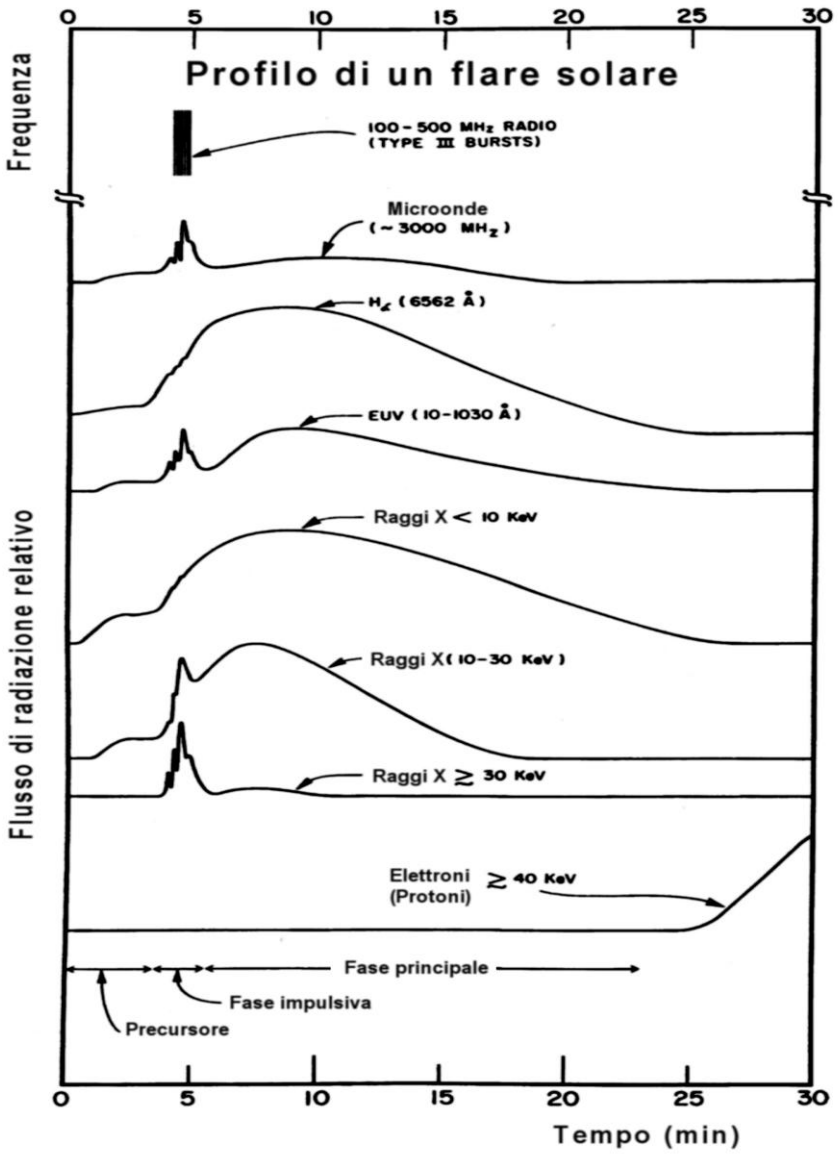

Fig. 1.5 : Aspect of a solar flare versus electromagnetic wavelength. [15].

There is then an impulsive phase, where energy is emitted in sudden explosions, and a long duration main phase. Finally, in fig. 1.5 the diverse region sources for the various emissions; those regions are placed in a range going from the lower chromosphere to several solar radii from solar surface; so the time coincidence between different portions of flare plot at diverse wavelengths does not imply a causal connection [16, 17, 18, 19].

1.4 Geomagnetic field and magnetosphere

The Earth is partly shielded from space particles by its magnetic field. Even if this field is relatively weak (about 1 Gauss at earth surface) its extension in the volume around Earth provides a shield which deflects impinging particles following Lorentz law. Cosmic rays are deflected in more populated regions, while flux increases in polar regions. Magnetic field topology traps more energetic particles in belts surrounding the Earth.

Earth magnetic field is produced by convective movements of magma; these movements inside the magnetic field induce electric currents which reinforce the field itself (auto induced dynamo effect). The field structure is altered by the external effect of Solar Wind, which brings interplanetary magnetic field. So geomagnetic field undergoes long term periodic modifications (100-year period) and short term ones, bound to solar cycles (20-year period). Geomagnetic field is dipolar at first order, 11° inclined in respect to Earth rotational axis.

Radial and angular components of the field (fig. 1.7) in polar coordinates are:

$$B_r = -B_0 \frac{2\cos\theta}{r^3} \qquad B_\theta = -B_0 \frac{\sin\theta}{r^3} \tag{1.4}$$

with r in Earth radius unit (R_E=6.37 x 10^3km). Dipolar field is symmetrical around its axis, so B_φ=0 everywhere. B_0 is field average value at geomagnetic equator (λ=0) at earth surface and its value is 0.31 gauss.

Dipolar field magnitude is:

$$B = \sqrt{B_r^2 + B_\theta^2} = B_0 \frac{\sqrt{1+3\cos^2\theta}}{r^3} \tag{1.5}$$

Field magnitude decrease as r^3 going away from earth. At a fixed r magnitude increases going towards poles, being double at the poles than at equator. Integrating (1.4):

$$r(\theta) = R_0 \sin^2\theta \tag{1.6}$$

where R_0 is r value, in earth radius units, when θ = 0, and it represents the distance between dipole and the point in which field line crosses equatorial plane.

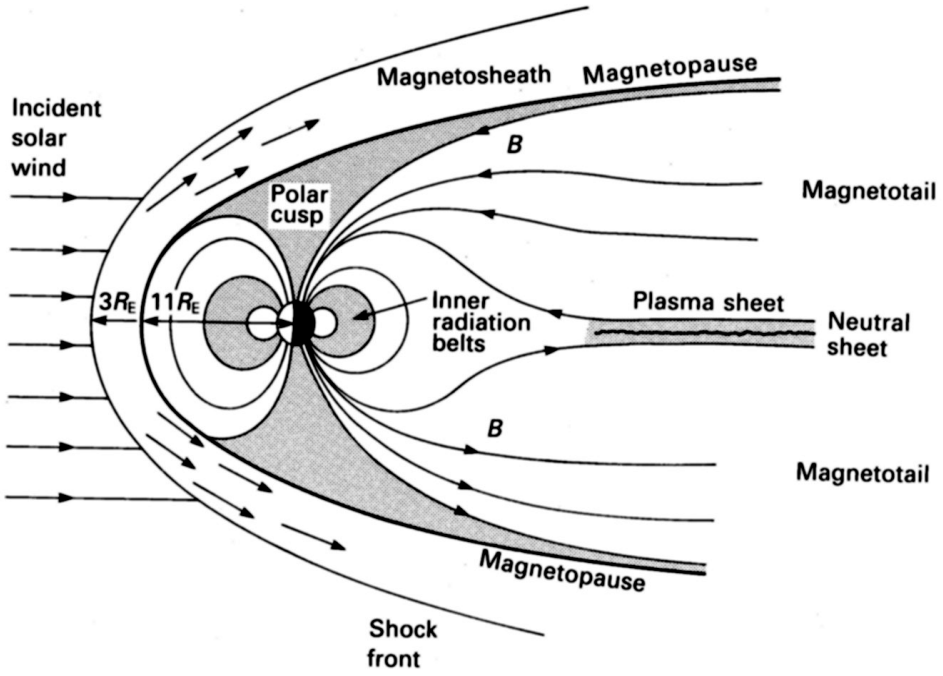

Fig. 1.6 : Diagram of Earth magnetosphere structure.

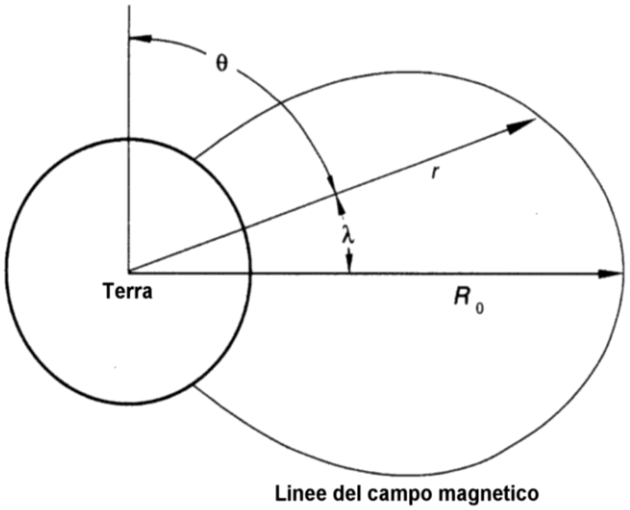

Fig. 1.7 : Coordinate system in dipolar field.

Field magnitude and force fields can be expresses in terms of latitude λ:

$$B(r,\lambda) = \frac{B_0}{r^3}\sqrt{(1+3\sin^2\lambda)} \tag{1.7}$$

$$R(\lambda) = R_0 \cos^2\lambda \tag{1.8}$$

If earth field was a pure dipole located in the center of the planet constant B curves would be constant latitude lines. But asymmetries in current internal system introduce higher order terms in field expression and actual isointensity curves are showed in fig. 1.8.

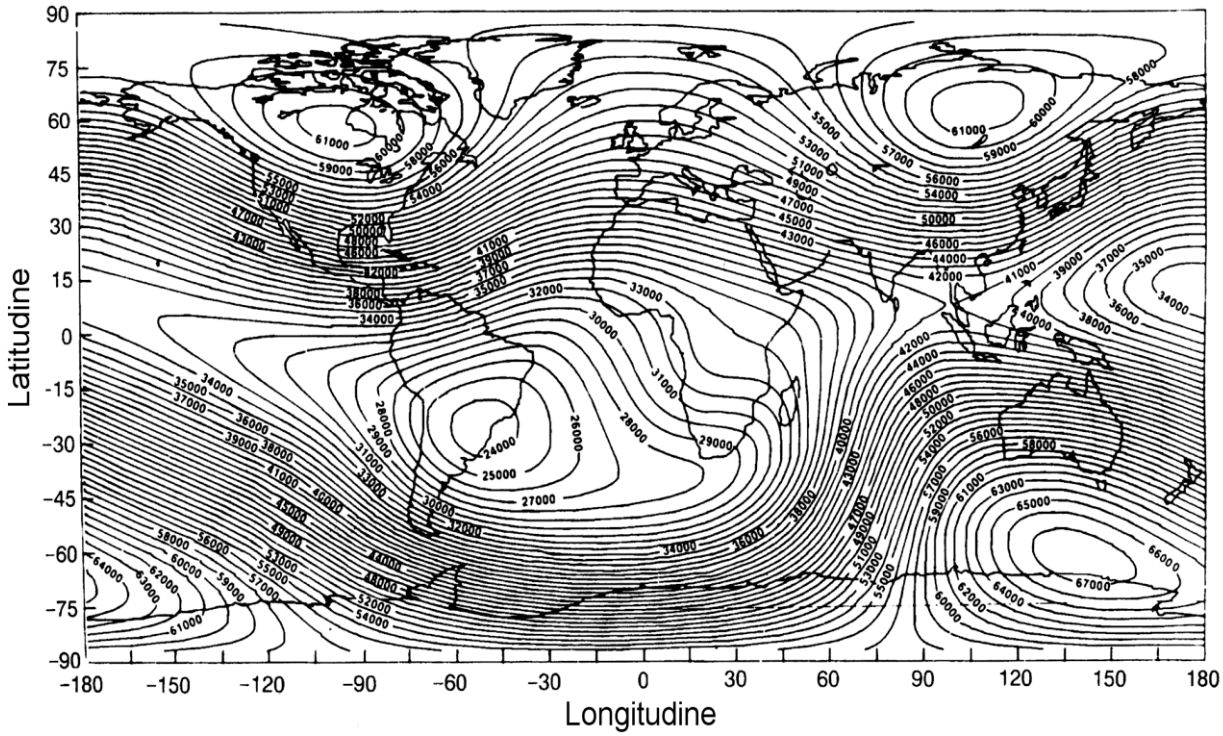

Fig. 1.8 : Isintensity lines of geomagnetic field on Earth surface. Magnetic field intensità is in unit of 10^{-9} tesla. In a pure dipolar field isintensity lines should be horizontal.

Main cause of distortion is the non-alignment between magnetic axis and rotation axis; besides the center of the dipole is not exactly located at Earth center [21]. Poles are located in north Canada and below Australia. A very evident deviation from dipolar field is a zone located over Brazil called South Atlantic Anomaly (SAA). Given that in this region magnetic field magnitude is much lower than predicted by the dipole law, particles from external space enter deeper in the atmosphere: flux increases up to three orders of magnitudes. Multipole description of the field is very accurate near to the surface as far as three or four earth radii; beyond that there is a big distortion due to the interaction with the solar wind.

Earth magnetic field is often described in terms of B and L McIlwain magnetic coordinates [22,23]: B is field magnitude and L represents at first order the distance, in earth radii, between field line passing through a given point and the geomagnetic equator. A B-L couple is univocally assigned to each point in space.

These coordinates are important because the charged particles spiralize along the field lines and bounce between points with the same L value *(mirror points)*.

Three regions are individuated by the value of the McIlwain coordinates:

- L > 2, correspondent to the galactic cosmic ray region;
- L < 2 and B < 0.25 Gauss, correspondent to the SAA;
- L < 2 and B ≥ 0.25 Gauss.

In order to comprehend mechanism of interaction between magnetic field transported by the Solar Wind and geomagnetic field, it has to be considered that Solar Wind is supersonic and when it invests the Earth and its magnetic field, they can be considered as spherical obstacles to the wind blowing. The fact that the Solar Wind is supersonic implies that its velocity is greater than any plasma wave propagating in the flux direction.

Despite obvious differences between the case of a solid obstacle placed in front of a supersonic gas and the case of the Solar Wind impinging the Earth, the structure described nearby the Earth can be efficiently described in term of classical gas dynamics.

Geomagnetic field and particle distribution close to the Earth were studied with several experiments; results are summarized in fig. 1.6.

A *bow shock* is created at about 14 R_E (Earth radii) in the Solar Wind incidence direction. At a distance of about 11 R_E is found the region called *magnetopause*, that is the limit of the area dynamically dominated by the magnetic field of the Earth. The Solar Wind blows around the Earth between the bow shock and the magnetopause. The region inside magnetopause is called *magnetosphere*.

The dipolar magnetic field of the Earth is strongly perturbed by the flux of particles coming from the Sun, so that it can be considered dipolar only very close to the Earth surface. The most significant distortion can be seen in the field lines structures behind the Earth in respect to Solar Wind incidence direction: the magnetosphere cavity is stretched so to obtain a cylindrical region that near the lunar orbit (at about 60 R_E) has a radius of about 25 R_E. This region is known as *magnetic tail*.

The magnetosphere is not a stationary structure as seen in fig. 1.6, but it undergoes variation according to density and Solar Wind speed: this internal instability causes changes in the tail structure.

The geomagnetic field constitutes a sort of a shield for particle incident from space. *Geomagnetic cut-off* G is a measure of this shielding effect: it is defined as the momentum below which particles with z charge coming orthogonally respect to the B flux line cannot reach the Earth. The G value is given by:

$$G = 14.9 z \cos^4 \lambda \quad \text{(GeV/c)} \tag{1.9}$$

where λ is the geomagnetic latitude. Particles with the same momentum have different probability to penetrate the field lines according to the considered latitude value.

In the magnetopause there are two regions, called *solar cusps* , where the direction velocity of the incident particles is parallel to the magnetic field lines, so that the Lorentz force is null.

After what previously told, two regions exist where the particle flux is high, the SAA and polar areas. While in the polar regions particles coming from outside magnetosphere are trapped, in the SAA there are particles (mostly protons and electrons) of different origin: they may come from the decay of neutral particles, that not suffer of the geomagnetic field action and so they can enter the geomagnetic cavity, or they may be particles with such a charge to penetrate the field lines, lose energy by ionization and then be trapped.

Trapped particles undergo the combination of three fundamental motions:

- circular rotating motion along plane orthogonal to the strength lines;
- spiral motion along the field lines with inversion in the *mirror points*, where the magnetic field is more intense and it can cancel the velocity component parallel to the field;
- longitude drift motion, toward east for particles with negative charge and toward west in case of particles with positive charge.

Protons and electrons are the most abundant trapped particles; they are confined into two regions, the *Van Allen belts*. The internal belt, extending until about 2.5 R_E from the Earth surface, is mainly populated by protons with energy of few tens of MeV and by electrons with energy above MeV; the external belt, extending over 3 R_E, is populated by electrons and protons with energy below MeV [24].

It is important the comprehension of mechanisms through which particles are trapped in the Van Allen belts, as it is important the study the particle lack, without that fluxes should grow up indefinitely. Today it is known that particles in the internal belt origin from the neutron decay, that come from very energetic protons of primary cosmic rays as in the reactions:

$$p(E \approx GeV) + X \rightarrow p + n; \qquad n \rightarrow p + e^{-} + \overline{\nu_e}$$

These kind of protons can lose energy in ionization processes and in nuclear collisions, while electrons can suffer scattering with angles big enough to escape out of the belts.

In the outer belt particles enters from magnetosphere cusps, but acceleration and input mechanisms are not yet clear enough. The comparison between solar activity and flux variations shows that electrons found in this belt generally originate from sun.

1.5 Energy loss for heavy charged particles

Energy loss mechanisms for charged particles will be described in this chapter.

There are two main effects of particle passages through a material medium: particle energy loss due to inelastic collisions with the atomic electrons of the material, and particle deflection from its incidence direction, due to elastic scattering with nuclei. These interactions happen many times for unit path so that a resultant macroscopic energy loss and deflection from initial direction is found.

The energy transferred by a charged particle through a material medium is provided by the Bethe-Bloch formula:

$$-\frac{dE}{dx} = 2\pi N_a r_e^2 m_e c^2 \frac{\rho Z}{A}\frac{z^2}{\beta^2}\left[\ln\left(\frac{2m_e\gamma^2 v^2 W_{\max}}{I^2}\right) - 2\beta^2 - \delta - 2\frac{C}{Z}\right] \tag{1.10}$$

where:

r_e: classical electron radius — ρ: material density

m_e: electron mass — z: charge of incident particle

N_a: Avogadro number — A: atomic mass of material

I: mean excitation potential — β: v/c of incident particle

Z: atomic number of material — γ: Lorentz factor

C: shell correction — δ: density correction

W_{max}: maximum energy transferred in a single collision

The maximum energy transferred in a single collision is for a head-on collision; for a particle with mass M cinematic provides:

$$W_{\max} = \frac{2m_e c^2 \eta^2}{1 + 2s\sqrt{1+\eta^2} + s^2} \tag{1.11}$$

where $s = m_e/M$ e $\eta = \beta\gamma$. Then, if $M \gg m_e$, W_{max} can be written as follows:

$$W_{\max} \cong 2m_e c^2 \eta^2 \tag{1.12}$$

The mean excitation potential I is the main parameter of the Bethe-Bloch formula and it is essentially given by the orbital frequency $\bar{\nu}$, averaged on all bound states, multiplied for the Planck constant *h*.

δ and C are corrections to the Bethe-Bloch formula; they are relevant at high and low energy respectively. The *density effect* is caused by the fact that electric field transported by the particle

tends to polarize atoms along its path. Because of this polarization, electrons far from particle trajectory will be shielded from the full intensity of electric field, so interactions with these far electrons will contribute less to the particle energy loss predicted by Bethe-Bloch formula. This effect become more important when the particle speed increases and clearly depends on density of crossed medium. The *shell* correction accounts situations when particle speed is comparable o lower than the orbital velocity of bound electrons; in this case some hypothesis needed at the Bethe-Bloch calculation not succeed (for example, electron cannot be considered stationary during interaction) and the formula fails.

The ionization energy loss measured by the Bethe-Bloch formula depends on kinetic energy of incident particle. In fig. 1.9 the energy loss dE/dx for different particles is showed; the energy loss is dominated by $1/\beta^2$ at not relativistic energies and it decreases when the particle speed increases until reaching a minimum for $v \approx 0.96c$, when particles are at *minimum ionization* point. Energy released by different particles at minimum ionization is almost the same if particles have the same charge. If the kinetic energy further increases, the energy loss flattens because the term $1/\beta^2$ becomes almost constant and the dominant term is the logarithmic rise, known as *relativistic rise*. However the relativistic rise is practically cancelled by the correction density. For energy below the minimum ionization energy, particles have a different behaviour. This feature is often used in particle physics in identification of different particles in this energy range. In the plot the very low energy region is not showed; there the Bethe-Bloch fails for phenomena as electronic pick-up.

In fig. 1.10 the variation of energy loss, then the amount of ionization, versus the particle penetration deep in the material medium is showed; this curve is known as the *Bragg curve*.

Particle loses most of the energy almost at the end of its trajectory, until it slows down and the electronic pick-up begins and dE/dx falls down.

This behaviour is really important in medical use of charged particles, for example in irradiation of an ill tissue, when the knowledge of the exact point where energy is released is crucial to avoid the destroy of surrounding tissues.

A particle can lose energy also for other processes, such as emission of Cherenkov radiation, bremsstrahlung, nuclear reactions.

There is emission of Cherenkov light when the particle in the material medium is greater than the light speed in the same medium:

$$v_{part} > \frac{c}{n} \quad \Rightarrow \beta = \frac{v_{part}}{c} > \frac{1}{n} \tag{1.13}$$

where n is the refraction index of the material.

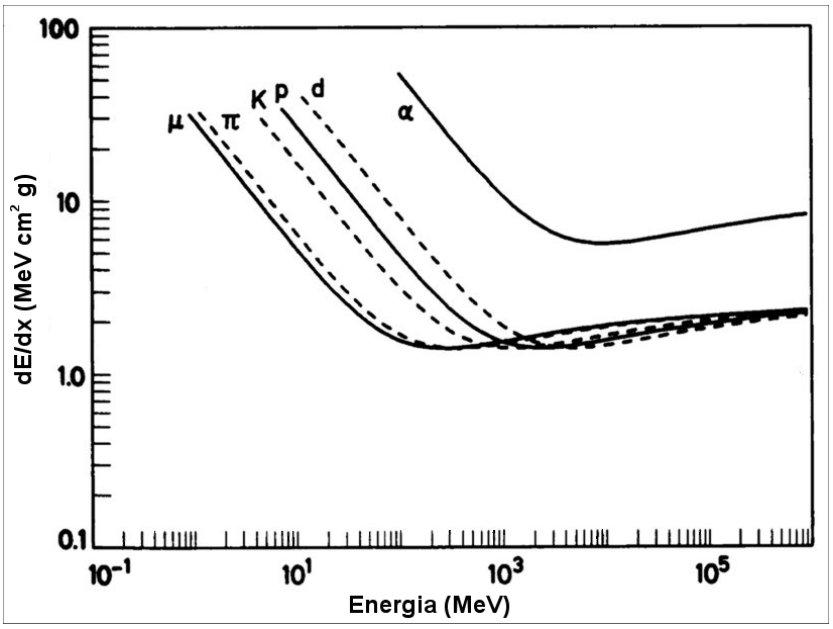

Fig. 1.9 : Energy loss dE/dx for different particles.

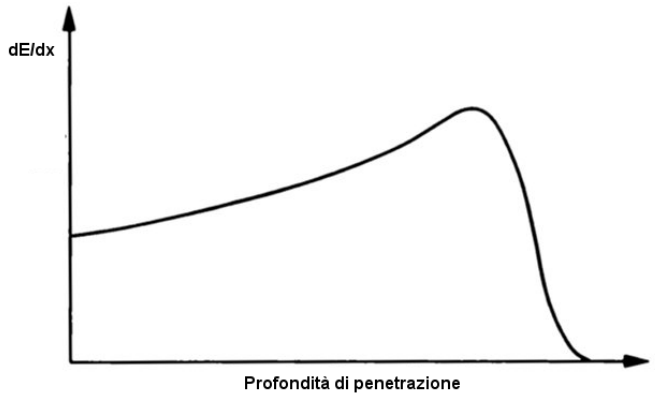

Fig. 1.10 : Typical Bragg curve of dE/dx variations versus the particle penetration deep in the matter.

The Cherenkov light is a directional light (the angle between the wave front and the incident particle direction varies between 0 e θ_{max} = arcos(1/n) at β variation) and it is polarized in the plane formed by the wave propagation direction and particle direction. Conditions for Cherenkov emission are satisfied foe wavelengths between ultraviolet and the near infrared, then in the visible region. Cherenkov effect is one possible cause of Light Flash (see further).

The bremsstrahlung is the particle energy loss caused by scattering with the electric field of a nucleus. When a particle is deflected by the straight trajectory for electrostatic interaction with a field, it is accelerated following the emitted radiation power given by the Larmor formula:

$$P = \frac{dW}{dt} = \frac{2}{3}\frac{(ze)^2 a^2}{c^3} \tag{1.14}$$

where ze is the particle charge and a is its acceleration.

Since a ~ F/m, irradiated power depends on $(1/m)^2$, where m is the particle mass; then, also if there is always energy loss for radiation, it is important only for light particles, especially for electrons, while it is negligible for the heavier ones.

Energy considered since now is actually the mean value of energy loss when a particle crosses a material medium. Generally energy loss by a particle will not be equal to this mean value for the statistical fluctuation in the collision number and in the energy loss in each collision. Calculation of energy loss distribution in a certain thickness of a material is a difficult mathematical problem. Usually only two cases are considered: thick and thin absorbers. In the first case, a lot of collision are supposed to happen, then a Gaussian distribution can be considered for the central limit theorem, taking the energy loss in a single collision as random variable. Collisions are supposed to happen with a negligible speed variation; obviously this hypothesis is valid until absorbers are not too much thick. In the case of thin absorbers, the central limit theorem cannot be applied because collision number is not so high; the energy distribution has a tail accounting for the big energy transfers in a single collision, also if those events are not probable. So the distribution is not Gaussian (see fig. 1.11) and the most probable energy loss value is not equal to the distribution mean value; it is a Landau distribution, that can be written as follows:

$$f(x,\Delta) = \frac{\phi(\lambda)}{\xi} \tag{1.15}$$

where :

$$\phi(\lambda) = \frac{1}{\pi}\int_0^\infty \exp(-u\ln u.u\lambda)\sin\pi u du \tag{1.16}$$

$$\lambda = \frac{1}{\xi}(\Delta - \xi(\ln\xi - \ln\varepsilon + 1 - C)) \tag{1.17}$$

with C the Euler constant and:

$$\ln\varepsilon = \ln\frac{(1-\beta^2)I^2}{2mc^2\beta^2} + \beta^2 \tag{1.18}$$

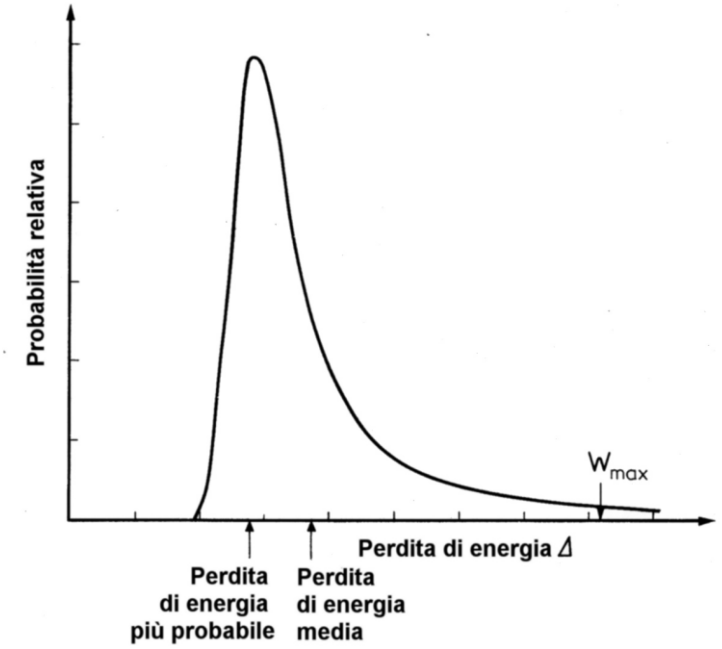

Fig. 1.11 : Typical energy distribution of energy loss by a charged particle in a thin absorber (Landau curve).

In addition, x is the absorber thickness, Δ is the energy loss in the absorber, ξ is the mean energy loss. In this theory it is assumed that the maximum available transferred energy tends to infinite and that the single energy transfer is big enough for electrons to be considered free.
Finally, the most probable energy loss value is found to be:

$$\Delta_{mp} = \xi\left[\ln\left(\frac{\xi}{\varepsilon}\right) + 0.198 - \delta\right] \tag{1.19}$$

where the density correction δ was also included [25].

1.6 Dosimetry and biological radiation damage

Dosimetry is an essential component of all space missions in order to study the crew protection.
The safe assurance in the long duration space flights has different goals to be achieved:

- development of an optimized crew protection system for the ionizing radiation sources, such as galactic cosmic rays, trapped radiation and solar particles during maximum solar activity periods
- collection of dosimetry data during space flights in different altitude, orbital inclination, solar activity conditions.

- evaluation of radiation risks for exposure during the missions.

As seen in the previous chapter, radiation in the low orbits and outside terrestrial magnetosphere is complex and characterized by an energy spectrum ranging from few keV to hundreds GeV. Distribution of energy received during a space flights is irregular; the maximum of exposition can happen in different flight phases.

Many experiments conducted on Skylab and on the MIR station produced some references for the total dosimetry [26,27,28]. Since now, dosimetry was performed with passive detectors [29,30], in particular nuclear emulsions, scintillators or TDL (*Thermo Luminescence Detectors)*. Today silicon detectors are used, also capable to have a time measurement of radiation fluxes [31,32].

Usually concept of *absorbed* is used in evaluation of radiation risks.

The *absorbed dose D* is a measure of the energy deposited in a medium by ionizing radiation. It is equal to the energy deposited per unit mass of medium, and so has the unit J/kg, which is given the special name gray (Gy). It has to be noticed that the absorbed dose is not a good indicator of the likely biological effect of radiation. 1 Gy of alpha radiation, for example, would be much more biologically damaging than 1 Gy of photon or electrons. Difference is due to the diverse LET (*Linear Energy Transfer*), energy deposited in the path unit. For many purposes the LET coincides with the dE/dx calculated by the Bethe-Bloch formula, but it does not include energy losses for bremmstrahlung. Biological damage is as high as particles are ionizing.

In order to take into account these differences the *equivalent dose* H_T is defined. It is a measure of the radiation dose to tissue where an attempt has been made to allow for the different relative biological effect of different types of ionizing radiation. Equivalent dose is therefore a less fundamental quantity than radiation absorbed dose, but is more biologically significant. Equivalent dose has units of sieverts (Sv). The equivalent dose should not be mistaken for dose equivalent. Dose equivalent (H) presents the absorbed dose at a specific location in tissue weighted by a distribution of quality factors (Q). These are influenced by the LET (linear energy transfer) distribution of the radiation at that site.

Equivalent dose (E) is calculated by multiplying the absorbed dose (D) with the evaluation factor. Formerly, The International Radiological Protection Commission recommended the use as the evaluation factor of the quality factor Q (that estimates the relative biological effectiveness, RBE) only. The value of Q is 1 for x-rays, gamma rays and beta particles, but higher for protons, neutrons, alpha particles etc [33].

The biological effects of radiations will be now briefly described. Radiations are harmful because of their ionizing power. This ionization can damage the cells directly, breaking chemicals bounds of some important molecules, or indirectly, through formation of free radicals from the water

molecules inside the cells. The free radicals chemically attach the cells. In a certain measure, damaged molecules are repaired by natural biological processes, but the reparation degree depends on the damage amount.

If reparation is effective no effect is observed, otherwise the damaged cell can experience three evolutions:

- cellular death;
- impoverishment of natural cellular functionality, conducting to somatic effects (physical effects suffered individually by the irradiated cell) as cancer;
- permanent DNA alteration transmitted to the successive generations (genetic effect).

Biological consequences can be immediate or at long term, depending on the absorbed dose.

Effects of high radiation($\geq$ 1 Gy) dose received in a short time (few hours) are known; the immediate consequence is the break of the reproductive process in some kind of cells, among them the white blood cells, the bone marrow cells and the one covering intestine. If the dose is greater than 2-3 Sv there can be the death for the mitotic cell depletion. In case of surviving, some consequence are found, such as sterility, cataract, rashes. For each of them, a specific threshold exists, below which those effects do not subsist. The existence of a threshold is a natural consequence of the fact that for an organ to be weakened a certain number of cells has to be compromised. In this case, all the experienced effects are called *deterministic* or *non stochastic.*

In case of exposition to doses of 0.2 Gy or less, or to higher doses at the maximum acceptable rate, the development of tumours or genetic anomalies are the most probable consequences, also if those effect are not easily and exclusively linkable to the radiation exposure, especially because a long time can pass between the exposition and the symptom manifestation. However, those effects have not a threshold (no minimum radiation amount with certainly no consequences exists) and do not depend on the irradiation rate but on the total accumulated dose. Tumours and genetic anomalies are called *stochastic effects.*

Deep study were conducted on Hiroshima and Nagasaki survivors: 9000 Japanese were irradiated by neutrons and γ rays. The dose absorbed by each person was estimated from his position at the explosion time; the estimations result uncertain.

Most of the manned space flights happen at LEO (*Low Earth Orbit*) orbits, with altitude between 200 and 500 km. Usually LEO missions (as the ones performed by MIR, the Shuttle and ISS) have an inclination (51.6°); this inclination permits to avoid regions at high latitude, where the geomagnetic cut-off is low and then a higher cosmic ray flux. In fig. 1.12 particle acquisition rate measured on board MIR in function of the orbit during Sileye-2 experiment [34] is showed. The

greatest contribution to the absorbed dose is due to protons trapped in the South Atlantic Anomaly. In order to estimate the total dose the differential LET L(E) has to be integrated according to the formula:

$$D = \int L(E)EdE$$

A dose of 0.516 mGy/day was found, with a rate of 0.120 μGy/min for the galactic component and 4.80 μGy/min for the trapped proton component.

The dose absorbed in orbit is very much higher than on the Earth (about few μGy/year): on board MIR station it resulted equal to 188 mGy/year [35], it is supposed not to be very different from the one on board ISS.

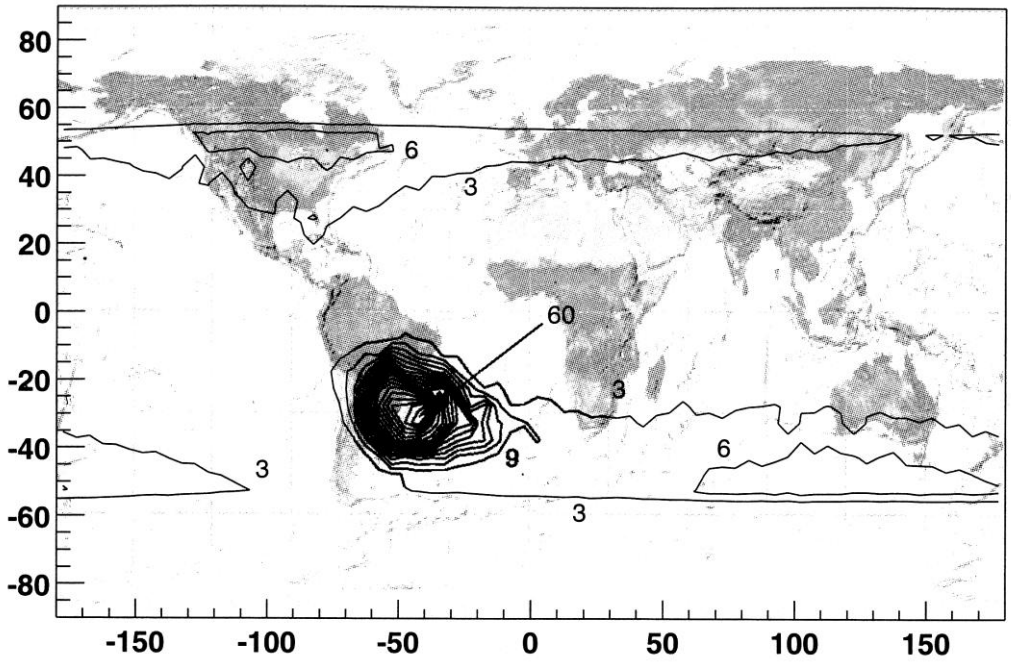

Fig. 1.12 : Particle acquisition rate measured by Sileye-2 experiment dependent on the position. On x axis longitude values are reported, while in y axis there are the latitude values, both measured in degrees. Rate increment in SAA region is visible. Each contour represents a 3 Hz flux increment.

Finally, doses received on orbit are higher in comparison with the ones received in the terrestrial environment; besides that, they sensibly vary with orbit and in presence of solar flares. Then, since the exposition conditions in space are very peculiar, the dose-effects statistics elaborated on Earth are not always usable. Realization of an appropriate dose-effect statistics for the space has to be completed; it will bring to define a risk factor linked to the local flux and to the energy spectrum of the single particle species.

Such a detailed analysis can be performed with active detectors, capable to analyze both spatially and timely the ionizing particle flux.

The most frequent problems experienced by astronauts in microgravity conditions, especially during long duration space flights, are osteoporosis [58] and cataract [59,60]. Some countermeasures are studied in order to contrast those effects and improve the repair mechanisms normally adopted by organisms.

Then, all astronauts refer to perceive 'light flashes' during their missions in space; those flashes are a direct consequence of interaction between cosmic radiation and visual system, but they probably do not imply a permanent damage to the eyes or to the brain. Investigation on so called Light Flashes, described in details in the next chapter, is important in order to point out a specific brain pattern having reference to that interaction and look for similar patterns also in other brain areas.

Chapter 2:
The ALTEA program

The ALTEA program belongs to a research field aimed at studying the interaction between the cosmic radiations and the Central Nervous System and at understanding the possible functional effects emerging during long duration space flights, in particular out the terrestrial magnetosphere, as in a future travel to Mars.
The ALTEA program consists of several experiments, both ground-based and in the space, that will be described in this chapter.
The principal in-space experiment of ALTEA program is ALTEA-Space, a facility devoted to study the charged particles hitting the head of the astronauts and to measure concurrently the electrophysiological activity of the brain, performing in this way the first functional dosimetry measure in the space. Signatures of possible cumulative effects and transient anomalies, that can cause emergency situations in managing the Space Station, are searched. In particular ALTEA-Space wants to find the mechanism(s) inducing the anomalous visual perceptions called Light Flashes investigating the spatial correlation between cosmic radiation and functional responses of bioelectrical brain activity.
The ALTEA program is funded by the Italian Space Agency (ASI).

2.1 Background

The most known effect of interaction with cosmic radiation is the Light Flash (LF) phenomenon. Light Flashes are unexpected visual perceptions caused by cosmic rays interacting with astronauts visual apparatus; these perceptions happen with modality and frequency depending strongly by the subject. Light Flash were theoretically predicted by Tobias [36] in 1952 and in 1969 astronauts Edwin Aldrin, Neil Armstrong e Michael Collins first referred this kind of perceptions in dark conditions during Apollo 11 mission [37, 38]. In the 70s several studies were made on board Apollo [39], Skylab [40] and Apollo-Soyuz [41] and on ground with low energy particle beam on human subjects to understand the causes of Light Flash phenomenon [42,43,44,45]. A nitrogen beam used to scan different eye regions showed that LF seemed to happen mainly in the rear side of the

eyeball, probably due to direct ionization of the retina [46]. Nevertheless this result did not concluded the research because LF observed in space can depend strongly on the different particle species and on their energy, on the orbit and on the spacecraft shielding.

Recently LF have been investigated within Sileye project with Sileye and Sileye2 experiments between 1995 and 2000 [34,47].

Astronauts refer several kind of LF perceptions: bright dots, lines or segments, bright clouds etc., perceivable both with closed and open eyes, usually after dark adaptation (fig. 2.1).

The origin of LF observation is still uncertain, because many mechanisms can cause light perceptions: ionizing radiation, mechanical trauma, electrical currents, magnetic fields, brain cortex stimulation, besides pathological situations.

Some of those has been excluded (electrical currents, magnetic field and mechanical trauma) to cause LF, because easily identifiable and because causing different visual phenomena.

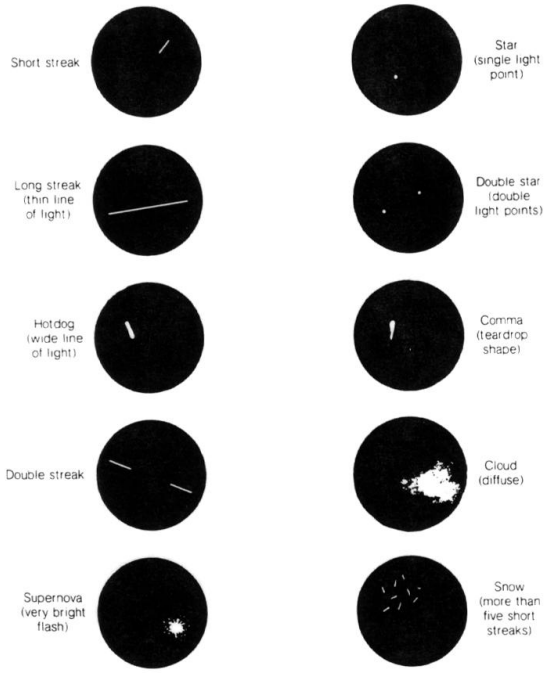

Fig. 2.1: Different kinds of LF as referred by astronauts.

Possible causes of LF are considered:

- ionization caused by heavy nuclei in cosmic rays interacting with the rear part of the eye
- emission of Čerenkov radiation
- direct brain stimuli

- interaction between electrons and vitreous humour

In order to understand LF phenomenon it is important to establish the visual apparatus portion involved in the interaction; retina, vitreous humour, lens, optic nerve or cortex of occipital lobe of the brain are all possible sites of processes bringing to phenomena like LF.

Sileye and Sileye2 experiments showed that a proportionality relation between LF observation frequency and measured particle flux exists, except that in the South Atlantic Anomaly. The observation frequency, however, does not grow during the passages in SAA, so it seems that protons (the main component of particles trapped in the SAA) do not represent the only cause of LF.

A recent work on Sileye2 experiment data shows results compatible in considering both protons and heavy nuclei as capable to cause LF phenomena [48]. In the figure 2.2 the LF observation frequency versus particle flux is showed.

Many questions remain open, as the mechanisms that origin the anomalous perceptions and the nuclei that most probably cause those mechanisms. Then it would be important to understand if interaction with cosmic rays, of which LF are the best known manifestation, can generate other effects, transient or permanent, also in other apparatus'.

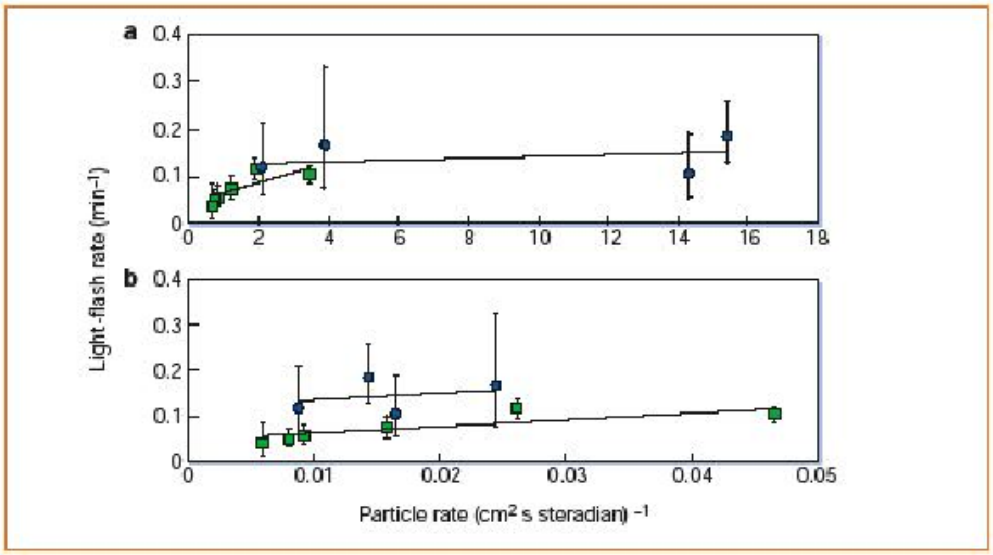

Fig. 2.2: LF observation frequency versus particle flux.

2.2 *The ALTEA program*

The ALTEA program consists in several different experiments devoted to investigate on open questions mentioned in the previous paragraph about the effects of interaction between cosmic radiation and man in the space [49].

The investigation proceeds on different levels: a measure of particle flux on board ISS is the first goal, also to test on ground the shielding effectiveness of different materials. Concurrently the brain activity of astronauts is monitored during their staying on board ISS, while the possible causes of LF perceptions is studied with experiments in the accelerators on ground.

Scientific goals of ALTEA program are summarized as follows:

- to collect the existing knowledge about the interaction between charged particles and the different human functional apparatus', in particular all about LF;
- to define and study objective descriptors of LF;
- to study the interaction between passage of particles and LF;
- to classify the ions depending on interaction risk;
- to perform a measure of radiation environment on board ISS;
- to extend validity of measure of radiation flux on board ISS to different vessels and out of the magnetosphere;
- to find materials acting as an appropriate screen to minimized risks of interaction;
- to test these materials both on ground and in the space.

The ALTEA program includes:

- ALTEA-Space, a facility on board ISS since July 2006;
- different experiment that will use the ALTEA-Space facility;
- ALTEA-ground, ground-based experiments supporting and extending the measures in the space to look for electrophysiological signatures of LF origin.

A brief description of experiments within ALTEA program will follow.

2.2.1 ALTEA-survey

ALTEA-survey is a questionnaire realized the astronauts to gather their experiences about LF [50].

The summary of the answers obtained by a sample of 59 astronauts is the following:

- 47 referred LF perceptions
- LF description: 41 'dark', 11 'dim', 2 'bright'
- no correlation with the work load
- 39 perceived a moving LF
- no perception of vertical motion of LF
- colours: 'white', 6 'yellow', 3 'orange', 3 'blue', 2 'green', 1 'red'
- 8 referred an increased frequency or intensity of LF perception above SAA

2.2.2 Alteino

Alteino-Sileye3, precursor of ALTEA-Space, was the first experiment of the program to work in space between April and May 2002 [51]. The device was brought on board ISS from the Italian astronaut Roberto Vittori with the Russian vessel Soyuz during Marco Polo mission. Alteino consists of a particle detector, a silicon telescope similar to the ones used in ALTEA, an electroencephalograph (EEG) and a pushbutton (fig. 2.3). Scientific goals of Alteino-Sileye3 are analogous to the ones of ALTEA-Space: to monitor the electrophysiological astronaut brain dynamics, in particular during LF perceptions, and to measure particle flux on board ISS (fig. 2.4).
Alteino-Sileye3 gathered 131 hours of data, in that time 44 LF observations occurred [52]. Data suffered from a low statistics; Alteino-Sileye3 is still on board ISS and is collecting new data since December 2005.
Beyond the low statistics, Alteino data are not really effective to correlate particle flux, EEG activity and LF because of the not optimal angular coverage of particle detector, the absence of a spatial correlation between astronaut and particle detector and the absence of a monitor system of visual apparatus. As it will be showed in the next chapters, ALTEA-Space hardware overcame these limitations: it has a large angular coverage (particle detectors are disposed on a helmet-shaped support to cover astronaut's head) and the position of the head inside the helmet is fixed. Then a method of stimulation and monitoring of visual system is included.

Fig. 2.3: Alteino-Sileye3: particle detector and Electroencephalograph.

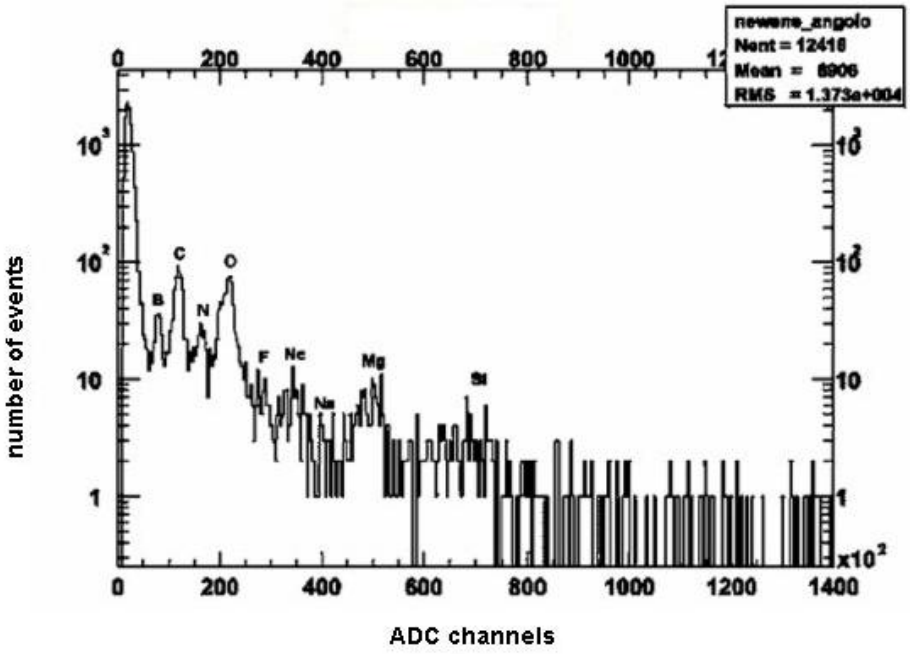

Fig. 2.4: Energy distribution of events acquired by Alteino-Sileye3 during Marco Polo mission.

2.2.3 ALTEA-MICE

ALTEA-MICE (*Mice intermittent Irradiation with Concurrent Electrophysiological monitoring*) supports the ALTEA-Space study on astronauts. Scientific goals of ALTEA-MICE are: investigation on effects induced by heavy ions on the retina of mice normal and with retinal defects, definition of experimental conditions reliable for the space research, development of animal models to study the physiological consequences for humans during space travels [53].

The experiment consists in irradiation of mice with charged ions at different fluences; during irradiation electroencephalographic activity of mice is monitored with electrodes implanted in the skull. Measurements are taking place in accelerators of BNL at Brookhaven, New York and GSI at Darmstadt.

From the analysis of data taken in the last run at GSI, the first electrophysiological evidence of the effect of charged particle passage was found; the dependence of the brain signal amplitude from particle fluence was also found out.

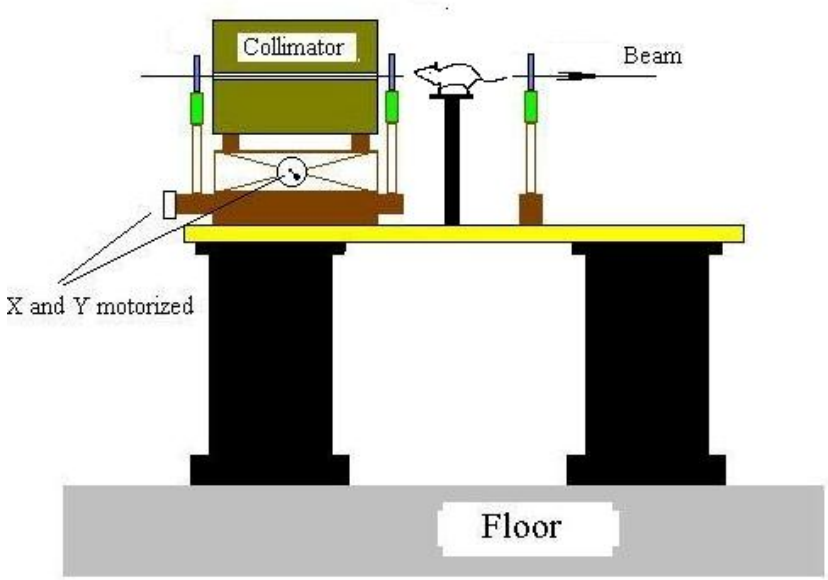

Fig. 2.5: Cartoon of the positioning of the mouse in front of the beam.

2.2.4 ALTEA-HIT

ALTEA-HIT (Heavy Ion Therapy) is based on an observation: people undergoing to hadron-therapy because having a brain cancer (the tumour is irradiated with charged ion beam at controlled energies and intensities) refer sometimes to have light flash perceptions during the therapy.
ALTEA-HIT involves few consenting patients undergoing hadron-therapy at GSI in Darmstadt; these patients are invited to refer their perceptions of light flash pushing a pushbutton. Concurrently the pushbutton signal, the position, the beam energy and the time are acquired. First results showed signatures of LF; then a correlation between LF and beam energy and a time correlation with the coming bursts were found. Some patients referred a decreasing in LF intensity in time. From data analysis a possible suppression of brain alfa waves in correspondence to charged particle passage was theorized [54].

2.2.5 ALTEA-Biophys

ALTEA-Biophys searches for causes of LF perceptions with chemical and biological approaches; in particular, the rhodopsin is studied. Rhodopsin is a molecule directly involved in the photo-

transduction, ALLA BASE of visual process. Rhodopsin is founded in the retina and it is activated (isomerised) by photons.

In the experiments carried out within ALTEA-Biophys rhodopsin, extracted by bovine eyes and purified with standard methods, is irradiated with C or Cr ions at different energies. Then the number of activated and denaturated molecules are counted and their percentage is checked; by a quantitative comparison between the light and the irradiation with charged particles it could be understood if the eventual rhodopsin isomerisation caused by charged particle can be responsible of anomalous perceptions in space.

Experiments performed since now showed the validity of this approach and first results indicated a probable interaction of radiation and the isomeric structure of rhodopsin, that can results functionally compromised at high absorbed doses.

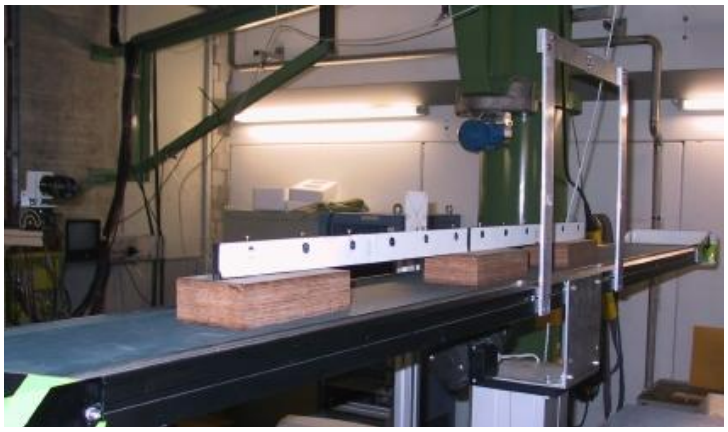

Fig. 2.6 : Positioning of rhodopsin vials at GSI.

Chapter 3

The ALTEA-Space facility

The ALTEA-Space facility (from now called simply ALTEA) was planned to perform a multidisciplinary investigation, in particular it is aimed to get a measurement of cosmic radiation and to monitor the human brain activity in microgravity conditions. Because of this complexity, ALTEA is constituted by different subsystems:

1. Silicon Detector Subsystem (SDS)
2. Push Button subsystem (PBS)
3. Visual Stimulator Subsystem (VSS)
4. ElectroEncephaloGraph Subsystem (EEGS)

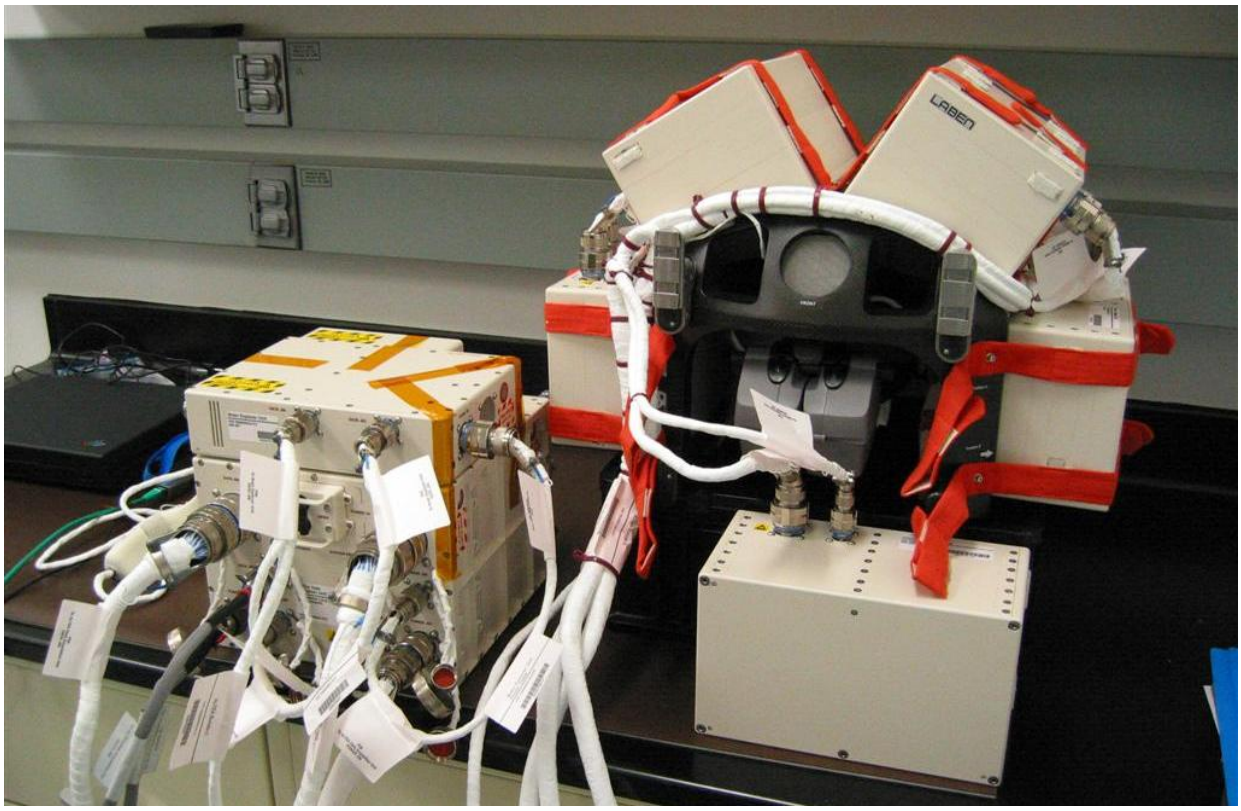

Fig. 3.1: ALTEA Flight Model during PTCS test.

In fig. 3.1 a picture of ALTEA flight model is showed, most of its components are visible. In this chapter a general description of the facility and of all its components will be given. The system for particle detection will be described in details because it produces data studied in this thesis.
Experimental configurations of measure will be also introduced.
Each subsystem is devoted to specific measurements and checks. To guarantee a high level of flexibility to the facility, all subsystems can be used both independently and in any combination; in particular it is possible they work concurrently with the same clock, with a millisecond synchrony.
From a mechanical point of view, ALTEA is composed by the following units:

- Laptop (LTU)
- Data Acquisition Unit (DAU)
- Six Silicon Detector Unit (SDU)
- Push Button Unit (PB)
- Head Mounted Display Unit (HMD)
- Brain Explorer Unit (BEU)
- Electroencephalografic Cap (EEG Cap)
- Support Structure (SS)
- Harness (HNS)

In the table 3.1 relations between different units and subsystems are showed.

	LTU	DAU	6 SDU	PB	HMD	BEU	EEG Cap	SS
SDS	X	X	X					X
PBS	X	X		X				
VSS	X	X			X	X		
EEGS	X	X				X	X	

Tab. 3.1: Relations between different units and subsystems composing ALTEA.

3.1 Operative Modes

From an operative point of view, ALTEA has two possible functioning modes: DOSI and CNSM. DOSI will work continuously for at least six months, interrupted only to run the three foreseen CNSM sessions.

3.1.1 DOSI

In this configuration, ALTEA will perform automatically dosimetry measures on ISS. This activity is not manned, the astronaut is needed only during configuration and activation and during deactivation. In DOSI mode the SDS subsystem is the only active system with the DAU and the Laptop. Acquired data are transmitted in real-time from DAU through RIC without storing them on Laptop hard-disk. In the figure 3.2 ALTEA is showed connected to the EXPRESS Rack of USLab, as for the DOSI configuration. Structure is tilted on the rack to minimize protrusion.

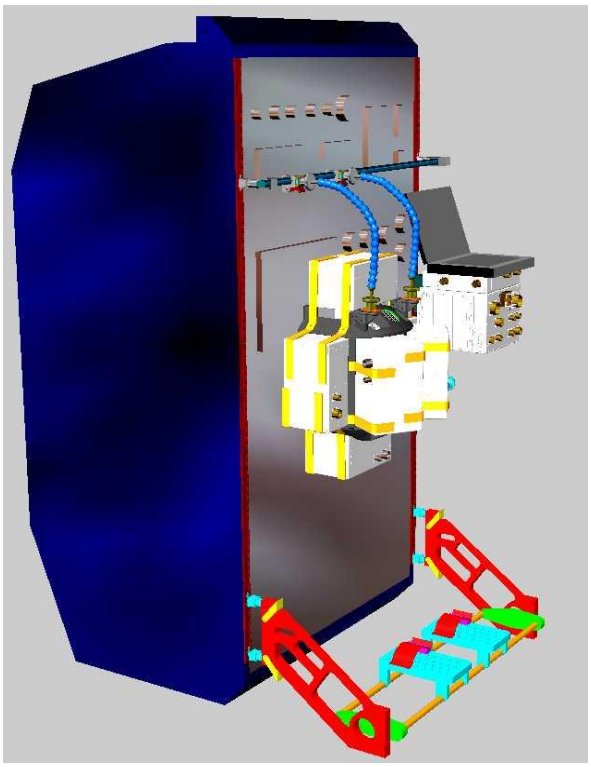

Fig. 3.2: ALTEA in DOSI mode.

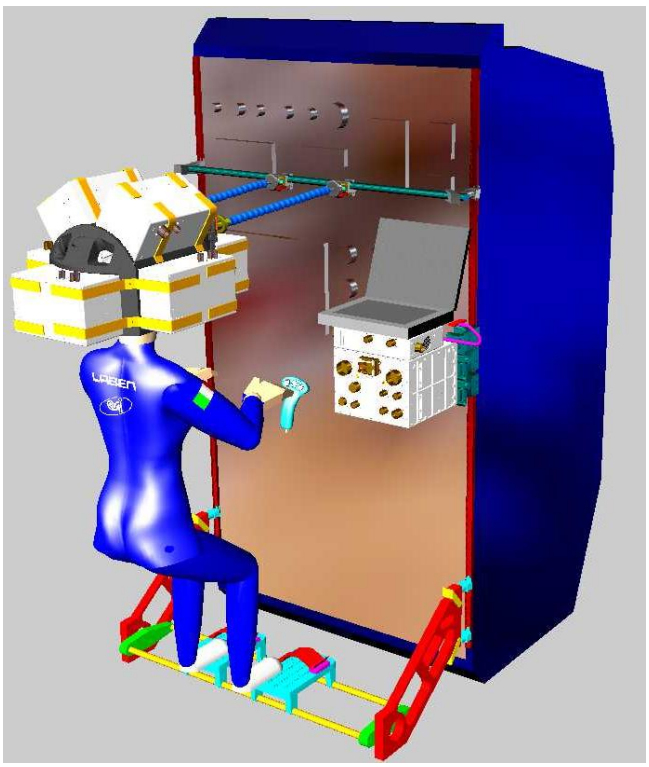

Fig. 3.3: ALTEA in CNSM mode.

3.1.2 CNSM

In CNSM mode, ALTEA monitors interactions between particle flux that constituting cosmic radiation and central nervous system. During the CNSM sessions, a crew member is needed: he or she wears the EEG cap, slides into the structure, puts the visor in front of the eyes and grasps the

pushbutton. Each session lasts for 90 minutes, the time needed to the ISS to complete an orbit around the Earth.
There are an initial set-up and a final set-down before and after the measure session; during these operations another crew member is needed to assist the one under measure. In the set-up and set-down operations astronauts have an audio-video connection to the ground-support team.
In the CNSM configuration all ALTEA subsystems are active. Data are stored on the Laptop hard-disk and downloaded via RIC to the ground at the end of each session on astronaut's request. In the fig. 3.3 there is a cartoon of ALTEA in CNSM mode; the connection between the device and the Express Rack in the USLab is visible.

3.2 System description

All single subsystems composing ALTEA will be briefly described. All seen in table 3.1, all subsystems include DAU and Laptop.

3.2.1 SDS

The SDS subsystem is composed by the DAU, the support structure, 6 SDU (Silicon Detector Unit) and the Laptop (LTU). The six SDUs are silicon telescopes mounted on the support structure so to maximize the head angular coverage.
In fig. 3.4 the six SDUs on the support structure is visible. The SDU will described in detail in the paragraph 3.3.1.
This subsystem is devoted to detect particles releasing energy between 3 and 2400 MIP (Minimum Ionizing Particles, 1 MIP = 30400e^- = 109 keV in 380 μm of silicon); in particular, the helmet shape of the entire structure allows to reveal particle passing through the astronaut's head. Each SDU can reveal trajectory and energy deposited by particles in the silicon planes and communicates with the DAU via a dedicated serial interface.

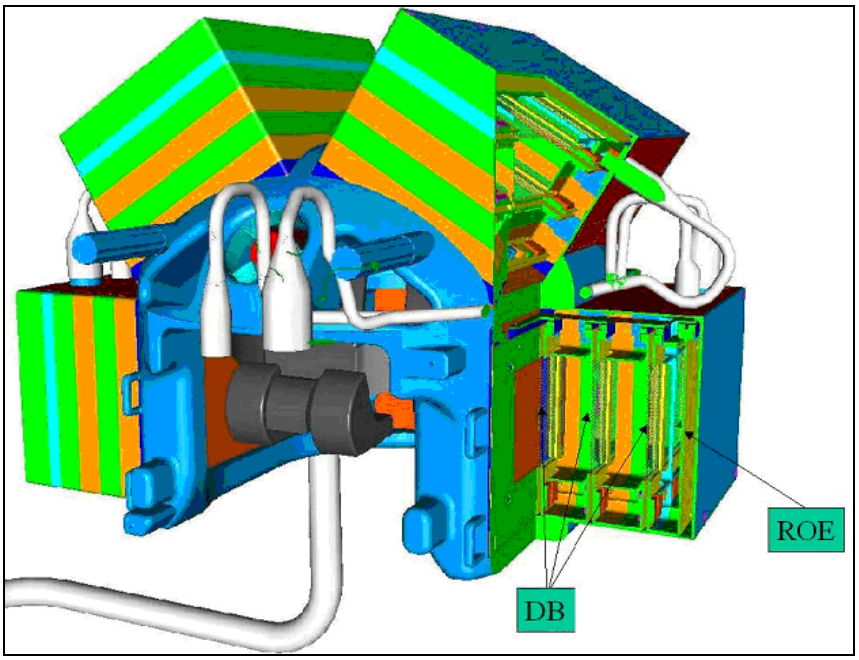

Fig. 3.4: Assembly of SDS.

The DAU adds the time information and transfers data via Ethernet to the Laptop, if ALTEA is in CNSM configuration, or directly to the ISS, if in DOSI configuration. During CNSM mode, the Laptop stores data that are then transferred via Ethernet to the ISS at the end of each session on astronaut's request.

3.2.2 PBS

The pushbutton system (PBS) is for the astronaut to signal the Light Flash perceptions. The PBS is constituted by the pushbutton (PB), the DAU and the Laptop. The PB consists in a three button joystick; it is grasped by the astronaut during the CNSM sessions and when it is pressed or released the DAU tags data with the time and the Laptop records them. During a CNSM session one of the button is to signal the LF, the other two are to confirm or cancel the perception.

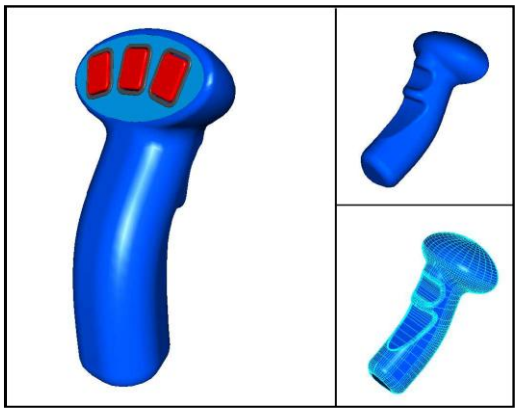

Fig. 3.5: PushButton

Fig. 3.6: Head Mounted Display

3.2.3 VSS

The visual stimulator (VSS) allows a complete stimulation of the visual system of astronaut. It is composed by a goggle HMD (fig. 3.6), the video board in the BEU and the DAU. The goggle HMD contains two miniaturized displays LCD, one for each eye; the BEU includes the electronics (VI board) to guide the HMD with a VGA signal; the VI is configured through a serial connection RS-232 by the DAU. The DAU and the BEU exchange also trigger signals to synchronize the visual stimulator and the EEGS.

3.2.4 EEGS

The EEGS records the electroencephalograph of the astronaut under test to monitor the dynamics of the brain signal. It consists in the EEG cap, the BEU and the LTU. The EEG cap includes also the electrodes, that are mounted on the cap itself to reduce the time needed to their correct positioning. The BEU includes the electronic board (BEM), that permits the EEG signal amplification, the analogical filtering and the analogical/digital conversion.

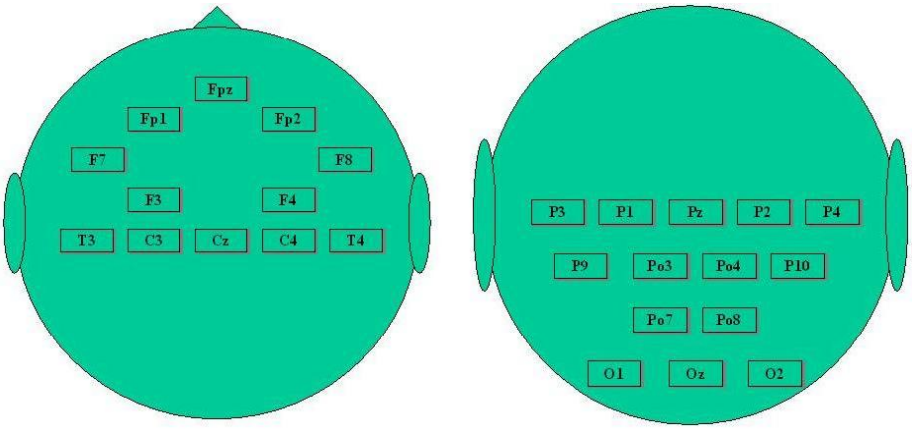

Fig. 3.7 Cartoon of the electrode position on astronaut's head.

The BEU transmits the digitalized signal to the Laptop through a dedicated optical fibre connection. The Laptop storages data and transfer them via Ethernet to the ISS at the end of the CNSM session. The DAU and the BEU exchange also signals to synchronize the EEG acquisition and particle data acquired by the SDS. In fig. 3.7 the position of the EEG electrodes is showed.

3.2.5 DAU

The DAU is devoted to give power, to synchronize and to gather data of all ALTEA units. The only exception are the EEG data that are acquired from the Laptop through a dedicated fibre optical connection. The DAU is connected to the ISS with a single ethernet connection; in fact it is not directly connected to the Laptop, but it communicates with it through the net of the station. In the figure 3.8 one of the front panels is showed; in the panel all the connectors for data and power are visible.

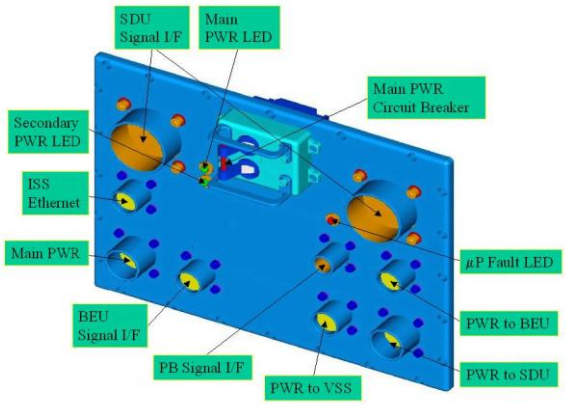

Fig. 3.8: Front panel of the DAU.

3.2.6 LapTop Unit (LTU)

The Laptop used for ALTEA is an IBM 760-XD supplied by NASA.

3.2.7 ALTEA block diagram

In figure 3.9 the block diagram of the facility is showed; the connections between the different units are highlighted.

3.3 Particle detection system (SDS)

The SDS, system devoted to detect particles, will be now described in details. As already mentioned, the main goal of the particular structure of the SDS is to obtain the biggest possible head coverage, considering the dimensional bonds of each SDU. The bidirectional geometrical factor for the SDS results 1071 cm^2 sr. Figure 3.3 shows as astronaut will be into the helmet-shaped structure during CNSM sessions.

Boxes are positioned as near as possible to the head (see fig. 3.4) to minimize the error in the reconstruction of intersection point between particle trajectories and the head itself. The read out electronic board (ROE, *Read Out Electronics*), instead, is placed at the outer side in respect to the head not to influence particle trajectories. In fig. 3.10 the 3D scheme of SDS is showed and the open silicon detectors are visible.

The SDU position on the support structure (SS) is fixed with specific pins and velcro strips so to guarantee the structure solidity. Each box has a specific assembly site on SS.

3.3.1 SDU

Each SDU is composed of six silicon planes alternatively oriented along X and Y directions. On each plane there are two 8x8 cm^2 silicon chips 380 μm thick positioned side by side with a 5.5 mm gap between. Each silicon chip is segmented in 32 strips with a pitch of 2.5 mm and each XY plane

couple contains a 32x64 strip grid. The distance between an X plane and the correspondent Y plane is 3.75 mm, while the distance between each XY couple is 37.5 mm.

The outer box of the SDU is made of aluminium 1.3 mm thick.

The bidirectional geometrical factor for a single SDU is 250 cm^2 sr, the maximum angular reconstruction error is ±1.8°.

Each silicon wafer is managed by two integrated chip CR2.0, so a plane has four chips, and each chip has 16 channels. The internal design of the chip is showed in fig. 3.11.

A channel consists in a charge-sensitive preamplifier, a forming amplifier, a track-and-hold circuit and a switch. The output analogical signal coming from each channel of CR2.0 is sent to a multiplexer that allows to select the channel to be sent to the 12 bit ADC that is in the ROE (*Read Out Electronics*), containing all read out electronics. The ROE is positioned as a seventh plane in the DB stack.

Self Trigger signals are compared with a threshold signal selectable via software between predefined values. As can be seen in fig.3.11, the trigger signal is formed by summing signals of four channels; if there is a trigger signal, the system reads the four correspondent channels. A direct consequence of this design is that the sum of four signals above the selected threshold value can trigger the system also if no one of the signals is big enough.

The trigger signals coming from the two silicon wafers form a plane trigger. Only signals from X planes can trigger; these signals can be combined with logic AND or OR.

All analogical signals arriving to the ROE are converted by the 12 bit ADC converter. The energy resolution is 0.64 MIP/ADC channel (MIP, *Minimum Ionizing Particle*, 1 MIP = 30400e^- = 109 keV in 380 μm of silicon). The dynamic range of the instrument varies between 5 and 2400 MIP.

All analogical signals arriving to the ROE are converted by the 12 bit ADC converter. The energy resolution is 0.64 MIP/ADC channel (MIP, *Minimum Ionizing Particle*, 1 MIP = 30400e^- = 109 keV in 380 μm of silicon). The dynamic range of the instrument varies between 5 and 2400 MIP.

In figures 3.12 and 3.13 are showed a schematic lateral view of a SDU, with silicon planes and the ROE, and the scheme of a SDU seen from the above (position of connectors, CR2.0 and the strip numbers are also visible. It is important to notice that the strip reading order does not follow the logic consecutive numbers (strip 0-63), but it is the one showed in table 3.2.

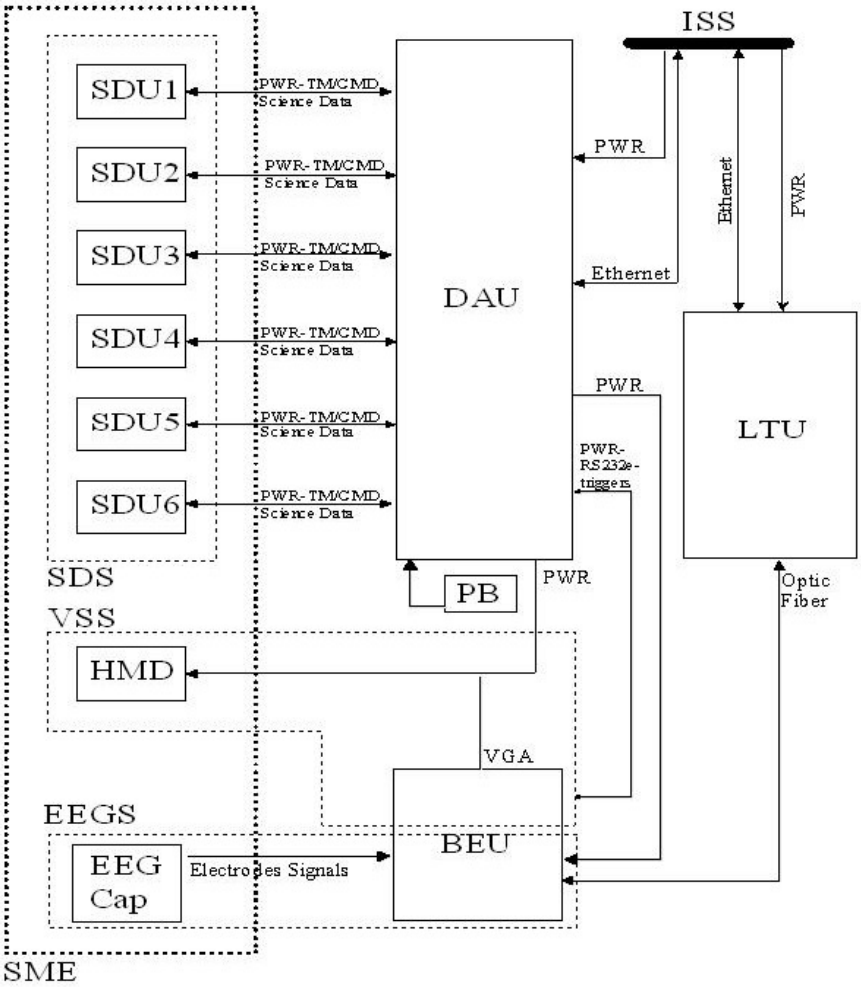

Fig. 3.9 : ALTEA block diagram; subsystems are showed.

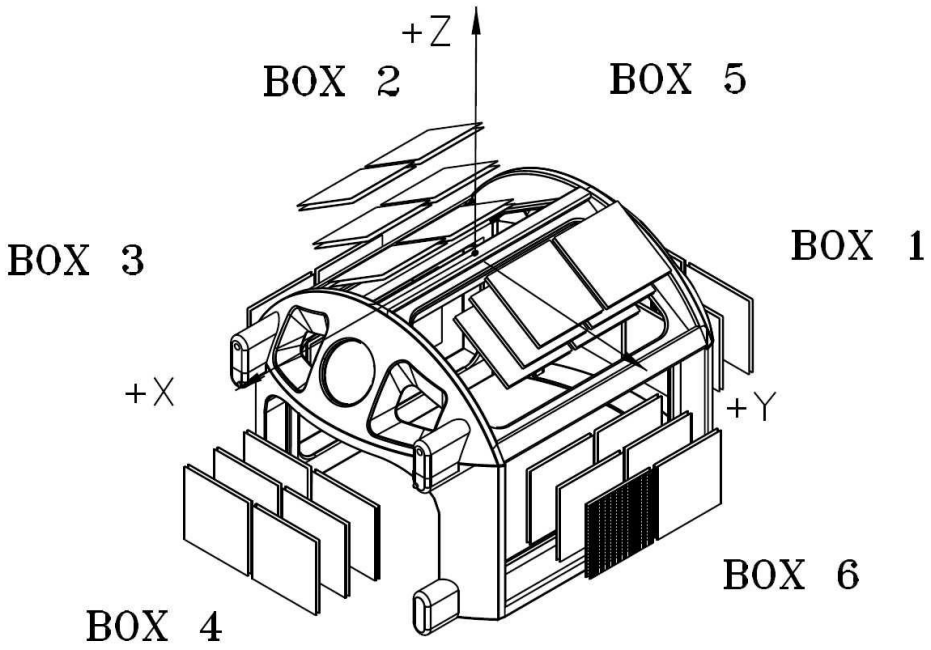

Fig. 3.10: Scheme of silicon detector and SDU numbers.

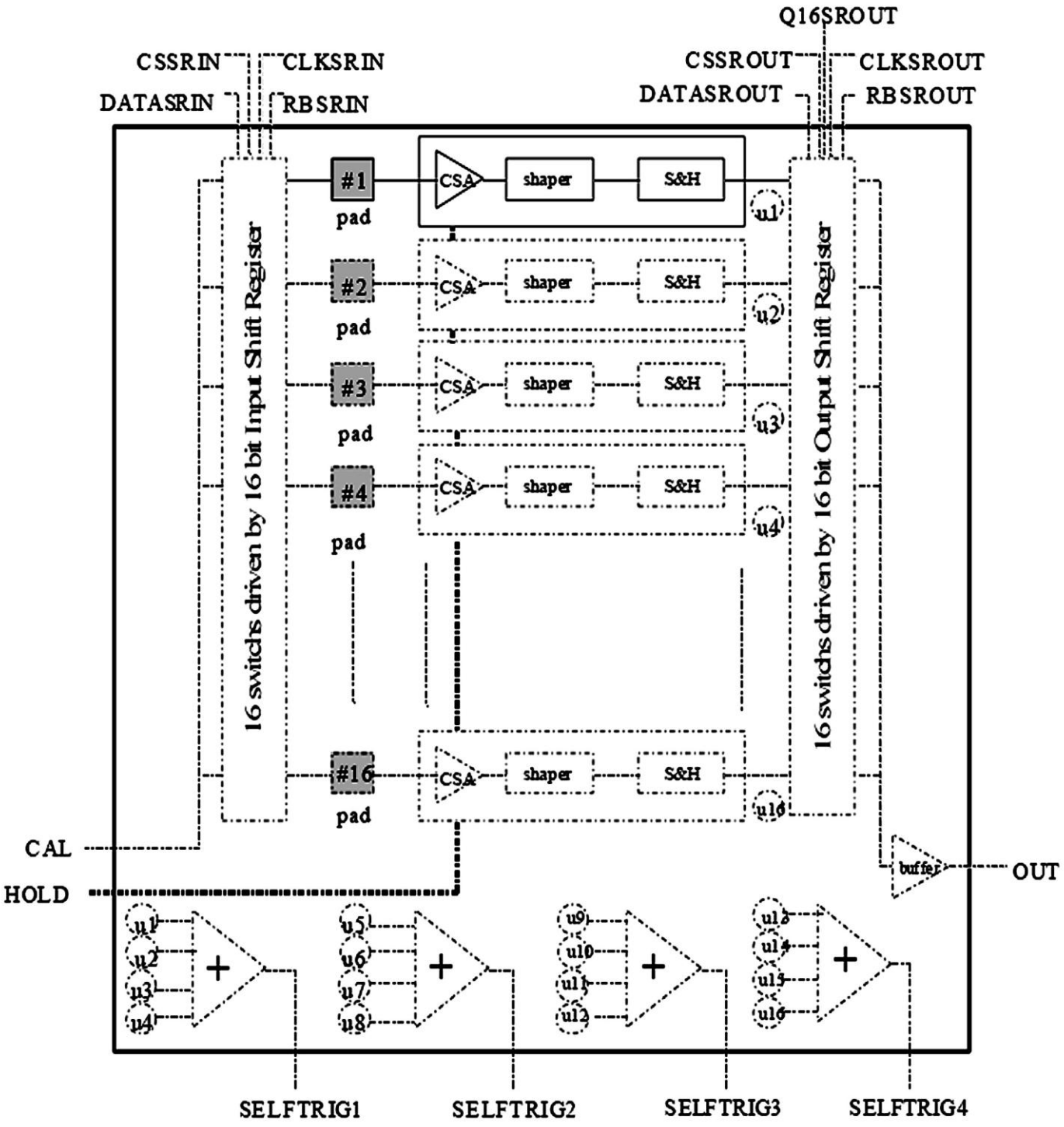

Fig. 3.11: Internal view of a CR2.0

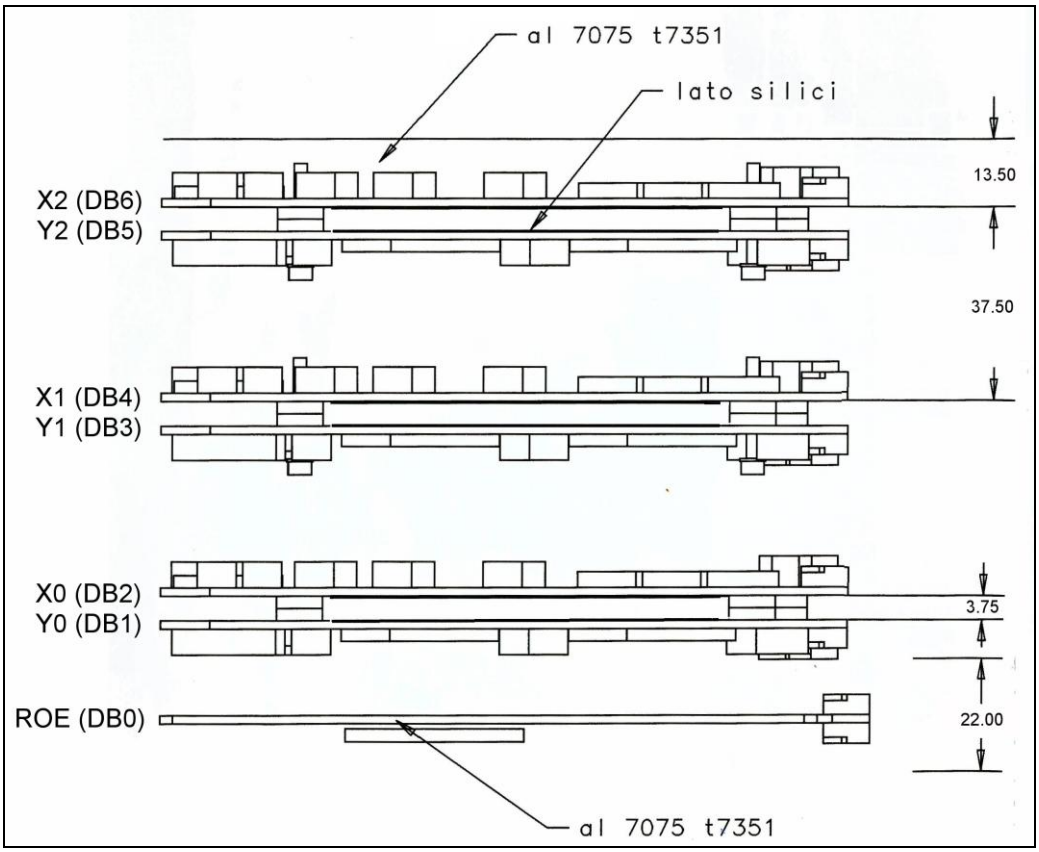

Fig. 3.12: Lateral view of a SDU; the interplanar distances are reported.

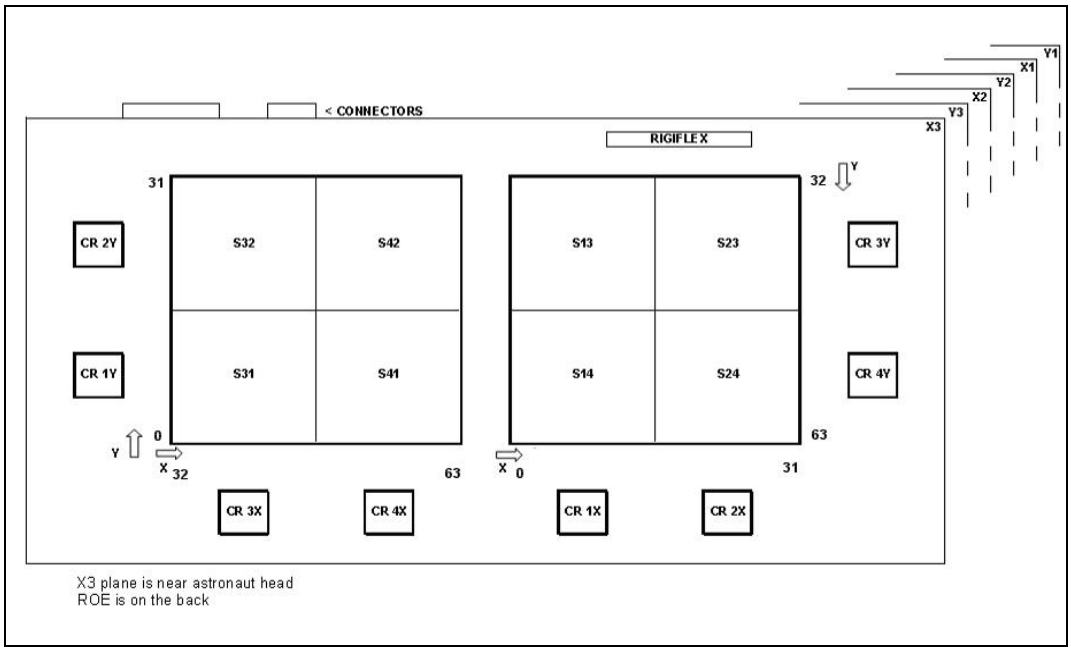

Fig. 3.13: Scheme of a DB from above; peculiar strip numbers are showed.

	DBX DB2	DBX DB4	DBX DB6	DBY DB1	DBY DB3	DBY DB5
S0	2	4	6	1	3	5
S1	26	28	30	25	27	29
S2	50	52	54	49	51	53
S3	74	76	78	73	75	77
S4	98	100	102	97	99	101
S5	122	124	126	121	123	125
S6	146	148	150	145	147	149
S7	170	172	174	169	171	173
S8	194	196	198	193	195	197
S9	218	220	222	217	219	221
S10	242	244	246	241	243	245
S11	266	268	270	265	267	269
S12	290	292	294	289	291	293
S13	314	316	318	313	315	317
S14	338	340	342	337	339	341
S15	362	364	366	361	363	365
S16	8	10	12	7	9	11
S17	32	34	36	31	33	35
S18	56	58	60	55	57	59
S19	80	82	84	79	81	83
S20	104	106	108	103	105	107
S21	128	130	132	127	129	131
S22	152	154	156	151	153	155
S23	176	178	180	175	177	179
S24	200	202	204	199	201	203
S25	224	226	228	223	225	227
S26	248	250	252	247	249	251
S27	272	274	276	271	273	275
S28	296	298	300	295	297	299
S29	320	322	324	319	321	323
S30	344	346	348	343	345	347
S31	368	370	372	367	369	371
S32	14	16	18	13	15	17
S33	38	40	42	37	39	41
S34	62	64	66	61	63	65
S35	86	88	90	85	87	89
S36	110	112	114	109	111	113
S37	134	136	138	133	135	137
S38	158	160	162	157	159	161
S39	182	184	186	181	183	185
S40	206	208	210	205	207	209
S41	230	232	234	229	231	233
S42	254	256	258	253	255	257
S43	278	280	282	277	279	281
S44	302	304	306	301	303	305
S45	326	328	330	325	327	329
S46	350	352	354	349	351	353
S47	374	376	378	373	375	377
S48	20	22	24	19	21	23
S49	44	46	48	43	45	47
S50	68	70	72	67	69	71
S51	92	94	96	91	93	95
S52	116	118	120	115	117	119
S53	140	142	144	139	141	143
S54	164	166	168	163	165	167
S55	188	190	192	187	189	191
S56	212	214	216	211	213	215
S57	236	238	240	235	237	239
S58	260	262	264	259	261	263
S59	284	286	288	283	285	287
S60	308	310	312	307	309	311
S61	332	334	336	331	333	335
S62	356	358	360	355	357	359
S63	380	382	384	379	381	383

Table 3.2: Reading order of the strips.

3.3.2 Particles and energy intervals detectable

An important feature of the detection system of SDS consists in the particle species and energy detectable. Energy losses for particle from proton to Molybdenum (Z=42) were simulated with the Montecarlo code SRIM2003: detection range of single particle was obtained considering the maximum incidence energy (corresponding to the minimum energy loss) that allows the particle going through the six silicon planes and the minimum incidence energy (corresponding to the maximum energy loss) that releases in silicon energy of the order of magnitude of the saturation energy of the device.

Dynamic range of the device varies between 5 and 2400 MIP, with energy resolution of 0.63 MIP/ADC channel. The MIP is equivalent to the energy loss of 109 keV in 380 μm of silicon (see Appendix B).

Two different threshold values were considered for the minimum energy loss, 5 and 10 MIP, corresponding to 0.14 eV/Å and 0.28 eV/Å respectively, while the saturation value of 2400 MIP corresponds to 68 eV/Å.

In table 3.3 the maximum and minimum incidence energy for the considered nuclei are showed. It is important to notice that at 10 MIP threshold all nuclei heavier than Helium are detected at the minimum allowed energy loss (corresponding to 2 GeV/n), while at 5 MIP threshold only protons at minimum are detected. Talking about the maximum energy loss, nuclei until Carbon release energy does not reach the saturation value because they stop in the last silicon plane, while Molybdenum is the heaviest detectable nucleus because also at the minimum energy loss (at 2 GeV/n) it releases an energy near to the saturation value.

Nucleus	**Maximum Energy (MeV/n)**		**Minimum Energy (MeV/n)**
	5 MIP Threshold	**10 MIP Threshold**	
H	100	45	25*
^{4}He	n.a.	250	25*
^{7}Li	n.a.	n.a.	28*
^{12}C	n.a.	n.a.	45*
^{48}Ti	n.a.	n.a.	145
^{56}Fe	n.a.	n.a.	190
^{98}Mo	n.a.	n.a.	2000

Tab. 3.3: Range of detectable energy for different particles. In the Minimum Energy column (corresponding to the maximum energy loss) nuclei indicated with (*) stop in the last plane, while the rest reach the saturation energy.

In the figures 3.14 and 3.15 the plots of Montecarlo simulations of energy loss of H, He, Li and C are showed in conditions of the maximum and minimum energy loss presented in the table.

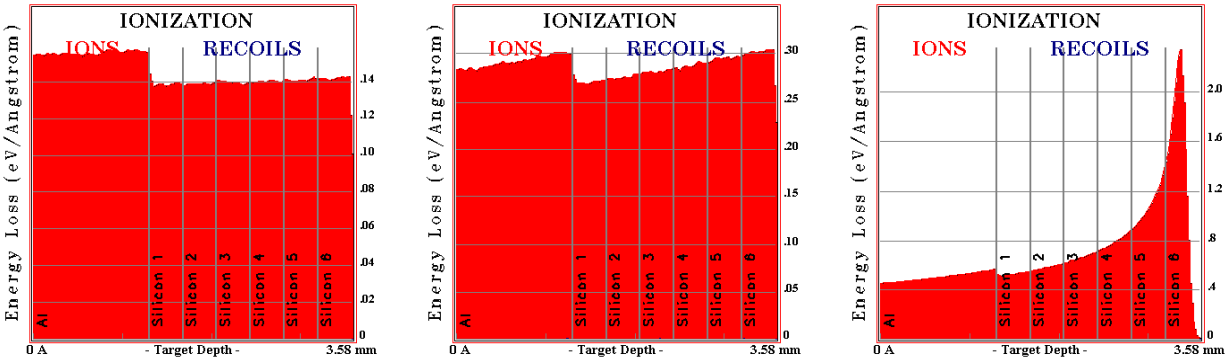

Fig. 3.14: H energy losses at 100 MeV, 45 MeV and at 25 MeV

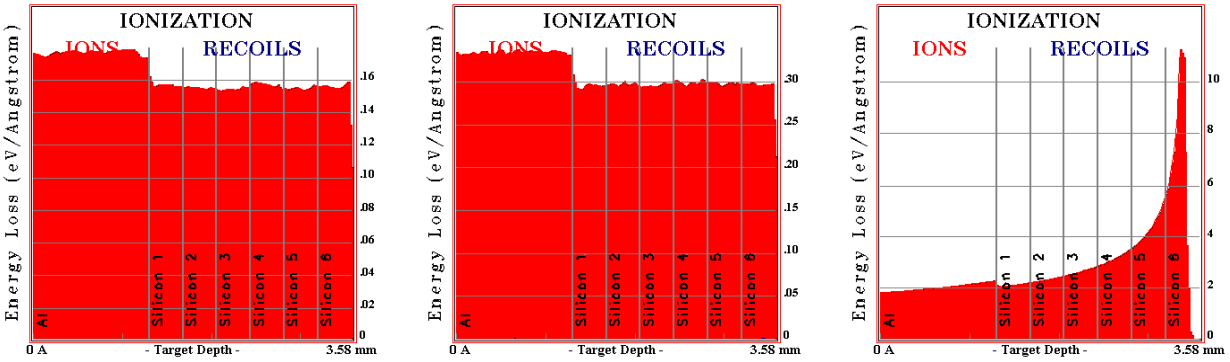

Fig. 3.15: ^{4}He energy losses at 2 GeV/n, 250 MeV/n and at 25 MeV/n

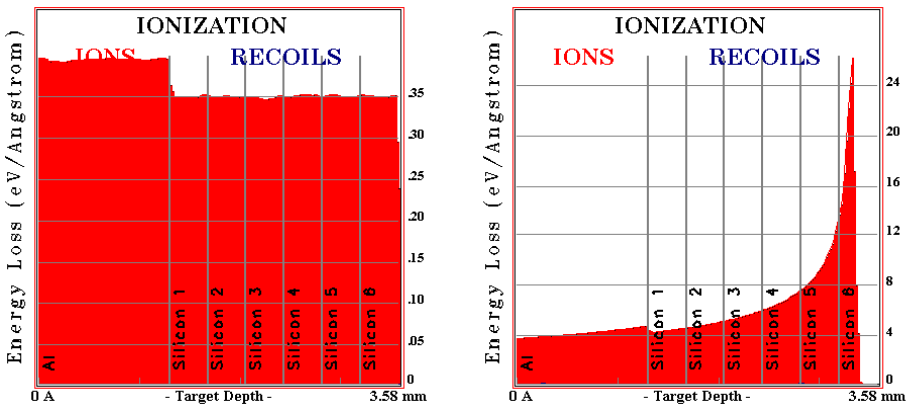

Fig. 3.16: ^{7}Li energy losses at 2 GeV/n and at 28 MeV/n

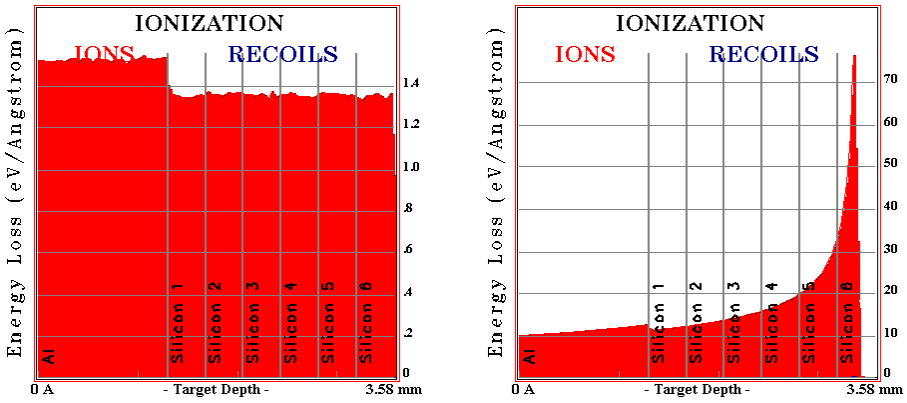

Fig. 3.17: ^{12}C energy losses at 2 GeV/n and at 45 MeV/n

Chapter 4:
Expected particle simulated with CREME

Before starting in describing the work done concerning detector calibration, simulation and preparation of ALTEA operations, the simulation considered to give an estimation of the expected particle number impinging the International Space Station will be described. The simulation was performed using CREME96. A comparison between simulated data and data acquired with Alteino-Sileye3 inside ISS during Marco Polo mission in 2002 will be also given, together with an evaluation of the Light Flashes referred during that mission and the number and the species of expected and found particles.

4.1 Simulation: number of expected particles by CREME

In this paragraph the simulation performed to estimate the rate of particle hitting the ISS will be described.

Nuclei of Hydrogen (protons), Helium, Carbon, Nitrogen and Oxygen were considered; they are the most abundant in cosmic rays. Nuclei of Fluorine, Neon, Sodium, Magnesium, Silicon, Sulfur and Iron were considered too, they are less abundant than the first ones but they are detectable with Sileye experiments (and with ALTEA).

Calculation was performed considering first of all the different fluxes expected by CREME, a software suite developed with NASA support devoted to the calculation of cosmic ray fluxes and magnetic field values in a certain orbit; CREME considers also the convolution of particle flux value and the magnetic field values so to keep in consideration the geomagnetic cut-off, in order to have a realistic estimation of expected particles.

Considering a typical LEO (*Low Earth Orbit*) orbit, CREME provides for different nuclei with energy between 1 and 10^5 MeV/nucleon the differential fluxes showed in fig. 4.1.

The integrals of curves relative to the examined nuclei were estimated considering the sum of the trapeze areas obtained selecting the plot portion below the differential flux curve of each nucleus.

In the calculation two energy ranges were considered for the kinetic energy of incident particles: between 1 and 2000 MeV/nucleon and between 1 and 10000 MeV/nucleon.

In fig. 4.2 the trend of expected number of Carbon nuclei in solid angle, time and kinetic energy units versus kinetic energy of particles incident on the whole energy range is showed; in fig. 4.3 the same curve is zoomed.

Considering the flux through a little sphere of unitary radius (1 cm) expected values reported in table 4.1 are obtained.

Varying the energetic range for kinetic energy of incident particles, the number of expected particle per second considerably changes, in some case it can be two times the first evaluated number. It appears really important selecting correctly the energetic range to consider, optimizing the choice knowing the dynamic range of the detector that will be used to detect the particles.

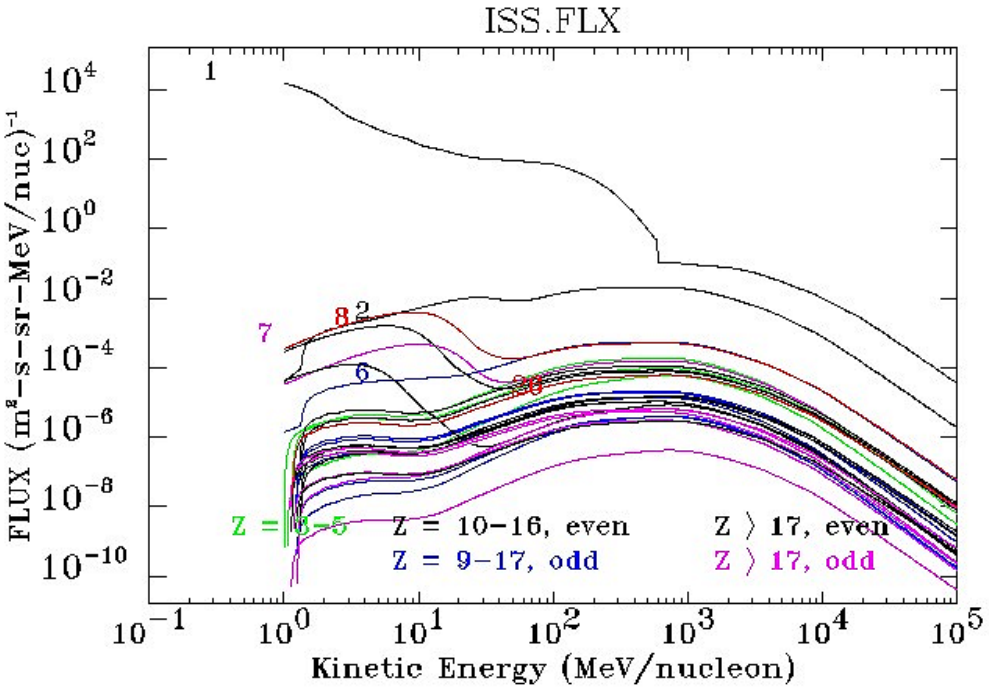

Fig.4.1: Differential fluxes for different nuclei calculated by CREME.

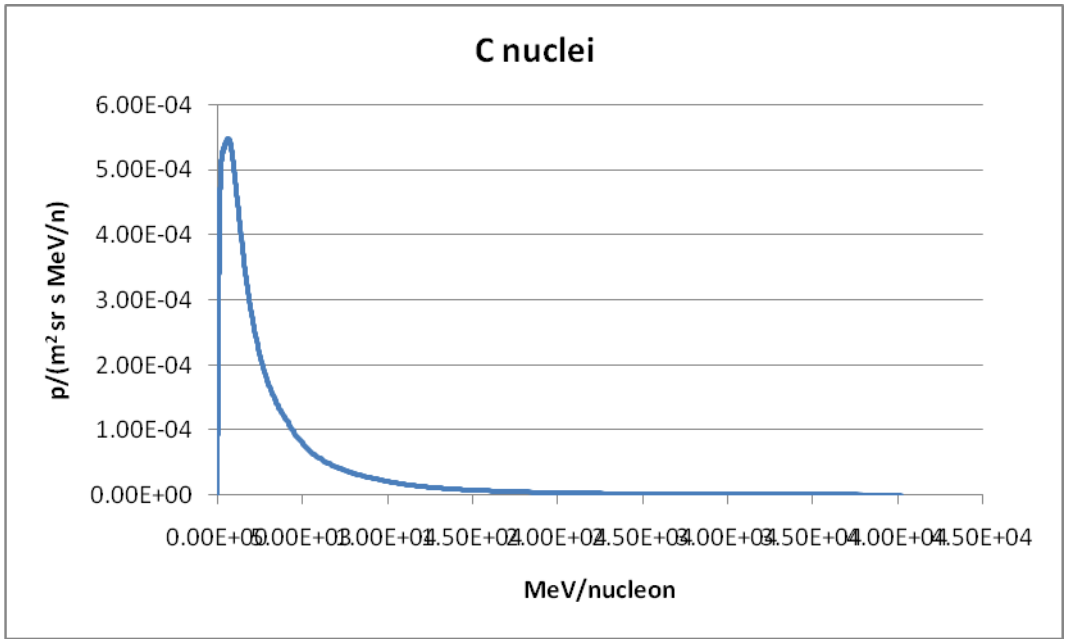

Fig. 4.2: Differential theoretical flux of C nuclei versus kinetic energy of incident particles.

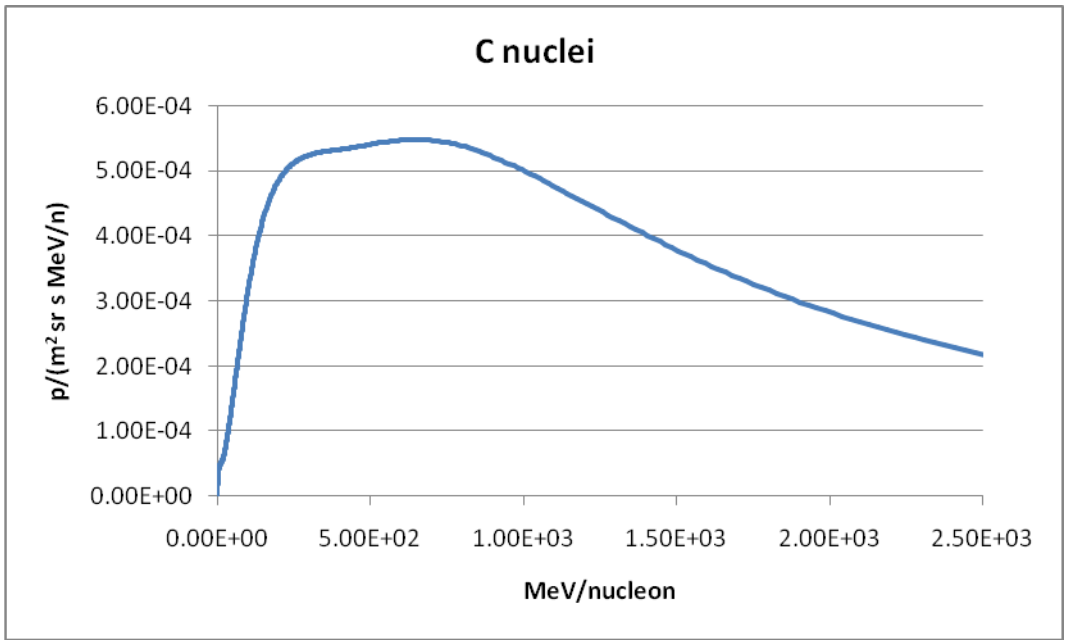

Fig. 3: Differential theoretical flux of C nuclei in the low energy range.

nucleus	atomic number	energetic range	
		1 – 2000 MeV/nucleon	1 – 10000 MeV/nucleon
		expected flux (p/s)	expected flux (p/s)
H	1	$4.15 \cdot 10^{1}$	$4.18 \cdot 10^{1}$
He	2	$4.06 \cdot 10^{-2}$	$7.17 \cdot 10^{-2}$
C	6	$1.08 \cdot 10^{-3}$	$1.93 \cdot 10^{-3}$
N	7	$3.12 \cdot 10^{-4}$	$5.29 \cdot 10^{-4}$
O	8	$1.09 \cdot 10^{-3}$	$1.93 \cdot 10^{-3}$
F	9	$2.61 \cdot 10^{-5}$	$4.29 \cdot 10^{-5}$
Ne	10	$1.88 \cdot 10^{-4}$	$3.19 \cdot 10^{-4}$
Na	11	$3.73 \cdot 10^{-5}$	$6.23 \cdot 10^{-5}$
Mg	12	$2.18 \cdot 10^{-4}$	$3.95 \cdot 10^{-4}$
Si	14	$1.54 \cdot 10^{-4}$	$2.88 \cdot 10^{-4}$
S	16	$3.01 \cdot 10^{-5}$	$5.67 \cdot 10^{-4}$
Fe	26	$1.22 \cdot 10^{-4}$	$2.30 \cdot 10^{-4}$

Table 4.1: Particle fluxes expected inside a 1 cm radius sphere in two energetic ranges.

4.2 Comparison between simulation and experimental data

In order to evaluate results from simulation, a comparison with experimental data obtained with Alteino-Sileye3 experiment was performed.

Alteino-Sileye3 flew on board ISS during Marco Polo mission with a Soyuz flight in April 2002. It consisted of a single silicon telescope (8 silicon planes oriented along two views) with a dynamic range between 0.4 and 1200 MIP, optimized to detect cosmic rays component with energy bigger than 50 MeV/nucleon. At the top and at the bottom of the silicon tower there are two plastic scintillators providing the trigger. Alteino-Sileye3 included an electroencephalograph devoted to monitor the astronaut brain activity for the Light Flash investigation.

4.2.1 Expected particles during Light Flash observation time

This device was working for a total time of about 131 hours; the time dedicated to Light Flash observation was 7 hours, 41 minutes and 20 seconds (27680 s). Considering this observation time in

respect to the number of particles expected in the 1 cm radius sphere results summarized in table 4.2 are obtained.

nucleus	atomic number	energetic range	
		1 – 2000 MeV/nucleon	1 – 10000 MeV/nucleon
		expected number of nuclei	expected number of nuclei
H	1	$1.15 \cdot 10^6$	$1.16 \cdot 10^6$
He	2	$1.12 \cdot 10^3$	$1.98 \cdot 10^3$
C	6	29.89	53.42
N	7	8.64	14.64
O	8	30.17	53.42
F	9	0.72	1.19
Ne	10	5.19	8.83
Na	11	1.03	1.73
Mg	12	6.04	10.93
Si	14	4.26	7.96
S	16	0.83	1.57
Fe	26	3.37	6.37

Table 4.2: Number of particles expected in a 1 cm radius sphere during the time of Light Flash observation in Alteino-Sileye3 experiment.

If the number of expected protons and Helium nuclei is separated from the number of all other nuclei the table can be filled as table 4.3.

nucleus	atomic number	energetic range	
		1 – 2000 MeV/nucleon	1 – 10000 MeV/nucleon
		expected number of nuclei	expected number of nuclei
H	1	$1.15 \cdot 10^6$	$1.16 \cdot 10^6$
He	2	$1.12 \cdot 10^3$	$1.98 \cdot 10^3$
altri	Z > 2	90.15	160.06

Table 4.3: Comparison between expected number of protons and Helium nuclei and nuclei with Z >2.

Contribution of protons and Helium nuclei is substantial in respect to all other nuclei.
A 1 cm radius sphere can simulated a human eye. Actually, no certainty about the eye region where mechanisms originating Light Flashes take place was reached. Probably more than one mechanism concur to create those perceptions (see chapter 1), such as the Čerenkov interaction or the direct ionization of the retina. Then a precise simulation should need the evaluation of the only sensitive region(s) to better estimate the cross sections of interaction processes.

4.2.2 Alteino-Sileye3: experimental data

Particle data gathered by Alteino-Sileye 3 were compared with the simulation results. Unfortunately, the low statistics did not permit a more accurate analysis of fluxes.
Results obtained for the absolute fluxes both from standard analysis (fit) and from CREME simulation are reported in table 4.4.

nucleus	number of nuclei (fit)	number of nuclei (CREME)	ratio
B	155±12	329	0.47
C	467±22	1110	0.42
N	163±13	294	0.55
O	534±23	1073	0.5

Table 4.4: Absolute fluxes obtained with Alteino-Sileye3 experimental data compared with the simulated ones (CREME).

It has to be noticed that absolute fluxes showed in table 4.4 refer to the total experiment time (131 hours).
In the last column of table 4.4 the ratio between the number obtained with analysis and with simulation is given; the comparison between experimental and simulated values can provide an estimation of detector efficiency.
It has to be considered that those results refer to events satisfying several conditions, among them an almost constant energy loss (relativistic particles) in the silicon planes constituting the particle detector. Showers were not analyzed. The total events satisfying all conditions were 12416.
In order to improve statistics, Alteino-Sileye3 data were re-processed relaxing condition on relativistic particles; in that way events grew up to 52861.

With those new conditions, however, the peak discrimination decreased and the Boron peak is not more visible. In table 4.5 those new results are summarized. In the last column the rate obtained considering the Alteino-Sileye3 total functioning time was calculated.

nucleus	number of nuclei (fit)	rate (p/s)
p + He	48939±221	0.1
C	958±31	$2.03 \cdot 10^{-3}$
N	398±20	$8.44 \cdot 10^{-4}$
O	816±29	$1.73 \cdot 10^{-3}$
B, C, N, O	2635±51	$5.59 \cdot 10^{-3}$
Z > 8	1288±36	$2.73 \cdot 10^{-3}$

Table 4.5: Number of nuclei found with Alteino-Sileye3 experiment and rate of different nuclear species in the detector total functioning time.

As mentioned in the previous paragraph, during Alteino-Sileye3 experiment 27680 s were dedicated to the Light Flash observation; during this time 44 LF events were reported. The LF rate was then $1.6 \cdot 10^{-3}$ Hz.

4.3 Simulation conclusions

By comparison values of table 4.1 and 4.5, the observed rate for Carbon, Nitrogen and Oxygen nuclei are in agreement with the expected one. A bigger discrepancy can be found for lighter nuclei, probably due to the lower detector efficiency for those particles. For nuclei heavier than Oxygen the estimation is not accurate because of the low statistics.

Light Flash observation rate is compatible with rate of different nuclei, but in the simulation the heavy nuclei have a lower rate.

Chapter 5:
ALTEA-UHB architecture

In this chapter the architecture of the ALTEA User Home Base (UHB) will be described in details. The UHB is devoted to control and manage the planning of the mission; in particular it is the place where data are received and analyzed in Real-Time and where data are storage, managed and distributed.
First the UHB features will be presented and then the design of its structure will be showed.

5.1 Mission support

Mission support consists in several activities: audio and video communications, consultation and modification of planning and procedures, request of playback data stored at POIC.
Audio communications for coordination between the ALTEA UHB, the MARS USOC, the POIC of the Marshall Space Center and the Johnson Space Center of Houston and for possible communication with astronauts take place through IVoDS, a VoIP system. The configuration includes two IVoDS machines (AlteaVoice1 and 2), one directly connected to the NASA server through the GARR and the other that receives via MARS the audio flux coming from ASI-net.
Video flux coming from Johnson is utilized to monitor the mission operations, in particular during experiment setup and during CNSM sessions. The video flux is received from a videoconference system connected to the MARS Center that receives it from the JSC through ASI-net.
Two others machines are devoted to the rest of the activities with several NASA software installed (the EHS client, the IPV client and the OSTP client).
The EHS (Enhanced HOSC System) client is a Java web application that is the interface for several software tools. In particular the Telemetry Database, the NRT Data Request and the OCR (Operation Change Request) are used for ALTEA.
The Telemetry Database is the interface to an Oracle DB that contains all telemetry parameters of ISS and of ALTEA and it allows to select some of them to create the packets to send to the final user. The ALTEA telemetry packets are identified by the APID 458.

The NRT Data Request allows to explore the whole data set contained in the HOSC server to select part of them considering some parameters such as the packet time generation or the time when they are saved at the HOSC, the kind of packet, the transmission mode (real time, dump, etc.).
The OCR is utilized to submit procedure modifications for the crew.
Most of the procedures used onboard ISS are available as electronic files. The IPV (International Procedure Viewer) is the same software used by the crew to visualize the procedures; in this way the different experiment operators can follow the operations and help the crew if it is the case.
The OSTPV client (On Board Short Term Planning Viewer) allows to visualize the planning of the activities that take place on board the Station, with the possibility to see the activity details and to recall the IPV with the correspondent procedures.

5.2 Real-time data

During the DOSI mode, ALTEA generates scientific telemetry continuously and sends it to the ground in real-time. Because the Station is not continuously connected to the ground segment to transmit scientific data, during operations there are time period with signal availability (Acquisition Of Signal – AOS) and other time period without signal (Loss Of Signal – LOS), as in the fig. 5.1.
Telemetry is immediately sent to ground only during AOS period, while during the LOS period it is recorded on board the Station and it is sent to the ground in the following AOS periods, non necessarily in the first one.

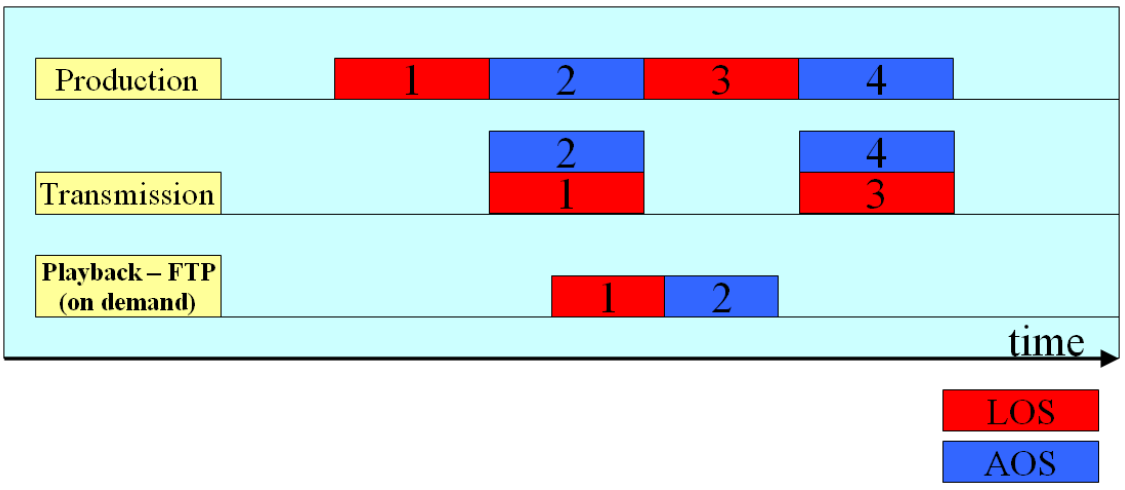

Fig. 5.1: Scheme of production and transmission of data both in streaming and on request.

In the buffer of the Station data are labeled as Dump. Real-Time and Dump data fluxes are both transmitted by POIC towards final users in UDP mode on two different channels. It was decided not to receive Dump data and analyze only Real-Time ones, so the ones acquired during AOS (*Acquisition Of Signal*) periods. Those data are sent by POIC to MARS center in Naples through the ASI-net dedicated net in UDP mode. MARS center send again data towards ALTEA UHB in TCP mode. In fig. 5.2 the last part of data flux, from HOSC through MARS center to UHB, is showed.
In the ALTEA UHB the AlteaRT machine is devoted to receive and analyze Real-Time data. In particular, the hardware functioning parameters contained in the housekeeping packets are monitored and some results of the scientific data analysis (for example, particle flux, energy distribution, etc.) are showed.

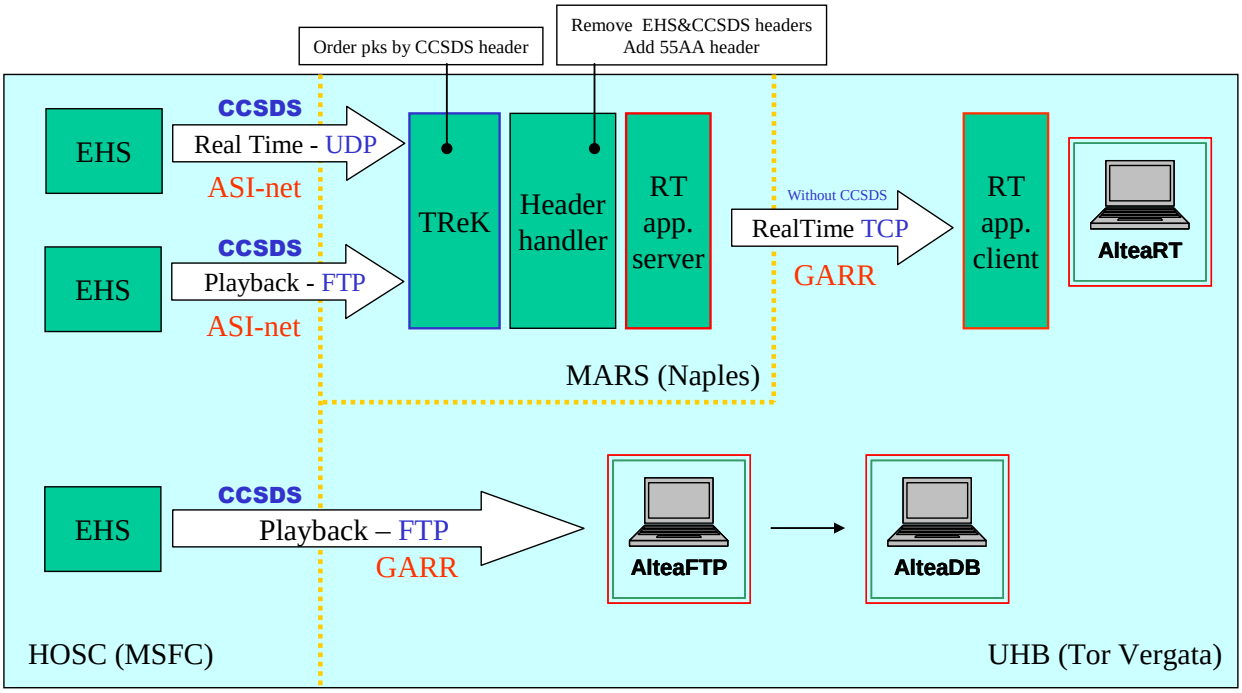

Fig. 5.2: Data fluxFlusso dati dall'HOSC all'UHB

5.3 Data on request

Real-Time data will not be used to store the whole ALTEA data production because they are not complete because of the LOS (*Loss Of Signal*) periods. So complete data are periodically request through the EHS web interface. In fact, after about two hours from data production both Real-Time and Dump data are stored, timely ordered and made available to be requested (see fig. 5.1). Data are requested with one of the computers called AlteaPlanning and they are transferred on the

computer AlteaFTP where the FTP server is mounted. FTP data flux is transmitted on the GARR geographical net. Rough data stored in AlteaFTP are then inserted in the AlteaDB database that will contain all Altea data rationally organized; data will be available to all wanting analyze them.
Also CNSM data are requested in FTP mode and they are analyzed immediately after they are received to check their integrity and authorize data deletion from the ISS laptop.
Data playback can be requested also in telemetry format and received by TReK, installed on AlteaFTP.
For details of data flux see [55].

5.4 UHB scheme

The User Home Base is dived in two independent subnets, one directly connected to HOSC through GARR and the other connected to the MARS center and then to ASI-net. The two AlteaPlanning machines, AlteaVoice2 and AlteaFTP belong to the first subnet, while AlteaVoice1 AlteaRT belong to the second one. AlteaFTP is connected to AlteaDB that will be accessible from outside through a web interface. In figura5.3 the ALTEA UHB scheme is showed, with the links and the assigned IP addresses.

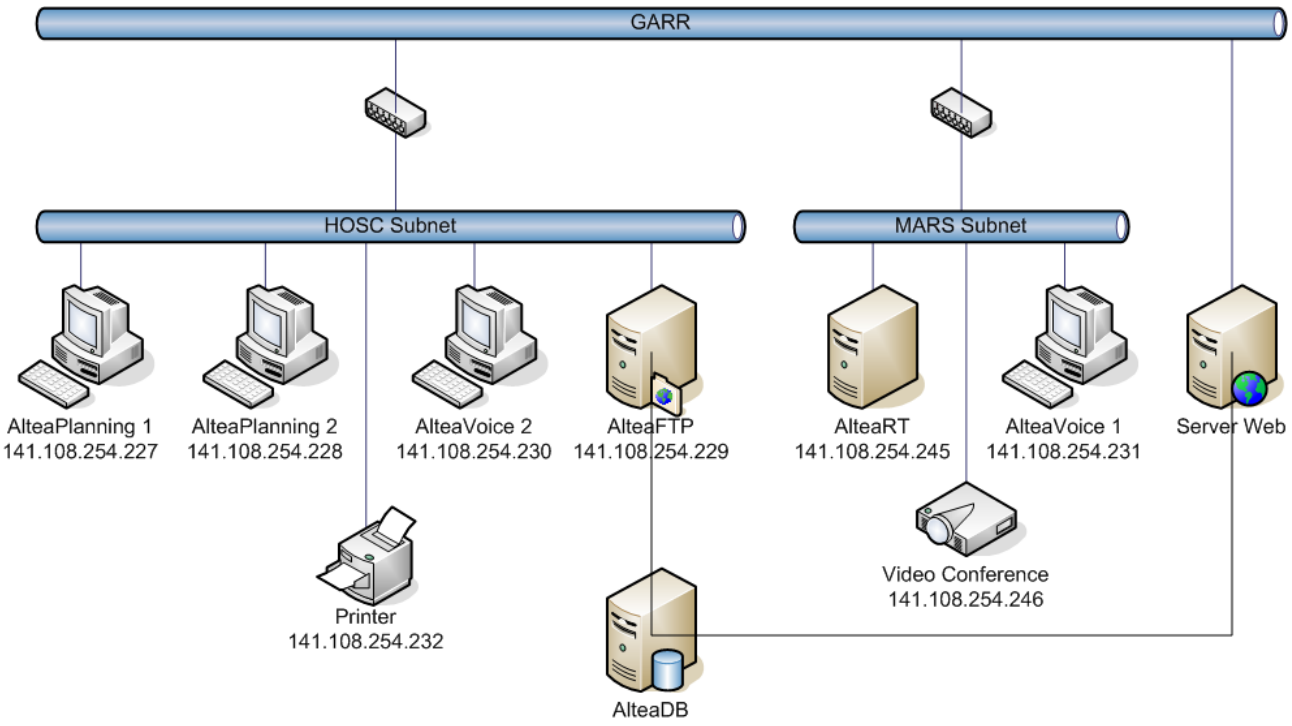

Fig. 5.3: ALTEA UHB scheme with the computer IP addresses.

Chapter 6:
Detector performances and characterization

In this chapter the results of analysis on tests performed in the laboratory of Alcatel-Alenia Space in Milan on the boards constituting the ALTEA-space hardware Flight Model and at the University of Tor Vergata will be presented. With these results a complete characterization of the device, its features and performances was provided.

6.1 Pedestals and rms

In the period between September and October 2003 the Alcatel-Alenia Space performed several tests on the boards constituting the ALTEA-space Flight Model.
For each board 100 pedestals were considered, a pedestal being the signal acquired without particles event; the characteristic of pedestal mean value and standard deviation in time was studied for the boards with and without silicon planes mounted. Two different situations were tested: the six SDUs with the silicon planes non bonded and the SDU FM1 with all the six silicon planes bonded.
Obtained results are showed in this paragraph; in the plots in the fig. 6.2 to 6.13 the mean value of pedestal and the standard deviation in ADC channels of each strip for the SDU FM1 to FM6 are showed. The single plots are included in Appendix. In fig.14-15 the same plots are reported for the SDU FM1 with the silicon plane bonded.
It has to be mentioned that in most of the cases the first pedestal acquired had to be rejected because it was far from the medium value, probably for an electronic tail on the capacitor; in such cases only pedestals from 1 to 99 were considered to calculate medium value and standard deviation. After plots of single SDU, the summary pedestal mean value and rms plot for each SDU is showed.
The standard deviation mean values are around 0.5-0.6 ADC channels for each plane in each SDU, also if sometimes can be bigger, about 0.7-0.8 ADC channels. In such cases the pedestal trends in the single strip show a growth with time, the pedestal mean value having a drift motion. Two examples are showed in fig. 6.1.

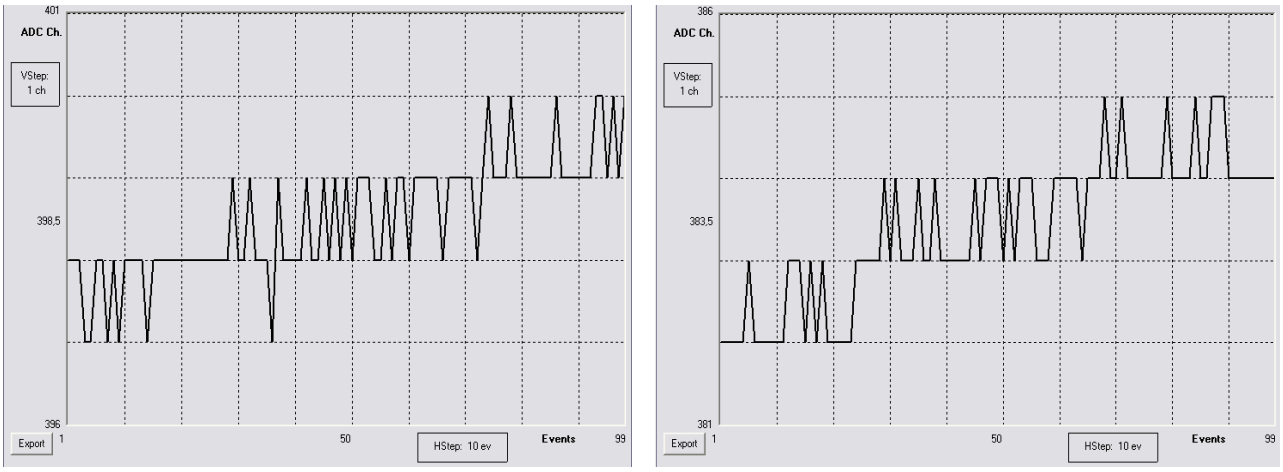

Fig. 6.1: Rms values versus time of strip 28 FM1 DB3 , left, and of strip 16 FM2 DB5, right.

In most of the cases the performances of the different silicon planes in the different SDUs are quite homogeneous, but the standard deviation calculated for the boards with the silicon planes not bonded are higher than the one for the boards with the planes bonded.

The detector board db3 (silicon plane Y2) of SDU FM2 has a pedestal about 200 ADC channels lower than the ones of the other dbs; this characteristic still appears in the SDU FM2 with the silicon planes bonded and it does not implies any other difference in the plane performance.

No evidence of detector board malfunctioning was found. The higher rms found in some cases, as written before, is caused by the thermal drift of pedestals; selecting a minor number of events on which calculate the medium value, in fact, it results more uniform between the boards and is about 0.5 ADC channels.

There are often some ‘edge effect’ in correspondence of strips 1, 16-17, 32-33, 48-49 e 64 due to a different CR2 reading the strip.

It has to be noticed that for the db6 (silicon plane X2) of SDU FM1 with the silicon planes bonded an anomalous value of rms, about 4-5 ADC channels, was found. Files analyzed were not enough to investigate this anomaly.

FM1 without silicon planes bonded :

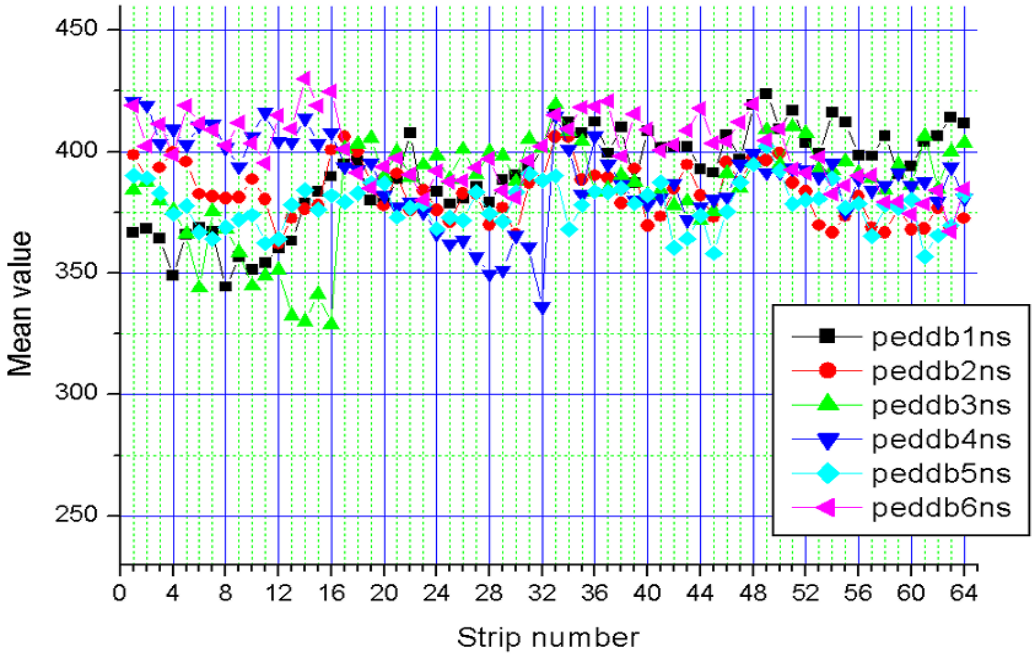

Fig. 6.2: pedestals of FM1 detector boards (db) without silicon planes bonded.

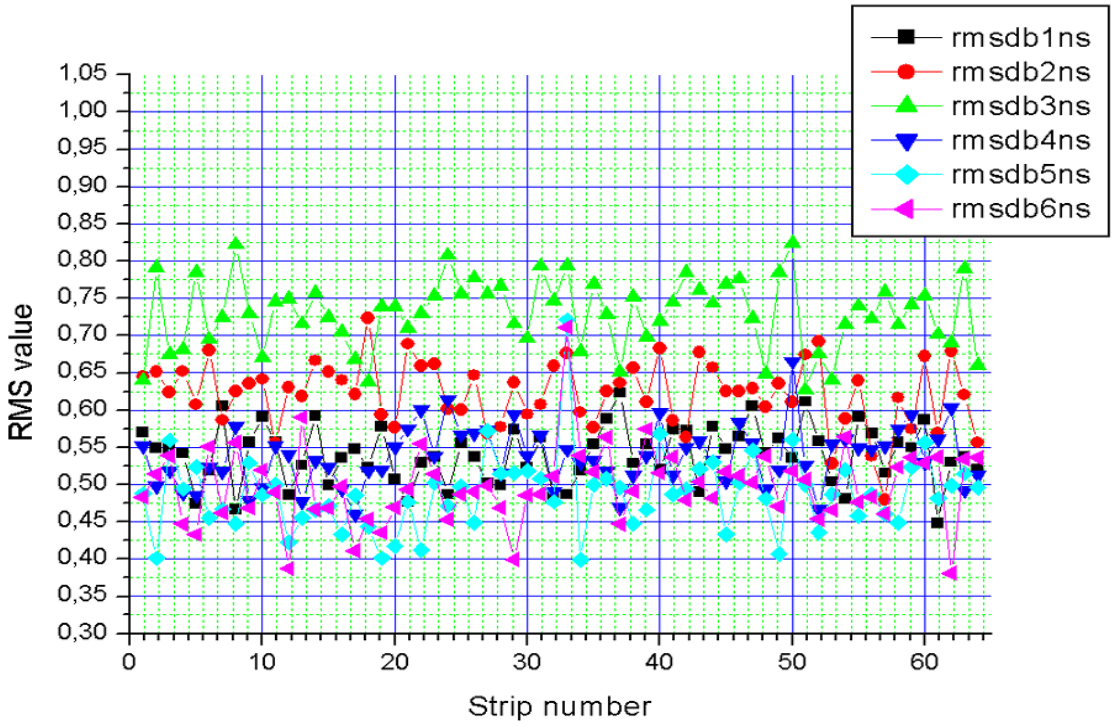

Fig. 6.3: rms of FM1 detector boards (db) without silicon planes bonded.

FM2:

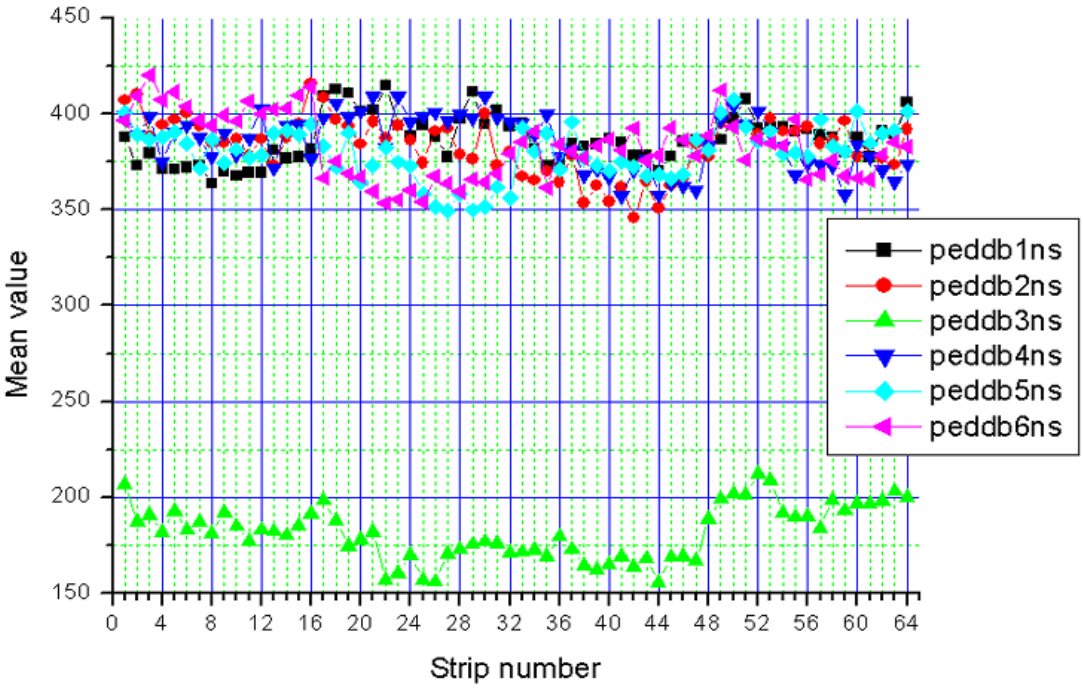

Fig.6. 4: pedestals of FM2 detector boards (db) without silicon planes bonded.

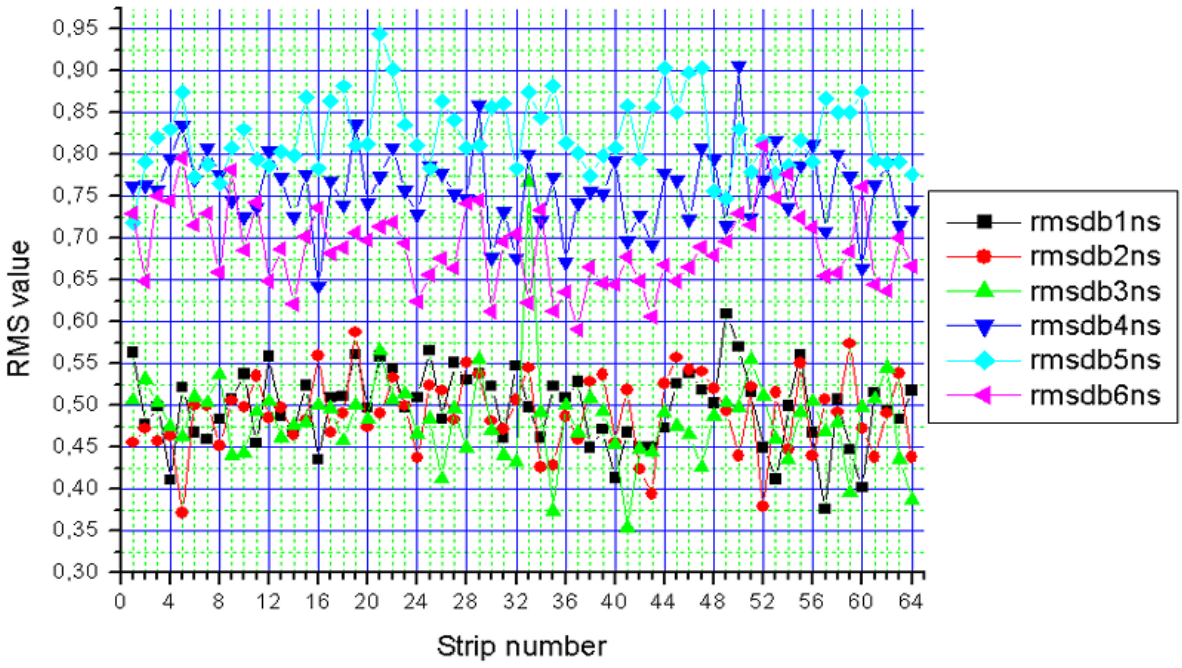

Fig. 6.5: rms of FM2 detector boards (db) without silicon planes bonded.

FM3:

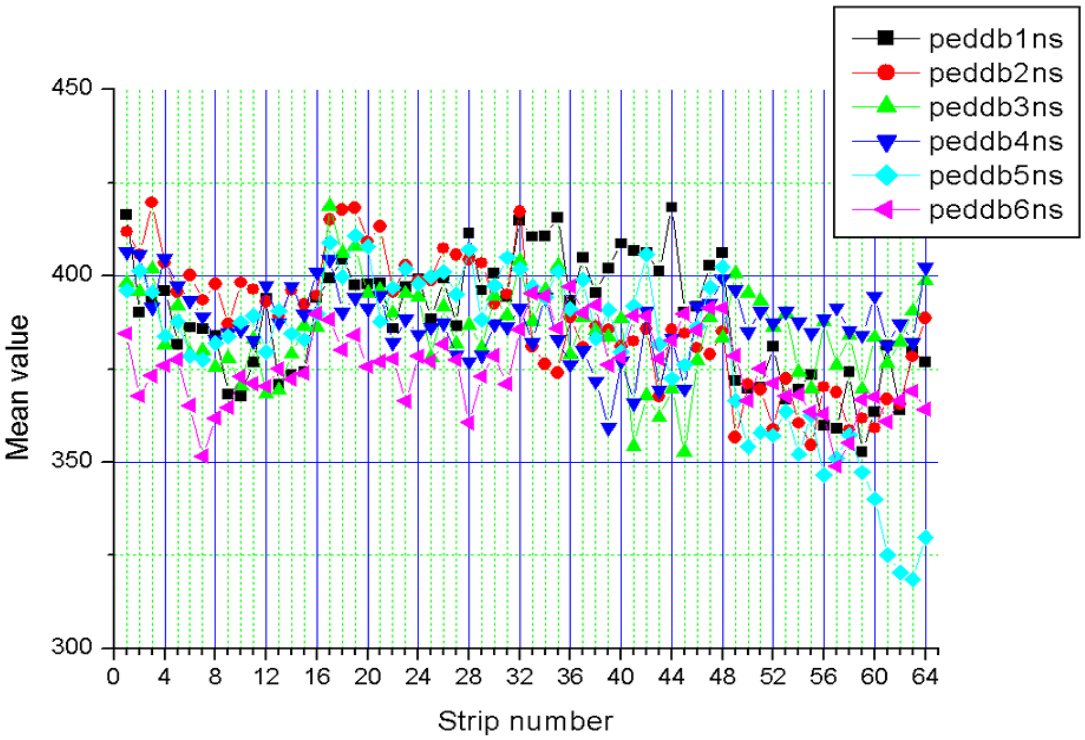

Fig. 6.6: pedestals of FM3 detector boards (db) without silicon planes bonded.

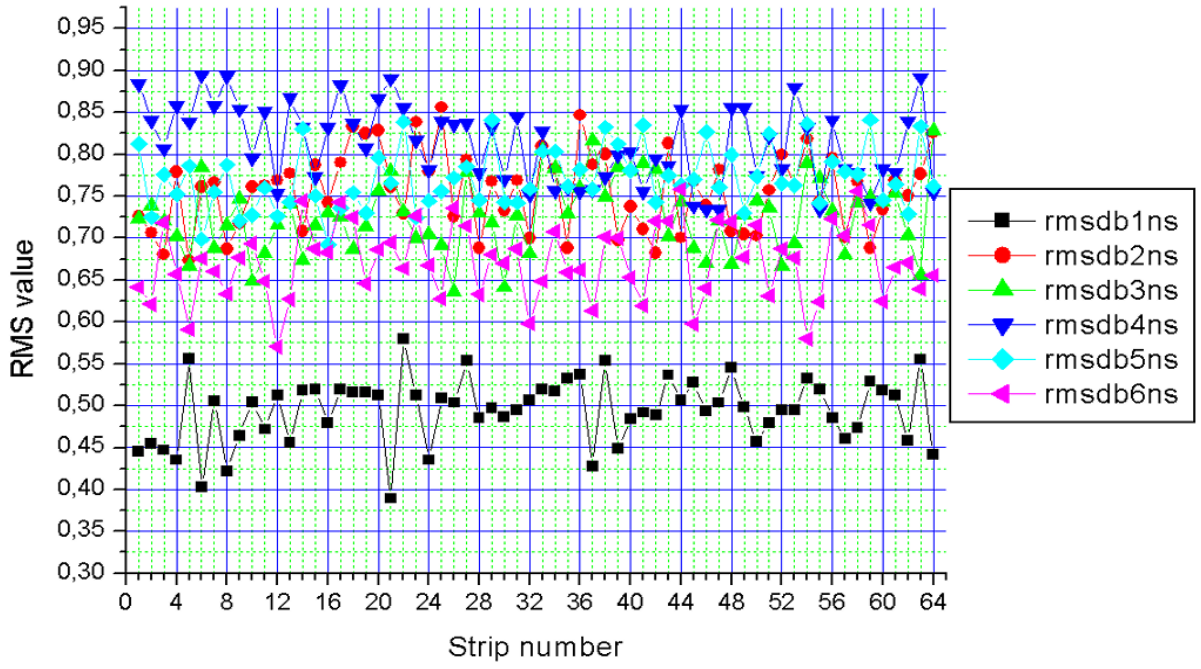

Fig. 6.7: rms of FM3 detector boards (db) without silicon planes bonded.

FM4:

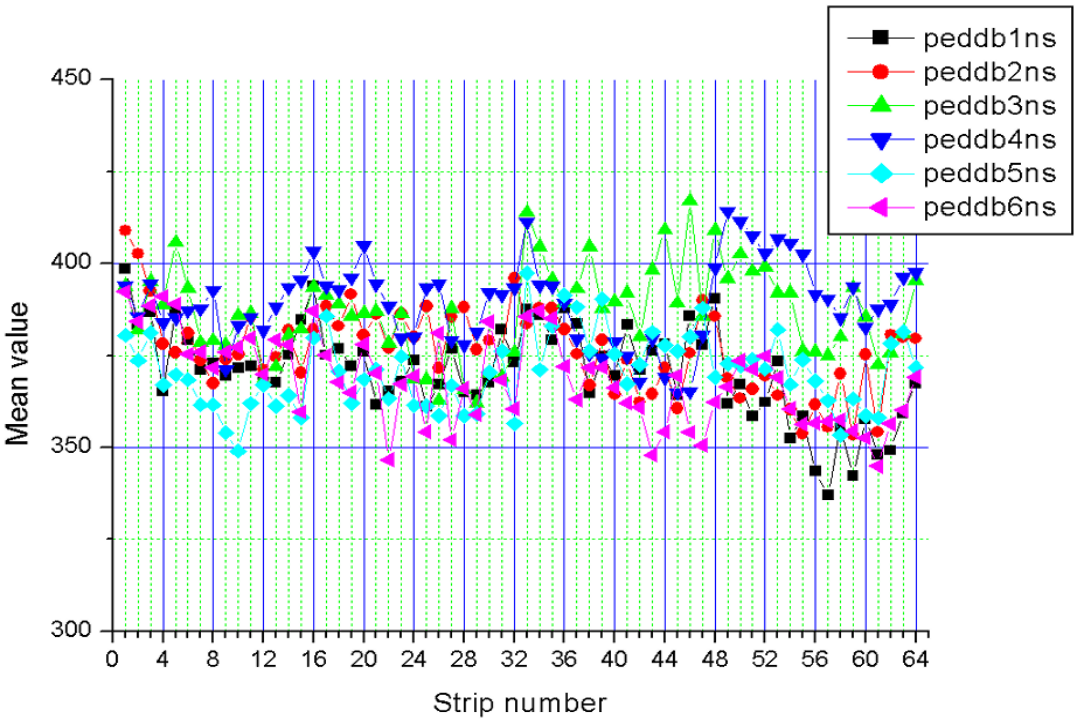

Fig. 6.8: pedestals of FM4 detector boards (db) without silicon planes bonded.

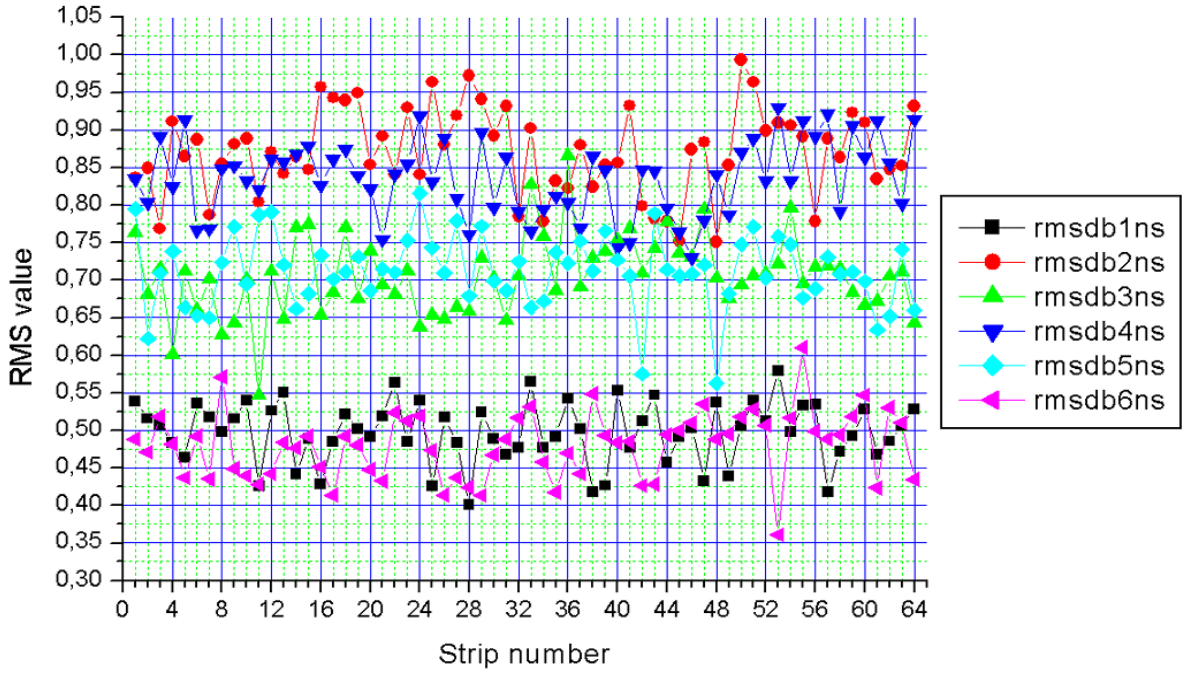

Fig. 6.9: rms of FM4 detector boards (db) without silicon planes bonded.

FM5:

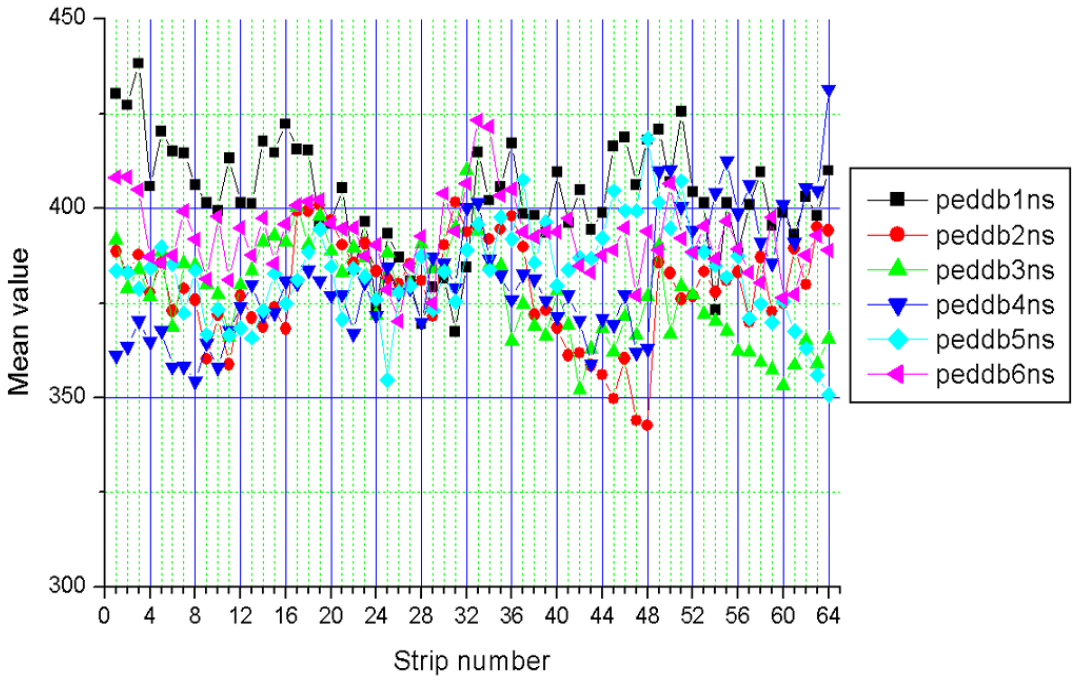

Fig. 6.10: pedestals of FM5 detector boards (db) without silicon planes bonded.

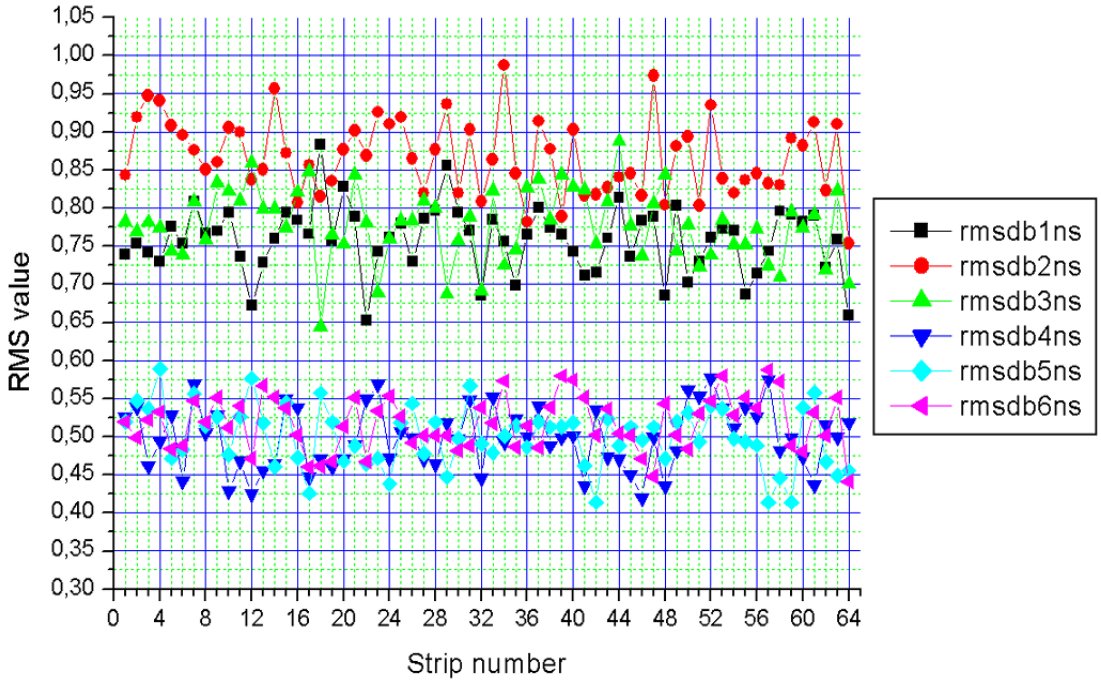

Fig. 6.11: rms of FM5 detector boards (db) without silicon planes bonded

FM6:

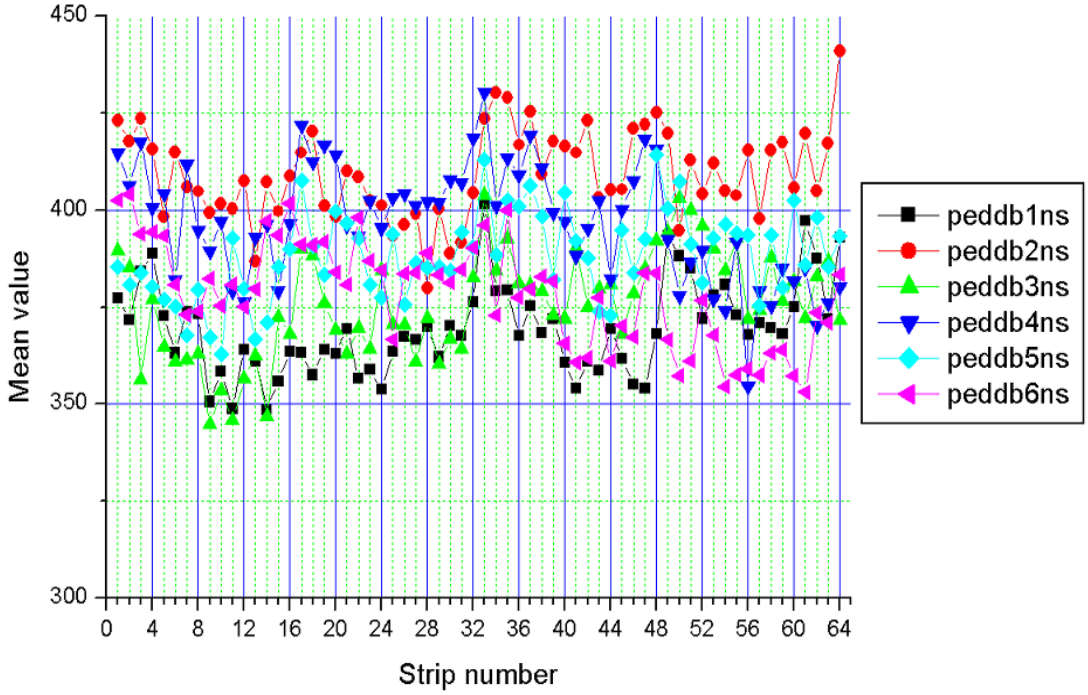

Fig. 6.12: pedestals of FM5 detector boards (db) without silicon planes bonded.

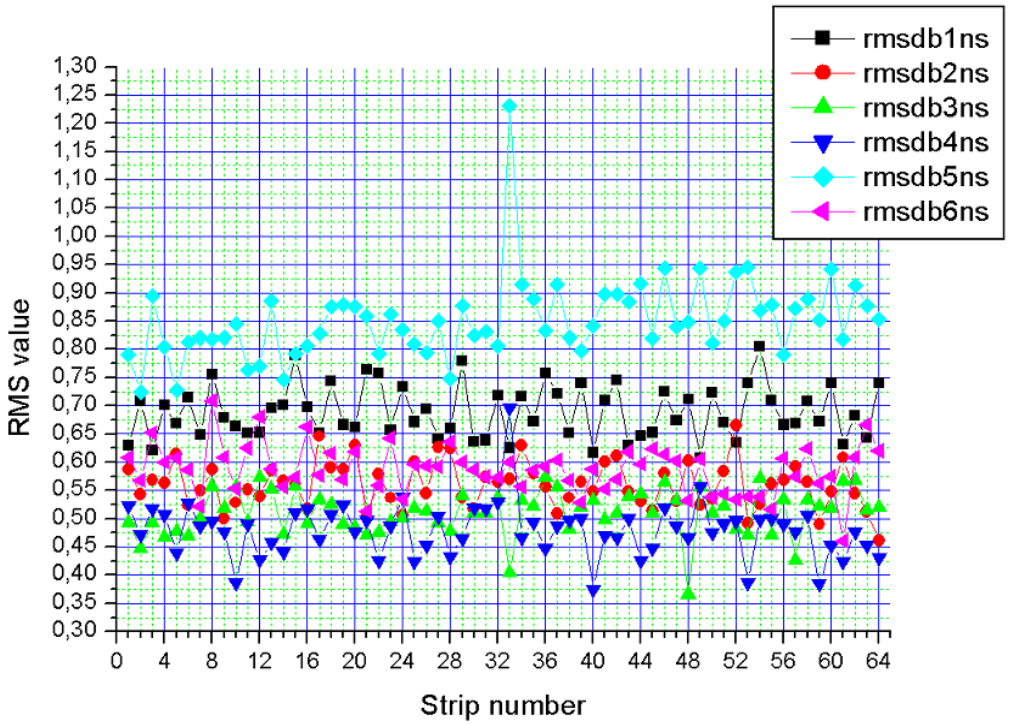

Fig. 6.13: rms of FM5 detector boards (db) without silicon planes bonded.

FM1 with silicon planes bonded :

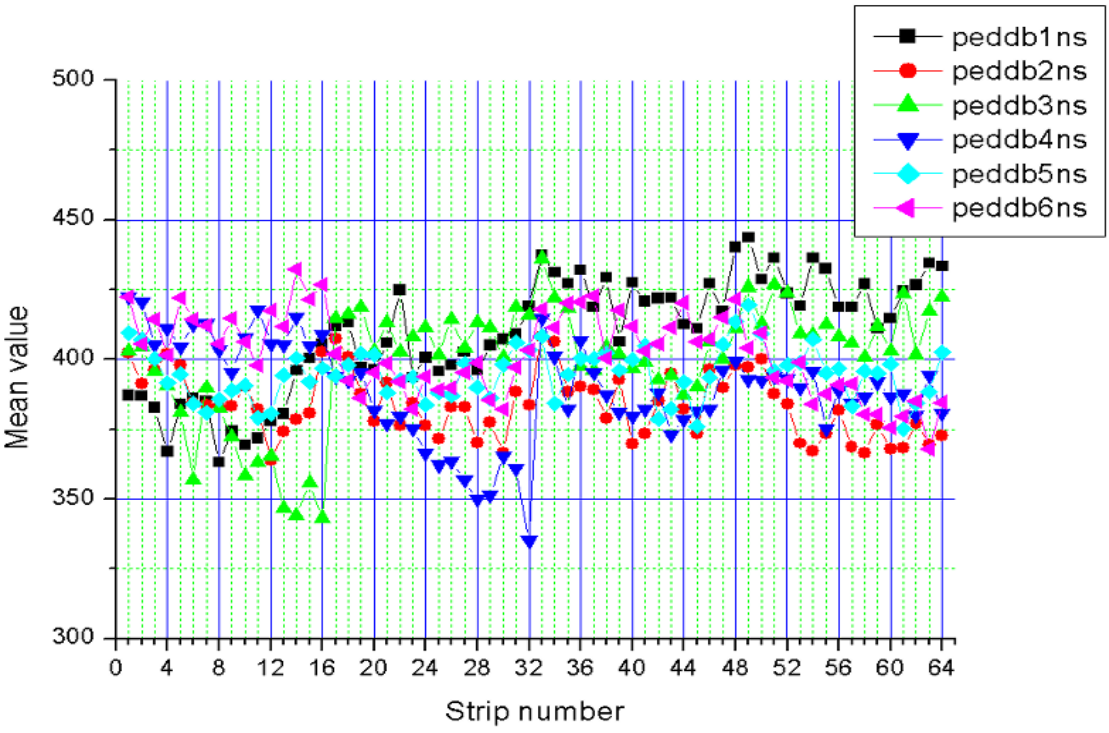

Fig. 6.14: pedestals of FM1 detector boards (db) with silicon planes bonded.

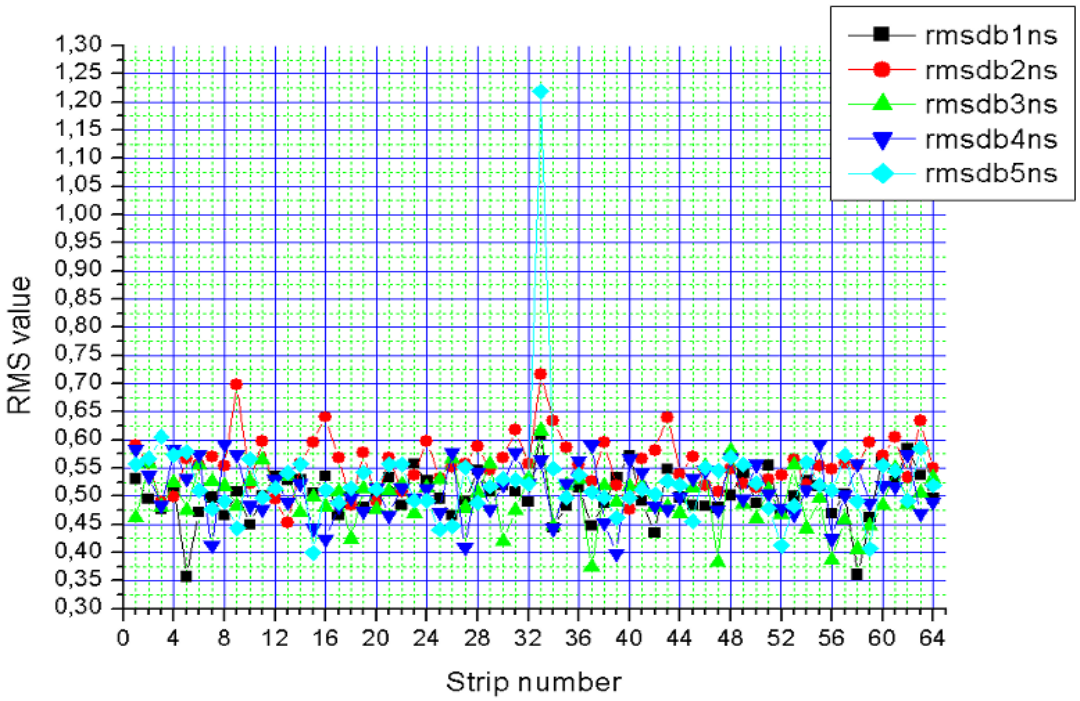

Fig. 6.15: rms of FM1 detector boards (db) with silicon planes bonded.

6.2 Big and Small response analysis

A test was carried out to evaluate the amplification of the detector silicon strips.
The analysis of values obtained injecting two charges of 4980 and 540 mV (called *'big impulse'* and *'small impulse'* respectively) in each strip of the SDU FM1 boards with and without silicon planes bonded was then performed. Each couple of 'big' and 'small' response values for each of the 64 strips of the single board were plotted versus injected charges to obtain a straight line the slope of which being the amplification factor of the single strip (ADC channels/mV). In order to study the difference in amplification in the boards with and without bonded silicon planes, the difference between the amplification factors obtained before and after the silicon plane bonding was plotted (see fig. 6.17-6.22). No signification with or without silicon planes was found, difference being about few per mil. In some cases a peculiar trend was found, for example in db1 or in db5, for edge effects. In fig. 6.16 the amplification of the single strip with and without silicon planes was plotted separately to better investigate those effects.

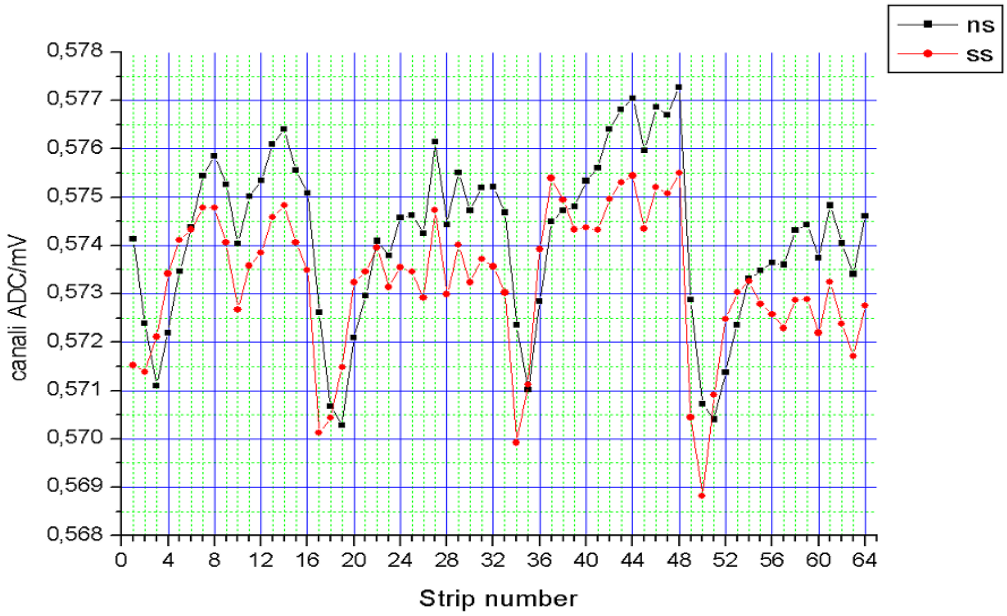

Fig. 6.16: difference in amplification in the SDU FM1 DB5 with and without silicon planes.

The amplification decreases slightly after the silicon plane bonding, probably due to parasite capacities. The amplification in the boards with silicon planes is a little more uniform for strip groups read by the same CR2.

6.3 Linearity in low range

A measurement to test the amplification trend in low ADC channel range was performed in Alcatel-Alenia Space laboratory on the TM2 ALTEA test model. With this test the study on the amplification linearity was completed.

The TM used had the silicon planes not bonded; several different charges were injected on 3 different strips, strip 6 on plane X0, strip 10 on plane X1, strip 20 on plane X2. The charges were injected only on X planes because the trigger consists in logical AND between signals coming just from those silicon planes. The threshold was chosen at 88, corresponding to 5 MIP. An analogical voltage generator 2020 was used to inject the charges, starting with the higher and decreasing step by step.

In table 6.1 voltages injected and the relative ADC values read on the three mentioned strips are reported. In the table there are two different voltage values because both voltages produced by the generator and the equivalent voltages on the strip are given. In order to obtain the MIP equivalent voltages the conversion factor 1 MIP = 0.41 mV was used. This conversion factor is obtained by the 'big' and 'small' charge injection (see Appendix B).

mV generator	mV equivalent injected	MIP	strip 6 X0	strip 10 X1	strip 20 X2
4800	120	50	162.71	156.94	151.72
4300	108	45	147.89	142.2	136.82
3840	96	40	131.26	126.66	122.3
3360	84	35	115.09	111.19	107.2
2880	72	30	99.139	95.911	92.532
2400	60	25	82.829	80.231	77.248
1920	48	20	66.768	64.889	62.246
1440	36	15	50.628	49.36	47.26
960	24	10	34.57	33.897	32.202
480	12	5	18.272	18.302	17.187
350	8.75	3.65	14.202	14.481	13.448
300	7.5	3.125	12.618	13.032	11.908
250	6.25	2.6	10.734	11.174	10.183

Table 6.1: Voltages used in the low range linearity test are showed together with correspondent ADC channels read on the detector strips

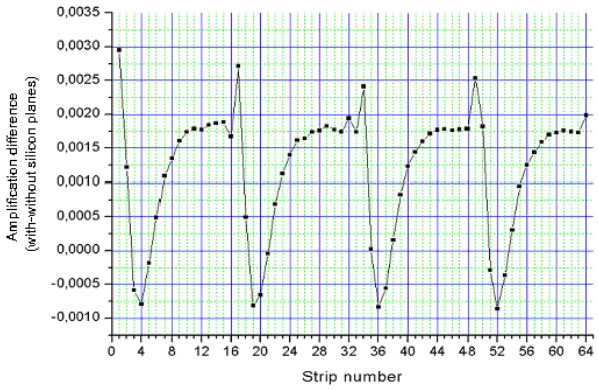

Fig. 6.17: Amplification difference in DB1.

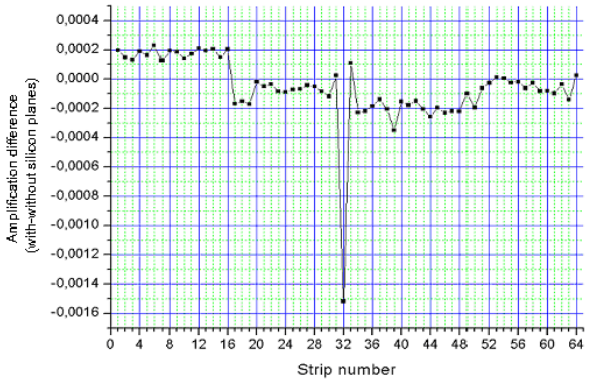

Fig. 6.18: Amplification difference in DB2.

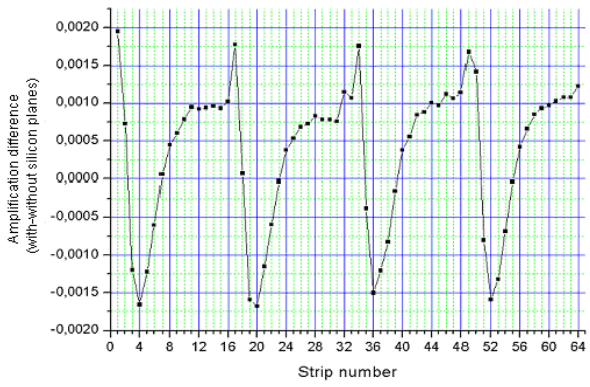

Fig. 6.19: Amplification difference in DB3.

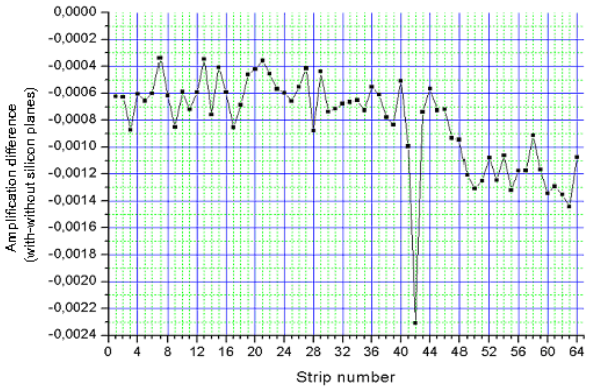

Fig. 6.20: Amplification difference in DB4.

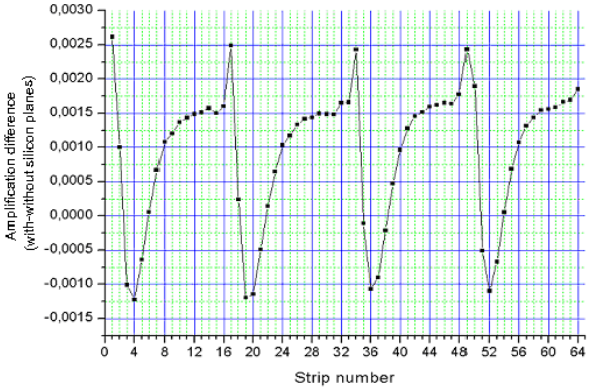

Fig. 6.21: Amplification difference in DB5.

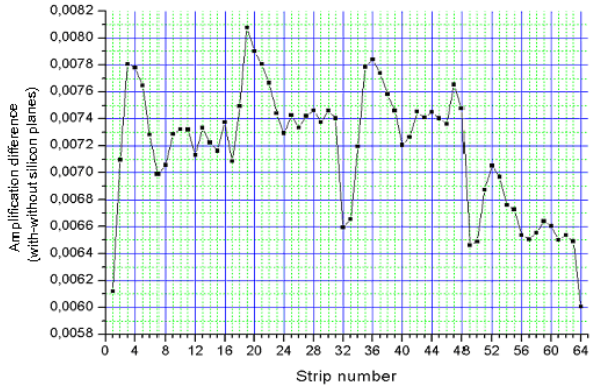

Fig. 6.22: Amplification difference in DB6.

In figures 6.23 and 6.24 the plots of the ADC channel values read on the strips versus the injected voltages are showed: in the first one, the whole range is reported with the correspondent linear fit for each strip, while in the second only the low ADC channel region is plotted. In both the plots the trends are quite linear for the three strips.

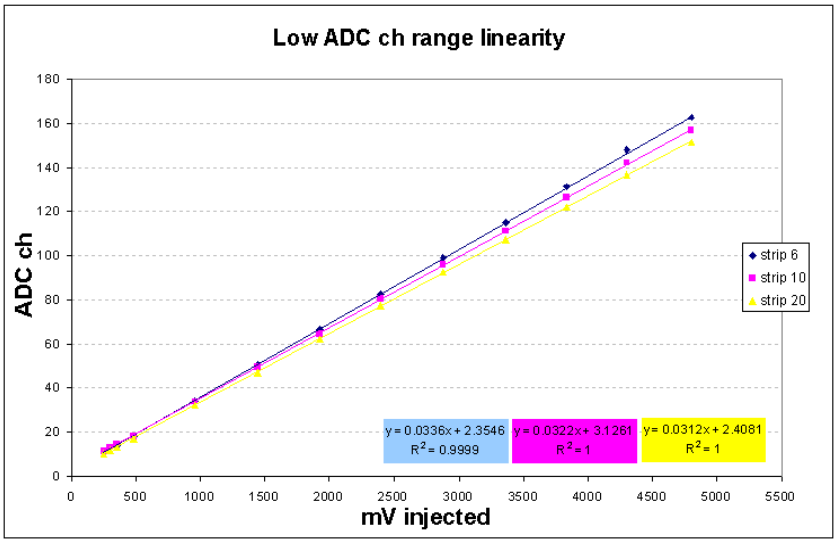

Fig. 6.23: ADC channels read on the tested strips versus the injected voltages in all a full range.

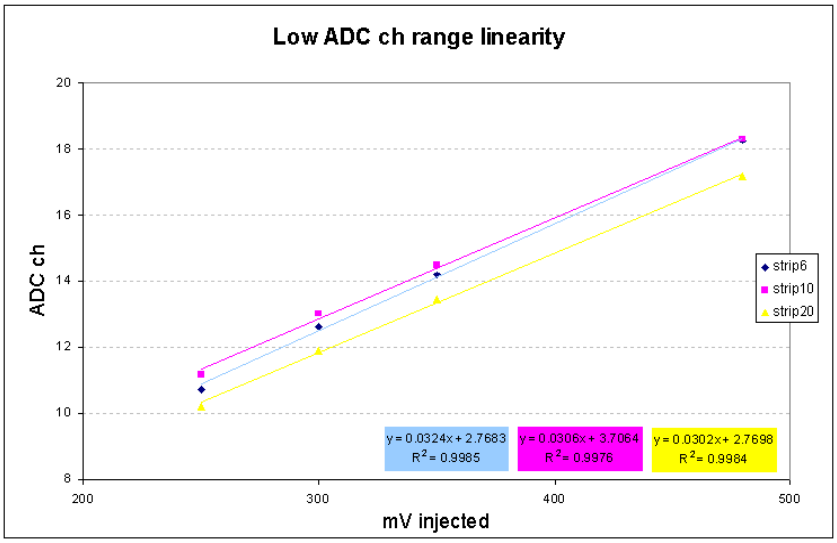

Fig. 6.24: ADC channels read on the tested strips versus the injected voltages in the low ADC channel range.

Chapter 7:

Detector tests and calibration

In order to better characterize the particle detector of ALTEA-space experiment two different measurement and test sessions were performed at the GSI particle accelerator in Darmstadt, Germany, in November 2003 and April 2004. In both of these sessions the SDS was tested, completely or partially, with Carbon and Titanium beams at different energies to verify the bonding of the strips, to check their functionality and homogeneity and to compare the instrument response with Montecarlo simulations calculating the instrument amplification. The experimental set-up is showed in fig. 7.1. Test and calibration results are summarized in this chapter.

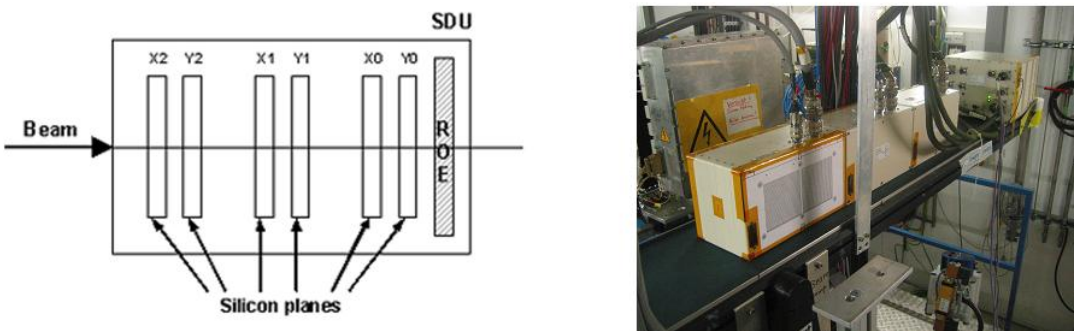

Fig. 7.1: ALTEA SDU beam test set-up.

7.1 GSI, November 2003: beam test

Between 19 and 24 November 2003 first tests on the SDU-FM1 (*FM*, Flight Model) of ALTEA were performed. In the same session also the SDU-TM1 (*TM*, Training Model) was tested. TM1 was tested at the GSI for the first time in February 2003, when some serious anomalies in its functioning appeared. In this second TM test the effect of the consequent modifications was also tested.

Both the SDUs were managed by the so-called TE, Test Equipment, a test apparatus simulating the Digital Acquisition Unit (DAU). The TE is an industrial pc with Windows NT4 with a specific motherboard realized for this kind of application. TE emulates the DAU and allows to manage one

SDU with a software realized by Laben. This software uses some scripts to send commands to the SDU and to acquire the messages from the SDU together with scientific and housekeeping data. In this way both the functional parameters (temperatures, silicon currents, voltages, etc) and the output signals of the device can be monitored.
Two plastic Hamamatsu scintillators, called H1 and H3, were used to monitor the beam.
In this measurement session a carbon beam at 100, 150, 400 and 600 MeV/nucleon was used as provided by the accelerator without any absorber between the beam and the device. For each energy different measurements were performed, as showed in details in table 7.1, where a summary of the beam condition, the SDU tested and the use of the scintillators is reported. In the tables the SDU-FM1 and the SDU-TM1 are simply called FM and TM.
Each data file started with a pedestal acquisition, followed by a 'big' and 'small' signal acquisition (see chapter 6)

7.2 GSI, November 2003: results

From the analysis of data collected in this session, some anomalies were founded. In the following paragraphs these anomalies and the strategies to correct them are described.

7.2.1 Software for data analysis

For the data analysis a quicklook software was developed: it could analyze data acquired by TE and provided the trend and the energy distribution for each strip of the SDU. It also managed pedestals, calculating the medium value and the standard deviation and performing the subtraction from the signal, and the 'big' and 'small' calibration signals. In fig. 7.2 an example of the visualization of the particle track (Carbon at 600 MeV/nucleon) obtained with the TEQuickLook software is showed. In that case the data were acquired in Full Mode.

7.2.2 FM1, Strip 63, silicon plane X0: an example of malfunctioning

The strip number 63 belonging to the X0 silicon plane showed a working anomaly. In the figure 7.3 the energy distribution of the strip X0 in a certain run is showed in comparison with the

le name	SDU		Total events	Ped	Beam energy (MeV/nucl)				Threshold (MIP)			Trigger			Mode		Absorber	
	TM	FM			600	400	150	100	10	5	3	Ext	Internal		F	N	Plex	Al
													AND	OR				
GSI_FM1_xrun		●	20910	●	●				●			●			●			
GSI_FM1_2run		●	41429	●	●				●			●			●			
GSI_FM1_3run		●	45510	●	●				●			●			●			
GSI_FM1_4run		●	3706		●				●			●			●			
GSI_FM1_5run		●	70179	●	●				●				●			●		
GSI_FM1_6run		●	34262	●	●				●				●			●		
GSI_FM1_7run		●	1473		●				●				●			●		
GSI_FM1_8run		●	7144		●				●				●			●		
GSI_FM1_9run		●	127869	●	●					●			●			●		
GSI_FM1_10run		●	3883	●				●	●				●			●		
GSI_FM1_11run		●	9506	●				●	●				●			●		
GSI_FM1_12run		●	3939					●		●			●			●		
GSI_FM1_13run		●	11205	●				●		●			●			●		
GSI_FM1_14run		●	4883	●				●		●			●			●		
GSI_FM1_15run		●	1210					●		●			●			●		
GSI_FM1_16run		●	125685	●				●		●			●			●	●	
GSI_FM1_17run		●	25443	●				●		●			●			●		●
GSI_FM1_18run		●	9639	●				●		●				●	●			●
GSI_FM1_19run		●	16454	●	●				●				●		●			
GSI_FM1_20run		●	30867	●	●					●			●			●		
GSI_FM1_21run		●	0	●	●							●			●			
GSI_FM1_21run		●	9255	●	●				~ 13 MIP			●			●			
GSI_FM1_22run		●	19066	●		●				●			●			●		
GSI_FM1_23run		●	156768	●		●				●			●			●	●	
GSI_TM1_24run	●		70374	●	●				●				●		●			
GSI_TM1_25run	●		110175	●	●				●				●			●		
GSI_TM1_26run	●		71953	●	●					●			●			●		
GSI_TM1_27run	●		11165	●	●				●				●		●			
GSI_TM1_27runcont	●		39810		●				●				●		●			
GSI_TM1_28run	●		17384	●	●					●			●			●		
GSI_TM1_29run	●		24704	●			●			●			●			●		
GSI_TM1_30run	●		266	●	●						●		●			●		
GSI_FM1_31run		●	73628		●					●			●			●	●	
GSI_FM1_32run		●	28390	●	●						●		●			●		
GSI_FM1_33run		●	15673	●			●				●		●			●		
GSI_FM1_34run		●	14315	●			●			●			●			●		
GSI_FM1_35run		●	95954	●	●						●		●			●	●	
GSI_FM1_36run		●	36032	●	●						●		●			●	●	
GSI_FM1_37run		●	133940	●			●				●		●			●	●	

Table 7.1: Summary of the acquired files.

distributions of the energy gathered by the analogous strips of plane X1 and X2. For the former the distribution is centred around the value of 6 ADC channels, while the latter two distributions are centred on the real value of energy released by Carbon in that measure.

7.2.3 Anomalous energy loss distributions of plane X2 and Y2

Some peculiar energy distributions were found both in FM and in TM.
For the FM, the anomalies appeared on X2 and Y2 silicon planes, not in particular strips; the anomalies consisted in a peculiar shape of the energy loss distribution, that is expected to be a Gaussian distribution (and we found such kind of distribution in the other silicon plane).
Data from run 6 and 9 were analyzed; the run details were :

Run 6: C beam at 600MeV/nucl, 10 MIP threshold, AND-trigger, Normal Mode

Run 9: C beam at 600MeV/nucl, 5 MIP threshold, AND-trigger, Normal Mode

The anomalous distributions show peaks and valleys equally spaced of 4 channels in run 9 and 2 channels in run 6. This peculiar distribution seemed to disappear in the strips 15, 31, 47 and 63, corresponding to the last strip read by each of the four CR2 reading the silicon plane.
A similar behaviour was noticed also in the TM during the accelerator session of February 2003.
Some example of the described anomalies is showed in fig. 7.3-7.6, where distributions on X2 and Y2 silicon planes are showed and compared to the ones in the other planes. It has to be noticed that the anomalous peaks are considerably larger than the normal ones.
This anomaly was not found in data collected in Full Mode acquisition, then in data collected downloading all the strips whatever the strips with a signal bigger than the trigger signal. In figure 7.7 distribution obtained in run 2, 19, 21

Run 2: C beam at 600MeV/nucl, 10 MIP threshold, External trigger, Full Mode

Run 19: C beam at 600MeV/nucl, 10 MIP threshold, AND-trigger, Full Mode

Run 21: C beam at 600MeV/nucl, 13 MIP threshold, External trigger, Full Mode

are showed.
In conclusion, the anomalous distributions were found only in data gathered in Normal Mode acquisition, on X2 and Y2 silicon planes; then this problem decreased in the last strip read by a CR2 chip (strip 15, 30, 47, 63).

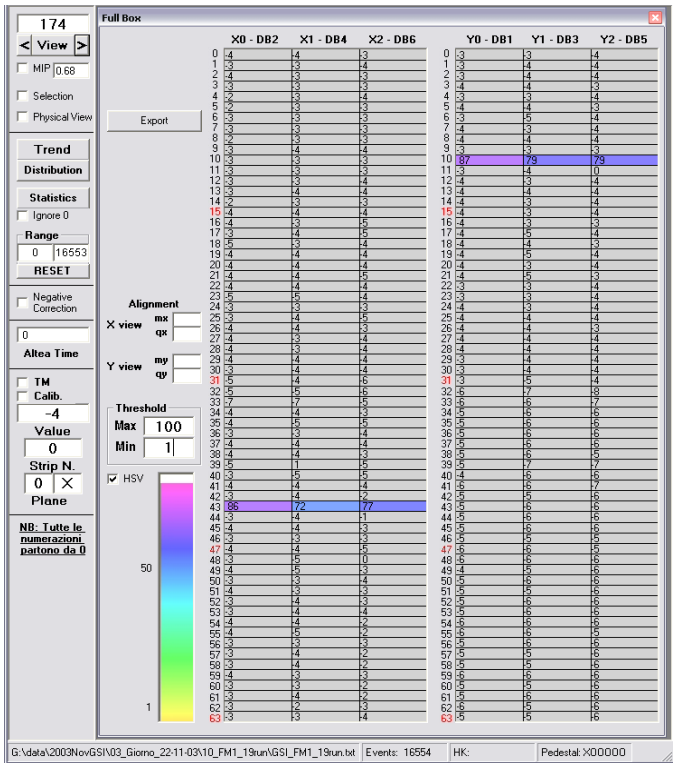

Fig. 7.2: A track visualized with the QuickLook software

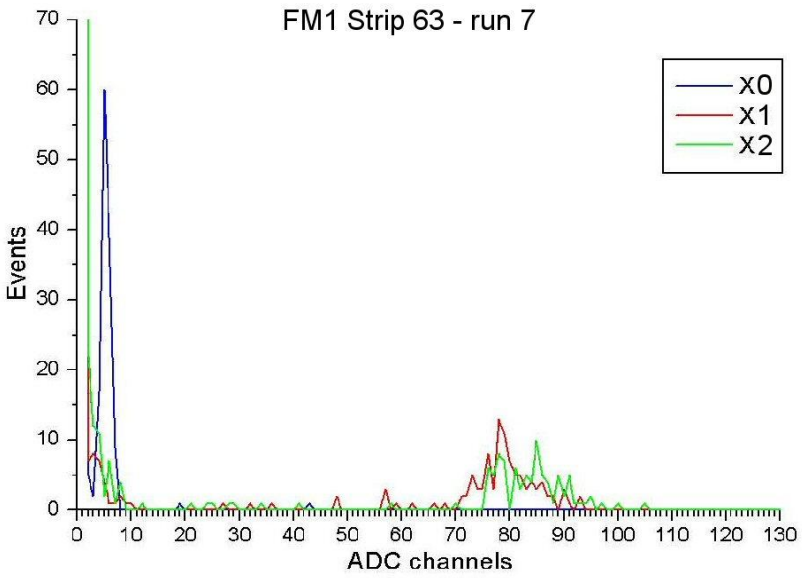

Fig.7.3: Energy distribution in strip 63 for planes X0, X1 and X2.

For the TM, this kind of problem was not found in data collected in the November measure session at GSI, while in data coming from the February test session at GSI some analogous phenomena appeared.

For TM1 data concerning the run 24, a silicon plane scan measurement, are showed in fig. 7.8. Run 24 details were the following:

Run 24: C beam at 600 MeV/nucl, 10 MIP threshold, AND-trigger, Full Mode

In fig. 7.9 data of February 2003 are reported for a comparison. It was not possible to perform a deep investigation on the behaviour of strip 15, 31, 47 e 63 for data from February due to the low statistics gathered and the non complete functionality of TM at that time. Details of measurement sessions were the following:

Fe beam at 1.5 GeV/nucl, 78 MIP threshold, OR-trigger, Normal Mode

The anomalies in the distributions in TM November data were not found neither in data acquired in Normal Mode, as in the run 25:

Run 25: C beam at 600 MeV/nucl, 10 MIP threshold, AND-trigger, Normal Mode

In conclusion, no peculiar distribution were found in any measurement conditions in any silicon plane.

FM1 – Piano X2 – run 9

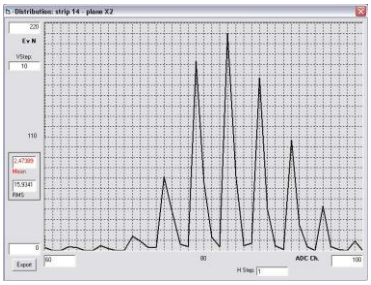

Strip 14

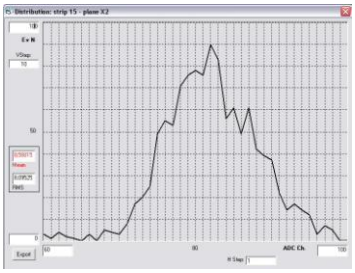

Strip 15

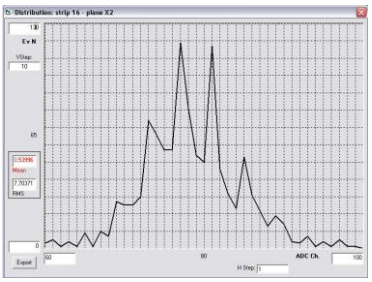

Strip 16

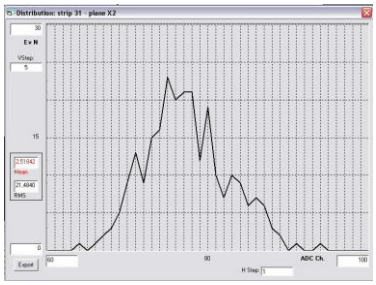

Strip 30

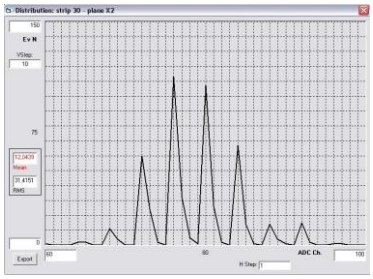

strip 31

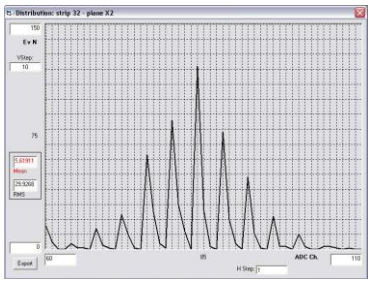

Strip 32

FM1 - Piano X1 - run 9

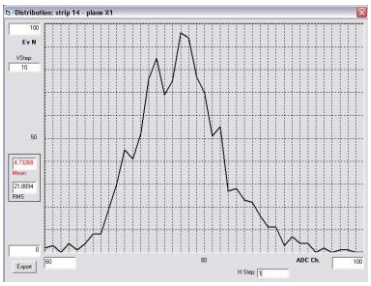

Strip 14

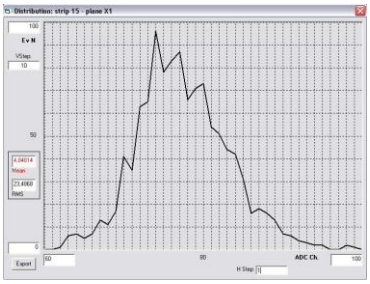

Strip 15

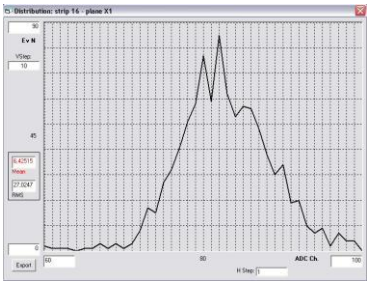

Strip 16

F**M1 - Piano X0 - run 9**

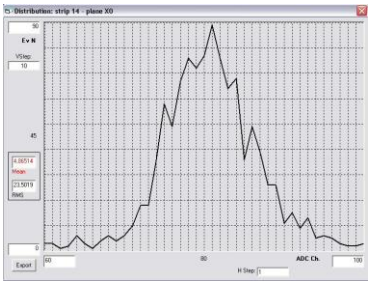

Strip 14

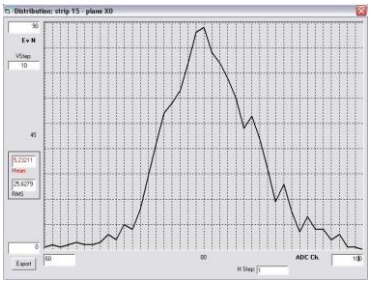

Strip 15

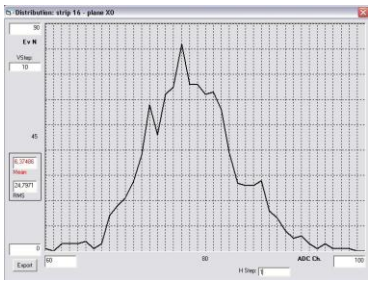

Strip 16

Fig.7.3

FM1 - Piano Y2 - run 9

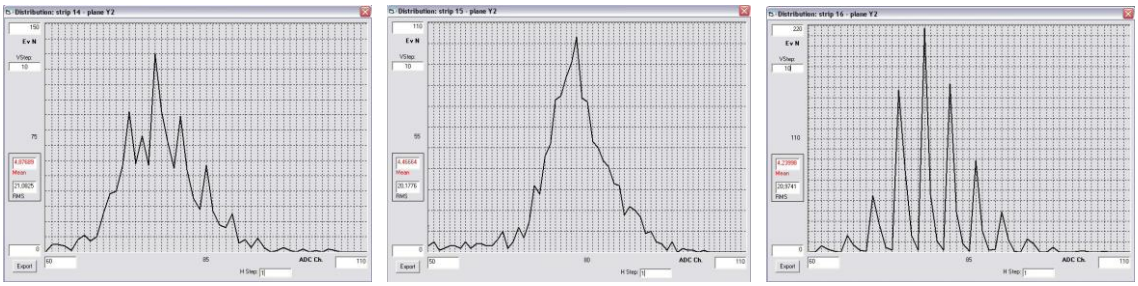

Strip 14 **Strip 15** **Strip 16**

FM1 - Piano Y1 - run 9

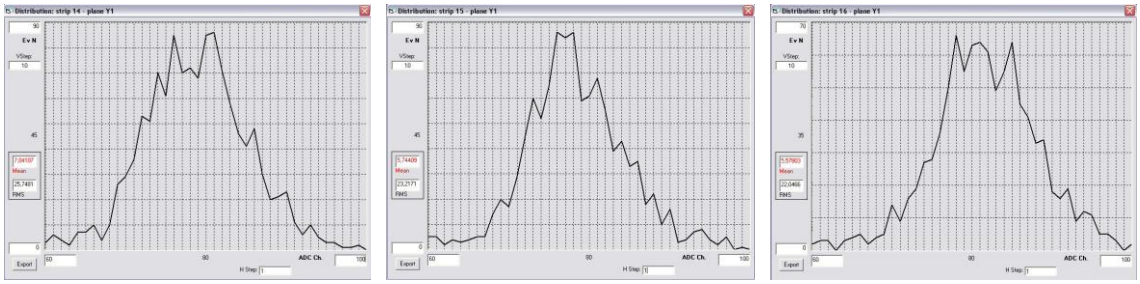

Strip 14 **Strip 15** **Strip 16**

FM1 - Piano Y0 - run 9

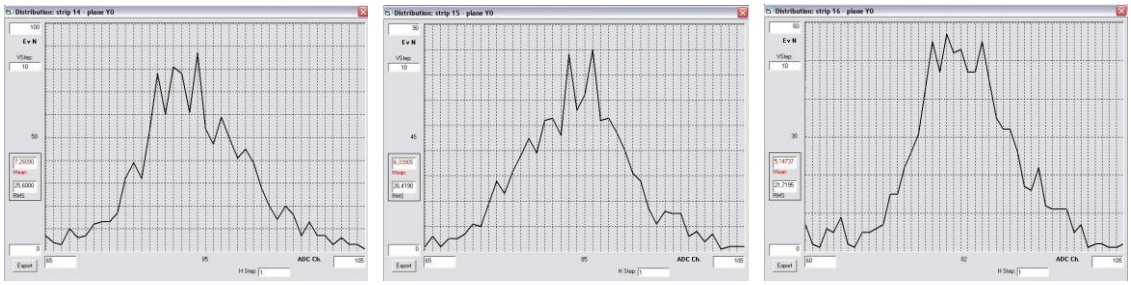

Strip 14 **Strip 15** **Strip 16**

Fig.7.4

FM1 - Piano X2 - run 6

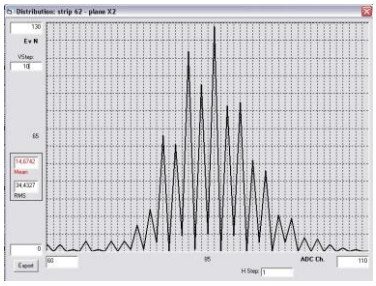

Strip 62

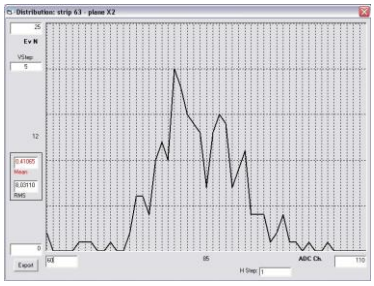

Strip 63

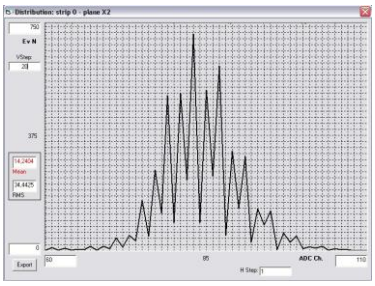

Strip 0

FM1 - Piano X1 - run 6

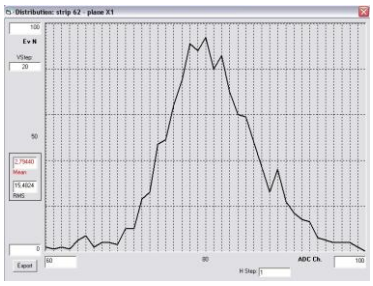

Strip 62

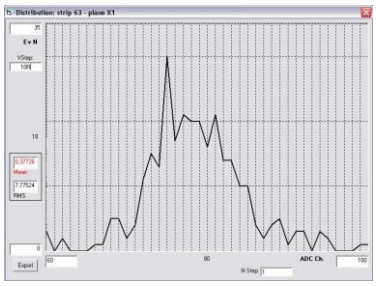

Strip 63

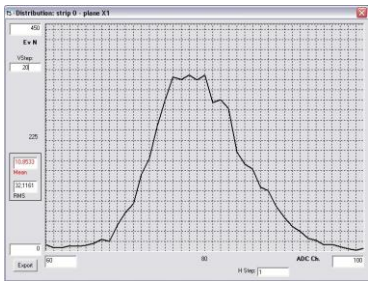

Strip 0

FM1 - Piano X0 - run 6

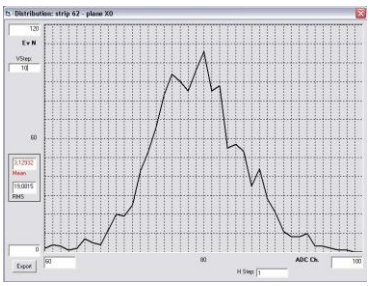

Strip 62

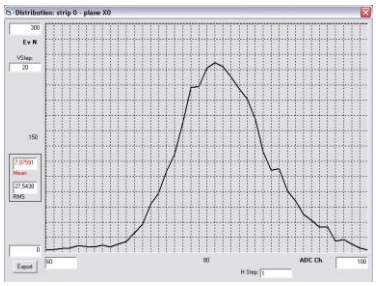

Strip 0

N.B. : la strip 63 del piano X0 è quella non funzionante.

Fig.7.5

FM1 - Piano Y2 - run 6

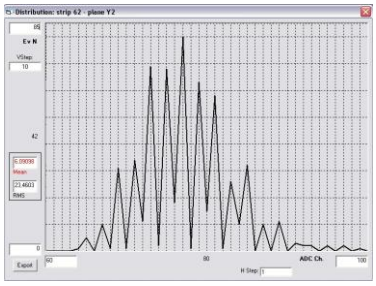

Strip 62

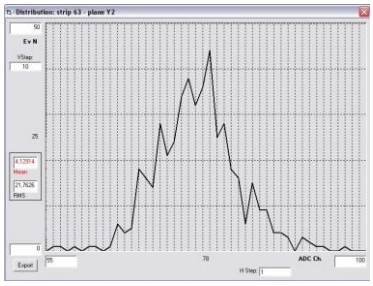

Strip 63

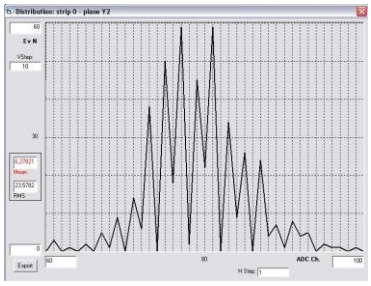

Strip 00

FM1 - Piano Y1 - run 6

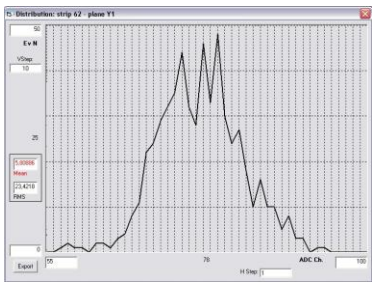

Strip 62

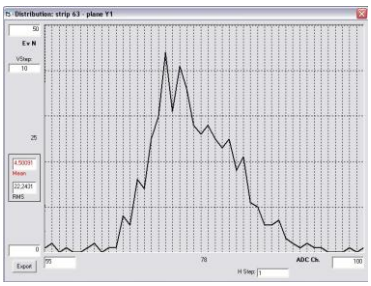

Strip 63

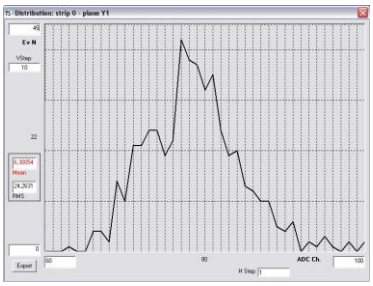

Strip 00

FM1 - Piano Y0 - run 6

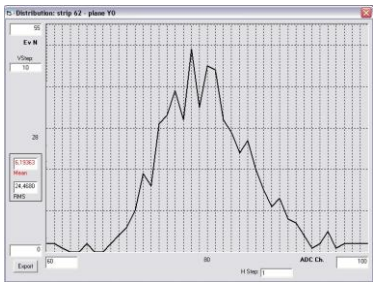

Strip 62

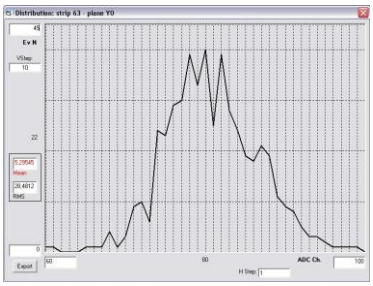

Strip 63

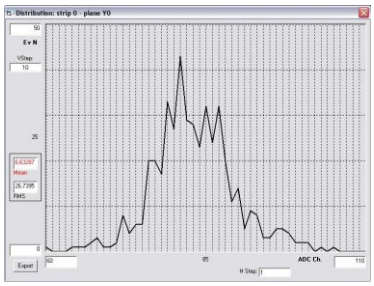

Strip 00

Fig.7.6

FM1 - Piano Y2 - run 2

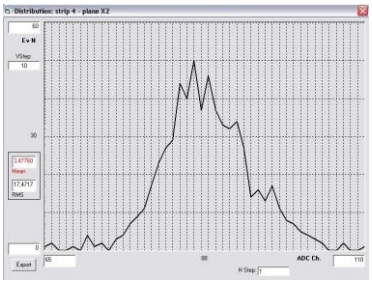

Strip 04

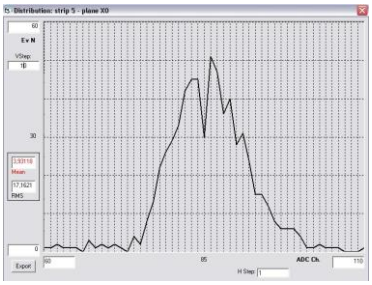

Strip 05

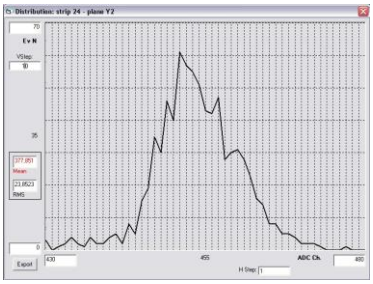

Strip 24

FM1 - Piano X2 - run 19

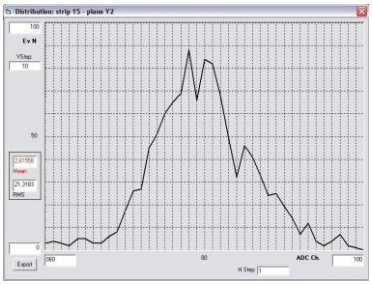

Strip 15

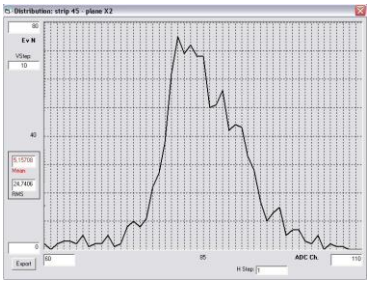

Strip 45

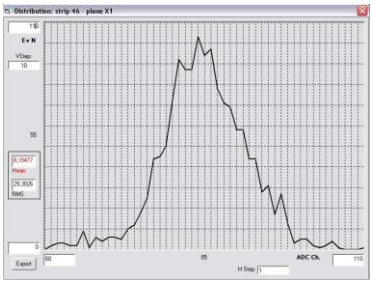

Strip 46

Fig.7.7

TM1 - Strip 11 - run 24

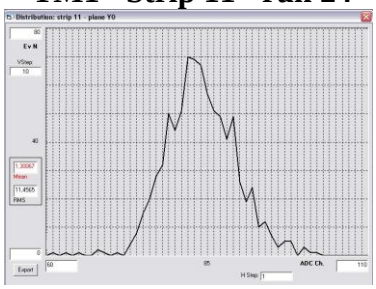

Y0

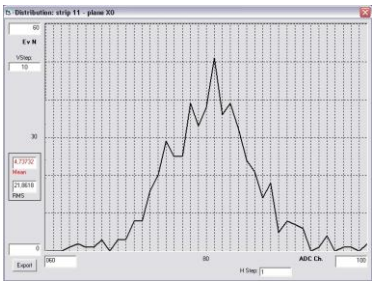

X0

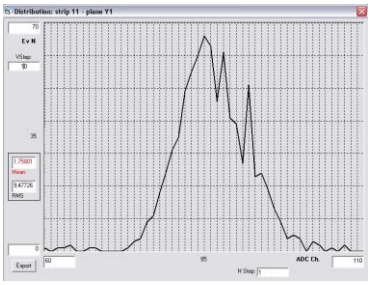

Y1

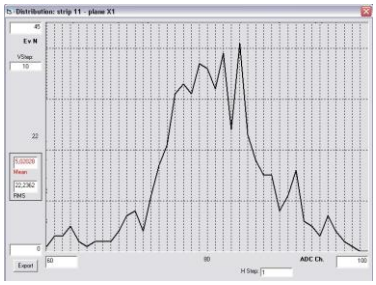

X1

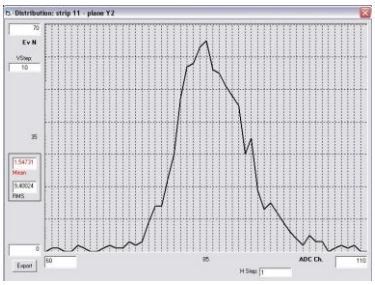

Y2

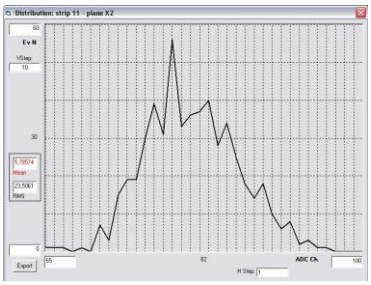

X2

Fig.7.8

TM1 - Piano Y0 - Feb 2003 **TM1 - Piano X0 - Feb 2003** **TM1 - Piano Y1 - Feb 2003**

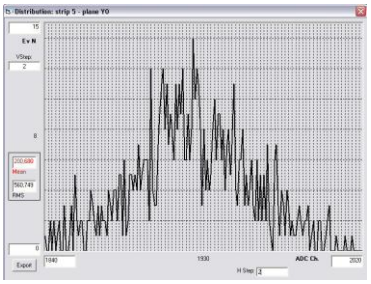

Strip 11 **Strip 56** **Strip 5**

TM1 - Piano X1 - Feb 2003 **TM1 - Piano Y2 - Feb 2003** **TM1 - Piano X2 - Feb 2003**

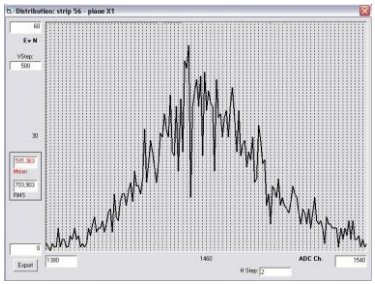

Strip 56 **Strip 5** **Strip 56**

Fig.7.9

7.2.5 Baseline movement

A particular investigation was possible because the file called GSI_FM1_9run_primo.txt, acquired in the following modality

Run 9: C beam at 600MeV/nucl, 3 MIP threshold, Internal trigger, Normal Mode

was constituted not by particle events but only by events due to a dummy trigger.

A part first 100 events, that are real pedestals, the rest of the file can be viewed as constituted by a sort of new pedestals acquired spontaneously because of the internal trigger.

Looking at the events of that file a peculiar behaviour was found (see fig. 7.10): real pedestals (events 0-99) result 3-5 ADC channels higher than the medium values of successive events. That

happened for all the six silicon planes and it is evident in the fig. 7.2 where all the strips not hit by the beam have a negative ADC channel value.

This investigation could only be performed on Full Mode acquisition file, when all the 384 strips of the SDU are read.

Looking at the file acquired with external trigger a different behaviour was found. Data from run 2, 3, 21, acquired as follows:

Run 2: C beam at 600MeV/nucl, 10 MIP threshold, External trigger, Full Mode

Run 3: C beam at 600MeV/nucl, 10 MIP threshold, External trigger, Full Mode

Run 21: C beam at 600MeV/nucl, 13 MIP threshold, External trigger, Full Mode

were studied. In run 2 pedestals and values on the not hit strips are quite the same (fig. 7.11); in run 3 pedestal are still 3-4 ADC channels higher than the not hit strips values (fig. 7.12), while in run 21 values of strips not hit by the beam are always higher that pedestals (fig. 7.13)

No univocal behaviour was found.

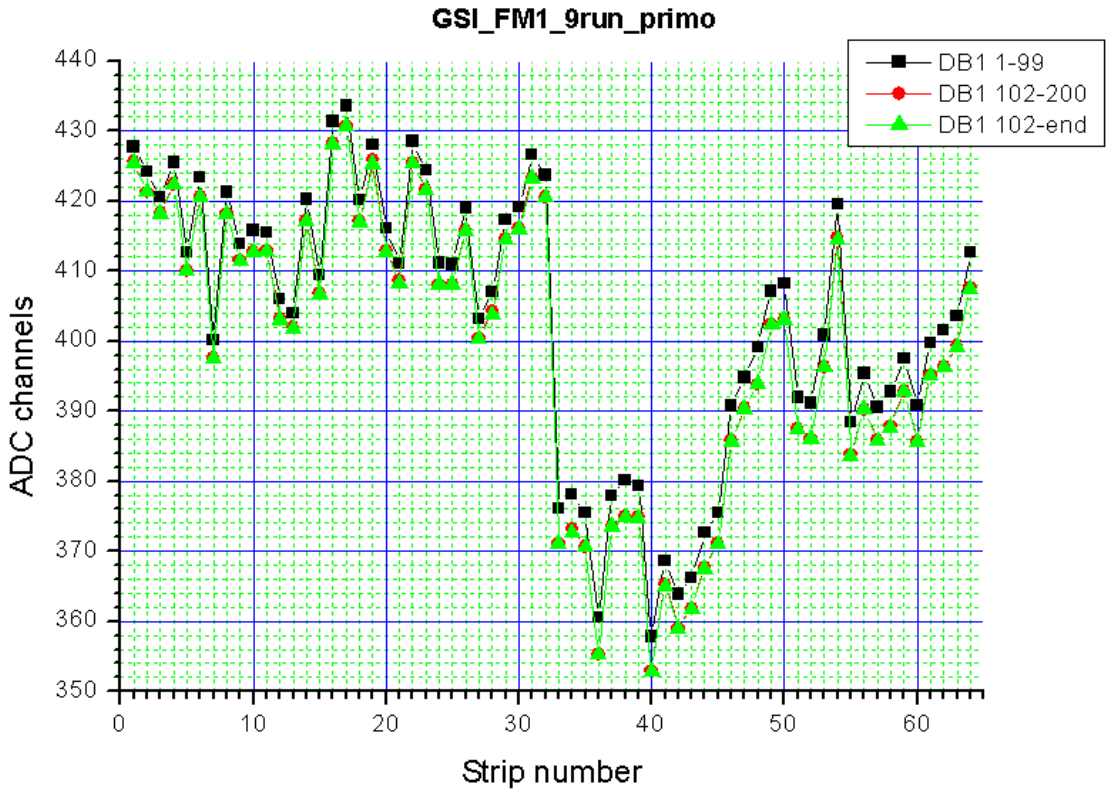

Fig. 7.10: Pedestal values in run 9.

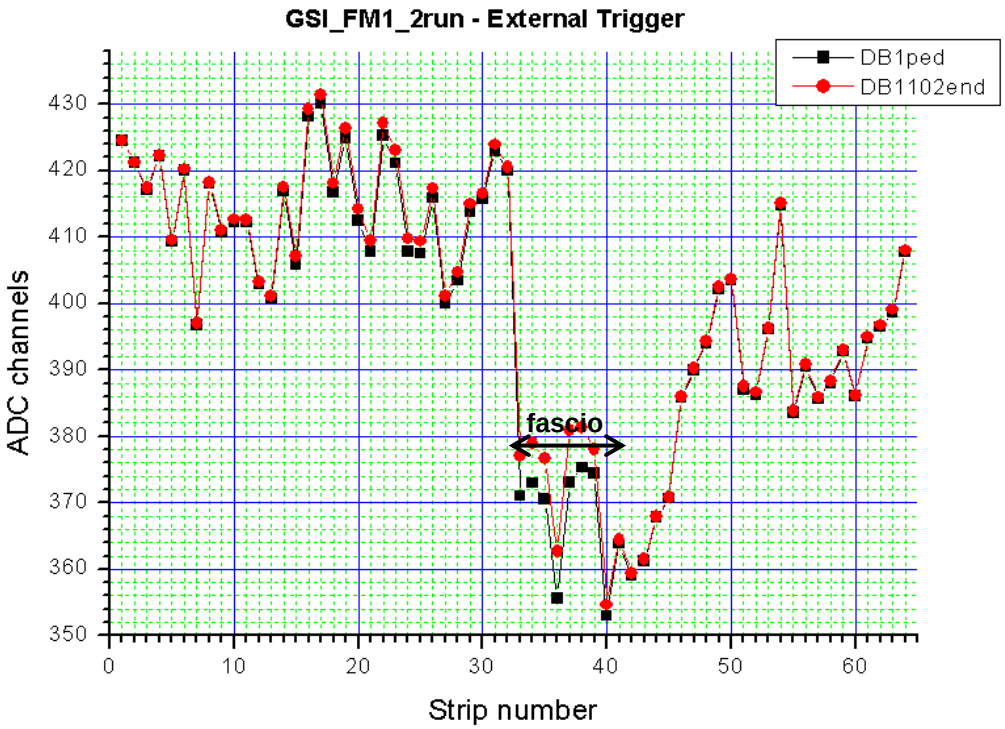

Fig. 7.11: Pedestal values in run 2.

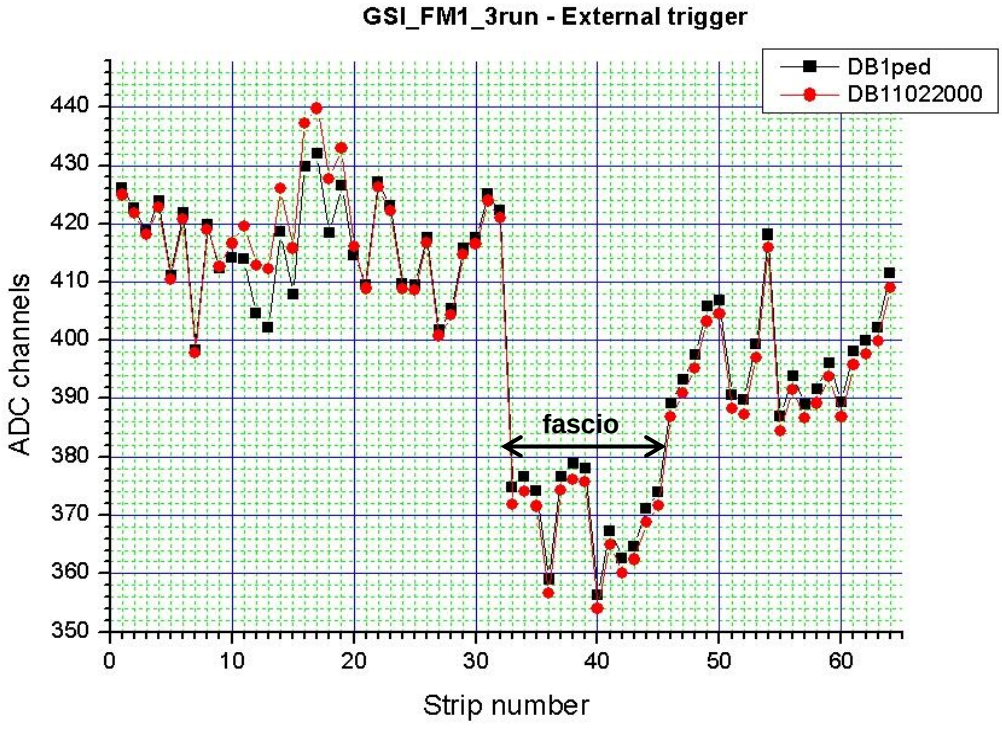

Fig. 7.12: Pedestal values in run 3.

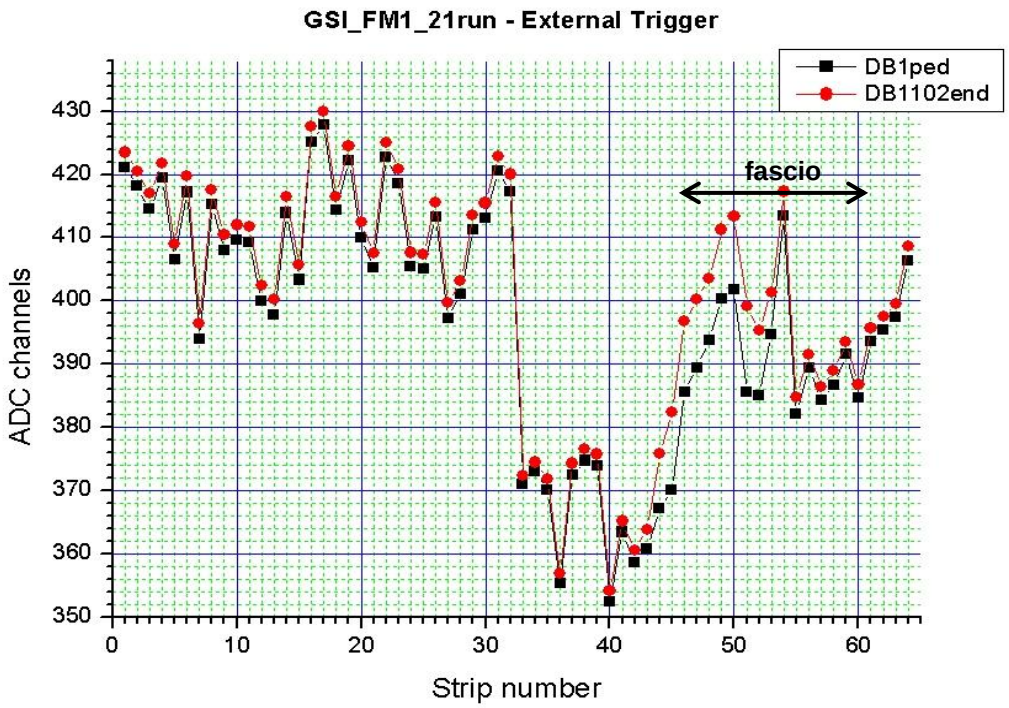

Fig. 7.13: Pedestal values in run 21.

7.2.6 SDU FM1 preliminary calibration

The calibration of FM1 was performed comparing experimental data with simulated values obtained by SRIM2003 and GEANT3 (they both provide medium values of energy loss distributions) and the obtained MIP/ADC channels conversion factor was compared with the expected value of 0.67 MIP/ADC channels estimated by Laben with electronic test .

Tests on FM1 were carried out using a Carbon beam at 600, 400, 150 and 100 MeV/nucleon.

In order to convert the energy loss provided by simulations, the definition 1 MIP = 109 keV in 380 μm of silicon was used (see Appendix B).

The simulations were performed considering the following configuration:

1 Aluminium plane 1.3 mm thick

6 Silicon planes, each 380 μm thick

that can be seen in fig. 7.1.

The rear part of the SDU, including the Read-Out-Electronic board (ROE) and another Aluminium plane was not considered because only energy losses in the six silicon is important for calculation of conversion factor.

In the following plots (fig. 7.14 to 7.17) and in table 7.3 results from SRIM2003 simulation are showed, while in table 7.4 results from GEANT3 simulation are reported. The little differences between these values are due to the different simulation conditions and techniques.

C a 600 MeV/nucl:

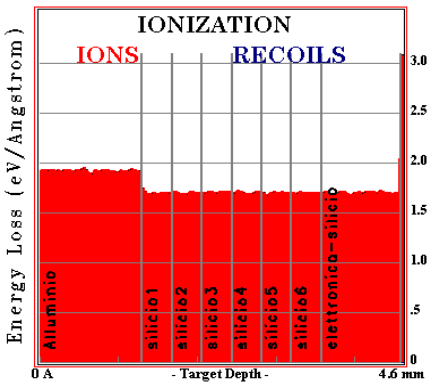

Fig. 7.14

C a 400 MeV/nucl:

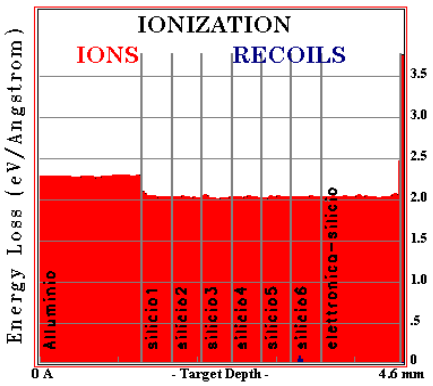

Fig. 7.15

C a 150 MeV/nucl:

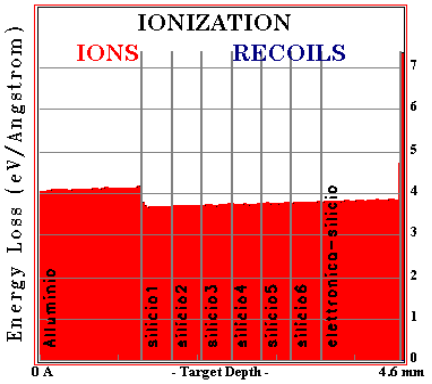

Fig. 7.16

C a 100 MeV/nucl:

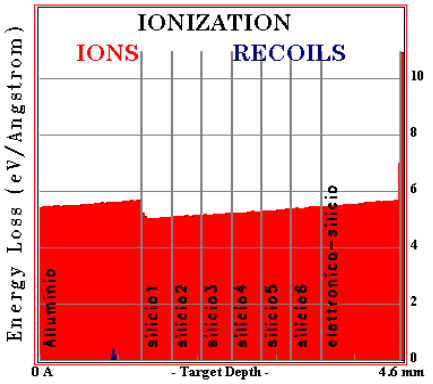

Fig. 7.17

SRIM				
beam energy (MeV/nucl)	**energy loss *silicon 1* (MeV)**	**energy loss *silicon 6* (MeV)**	**mean energy loss/plane**	
			MeV	**MIP**
600	6,460	6,460	6,460	59,27
400	7,600	7,600	7,600	69,72
150	13,870	14,250	14,060	128,99
100	19,000	20,520	19,760	181,28

Table 7.3: Simulation results (SRIM2003).

GEANT								
	energy loss/plane							
beam energy (MeV/n)	**600**		**400**		**150**		**100**	
plane	**MeV**	**MIP**	**MeV**	**MIP**	**MeV**	**MIP**	**MeV**	**MIP**
X0	6,526	59,87	7,893	72,41	14,75	135,32	21,29	195,32
Y0	6,527	59,88	7,888	72,37	14,62	134,13	20,91	191,83
X1	6,519	59,81	7,887	72,36	14,49	132,94	20,50	188,07
Y1	6,530	59,91	7,873	72,23	14,40	132,11	20,13	184,68
X2	6,514	59,76	7,869	72,19	14,27	130,92	19,73	181,01
Y2	6,521	59,83	7,856	72,07	14,16	129,91	19,46	178,53

Table 7.4: Simulation results (GEANT3).

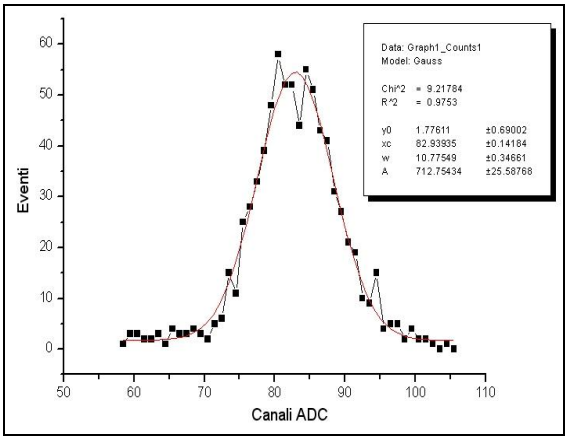

Fig. 7.18

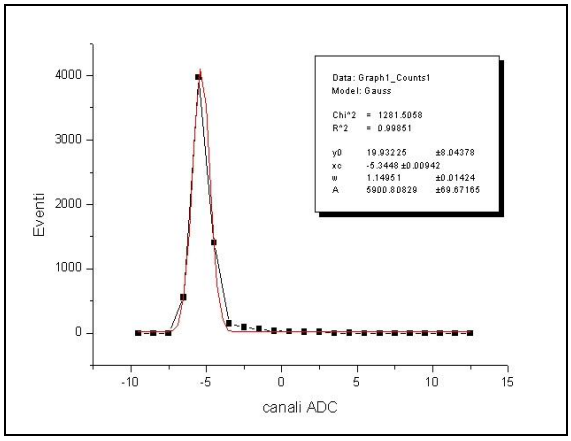

Fig. 7.19

Measurements were carried out placing the FM1 in front of the beam as in fig. 7.1; data were collected at the four different beam energies in order to have four calibration points. In the calibration runs the beam was pointed at the centre of one of the silicon wafer of the plane and the TE was left acquiring a variable number of events.

The analysis procedure was the following: after the subtraction of the pedestal mean value, the distributions of the energy lost in the strip hit by the beam were considered. In the tables 7.5 to 7.11 the peak values obtained from Gaussian fit are showed. Since it was noticed a negative tail accompanying the energy released by the beam particles, a correction was applied by subtracting from the signal value the peak value of a Gaussian fit on the negative values (fig. 7.18 and 7.19).

In the runs acquired in Normal Mode the peak at zero, due to the not triggered strips, was neglected.

The anomalous distributions described in paragraph 7.2.3 were often found in the X2 and Y2 silicon planes; in those cases the peculiar distributions appeared also in the negative value distributions. In

most of the cases it was still possible to consider the Gaussian fit because the curve shape and the peak position were kept despite the very low values of certain channels; in a limited number of cases some anomalous value have to be neglected in order to get the fit.

In the tables 7.5-7.11 both original and corrected values are reported; it has to be noticed that found values are similar for 16 strip groups read by the same CR2 (strips belonging to different groups are separated in the tables).

Table 7.5: Run 8 (600 MeV/nucl, 10 MIP, Internal Trigger, Full Mode, 7144 events)

	X0			X1			X2		
strip	**peak**	**negative peak**	**corrected peak**	**peak**	**negative peak**	**corrected peak**	**peak**	**negative peak**	**corrected peak**
10	83,58	-2,94	86,52	79,71	-3,22	82,93	84,31	-2,76	87,07
11	82,23	-2,70	84,92	79,53	-2,88	82,41	83,93	-2,87	86,79
12	81,28	-2,73	84,01	78,73	-3,36	82,09	83,23	-3,10	86,33
13	81,58	-2,96	84,54	78,56	-3,23	81,79	82,94	-3,50	86,44
14	81,99	-2,40	84,40	79,06	-3,18	82,24	83,64	-3,22	86,86
15	81,59	-3,34	84,93	78,76	-3,40	82,16	83,05	-3,45	86,50
16	78,13	-3,46	81,59	83,99	-2,80	86,80	80,35	-2,42	82,77
17	79,33	-3,10	82,43	83,42	-3,57	87,00	79,37	-3,56	82,93
18	79,91	-2,77	82,67	83,26	-2,74	86,00	79,41	-2,65	82,06
19	78,94	-3,59	82,53	-	-2,64	2,64	-	-	0,00
	Y0			**Y1**			**Y2**		
strip	**peak**	**negative peak**	**corrected peak**	**peak**	**negative peak**	**corrected peak**	**peak**	**negative peak**	**corrected peak**
44	79,70	-5,10	84,80	77,08	-5,34	82,43	76,53	-5,34	81,87
45	79,53	-4,86	84,39	77,55	-5,54	83,09	76,76	-5,63	82,39
46	79,68	-4,76	84,44	77,78	-5,40	83,18	76,18	-5,80	81,98
47	78,84	-5,60	84,44	77,78	-5,40	83,18	76,41	-5,48	81,89
48	80,21	-4,79	85,00	78,02	-5,27	83,29	76,04	-5,80	81,85
49	79,00	-5,57	84,58	76,90	-4,75	81,65	77,06	-5,14	82,20
50	79,27	-5,60	84,87	77,47	-4,90	82,36	75,52	-6,15	81,67
51	78,85	-5,65	84,50	77,58	-4,62	82,20	75,93	-5,85	81,78

Table 7.6: Run 10 (100 MeV/nucl, 10 MIP, Internal Trigger, Normal Mode, 3883 events)									
	X0			X1			X2		
strip	peak	negative peak	corrected peak	peak	negative peak	corrected peak	peak	negative peak	corrected peak
12	291,40	-3,17	294,57	274,70	-2,46	277,16	283,15	-2,83	285,98
13	294,63	-2,64	297,27	275,53	-2,05	277,58	281,66	-1,69	283,35
14	294,44	-2,46	296,90	274,96	-1,40	276,36	283,20	-0,32	283,52
15	294,65	-3,01	297,66	274,36	-1,44	275,80	281,52	-1,74	283,26
16	281,40	-2,74	284,14	290,67	-2,20	292,87	268,49	-0,82	269,31
17	283,30	-3,48	286,78	291,04	-2,24	293,28	269,83	-2,12	271,95
18	281,23	-4,07	285,30	-	-	-	-	-	-
	Y0			Y1			Y2		
strip	peak	negative peak	corrected peak	peak	negative peak	corrected peak	peak	negative peak	corrected peak
45	294,85	-5,10	299,95	-	-	-	-	-	-
46	294,12	-3,48	297,60	278,31	-4,37	282,68	267,73	-4,29	272,02
47	293,80	-3,70	297,50	279,94	-4,47	284,41	265,93	-4,42	270,35
48	294,49	-3,61	298,10	274,29	-3,81	278,10	266,23	-4,10	270,33
49	294,88	-3,94	298,82	273,65	-3,78	277,43	265,57	-3,78	269,35
50	297,01	-4,62	301,63	275,26	-4,46	279,72	264,49	-4,80	269,29

Table 7.7: Run 12 (100 MeV/nucl, 5 MIP, Internal Trigger, Normal Mode, 3939 events)									
	X0			X1			X2		
strip	peak	negative peak	corrected peak	peak	negative peak	corrected peak	peak	negative peak	corrected peak
12	299,15	-4,01	303,16	277,09	-3,43	280,52	281,07	-2,50	283,57
13	294,71	-2,40	297,11	276,35	-1,75	278,10	282,85	-2,02	284,87
14	295,49	-2,21	297,70	275,46	-0,98	276,44	283,35	-1,97	285,32
15	295,55	-2,85	298,40	274,43	-2,41	276,84	280,81	-2,86	283,67
16	282,42	-2,71	285,13	291,83	-1,76	293,59	268,30	-1,92	270,22
17	286,11	-3,46	289,57	290,58	-2,28	292,86	270,08	-2,01	272,09
18	287,28	-3,89	291,17	-	-	-	-	-	-
	Y0			Y1			Y2		
strip	peak	negative peak	corrected peak	peak	negative peak	corrected peak	peak	negative peak	corrected peak
46	295,03	-3,44	298,47	278,83	-4,12	282,95	267,50	-3,24	270,74
47	294,77	-4,60	299,37	281,32	-4,21	285,53	267,05	-3,66	270,71
48	295,86	-3,50	299,36	274,98	-3,56	278,54	266,82	-4,04	270,86
49	294,90	-3,70	298,60	274,28	-3,46	277,74	266,89	-3,38	270,27
50	297,00	-4,40	301,40	276,05	-4,02	280,07	-	-	-
51	294,63	-5,91	300,54	275,04	-5,31	280,35	-	-	-

Table 7.8: Run 20 (600 MeV/nucl, 5 MIP, Internal Trigger, Normal Mode, 30867 events)

	X0			X1			X2		
strip	**peak**	**negative peak**	**corrected peak**	**peak**	**negative peak**	**corrected peak**	**peak**	**negative peak**	**corrected peak**
10	-	-	-	79,29	-2,83	82,11	-	-	-
11	-	-	-	79,84	-3,02	82,86	84,17	-2,62	86,79
12	82,48	-3,04	85,52	78,95	-3,08	82,02	83,14	-3,83	86,97
13	81,64	-3,57	85,20	79,22	-3,11	82,33	83,27	-3,88	87,15
14	82,34	-2,95	85,29	79,05	-2,93	81,99	84,00	-3,78	87,79
15	81,64	-4,15	85,80	78,70	-3,34	82,03	83,93	-3,23	87,16
16	79,26	-3,32	82,58	83,63	-3,50	87,13	79,58	-2,74	82,32
17	79,14	-3,68	82,82	83,76	-3,64	87,40	79,72	-3,90	83,62
18	79,32	-3,37	82,69	84,18	-2,74	86,93	80,11	-2,90	83,01
19	78,37	-4,13	82,50	83,18	-3,78	86,95	80,12	-3,30	83,41
20	79,67	-3,28	82,95	83,39	-3,57	86,96	80,22	-2,60	82,82
	Y0			**Y1**			**Y2**		
strip	**peak**	**negative peak**	**corrected peak**	**peak**	**negative peak**	**corrected peak**	**peak**	**negative peak**	**corrected peak**
42	79,20	-5,11	84,32	78,25	-4,42	82,67	78,25	-4,17	82,41
43	80,01	-4,73	84,73	78,70	-4,35	83,05	78,70	-4,00	82,70
44	80,45	-4,64	85,09	78,31	-5,09	83,40	78,92	-3,21	82,13
45	80,24	-4,55	84,80	78,19	-5,07	83,25	78,19	-4,90	83,09
46	80,28	-4,50	84,78	78,40	-4,86	83,25	78,52	-4,17	82,70
47	79,58	-5,32	84,90	78,67	-5,18	83,85	78,67	-4,18	82,85
48	79,95	-5,13	85,09	77,18	-4,75	81,92	78,21	-4,13	82,34
49	79,97	-4,67	84,64	77,40	-4,59	81,99	77,79	-4,72	82,51
50	79,97	-4,55	84,52	76,95	-5,21	82,16	77,56	-4,19	81,75
51	80,28	-4,70	84,98	77,06	-5,11	82,17	77,65	-4,43	82,07
52	80,66	-4,59	85,26	76,92	-4,85	81,77	77,39	-4,12	81,51
53	81,10	-4,80	85,90	76,29	-5,24	81,53	77,61	-4,04	81,65

Table 7.9: Run 22 (400 MeV/nucl, 5 MIP, Internal Trigger, Normal Mode, 19066 events)

	X0			X1			X2		
strip	**peak**	**negative peak**	**corrected peak**	**peak**	**negative peak**	**corrected peak**	**peak**	**negative peak**	**corrected peak**
14	99,47	-2,86	102,34	96,98	-2,94	99,92	102,15	-2,52	104,67
15	99,82	-3,86	103,68	96,33	-3,13	99,45	101,01	-3,58	104,59
16	96,37	-3,20	99,56	102,21	-2,87	105,08	96,43	-3,38	99,81
17	95,77	-4,31	100,08	101,90	-3,26	105,16	96,55	-3,66	100,21
18	95,74	-4,27	100,00	102,41	-2,63	105,04	96,54	-3,79	100,33
	Y0			**Y1**			**Y2**		
strip	**peak**	**negative peak**	**corrected peak**	**peak**	**negative peak**	**corrected peak**	**peak**	**negative peak**	**corrected peak**
46	97,33	-4,71	102,05	96,45	-4,34	100,79	94,88	-4,11	98,99
47	97,91	-4,51	102,42	95,45	-5,18	100,64	94,42	-4,32	98,74
48	97,69	-4,82	102,51	94,11	-4,96	99,07	94,84	-4,20	99,04
49	97,32	-5,16	102,48	93,85	-5,13	98,99	95,27	-4,09	99,36
50	96,02	-5,48	101,50	93,13	-5,0837	98,21	94,94	-5,07	100,01

Table 7.10: Run 32 (600 MeV/nucl, 3 MIP, Internal Trigger, Normal Mode, 28390 events)									
	X0			X1			X2		
strip	peak	negative peak	corrected peak	peak	negative peak	corrected peak	peak	negative peak	corrected peak
42	82,72	-3,49	86,22	83,42	-3,63	87,05	87,11	-3,38	90,49
43	81,94	-3,36	85,29	83,51	-3,26	86,77	84,42	-3,96	88,38
44	82,31	-3,14	85,45	83,84	-3,60	87,43	86,37	-3,18	89,55
45	83,00	-2,71	85,71	83,78	-3,27	87,05	84,97	-3,83	88,80
46	82,93	-3,00	85,93	83,99	-3,42	87,41	86,10	-3,36	89,46
47	82,37	-3,67	86,04	82,96	-4,53	87,49	84,15	-4,46	88,61
48	78,09	-3,76	81,85	79,14	-4,15	83,29	84,82	-3,84	88,65
49	78,22	-3,63	81,85	78,65	-4,04	82,68	81,49	-4,53	86,02
50	78,55	-3,54	82,08	79,05	-4,28	83,33	85,58	-3,50	89,08
	Y0			Y1			Y2		
strip	peak	negative peak	corrected peak	peak	negative peak	corrected peak	peak	negative peak	corrected peak
10	83,99	-2,29	86,28	80,51	-1,83	82,34	79,49	-2,89	82,38
11	83,84	-2,28	86,12	79,86	-2,07	81,93	80,33	-2,05	82,38
12	84,56	-1,75	86,31	80,68	-2,03	82,70	79,74	-2,85	82,59
13	83,56	-2,95	86,50	80,37	-2,17	82,54	80,38	-2,31	82,69
14	83,99	-2,75	86,74	80,20	-2,13	82,33	80,16	-2,91	83,07
15	84,15	-3,20	87,35	79,99	-2,73	82,72	80,61	-2,63	83,23
16	83,50	-2,65	86,15	83,58	-2,61	86,19	81,05	-1,86	82,91
17	84,58	-2,04	86,62	84,01	-1,95	85,96	80,89	-2,70	83,59
18	84,09	-2,82	86,91	84,27	-2,07	86,34	81,51	-2,16	83,66
19	84,87	-2,20	87,07	84,60	-1,91	86,51	80,64	-2,78	83,41
20	84,17	-2,74	86,91	83,99	-2,22	86,21	80,53	-2,58	83,11

Table 7.11: Run 34 (150 MeV/nucl, 5 MIP, Internal Trigger, Normal Mode, 14315 events)									
	X0			X1			X2		
strip	peak	negative peak	corrected peak	peak	negative peak	corrected peak	peak	negative peak	corrected peak
45	198,94	-3,13	202,07	199,36	-4,03	203,39	199,26	-4,05	203,31
46	200,32	-2,63	202,95	202,17	-2,48	204,65	199,08	-2,24	201,32
47	199,36	-3,18	202,54	200,58	-3,49	204,07	199,44	-2,89	202,33
48	191,99	-2,04	194,03	191,73	-3,19	194,92	199,90	-1,27	201,17
49	190,54	-3,76	194,30	190,63	-2,86	193,49	197,65	-4,39	202,04
50	190,97	-3,93	194,90				197,42	-3,10	200,52
	Y0			Y1			Y2		
strip	peak	negative peak	corrected peak	peak	negative peak	corrected peak	peak	negative peak	corrected peak
13	203,35	-2,34	205,69	192,13	-2,02	194,15	188,05	-1,87	189,92
14	202,74	-2,52	205,26	191,34	-1,56	192,90	187,97	-2,06	190,03
15	203,37	-3,29	206,66	192,09	-0,77	192,86	189,18	-1,90	191,08
16	203,33	-1,48	204,81	198,89	-1,80	200,69	189,01	-0,28	189,29
17	203,06	-2,33	205,39	197,29	-1,35	198,64	189,60	-1,40	191,00

Values of energy losses in ADC channels showed in the tables were plotted versus the corresponding energy losses in MIP obtained with simulations. In fig. 7.20 this plot is showed for each of the six silicon planes. The slopes of the obtained lines provide the conversion factor MIP/ADC channels for the single silicon plane of SDU-FM1. It was still noticed that energy losses vary, sometimes significantly, with the strip group read by different CR2. Conversion factors were then calculated also for each group of 16 strips for each silicon plane; this was obviously possible only for 16 strip group hit by the beam, so only data collected at 100, 400 e 600 MeV/nucleon beam energy were considered, because the 150 MeV/nucleon beam pointed to a different silicon wafer. All calculated values are reported in table 7.12.
Considering a medium conversion factor of 0.63 MIP/ADC channels and a medium pedestal value of about 400 ADC channels, the ALTEA dynamic range resulted between 5 and 2300 MIP.

7.3 GSI, November 2003: conclusions

Results from November 2003 session at GSI highlighted some malfunctioning in the tested devices and some phenomena to investigate. The relative little beam time available prevented a deep study on the anomalies founded, but a further effort to test all the ALTEA-space hardware was needed.
A conversion factors ranging from 0.6 to 0.66 were obtained from calibration of SDU-FM1, with correlation coefficients between 0.9999 and 0.9996. A separate calculation for group of 16 silicon strips read by the same CR2 seemed to be convenient to get a punctual device calibration.

7.4 GSI, April 2004: beam tests

In the scenario opened by the previous test session of November 2003, the session of April 2004 at GSI was particularly important both for continuing the investigation on the problems found in November and to complete the calibration of all the components of ALTEA-space hardware.
In April the full Flight Model, 6 SDUs (SDU-FM1 through SDU-FM6) and the DAU (Data Acquisition Unit), and the SDU-TM1 were tested with Carbon nuclei (beam at 100, 600 and 1000 MeV/n) and Titanium nuclei (beam at 200 and 600 MeV/n) at the GSI accelerator. Both TE and DAU were used.

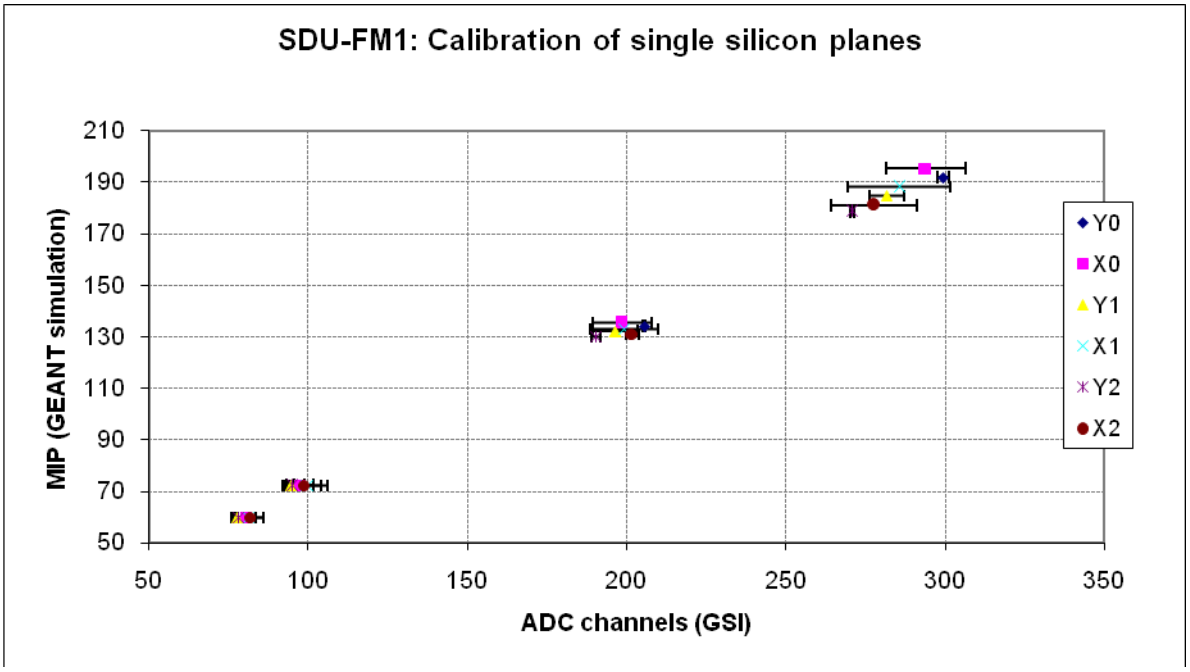

Fig. 7.20: Plot of conversion ADC channels (experimental) to MIP (GEANT simulation).

Table 7.12: MIP/ ADC channels conversion factors per single plane and for 16 strip groups

silicon plane	MIP/ ADC channels conversion factors		
	strip X 0-15 strip Y 32-47	strip X 16-31 strip Y 48-63	single plane
Y0	0,61	0,61	0,6
X0	0,63	0,66	0,63
Y1	0,62	0,63	0,61
X1	0,65	0,62	0,62
Y2	0,63	0,63	0,61
X2	0,61	0,64	0,61

Each SDU was completely scanned to check the homogeneity and functionality of all strips; for each ion at different energies the instrument response was compared with Montecarlo simulations to study its linearity and to calculate instrument amplification. A study of the nuclear recognition capability of the device was also performed using an Aluminium absorber placed in front of the

beam. Finally, some troubleshooting tests were carried out to investigate to the anomalous energy distributions described in paragraph 7.2.2.

7.5 GSI, April 2004: results

7.5.1 Software for data analysis

A specific software was realized to analyze data acquired by the DAU. The DAUTELook is capable to manage scientific data, pedestals and calibration signals as the QuickLook used for TM data in November. A screenshot of this software with a track of 600 MeV/nucleon Titanium beam is showed in fig. 7.21: the 'shadow' of low energy losses in the strips around the track is typical in case of high Z^2 particle.

7.5.2 GSI, April 2004: final calibration

Also in this session the system acquires 100 measures ('*zero signals'*) in standard conditions before starting acquisition; the mean values (in ADC channels) for each strip are taken as pedestal values. Pedestal gives the mean values of the noise of each strip. The analysis shows that detectors have a good stability, pedestal distribution have a standard deviation around 0.5 ADC channels (about 9000 e^-).

A charge injection test led to an amplification factor of about 0.57 ADC channels/mV.

For each measurement the distribution of the energy loss in the silicon plane is considered. In figure 7.22 this distribution (in ADC channels) is plotted; pedestal peak is stable and well separate from particle signal.

Because of the good detector stability the subtraction of pedestal from the distributions of the released energy in the detector planes is performed and the peak position is extrapolated. In fig. 7.23 a typical distribution of released energy, in ADC channels, from Ti nuclei at 600 MeV/n is showed; the superimposed curve is the gaussian fit used to determine the peak position.

All the beam conditions with different ions and energies and with absorbers in front of the beam have been simulated with GEANT 3 (see table 7.13), as described in paragraph 7.2.4; results from

simulation have been compared with experimental data for each plane of each of the six SDU to obtain the calibration curves as the one showed in fig. 7.20 for SDU. The conversion factors are summarized in table 7.14. The difference between all conversion factors is always less than 10%.
In figure 7.24 the Montecarlo simulation of released energy versus incident C beam energy is showed in comparison with experimental data. The axis are transformed using the conversion factor MIP/ADC channels and the offset term obtained from calibration of X2 silicon plane.

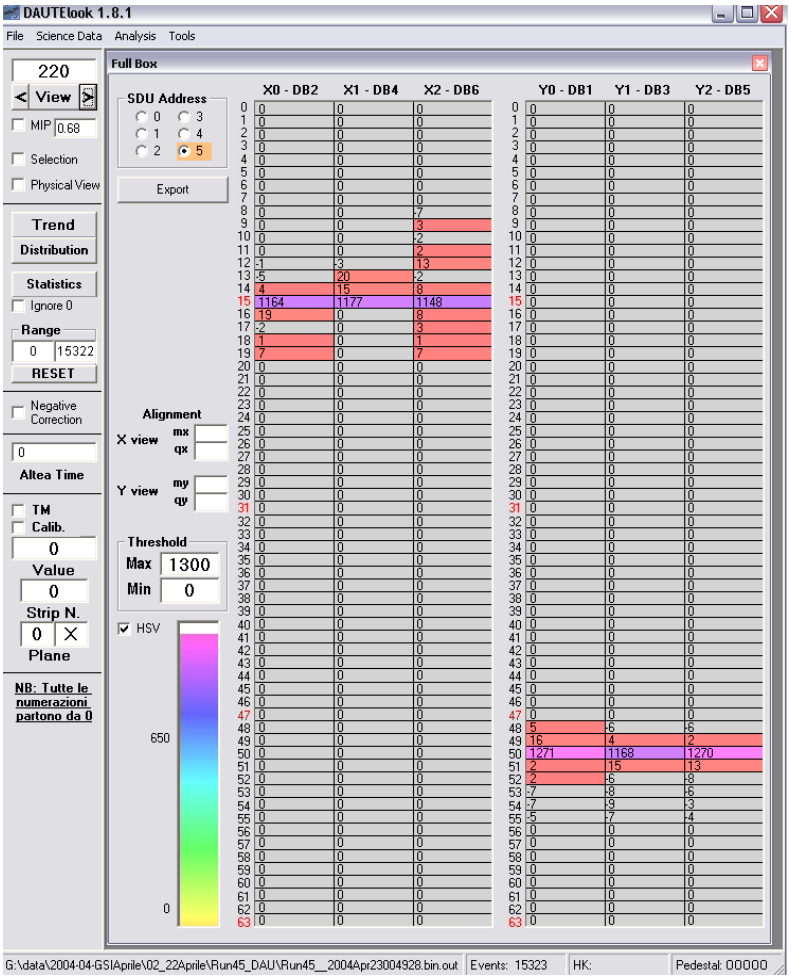

Fig. 7.21

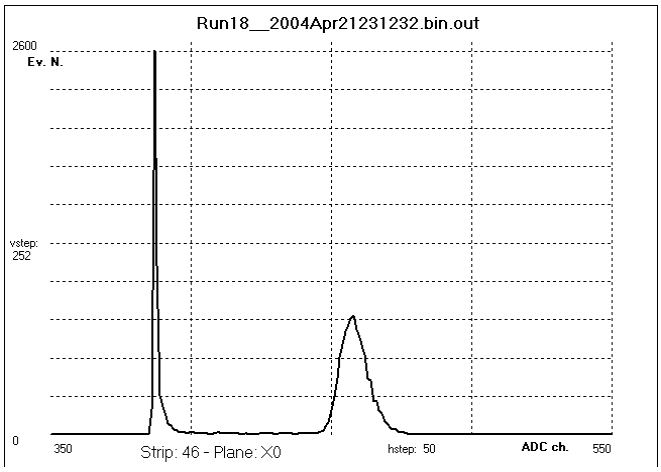

Fig. 7.22: Energy loss distribution in strip 46 in plane X0 without pedestal subtraction.

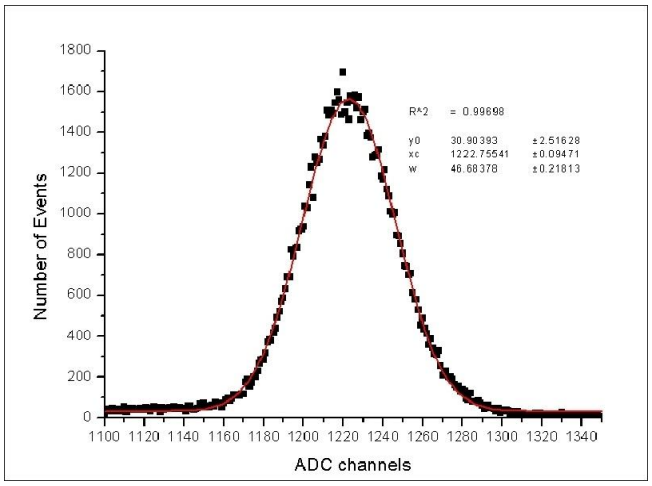

Fig. 7.23: Distribution of released energy from Ti nuclei at 600 MeV/n in one of the six detector planes. Superimposed the continuous curve of the gaussian fit is showed.

Beam	Silicon plane					
	Y0	X0	Y1	X1	Y2	X2
C1000	50.64	50.75	50.76	50.86	50.87	50.77
C600	59.87	59.88	59.81	59.91	59.76	59.83
C400	72.41	72.37	72.36	72.23	72.19	72.07
C150	135.32	134.13	132.94	132.11	130.92	129.91
C100	195.32	191.83	188.07	184.68	181.01	178.53
Ti600	807.43	808.44	807.34	803.21	804.22	806.33
Ti200	1607.34	1581.65	1554.13	1528.44	1500.92	1479.82

Table 7.13: Simulated energy losses in the six silicon planes (GEANT3).

SDU	Conversion factors (MIP/ADC channel) for silicon plane					
	Y0	X0	Y1	X1	Y2	X2
FM1	0.64	0.63	0.66	0.66	0.66	0.62
FM2	0.62	0.65	0.67	0.63	0.62	0.66
FM3	0.61	0.63	0.60	0.65	0.61	0.64
FM4	0.62	0.62	0.65	0.67	0.62	0.65
FM5	0.61	0.65	0.63	0.64	0.64	0.61
FM6	0.65	0.64	0.66	0.64	0.61	0.66

Table 7.14: Conversion factors MIP/ADC channels for each silicon plane for each SDU

In few runs the SDU was positioned inclined in respect to the beam direction and the obtained beam profiles are showed in fig. 7.25.

In order to study the nuclear recognition capability of the device, an Aluminium absorber 6 mm thick was also used to study fragmentations; it has been placed between the incoming beam (Ti at 600 MeV/n) and SDU-TM1. The energy distribution was considered and filters were applied to select particles releasing almost constant energy on the six planes; single track events were also selected. With these choices the distribution in figure 7.26 is obtained. Titanium peak is around 1200 ADC channels. The peak position was scaled by lower elements Z^2 values in order to identify fragments. Peak position and expected element positions are in very good agreement. In the low ADC channels region a better accuracy will be reached with the FM due to its optimized electronic boards.

Another test was performed putting two SDUs, SDU-FM4 and SDU-FM3, in front of the beam (C at 100 MeV/n) and the energy loss in the twelve planes was considered (fig. 7.27). These values are compared with the ones obtained with a Montecarlo calculation in which materials between the two SDUs have been simulated (the box covers are 2.6mm of Al and ROE board is 0.8μm of glass+0.8μm of copper+1μm of silicon).

All these results were published in [56].

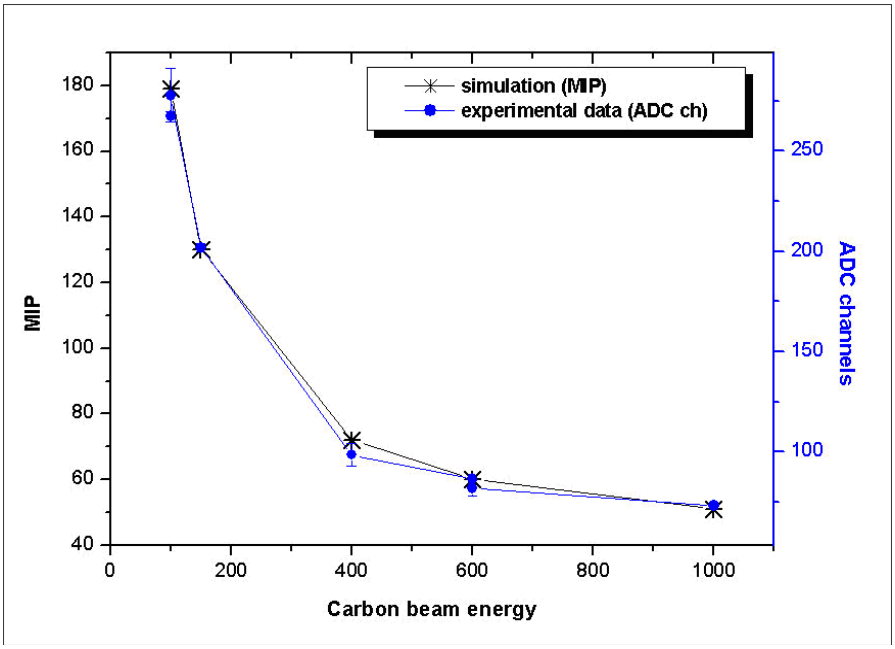

Fig. 7.24

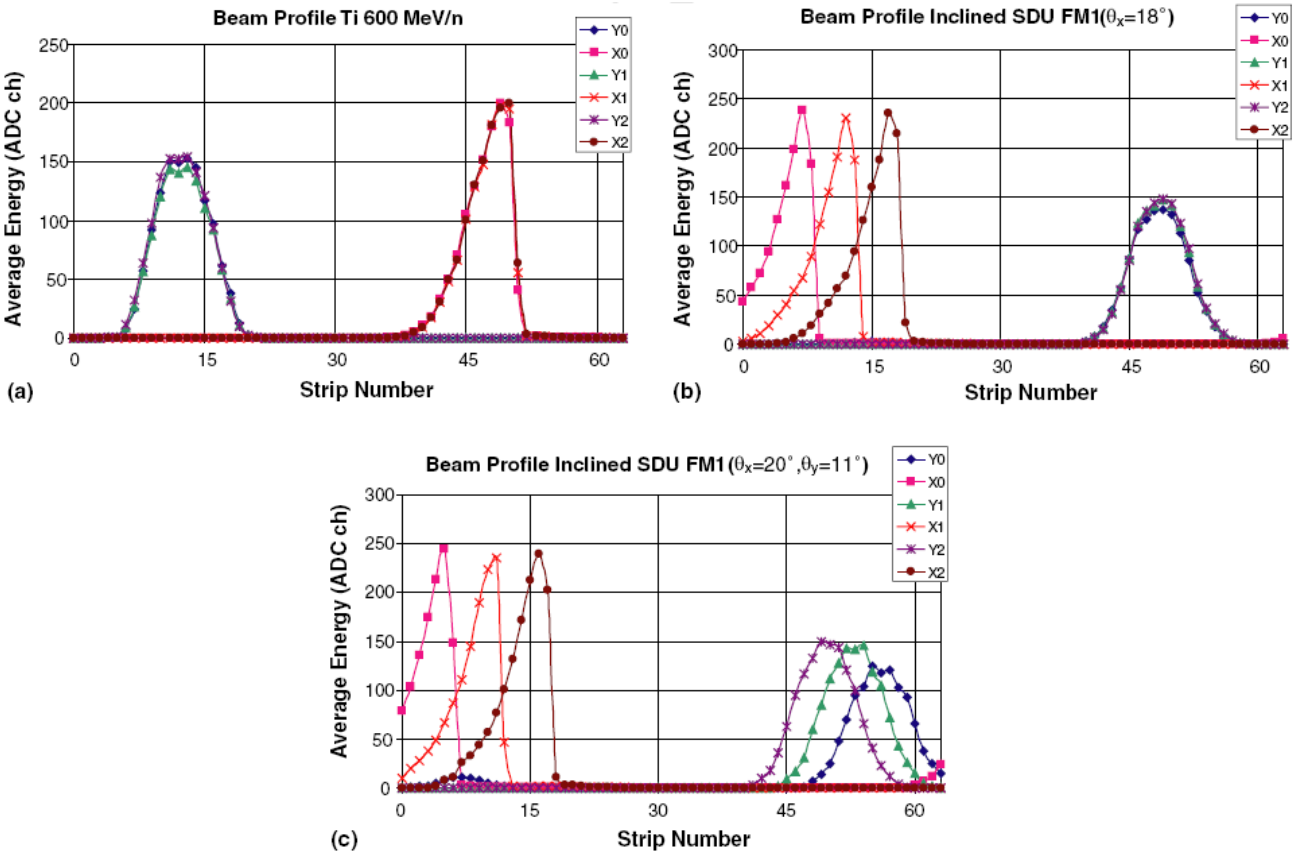

Fig. 7.25: Beam profile in three different experimental conditions: (a) SDU perpendicular at the beam, (b) SDU inclined of 18 ± 1_ (in respect to the direction of the incident beam) in X direction, (c) SDU inclined in both X (20 ± 1°) and Y (11 ± 1°) directions.

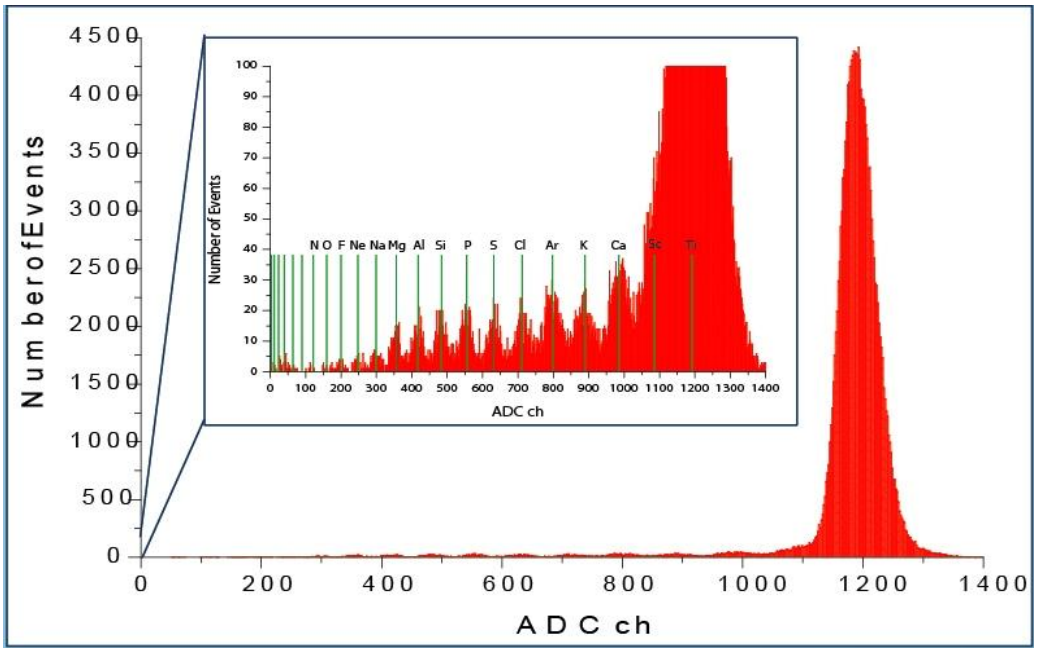

Fig. 7.26: Fragments obtained with titanium beam (600 MeV/n) on 6 mm of aluminium put in front of the detector.

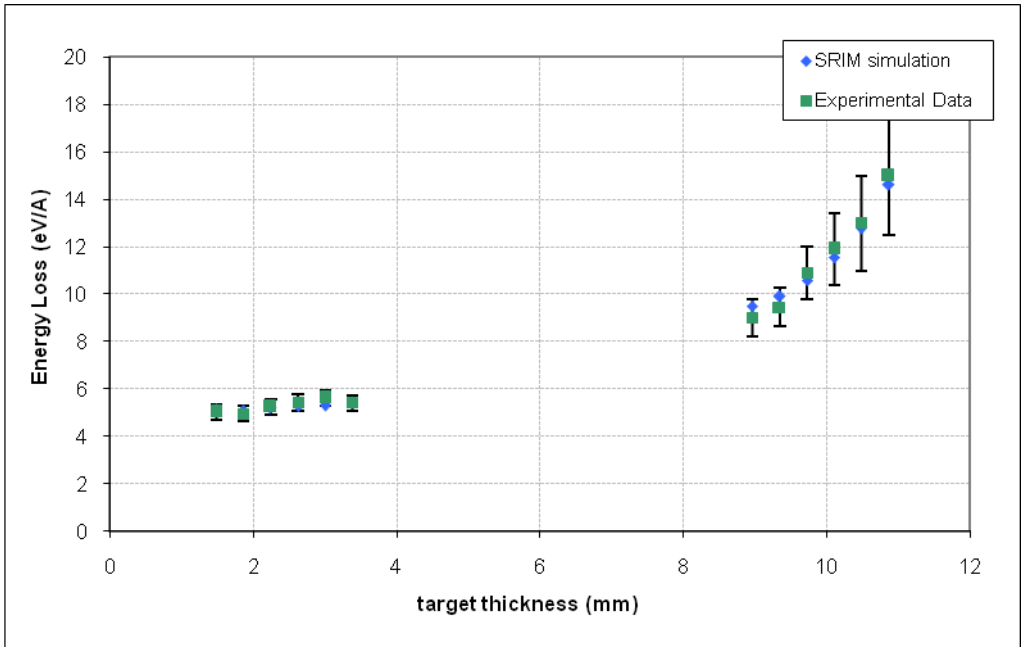

Fig. 7.27: Comparison between experimental data and simulation for two SDUs placed in front of the beam.

7.5.3 GSI, April 2004: troubleshooting

A not negligible time fraction of the available beam time was spent to carry out a deep investigation on the anomalies found in the previous test session at GSI, in particular on the energy distribution with the strange shape (see paragraph 7.2.3). The investigation consisted in a lot of measurements taken at different beam ion and energy, threshold, and acquisition modality (Full and Normal mode) in order to look for some correlation in anomalies appearing. Then a further test was performed using a 'kill mask' to switch off one of more of silicon planes of the SDU. From all these tests no univocal information raised: the anomalies were found both in Normal and in Full mode (also if in Normal Mode they were prevalent), but not at every threshold value and not for all ions at all energies. In particular this effect seemed to depend in some way on the energy loss because it was bigger at the higher energy losses (for example when Titanium beam was used). In some cases only very irregular distributions were found, in place of distributions in which a lot of ADC channels had value near to zero (as in fig 7.5 for example).

After this session the investigation was continued at the University of Tor Vergata and at the Alcatel Alenia Space (Laben) in Milan, where the ALTEA hardware was assembled and where an investigation in laboratory tried to reproduce the anomalous distribution with a pulse generator. The main reason why phenomena was not discovered before in the lab was that a charge injection has a very narrow distribution (few ADC channels), while the beam has a width of about 20 ADC channels. In order to perform the investigation a distribution with a comparable width was obtained in the lab and this allowed reproducing the anomalous distributions. Several tests were made to repeat the ones at the beam and to try correlation between the intensity of phenomena and the injected energy, the threshold and strip reading order.

At last it was found that the cause of the problem was interference between the ADC reference voltage on the ROE board, DB trigger signals and shift multiplexer selection signals. The converter on the ROE is a 12 bit SAR (Successive Approximation Register) ADC.

To perform a conversion, the successive approximation register is initialized so that the most significant bit is equal to a digital 1. This code is fed into a DAC which then supplies the analog equivalent of this digital code ($V_{ref}/2$) into the comparator circuit for comparison with the sampled input voltage. If this analog voltage exceeds input voltage the comparator causes the SAR to reset this bit and set the next bit to a digital 1. If it is lower, then the bit is left a 1 and the next bit is set to 1. This binary search continues until every bit in the SAR has been tested. The resulting code is the digital approximation of the sampled input voltage and is finally output by the ADC at the end of the conversion. Since the comparisons to set all the bit values of the conversion output refer to a

fraction of the V_{ref} (reference voltage), the V_{ref} itself is a very critical point. The reference is a 2.5V voltage generated by the ROE and if it is not stable during the conversion it could led to the anomalous distribution observed. If V_{ref} is not stable when setting B0 value, there will be more 0 than one, or vice versa, and an anomalous distribution of odd and even numbers is observed. A similar situation occurs with all the bit of the conversion, but the phenomenon is more evident with less significant bits, when voltages are in the order of mV. The effect of a stochastic noise on V_{ref} would be a flattening of the spectrum, but coupling between V_{ref} and following signals are observed:

-DB trigger signals

-Multiplexer selection signals of the shift register internal to the CR2.0

This means that corresponding to the above signals transitions, V_{ref} undergoes to fluctuations of some mV, that explains correlations with threshold level and with Normal/Full mode.

Applied solution was to stabilize V_{ref} with an extra capacitor, that led to a strong attenuation of the phenomenon.

Chapter 8:
Integrated FM test

After the system was calibrated and tested in each single components in the laboratory of Alcatel Alenia Space (Laben) and at the GSI accelerator, it was tested with all its part connected as in the DOSI and CNSM flight configurations. The tests took place in two occasions: in the lab of Alcatel Alenia Space in Milan and during the PTCS delivery test at the NASA lab of the Kennedy Space Centre (KSC), Florida.
In this chapter results from analysis of the files obtained in these sessions will be discuss.

8.1 Data analysis software

In order to perform the analysis of data acquired from the complete system, the software used for the beam tests was modified so to manage concurrently the six SDUs and the EEG. Then a new software was realized in order to divide the different data types acquired: scientific data, EEG data, Housekeeping data, DAU message data. Scientific data are particle data, in which the energy released on the silicon plane detector strips is read. EEG data are data acquired by the BEU (Brain Explorer Unit) and include the signals captured by the Electroencephalograph. Housekeeping data contain all information useful to monitor the device functionality as the temperatures of silicon planes, the currents, the voltages, and so on. DAU message data are generated by the DAU and concern the time when the pushbutton is pushed, when the images change on the visual stimulator and they can contain some error messages. In particular, science data can be analyze with the new version of the DAUTELook software.

8.2 File 'X17FEBPROVA19_somma.bin.out'

This file is the first file generated by the complete system of ALTEA-space. It was generated in the laboratory of Alcatel Alenia Space (Laben) in Milan; during its acquisition all systems (SDS, EEG, VSU) were switched on, also if the EEG cap was floating, no subject was undergoing the measure.
The acquisition lasted about two hours; it started few time after all systems were switched on. Pedestals were acquired after the acquisition of scientific data. Scientific data were acquired in Full Mode.
First temperatures and inverse currents of the silicon planes (from the Housekeeping data) were analyzed. They are crucial to characterize the detector and to define nominal functional values.
Temperature trends of the six SDUs are plotted in fig. 8.1. In each plot the temperature of each silicon plane is showed. On the abscissa axis there is the time, in seconds, since the acquisition start; the temperature are acquired each 10 seconds.
The temperature values on each plane grow from a value of about 10°C to about 32-33°C when they began to flatten; this is compatible with the start of the measure just after the system was switched on.
In the plot of fig. 8.2 the temperature trend for an acquisition time fraction for SDU4 is showed; from this plot it can be noticed that X planes have a slightly higher temperature of Y plane. This is found in the other SDUs, too, but it does not imply a different behaviour in planes belonging to different views. First 50 temperature values acquired concurrently by the six SDUs were then examined, together with 50 temperature values in the central parte of the acquisition time and 50 temperature values at the end of the measurement. Also from comparisons between such values a similar trends was found for all the SDUs, with a slight difference between X and Y plane temperatures.
The SDU4 has a temperature lower than the other SDUs one, but it has to be considered that this SDU was placed is in a different position, because during the measurement it was not mounted on the structure but it was on a table. The inverse current in the silicon planes was also analyzed; the inverse current is measured in each silicon wafer, so there are 2 measures for plane and 12 measures for each SDU (see fig. 8.3). The trend for the currents is similar to the one for temperatures, still reflecting the device was nearly started at the moment of measurements. Current value are usually similar for the two silicon wafers of each plane, except in SDU5 and SDU6 where two silicon wafer (second silicon wafer, plane Y2, strips 32-63 for SDU5 and first silicon wafer, plane X1, strips 32-63 for SDU6) shows a higher value, that however follows the trend of the other plane currents and remains stable in time.

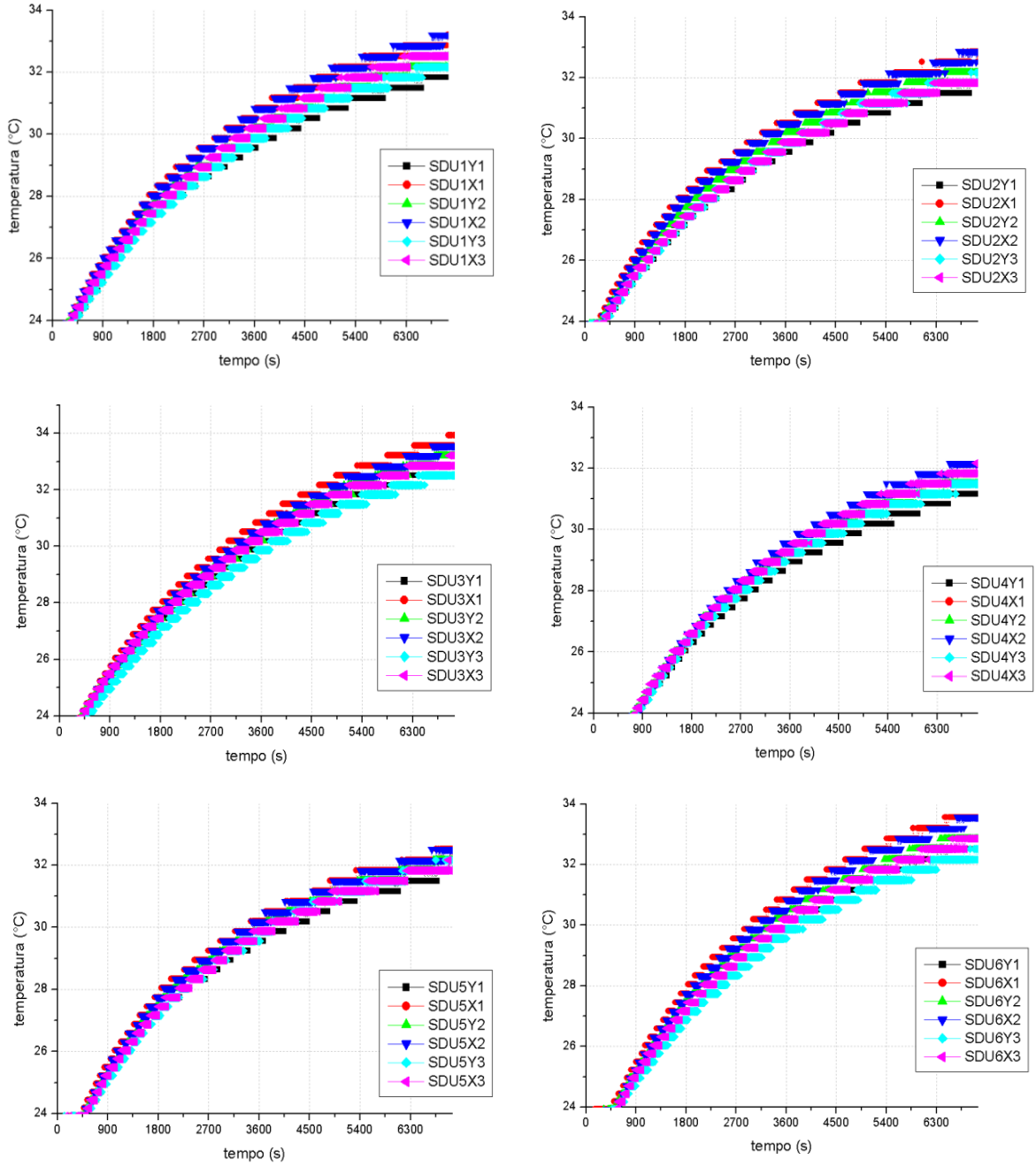

Fig. 8.1: Temperatures of the silicon planes for each SDU.

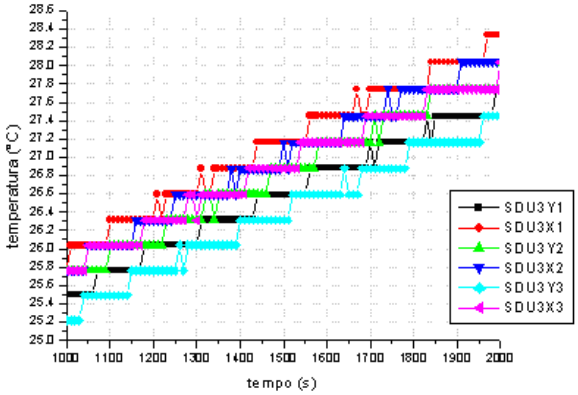

Fig. 8.2: SDU3 temperature trend for a fraction acquisition time.

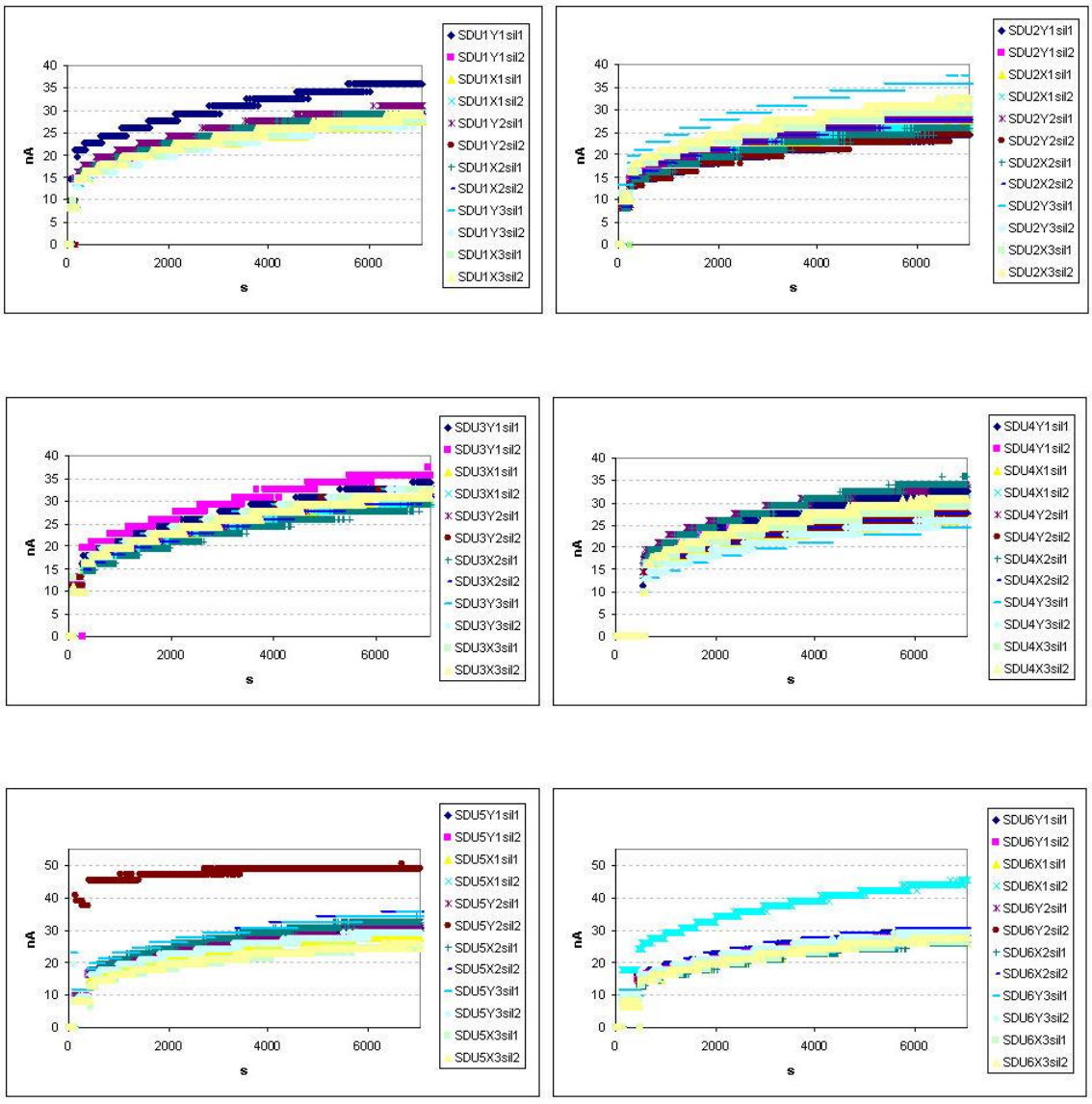

Fig.8.3: Current trend for the six SDUs.

After the Housekeeping data, scientific data were examined. The particles event collected in the file, consisting in cosmic ray protons and products of cosmic ray interaction with matter of the lab, are distributed as summarized in table 8.1. 55 events were acquired, but they resulted really noised, so that in most of the cases the eventual particle track is not recognizable (see fig.8.4, where two example of noisy event and particle track are showed). The fact that pedestals were acquired after the end of the measurement was reflected by the occurrence of negative values on almost all the strips. It has to be noticed that no algorithm was applied to reconstruct the particle tracks. The event number 36 is peculiar, because it shows some energy loss both on SDU2 and SDU6; in the SDU2 the track is complete, while in SDU6 values on X0 and Y0 are missing (see fig. 8.5).

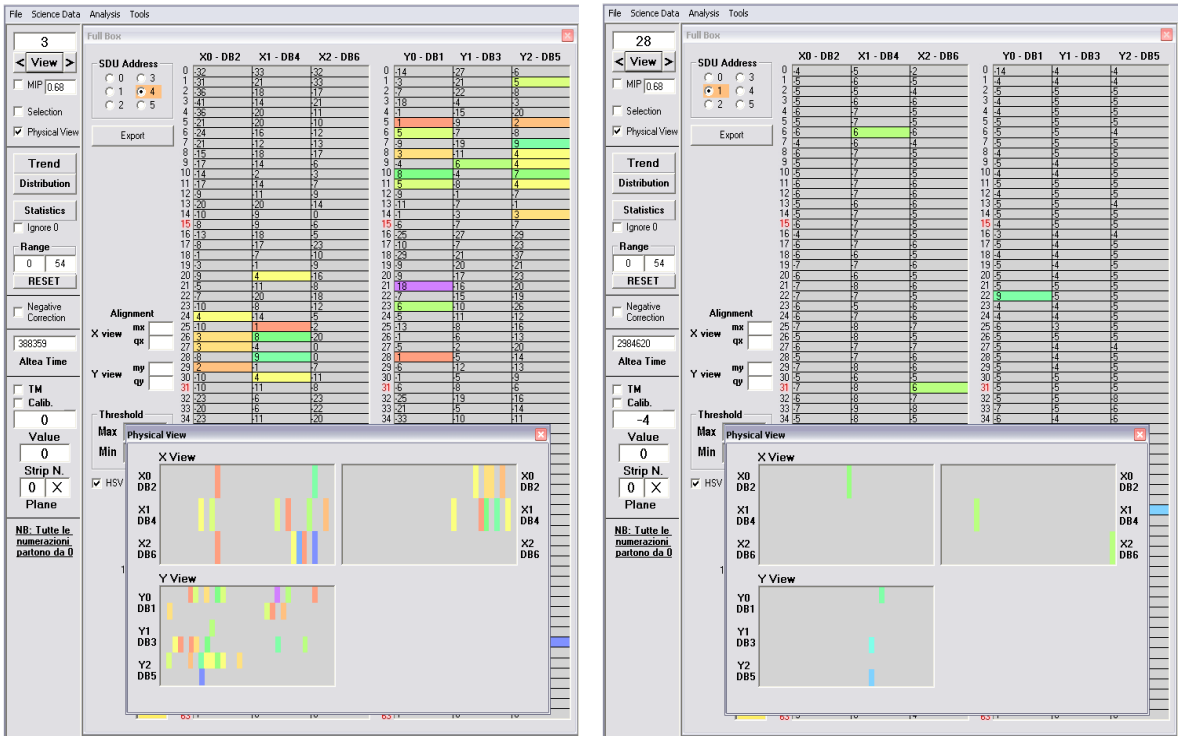

Fig. 8.4: Two examples of events acquired in file X17FEBPROVA19_somma.bin.out: a noisy events (left) and an event with a visible particle track (right).

event	SDU1	SDU2	SDU3	SDU4	SDU5	SDU6	track	note
1		x						
2		x					x	
3	x							
4					x			
5					x		x	
6			x					
7	x							
8		x						
9	x		x	x	x	x		
10			x					
11		x						
12			x	x	x			
13	x	x						
14			x					
15		x					x	lot of noise but visibile track
16		x						
17		x					x	
18			x				x	Y0 missing
19				x				
20	x							
21		x						
22	x		x	x	x	x		
23		x			x			
24	x	x		x	x	x		
25		x					x	
26					x			
27			x					
28		x					x	
29		x					x	
30					x			
31						x	x	Y0 missing
32		x						
33					x		x	
34		x						
35	x		x	x	x	x		
36		x				x	x	complete track on SDU2, X0 and Y0 missing on SDU6; not alligned
37		x					x	
38				x				
39		x						
40			x	x				
41	x	x	x	x				
42				x				
43			x					
44	x							
45			x					
46					x		x	
47					x		x	
48		x						
49	x	x	x			x		
50	x	x	x	x	x	x		
51	x				x	x		
52		x						
53					x			
54		x						
55		x					x	

Table 8.1: summary of events recorded in file X17FEBPROVA19_somma.bin.out.

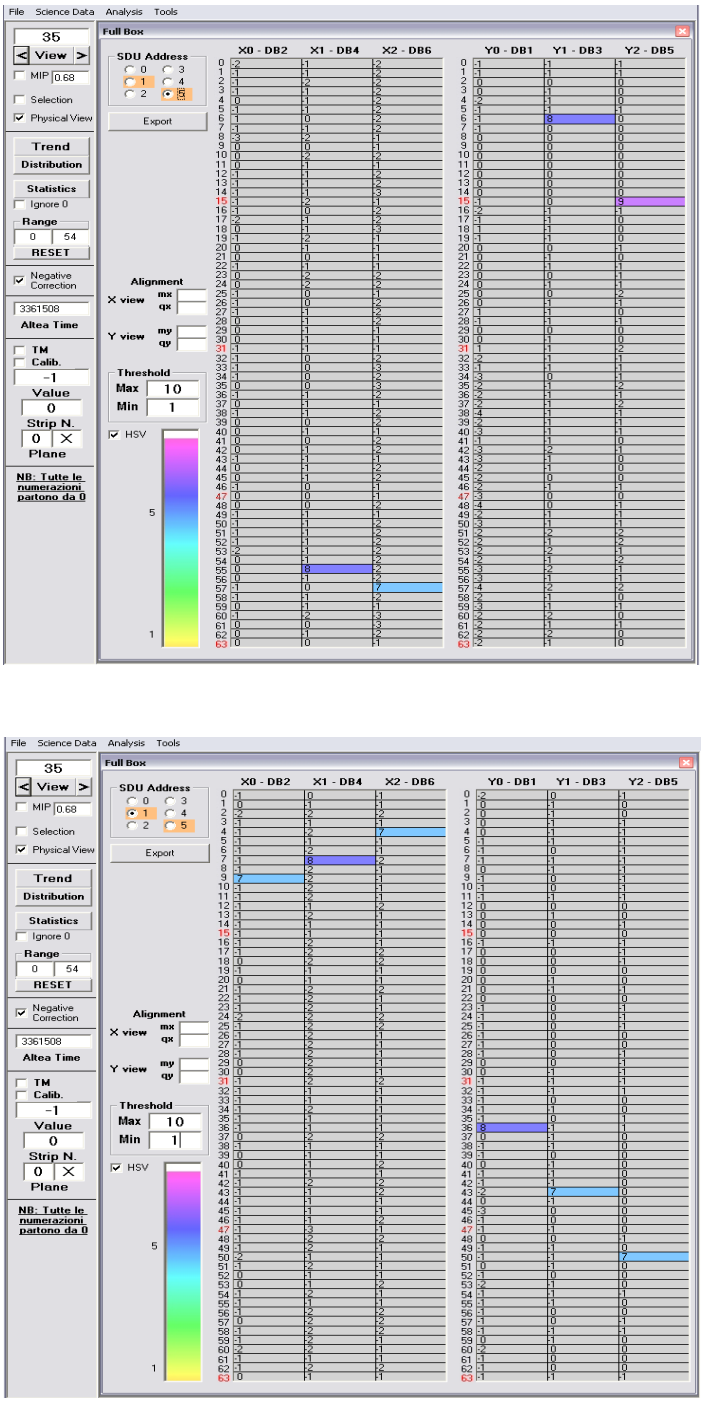

Fig. 8.5: Events 36 in file X17FEBPROVA19_somma.bin.out: complete track on SDU2, incomplete on SDU6.

In conclusion, this file is the first proof of functioning of the complete system, files of scientific, housekeeping and EEG data were correctly produced, the device was characterized with the nominal temperature and current values. Acquired scientific data a

were often noisy; in order to evaluate the noise reason the acquisition of other files on ground was crucial.

8.3 File AlteaLog_21032005_1921_000.log

This file was generated during the PTCS test in (KSC), when the ALTEA Flight Model was delivered to NASA. In that case all data flux was simulated and tested and scientific and housekeeping data were acquired. As for the file examined in previous paragraph, the housekeeping data were analyzed. In fig. 8.6 the temperature trend for the six SDUs is showed.

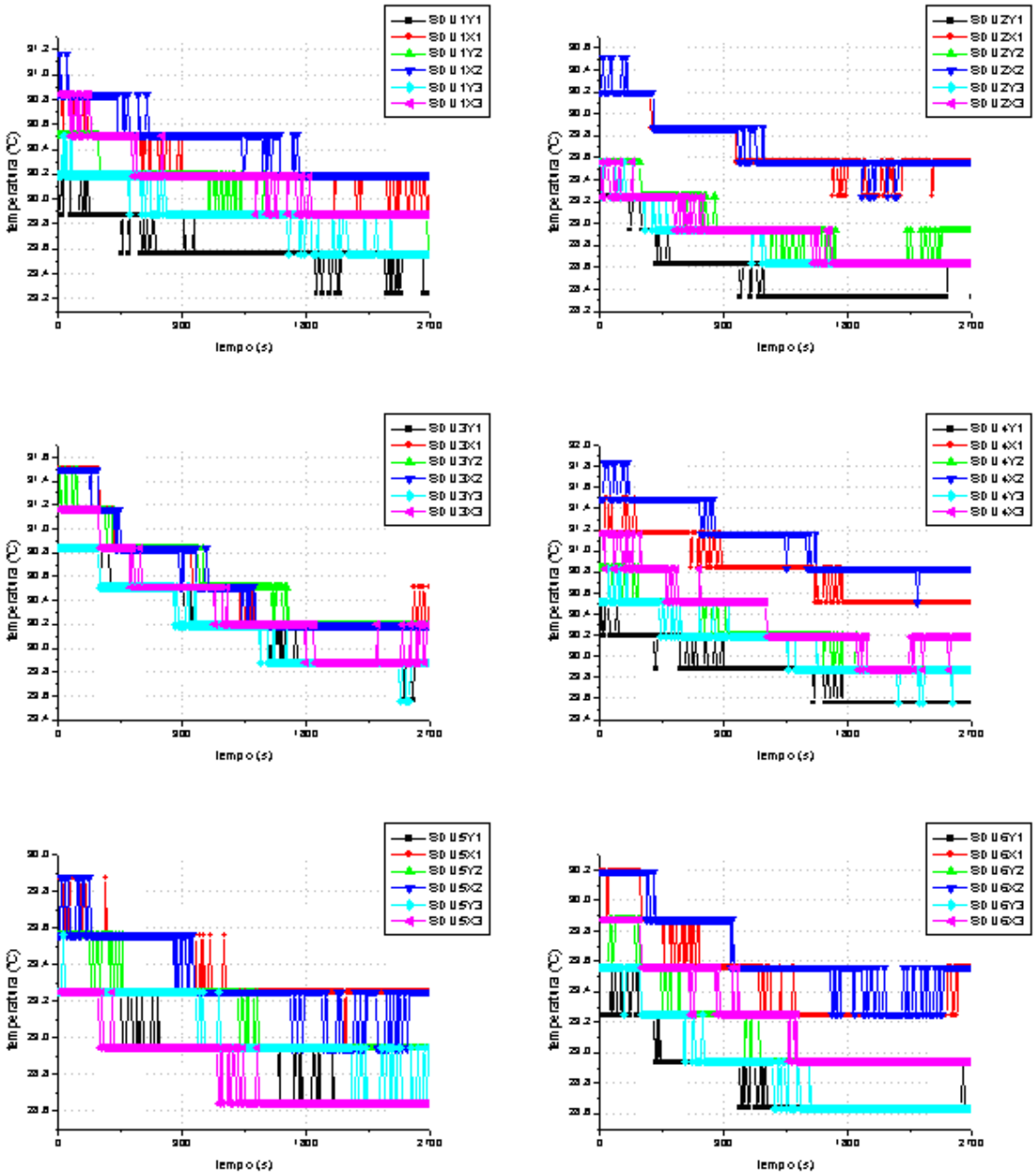

Fig. 8.6: Temperature trend for the six SDUs.

The acquisition of this file lasted a time shorter (about 45 minutes) in respect to the previous case and it started when the system was already switched on. For this reason the temperature values appear stable and the positive trend expected in case of recent system activation is not found. Actually the temperatures decrease of some fraction of degree, as if the system was adapting to a slight environmental variation.

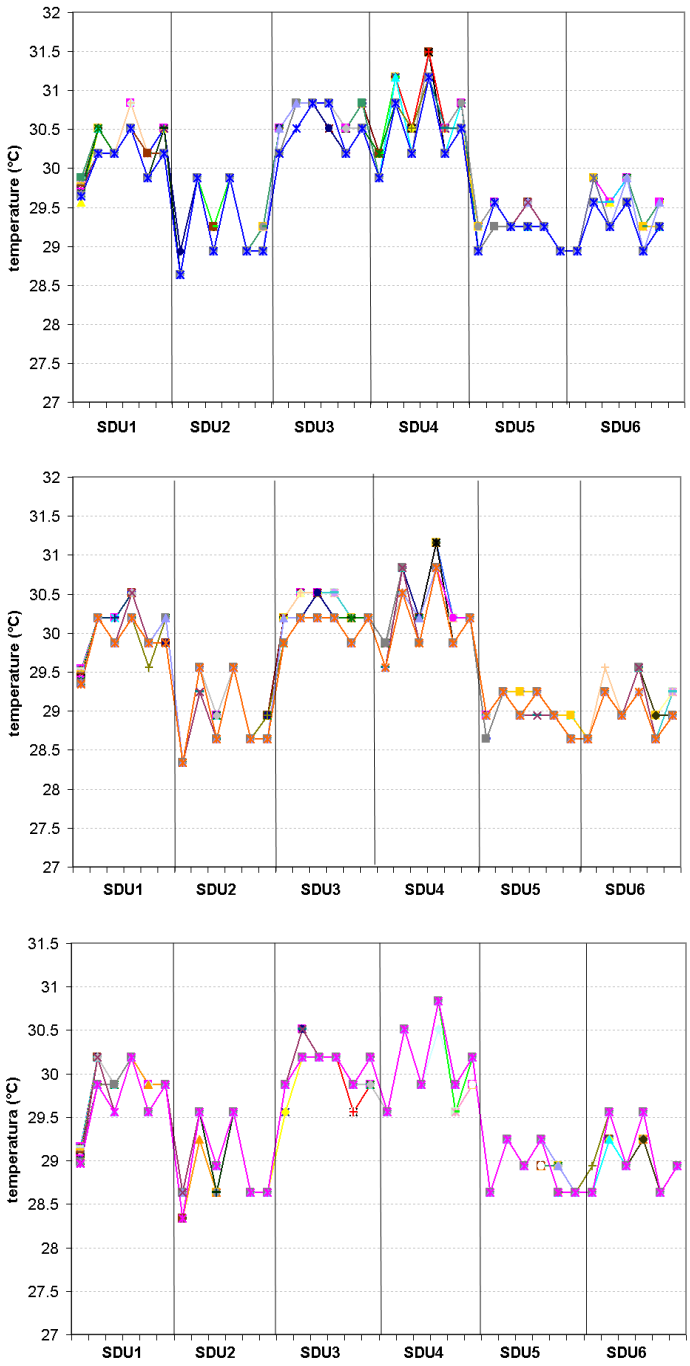

Fig. 8.7: Temperature value samples taken in different measurement moment.

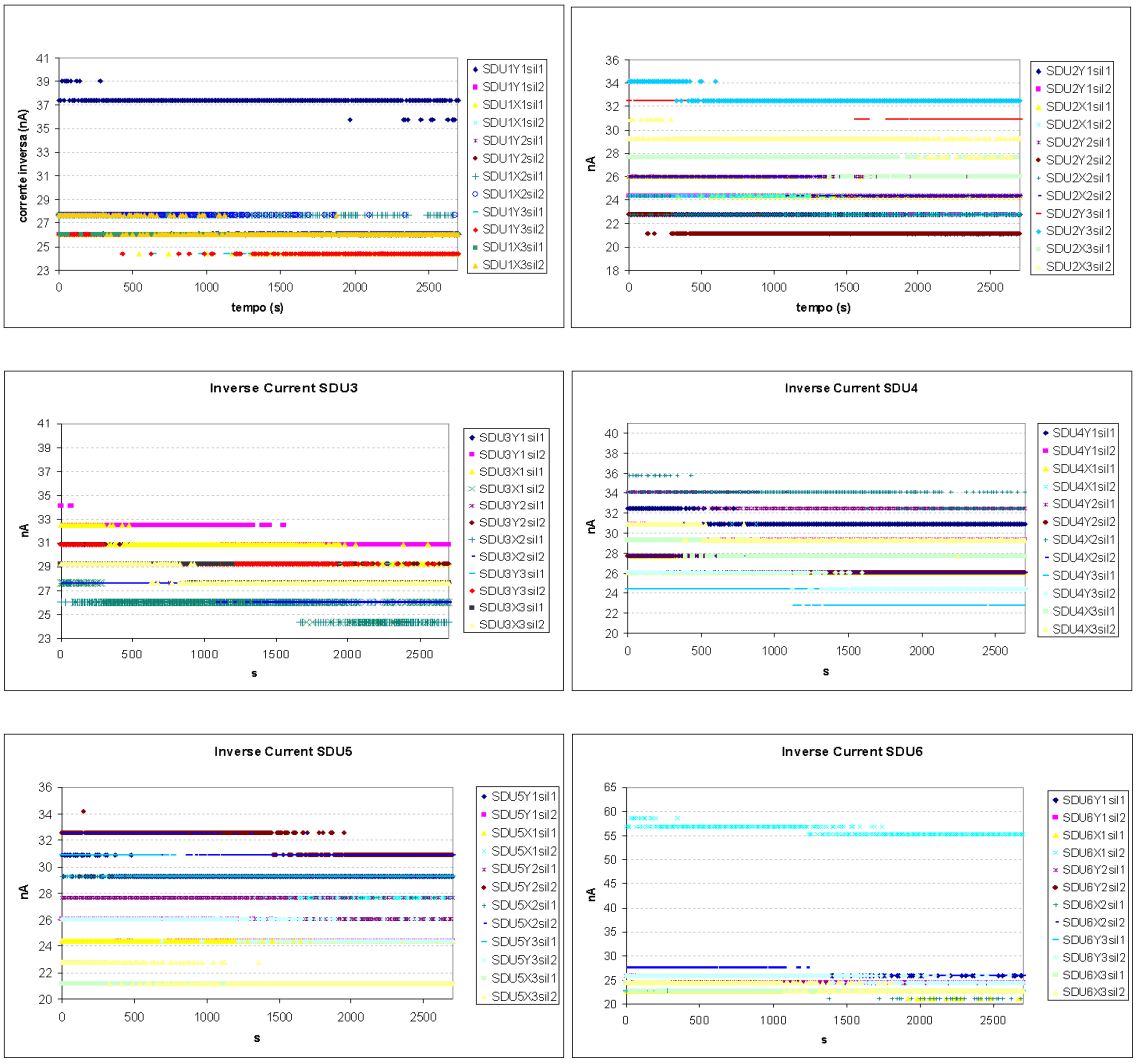

Fig. 8.8: inverse current values for file AlteaLog_21032005_1921_000.log.

There are no relevant difference in the diverse plane and SDU temperature. In the fig. 8.7 the plot of 50 temperature values taken (for all SDU planes) at the beginning, in the middle and at the end of the measurement are showed; no significant differences are found, fluctuation are of the order of few degree fractions. The inverse current of each silicon wafer was the plotted (fig. 8.8).

The current trends is similar to the one of the temperature, slightly decreasing in time. The current values are quite similar for the different silicon wafer, only for SDU1 (plane Y1, first wafer, strips Y 0-31) and for SDU6 (plane X1, second wafer, strips X 32-63); in the SDU6, in particular, the silicon wafer has a current double in respect to the other wafers. This value, however, is stable in time and reflects any malfunctioning.

Scientific data were then analyzed; the particle events acquired during the test are reported in table 8.2. Few differences in respect to the file taken in Milan have to be underlined: at KSC the measurement was performed in Normal Mode, so only the triggered strips were downloaded.

Probably this can be one of the reason, together with the minor environmental noise, of the better quality events. In fact, even though only 15 events were recorded, in 12 cases the particle track is clearly visible, also if some plane has a missing energy loss (this depends on the electronics).

evento	SDU1	SDU2	SDU3	SDU4	SDU5	SDU6	traccia	note
720					**x**		**x**	
721		**x**					**x**	
722	**x**						**x**	
723	**x**	**x**	**x**					
724		**x**					**x**	
725	**x**						**x**	
726		**x**					**x**	
727	**x**					**x**	**x**	manca Y0 su SDU6
728	**x**						**x**	
729	**x**						**x**	
730		**x**					**x**	visibile sui piani X,mancano Y0 e eY2
731						**x**	**x**	manca Y0
732	**x**						**x**	manca Y0
733					**x**			dubbia
734					**x**			dubbia

Table 8.2: Particle events acquired in file AlteaLog_21032005_1921_000.log.

8.4 Integrated tests: conclusion

The two files acquired before flight operations were extremely useful to test the functioning of all the subsystems together, to characterize the instrument and to evaluate the nominal values of parameter such as the temperatures and the currents of the silicon planes.

In particular, the acquired particle events were the only example of concurrent acquisition by the six SDUs of real particles on ground. The two measures are very different, also if the event rate is not so dissimilar (0.5 event/s in the first file, 0.3 event/s in the second); the difference can be probably ascribed to the much more noisy acquisition in the case of the first file and to the different measurement condition.

Chapter 9:
Simulations of flight operations

Before the start of the ALTEA flight operations, the ALTEA team, together with the teams of the other payloads of Increment 13, was involved in two simulations conducted by NASA. The purpose of the simulations was the training of ALTEA people in the practises needed during the flight operations: coordination and communications with the Marshall Space Flight Center (MSFC) and Johnson Space Center (JSC) teams, creation and submission of OCR (Operation Change Request), visualization of the operation planning and in general the use of the NASA software devoted to the mission control (IVoDS, iPV, EHS, etc.). During the simulations also some failures were simulated in order to learn the correct procedure to follow in such cases. At the end of the simulations ALTEA team was asked to partecipate to a debrief telecon together with all other teams to discuss and comment the just finished activity.
The simulations took place on February 14th and on March 14th 2006. In the following paragraph the summary of the succeeded events is reported.

9.1 Simulation #1 - 2006 February, 14th

First simulation of flight operations was performed on February, 14th from 1 pm to 9 pm CET.
The ALTEA UHB was connected via voice loop to HOSC in Huntsville and to MARS in Naples. Other participants were the teams of other payloads involved in the Increment 13.
During the whole simulation we were connected to iPV and to OSTPV in order to access the ALTEA procedures and to follow the exact operation timeline.
Following operations were simulated:

- ALTEA video s/u
- ALTEA DOSI deactivation
- ALTEA CNSM-DAT deletion

  Event: we were asked to clarify the ALTEA DATA OPS Procedure 2.005 step 3: it was not unambiguous what file has to be deleted.

Action: We noticed a missing line in the step 3.3 of the procedure. An OCR was written to add a line; the OCR altea002 was submitted and reviewed.

- ALTEA CNSM-OPR s/u
- ALTEA CNSM-SBJ activation

  Event: we were asked if the subject under CNSM measurement uses the laptop. **Action**: only the assistant uses the laptop, the subject does not.

  Event: we were asked if the subject of the CNSM session is aware of possible failures of one of the subsystems (laptop, DAU,…).

  Action: during first 20 minutes of measurement session the subject experiences visual stimuli; missing stimuli are a failure signature. After this first section the subject under measurement is not sensible to any kind of failures, but the assistant monitors the correct session development.
- ALTEA CNSM-OPR activation
- ALTEA CNSM-SBJ experiment

  Event: a "blue screen" of the laptop was reported. Correct procedure to follow was asked.

  Action: in case of laptop failure both laptop and ALTEA DAU have to be rebooted and the whole activation procedure has to be repeated. This procedure was confirmed by the ALTEA PD G. Gianelli, LABEN.

  Note: does any procedure to follow in case of a subsystem failure exist?

  Event: at about 4 pm CET POD communicated that there were power problems on Express Rack 4 and they had to keep it switched off.

  Action: ALTEA team did not ask to re-schedule the CNSM session.
- ALTEA video

  Event: at about 6 pm CET DMS asked if we wanted to receive the ALTEA VTR (video tape recorded) on Video Lan 1. We asked MARS about that. There were problems in understanding the correct way to receive it.

  Note: video was really received from MARS?
- ALTEA RT

  Event: at about 7 pm CET MARS asked POD the authorization to request data playback from EHS to test Real Time transmission. This test has to be considered out of the simulation, because the Express Rack 4 was still switched off.

  Action: POD authorized the test.

  Event: ASI-net between HOSC and MARS did not work.

Action: we received data of the time slice 2005:80:18:08:12/2005:80:22:00:28. Data from HOSC were routed through GARR to MARS and finally to UHB. Packets in the given time slice were 523503; packets received from MARS and resent to ALTEA-UHB were 523433; packets received from ALTEA-UHB were 523433.

9.1.1 Simulation #1: comments

Comments after the first simulation of flight operation were essentially about difficulties in the quick management of failure and in the answering to specific questions. ALTEA team experienced some confusion in performing the simulation and the transmission tests at the same time. Finally, a better practise in listening to several loops on IVoDS is needed, especially because in case of some questions coming from astronauts it is better to answer immediately on POD loop without waiting for being asked for.

9.2 Simulation #2 - 2006 March, 14th

Second simulation of flight operations was performed on March, 14th from 1 pm to 9 pm CET.
The ALTEA UHB was connected via voice loop to HOSC in Huntsville and to MARS in Naples. Other participants were the teams of other payloads involved in the Increment 13.
During the whole simulation we were connected to iPV and to OSTPV in order to access the ALTEA procedures and to follow the exact operation timeline (start time: 2004:301:08:00).
ALTEA was connected to the following Voice loops:

- ✓ SG2 sim
- ✓ POD sim
- ✓ ASI sim
- ✓ SCI2 sim
- ✓ OC sim

Following operations were simulated:

- ALTEA video s/u
- ALTEA DOSI deactivation
- ALTEA CNSM-DAT deletion

- ALTEA CNSM-OPR s/u
- ALTEA CNSM-SBJ activation

  Event: at 8.25 GMT (13.25 CET) OC asked to reduce, if possible, the two checks on FE-1 during CNSM session. We asked to maintain at least one check.

  Action: only one check on the astronaut during the CNSM session is performed between 9.55 and 10.00 GMT.
- ALTEA CNSM-OPR activation
- ALTEA CNSM-SBJ experiment
- ALTEA video

  Event: we were told ALTEA video transfer will start at 11.11 GMT.

  Action: play-back video transfer started at 11.11 GMT.

  Event: we were told transmitted video has not a good quality.

  Action: video transmission is repeated at 11.45 GMT.

  Event: at 14 GMT a new video transmission started.

  Action: we checked the video reception from MARS on IP address 141.108.250.39.

  Note: the real video transmission needs IP address receiving video belonging to the private subnet towards MARS?
- ALTEA CNSM-SBJ deactivation
- ALTEA CNSM data transfer

  Event: at 13.55 GMT crew confirmed that CNSM data transfer was successful.
- ALTEA DOSI RT

  Event: at 14.10 GMT (19.10 CET) we were told we were not receiving real time data. The DMC confirmed that data were correctly received and resent by HOSC.

  Action: we asked MARS to check about this failure.

  Action: after MARS restarted their transmission server and we restarted the MARS client, we confirmed on ASI loop we were correctly receiving data.

  Event: at 15.10 GMT (20.10 CET) sim coordinator told us we were not receiving data and that the failure is between HOSC and MARS. We can't solve the problem as we did at 14.10.

  Action: we involved MARS that tried to find out the failure reason.

  Action: MARS asked data to be sent on the backup machine via GARR. This procedure had to be request on OPS loop.

  Action: at 15.45 GMT MARS told on ASI loop that they solved the problem by asking the ASInet router rebooting.

Note: we understood transmission problem was a simulated failure but we did not have any procedure to apply in such case.

At 16.25 GMT (21.25 CET) Simulation #2 Debriefing began. Topics regarding ALTEA are the following:

- Data loss: in case of failure we have to ask DMC to have a data path tracking.
- It is not clear if Video setup is needed each time there is DOSI activation.

9.2.1 Simulation #2: comments

No particular comments on this second simulation. The team tried to be efficient and to face difficulties and manage the simulated failures.

Chapter 10:

ALTEA operations and preliminary results

ALTEA was finally brought on board the International Space Station within the STS-121 Shuttle mission on the July the 4th 2006 (fig. 10.1). After all docking operations and after the unstowing of all hardware components, the ALTEA flight operations were scheduled to start on the 7th August 2006. In this chapter the chronology of the ALTEA flight operations, the preliminary results from the analysis of data received in the first 3 months of experiment and the details about this analysis will be described. A description of some of the problems encountered and the relative comments will be also given.

Fig. 10.1: Shuttle Discovery launch on July the 4th 2006.

10.1 ALTEA operation chronology

The original schedule of ALTEA operations was as follows:

08/08/2006 ALTEA hardware unstowing
08/09/2006 ALTEA hardware setup and first DOSI activation (experiment Full10)
08/10/2006 ALTEA DOSI deactivation
08/10/2006 ALTEA CNSM setup and measurement
08/10/2006 ALTEA DOSI activation (experiment Normal5)

For the crucial phases of the setup and the measurement starting, a real-time video connection (only down) between the ISS and the ALTEA UHB was provided. The received video let the ALTEA team follow the hardware setup, help the astronaut Jeff Williams in following the procedure, check that all the needed steps were correctly performed and correct some errors if required.
After everything was ready, the procedure to start the DOSI experiment began. Unfortunately a first, not negligible problem suddenly happened: the astronaut heard a strong, mechanical noise coming from the helmet-shaped structure; he found the noise origin in the fan mounted on the helmet for the astronaut comfort during 90-minute CNSM acquisitions. After a while, he stated that the fan had stopped. The fan failure caused DOSI activation to be interrupted and NASA opened a PAR (Payload Anomaly Report) procedure to investigate the cause of the failure and the possible risks for astronauts in using ALTEA hardware. It took more than a week to investigate the problem and find a way to go back into the standard safety parameters. Finally it was proved that the fan was not really needed for safety, the decision to include it was taken when the first version of ALTEA components were chosen. So the fan was excluded by the astronaut with a dedicated procedure and operation start was rescheduled for August 17th 2006. It has to be noticed that after the fan exclusion, the software loaded on the ISS laptop had to be modified, so new CNSM scripts were uploaded with an OCR.
The real start of the operations, actually, was on the August 17th, when the DOSI activation procedure was correctly executed and first real-time data were received in the ALTEA UHB. As mentioned in the schedule reported above, for the first 24 hours of DOSI experiment, the Full 10 configuration was chosen. The reason for this choice was to perform a test on the SDU and strip functioning, this check being possible because in Full Mode all the detector strips are downloaded. The 10 MIP threshold was chosen in order to decrease the number of events and so the data volume.

After 24 hours of DOSI in Full 10 the first CNSM session was scheduled. Also in this case the setup and the measurement were performed during a video connection with the Station. At the end of the session, however, no data were found in the CNSM folder. The investigation on the reasons for this malfunctioning lasted for several weeks, also because the astronaut's time needed to perform troubleshooting was not easily available. Finally the problem was identified in the fiber optic cable (connecting the LTU and the BEU) and/or in the PCMCIA receiver on laptop. Both of them were substituted on November 2nd and the problem was solved. A new CNSM session is scheduled on the December 17th during STS-116 Joint Ops.

ALTEA DOSI has been running continuously in different experiment configurations since August 17th, apart from CNSM sessions and occasional shutdowns, for example during Shuttle STS-115 Joint Ops or when some problem happened (ER4 laptop substitution, power recycle of the Express Rack 4).

DOSI data are currently received in the ALTEA UHB in real-time; data are also daily requested in dump mode via ftp using the EHS software (both manually and automatically) so to have completed (in spite of periodical lack of real-time reception due to Loss of Signal periods) and time ordered data.

Unfortunately, the six SDUs are not always working concurrently. Often it happens that one or more SDUs stop acquiring and the cause of this malfunctioning is currently under investigation. For this reason the calculation of absolute fluxes is not obvious at this point, because the exact acquiring time for each SDU is needed. However the spectrum of energy released by particle events, calculated for each separate SDU and for all the SDUs working together, is not prejudiced by this problem.

10.2 ALTEA DOSI activation: first data

As described in the previous paragraph, the actual DOSI activation, and so the event acquisition start, took place on August 17th.

First check was on the housekeeping values: as described in the previous chapter, the housekeeping, as temperature and inverse current of the silicon planes, are monitored in order to quick alert in case of malfunctioning. Software used to receive and perform a preliminary analysis of real-time data is capable to read housekeeping data. They are showed in a panel in which the desired SDU can be selected and monitored. An example of this panel is showed in fig. 10.2: details of the current

measure (threshold value, acquisition mode, active systems) are displayed, together with system voltages and the max temperature measured on each SDU. At the bottom of the panel a specific SDU is selectable in order to visualize all the temperatures and currents of each silicon plane. In the figure the SDU1 is selected, all six silicon planes result switched on; it has to be noticed that current value of first silicon wafer of DB1 results higher of other wafer values. However, this value is not off nominal and this can be stated also looking at housekeeping data collected on Earth (see chapter 8); current value of SDU1 first silicon wafer also in those cases was higher than the others.

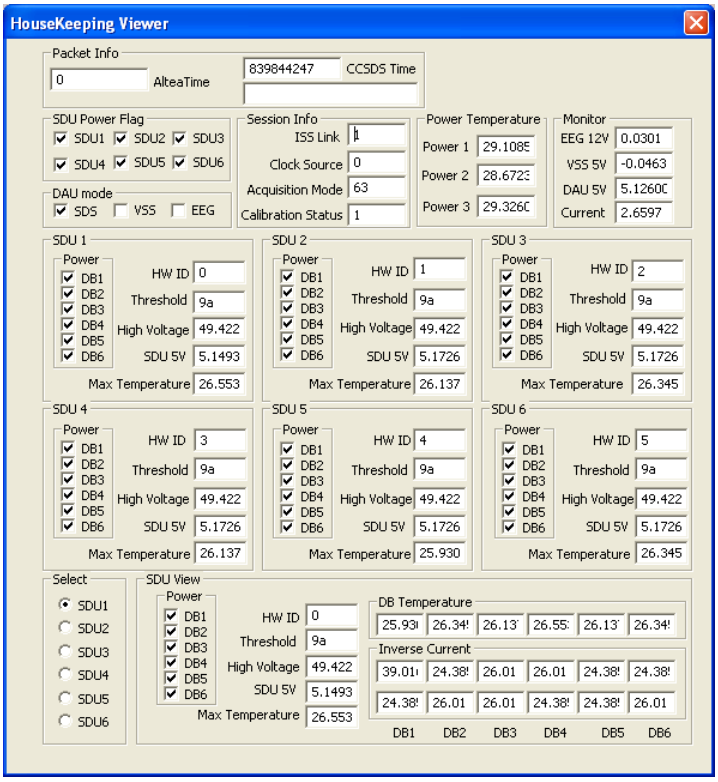

Fig. 10.2: The housekeeping panel as showed by the real-time software.

After checking that housekeeping values were nominal for all the SDUs, another important control was on particle tracks: it was important to verify the functioning of each detector strip, the pedestal stability and the quality of the acquired events. In order to do this, data were first analyzed with the quicklook software (DAUTELook.1.8) and it was verified that in that first acquisition all the strips had a maximum value different from zero (that file was in Full mode). In fig. 10.3 first acquired pedestals are showed: they are quite uniform and stable. In fig. 10.4 two examples of recorded events are showed; events appeared clear and with the expected rate (see next paragraph).

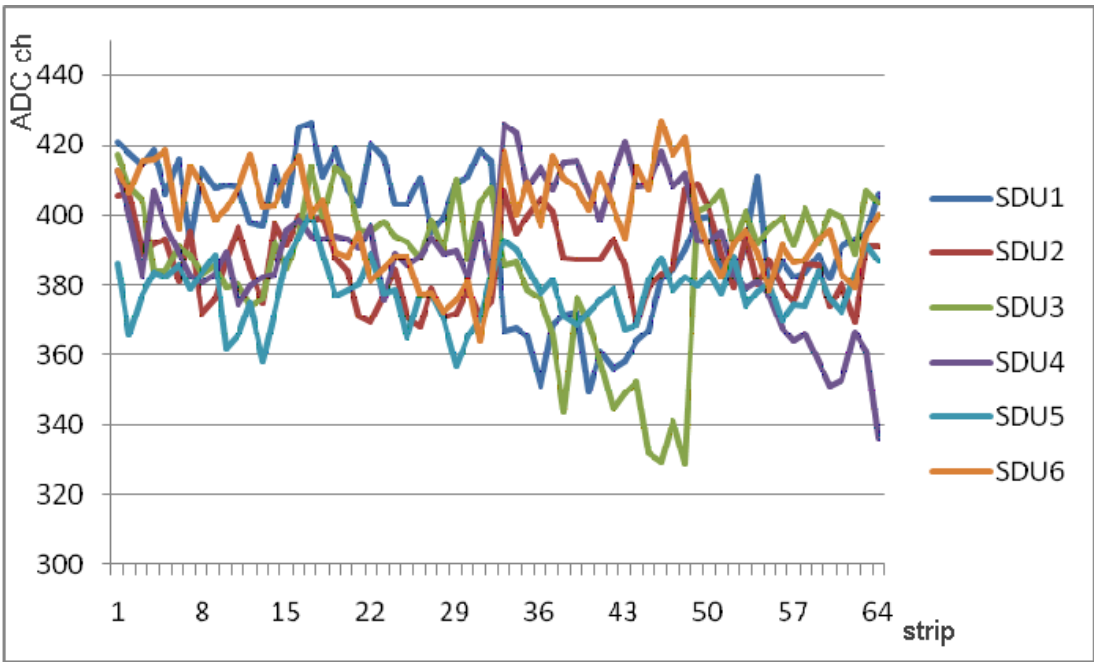

Fig. 10.3: Plot of first acquired pedestals.

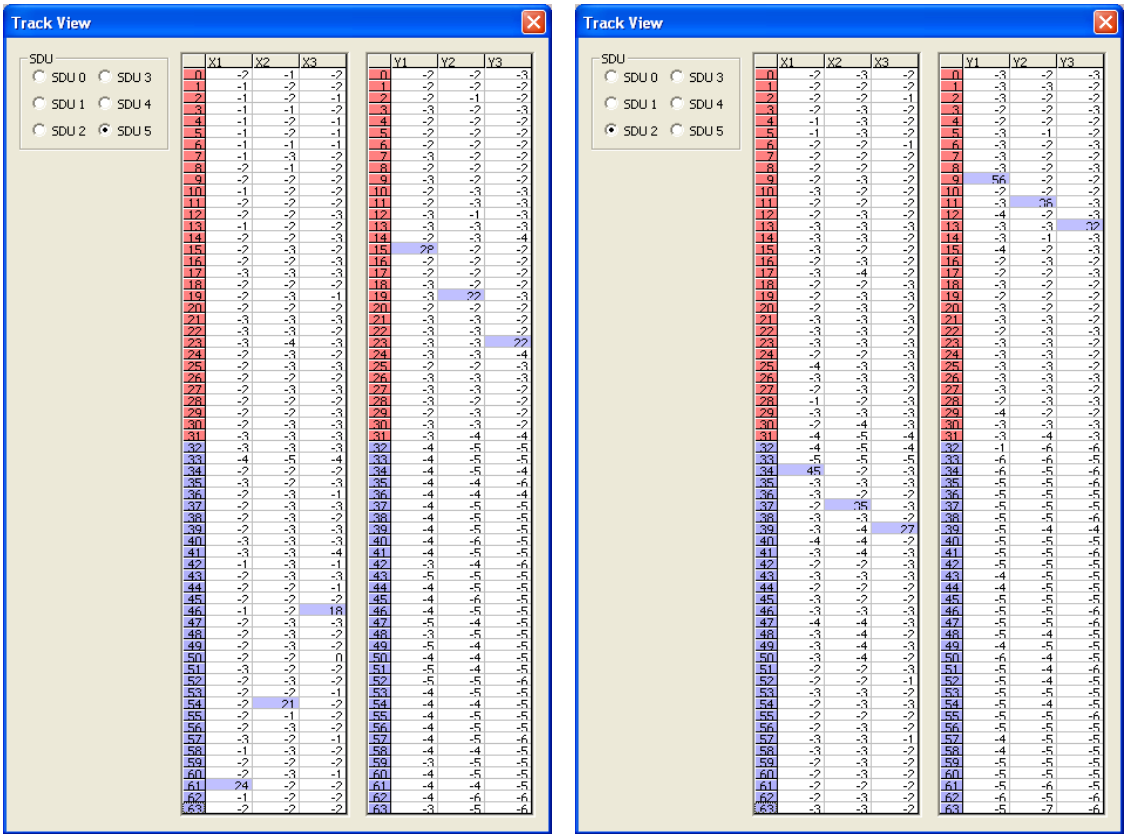

Fig. 10.4: Two tracks acquired in the first DOSI file: one with an almost constant energy loss (left) and another with a slowing down particle (right).

10.3 ALTEA operations: a summary

In table 10.1 the updated summary of the operations updated to 10/11/2006 is reported. Since the beginning of October it was chosen to set the DOSI measurement at Normal 10, meaning with a 10 MIP threshold. With this threshold value the high Z particle statistic is not decreased and the system, that is still experiencing some problems, seems to be more stable.

Data are separated in folders considering the different measurement conditions and/or the interruptions due to loss of communication between laptop and DAU or some other problems. In this way analysis is performed first of all for all the files taken in the same conditions, considering the performances of the single SDUs.

Start date	Stop date	Activity	Experiment mode	Duration	Notes
17/8/06			DOSI Full 10	22 hours	first activation
18/8/06		switch Full10/Normal 5			ALTEA remains in Full Mode
18/8/06		DEACT/ACT	DOSI Normal 5		no data sent
18/8/06	20/8/06	DEACT/ACT	DOSI Normal 5	37 hours	loss of communication
20/8/06	21/8/06	ACT	DOSI Normal 5	37 hours	loss of communication; cable swap between 233:21:55 and 234:17:20
22/8/06	24/8/06	ACT	DOSI Normal 5	37 hours	loss of communication
26/8/06		Upload SW and new scripts			reset ALTEA Time and new scripts for different measurement mode
26/8/06	28/8/06	ACT	DOSI Normal 10	31 hours	
28/8/06		CNSM	CNSM Normal 10		no packet acquired
29/8/06	31/8/06	ACT	DOSI Normal 5	2 days	loss of communication LTU due to a file transfer
31/8/06	11/9/06	ACT	DOSI Normal 5	11 days	
1/10/06	6/10/06	ACT	DOSI Normal 10	5 days	
6/10/06	18/10/06	ACT	DOSI Normal 10	12 days	laptop reboot
18/10/06	2/11/06	ACT	DOSI Normal 10	15 days	laptop reboot and swap of card and optic fiber
2/11/06	10/11/06	ACT	DOSI Normal 10	8 days	at 12.18 GMT laptop reboot
10/11/06		ACT	DOSI Normal 10		

Table 10.1: Summary of ALTEA operations up to 10/11/2006.

10.4 First analysis: particle rate

First analysis performed off-line on the acquired files is about the rate: we expect a certain trend in the particle rate, depending on the latitude and longitude. In fact, lower is the geomagnetic field higher is the particle rate; so we expect an oscillating rate depending on the passages on equator (high magnetic field, high cut-off) and on the poles. There is also a rate oscillation depending on the longitude, because of the inclination of terrestrial axis in respect to geomagnetic field axis and the orbit precessions; that modulation is called 'longitude effect'.

This is the first check to do in order to verify completeness and correct data structure. In figures 10.5 to 10.7 the particle rate for data acquired in Full Mode 10, Normal Mode 5 and Normal Mode 10 are showed.

The plots show the expected rate oscillation. The higher peaks represent ISS passages over the South Atlantic Anomaly (SAA), the region situated off of the Brasil coast having an anomalous low magnetic field. Protons are trapped in the SAA and this is the reason why the flux increases up to two or three order of magnitude in respect to the outer SAA one. ALTEA is capable to reveal only a fraction of protons, with energy between 25 and 45 MeV at 10 MIP threshold (between 25 and 100 MeV at 5 MIP threshold), and for this reason in our cases the rate increases of only one order of magnitude.

Times when rate is zero correspond to pedestal acquisitions: during those times, in fact, SDUs do not acquire scientific events.

In fig. 10.8 the rate of a wide time period of data (more than 4 days) is showed and in this case the general trend, the little and the big oscillations (longitude effect has a period of about 24 hours) and the passages over the SAA are still more visible. This plot refers to all particles with no selection in energy and without any other cut. In fig. 10.9 the same data set rate is showed for particles with energy bigger than 35 ADC channels ($Z \geq 5$, in blue) and 100 ADC channels ($Z \geq 8$, in red); it has to be noticed that the amount of detected particles drammatically decreases as predictable. It is still possible to appreciate the north-south oscillation and the longitude effect, but no increase over the SAA is found, exactly as expected knowing the nature of trapped particles. Further the energy cut, only particles resulting aligned and relativistic (see next paragraphs for more details) were selected. In fig. 10.10 the ratio between the energy filtered and the total particle rate is plotted for GMT 276-277 data.

For most of the time this ratio is under few percent because, as seen in fig. 10.8 and 10.9, the energy filtered particle rate is about two order of magnitude lower than the total particle rate.

An oscillation is still visible; its meaning is more clear looking at the fig. 10.11, where a comparison between this filtered particle rate and total rate divided by 100 is showed.

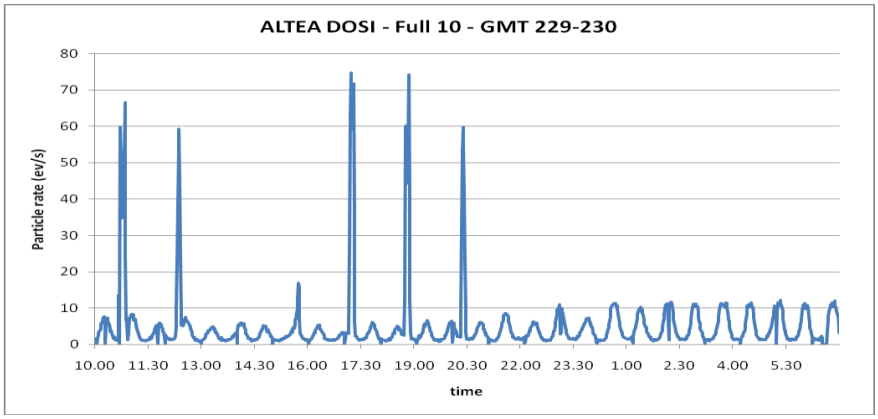

Fig. 10.5: Plot of event rate at 10 MIP threshold in Full Mode.

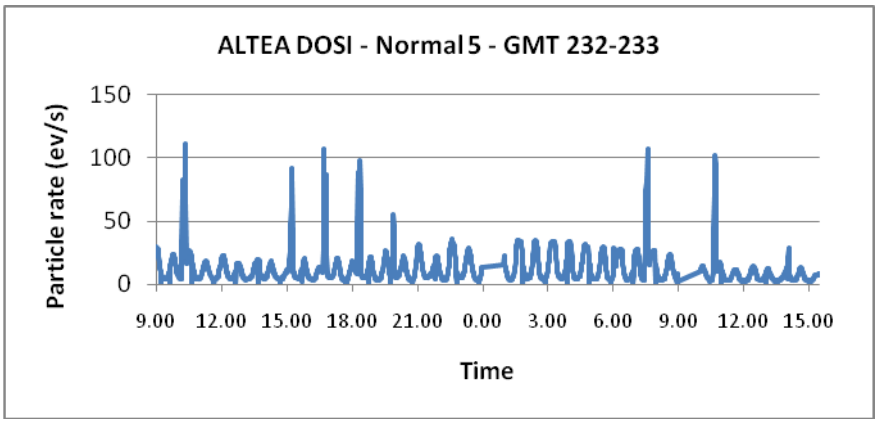

Fig. 10.6: Plot of event rate at 5 MIP threshold in Normal Mode.

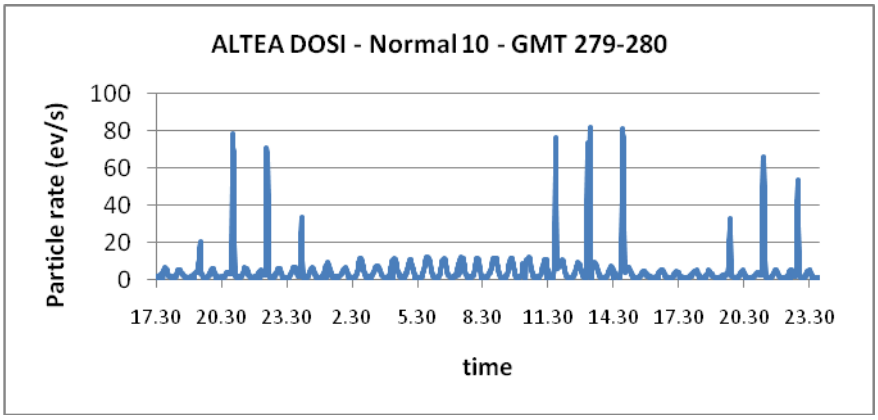

Fig. 10.7: Plot of event rate at 10 MIP threshold in Normal Mode.

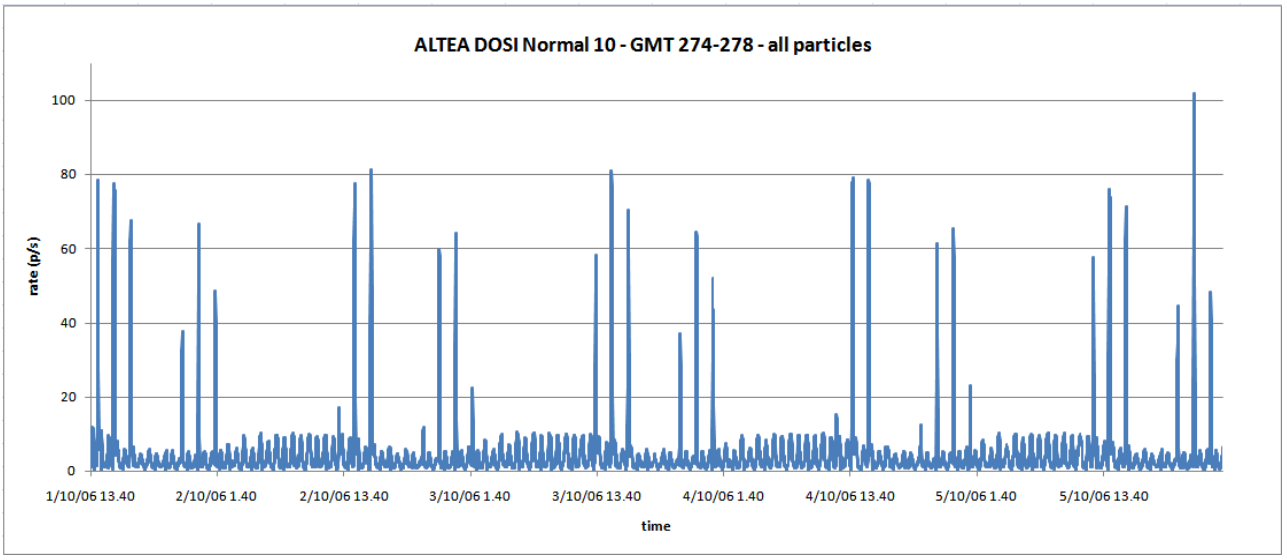

Fig. 10.8: Plot of event rate at 10 MIP threshold in Normal Mode on a wide time interval.

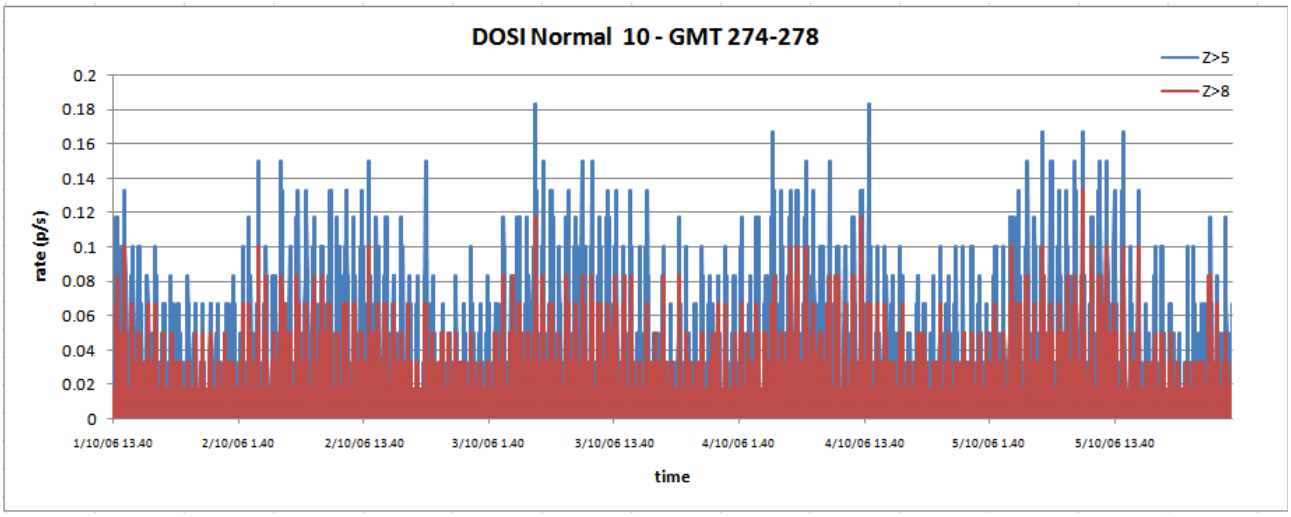

Fig. 10.9: Plot of the rate of relativistic and aligned particles with Z>5 and Z>8.

The oscillation seen in fig. 10.10 still reflects the different cut-off of the regions passed by ISS, but it is not so strict; in fact in fig 10.11 a peak in the ratio is found around 7.40, October 4th in correspondence of a minimum of total rate: the heavy ion component is detectable also having a high energy, while the low Z high energy component is not seen by ALTEA. It has to be noticed that during passages on SAA the ratio decreases to zero because the trapped particle component is constituted by protons.Data showed in fig. 10.8 to 10.11 were acquired with five SDUs active, SDU5 being out of work.

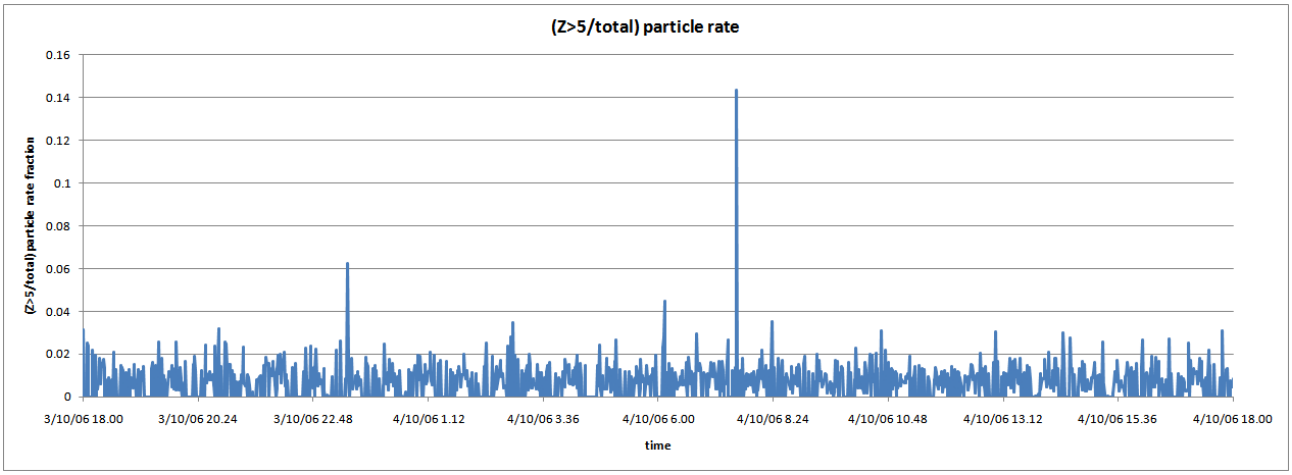

Fig. 10.10: Z>5/total particle rate fraction; GMT 276-277 data are showed (DOSI Normal 10).

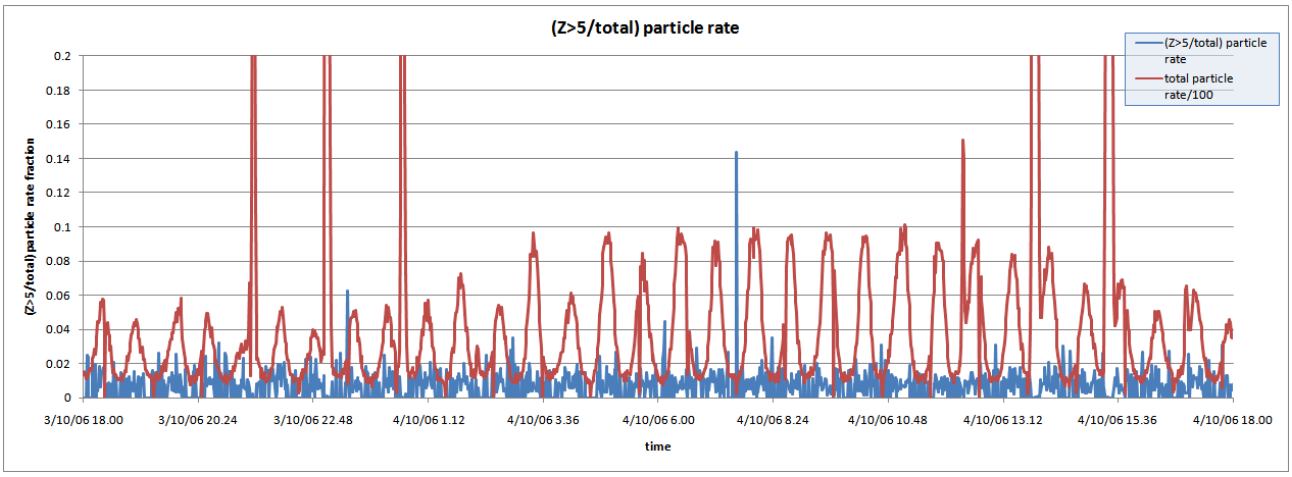

Fig. 10.11: Comparison between Z>5/total particle rate fraction and total particle rate divided by 100. Data are the same of fig. 10.10.

An additional interesting analysis involving the rate was the study of the counting between different SDUs, which are placed in a fixed position in respect to the station (see fig. 10.12 and 10.13). Even this simple analysis only based on the SDU positions can provide information on particle incidence directions, issue that will be treated in more details in the future.

The counting differences between faced SDUs (see fig. 3.10 in chapter 3) are considered when the ISS passes on SAA. In fig. 10.14 to 10.17 the particle rate in different time slice (all belonging to GMT 274-278 data) is showed together with the relative counting difference between the couple (SDU1 and SDU4) and the couple (SDU3 and SDU6). The plotted values (red curves) are obtained from the formula:

relative counting difference = ((SDU1+SDU4)-(SDU3+SDU6))*100/TOT + offset

where SDUn indicates the particle per second counted by that SDU and TOT is the sum of the rate for all the acquiring SDUs.

An offset term equal to 40 was considered in order to better visualize the curve together with the rate, so any value around 40 means an equal counting of both the SDU couples, then no preferential direction for particles.

In fig. 10.15 to 10.18 also the time, the number of total counting and values of the relative counting differences are showed. Nearby the latter a colored arrow shows the trend of the relative counting difference, a red arrow meaning a bigger contribution of (SDU3+SDU6), a green one a bigger contribution of (SDU1+SDU4). The yellow arrows indicate an about equal contribution from the two couples, but the arrow position is a tendency signal.

Fig. 10.12: ALTEA fixed to the EXPRESS RACK 4 in CNSM setup configuration.

Fig. 10.13: Increment 13 astronauts inside U.S. Lab. On the left ALTEA in DOSI configuration is visible

Each passage over SAA happening within consecutive orbits seems to have a specific trend. For example first group of passages showed in fig. 10.15 shows a substantially equal counting number between the two SDU couples, while in the second group the couple (SDU3+SDU4) have a rate about 15-20 % higher than couple (SDU1+SDU4). A different situation is found, for example, in fig. 10.18, where the prevalence of the counting changes almost gradually between the passages, the first one showing a prevalence of (SDU3+SDU6) counting, the last one a prevalence of (SDU1+SDU4) (counting about 10-15% more than the other couple).

A deeper analysis will be performed considering the counting of the different SDUs at latitude and longitude variations combined with angular distribution of particle tracks. Then it will be crucial the determination of the exact attitude of ISS during the various data acquisitions; it will be stated analyzing ancillary data, this work is still in progress.

In fig. 10.14 the particle rate obtained considering only DOSI Normal 10 events respecting some filters (see next paragraph) is showed. A single line refers to a single acquisition; those acquisitions are uniform for number of SDUs working, but not for lasting time. However there are some emerging features: in most of the cases the rate is quite uniform for the six SDUs; SDU2 and SDU5 result the most counting SDUs and this is something expected because of their protruding position inside ISS. It has to be noticed that the different passages over the SAA do not influence the rates because the mean number of passages is quite the same for each data interval.

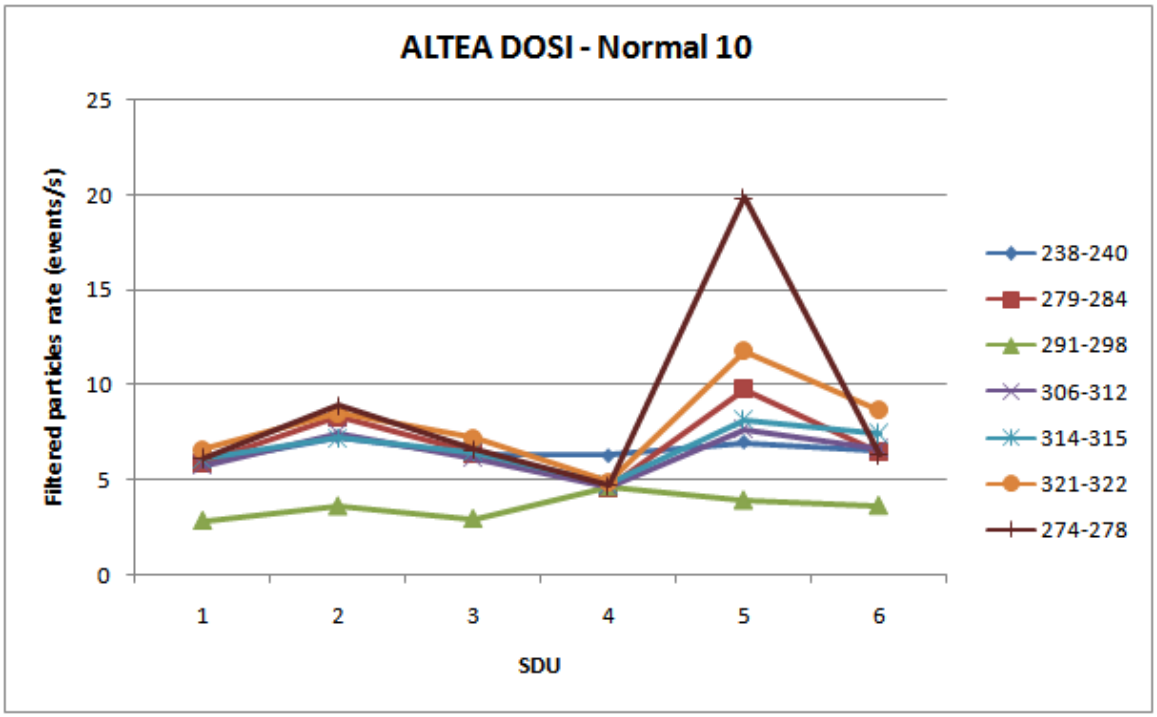

Fig. 10.14: Counting differences for SDUs at DOSI Normal10.

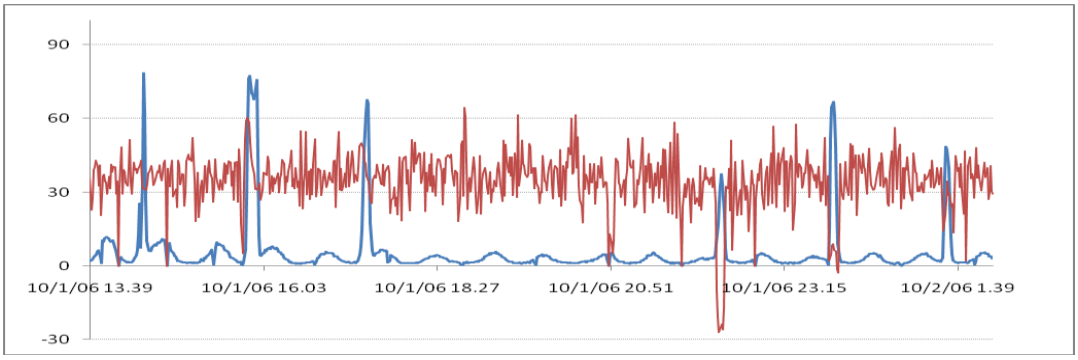

1/10/06 14.17	4.53	39.56
1/10/06 14.18	6.63	37.74
1/10/06 14.19	12.62	39.45
1/10/06 14.20	25.32	40.87
1/10/06 14.21	7.27	43.03
1/10/06 14.22	34.27	32.79
1/10/06 14.23	78.35	31.6
1/10/06 14.24	62.43	31.22
1/10/06 14.25	26.75	30.99
1/10/06 14.27	10.07	33.45
1/10/06 14.28	6.33	37.79

1/10/06 22.18	4.23	25.82
1/10/06 22.19	9.15	-10.05
1/10/06 22.20	16.85	-20.83
1/10/06 22.21	26.03	-27.04
1/10/06 22.22	32.73	-26.06
1/10/06 22.23	37.45	-23.79
1/10/06 22.24	33.12	-25.94
1/10/06 22.25	21.22	-17.16
1/10/06 22.26	7.2	14.86
1/10/06 22.27	2.73	32.31

1/10/06 15.47	1.72	34.19
1/10/06 15.48	6.67	51.69
1/10/06 15.49	27.07	59.06
1/10/06 15.50	57.43	60.34
1/10/06 15.51	76.17	58.35
1/10/06 15.52	77.38	50.25
1/10/06 15.53	70.18	44.35
1/10/06 15.54	69.75	41.12
1/10/06 15.55	67.68	37.09
1/10/06 15.56	69.3	31.33
1/10/06 15.57	75.6	31.51
1/10/06 15.58	44.2	30.79
1/10/06 15.59	12.05	33.78
1/10/06 16.00	4.47	26.8
1/10/06 16.01	4.2	28.81

1/10/06 23.51	2.58	31.47
1/10/06 23.52	0.3	36.67
1/10/06 23.53	15.25	2.164
1/10/06 23.54	52.22	4.496
1/10/06 23.55	64.62	8.446
1/10/06 23.56	66.67	8.907
1/10/06 23.57	61.07	6.53
1/10/06 23.58	48.48	5.862
1/10/06 23.59	26.63	-1.457
2/10/06 0.00	8.95	-2.793
2/10/06 0.01	3.27	14.31

1/10/06 17.23	4.55	48.57
1/10/06 17.24	7.85	49.3
1/10/06 17.25	14.38	50.08
1/10/06 17.26	29.68	47.88
1/10/06 17.27	46.8	42.65
1/10/06 17.28	62.13	41.43
1/10/06 17.29	67.58	36.54
1/10/06 17.30	66.05	34.1
1/10/06 17.31	42.93	29.63
1/10/06 17.32	17.45	26.36
1/10/06 17.33	6.2	25.48
1/10/06 17.34	4.48	35.09

2/10/06 1.25	1.63	40
2/10/06 1.26	3.43	26.59
2/10/06 1.27	17.78	14.24
2/10/06 1.29	36.23	20.62
2/10/06 1.30	48.42	26.39
2/10/06 1.31	47.33	34.53
2/10/06 1.32	39.85	28.73
2/10/06 1.33	24.3	29.3
2/10/06 1.34	11.73	24.06
2/10/06 1.35	4.57	25.12

Fig. 10.15: Particle rate (blue curve) and relative counting differences (red curve) between (SDU1+SDU4) and (SDU3+SDU6) in ISS passages over SAA (1/10/2006 13.40-2/10/2006 1.40).

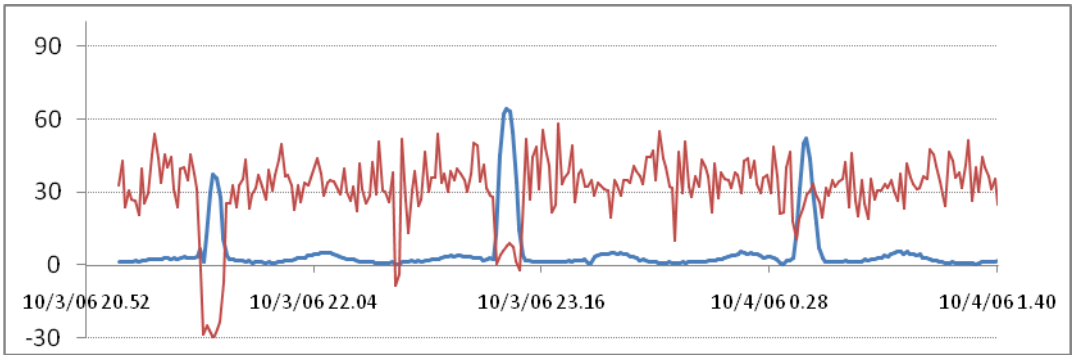

3/10/06 21.29	1.3	-28.46
3/10/06 21.30	11.72	-24.85
3/10/06 21.31	30.12	-26.77
3/10/06 21.32	37.1	-29.84
3/10/06 21.33	35.85	-26.11
3/10/06 21.35	27.88	-23.06
3/10/06 21.36	10.78	-6.846
3/10/06 21.37	4.1	25.61

3/10/06 23.00	2.8	28.57
3/10/06 23.01	2.52	28.1
3/10/06 23.02	12.37	0.631
3/10/06 23.03	45.37	4.117
3/10/06 23.04	61.9	6.107
3/10/06 23.05	64.4	7.826
3/10/06 23.06	63.1	9.033
3/10/06 23.07	54.75	7.562
3/10/06 23.08	34.03	1.769
3/10/06 23.09	14.72	-1.984
3/10/06 23.10	4.23	16.83
3/10/06 23.11	1.83	52.02

4/10/06 0.36	2.72	17.94
4/10/06 0.37	11.55	10.39
4/10/06 0.38	31.72	19.16
4/10/06 0.39	49.9	23.41
4/10/06 0.40	51.98	29.3
4/10/06 0.41	43.47	30.32
4/10/06 0.42	31.58	33.35
4/10/06 0.43	17.2	29.24
4/10/06 0.44	7.28	25.85
4/10/06 0.45	3.02	19.47

Fig. 10.16: Particle rate (blue curve) and relative counting differences (red curve) between (SDU1+SDU4) and (SDU3+SDU6) in ISS passages over SAA (3/10/2006 20.50-4/10/2006 1.40).

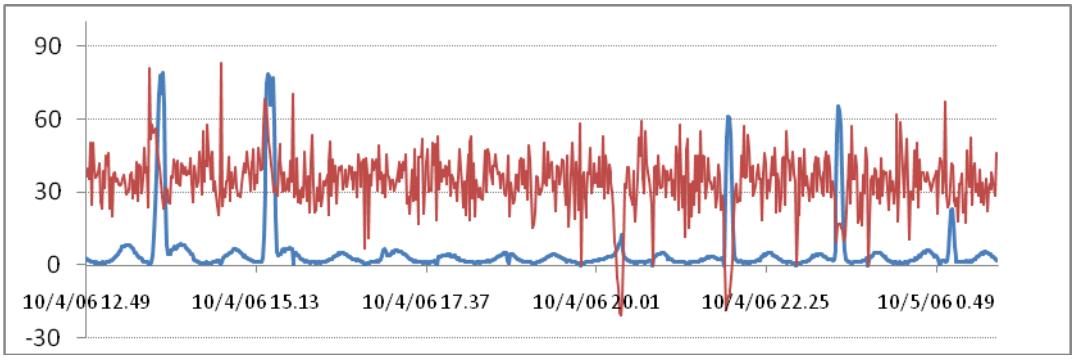

4/10/06 13.45	1.25	57.6
4/10/06 13.46	4.02	54.68
4/10/06 13.47	12.17	55.45
4/10/06 13.48	23.38	55.87
4/10/06 13.49	36.93	47.53
4/10/06 13.50	55	46.56
4/10/06 13.51	70.8	43.16
4/10/06 13.52	77.85	39.88
4/10/06 13.53	70.37	34.03
4/10/06 13.54	79.13	27.82
4/10/06 13.55	65.57	23.53
4/10/06 13.56	26.4	26.06
4/10/06 13.57	8.28	31.55
4/10/06 13.58	4.68	30.6

4/10/06 21.49	2.35	23.4
4/10/06 21.50	0	0
4/10/06 21.51	28.35	-18.2
4/10/06 21.52	52.68	-13.55
4/10/06 21.53	61.15	-12.72
4/10/06 21.54	60.5	-12.76
4/10/06 21.55	54.08	-10.11
4/10/06 21.56	35.7	-4.874
4/10/06 21.57	14.37	2.352
4/10/06 21.58	3.98	20.15
4/10/06 21.59	2.48	30.32

4/10/06 15.18	1.58	39.37
4/10/06 15.19	3.05	39.67
4/10/06 15.20	12.08	57.22
4/10/06 15.21	30.7	68.08
4/10/06 15.22	56.13	65.08
4/10/06 15.23	74.72	59.37
4/10/06 15.24	78.33	50.7
4/10/06 15.25	77.35	46.66
4/10/06 15.26	66.05	41.17
4/10/06 15.27	69.73	36.31
4/10/06 15.28	76.77	30.13
4/10/06 15.29	58.1	31.51
4/10/06 15.30	19.43	30.84
4/10/06 15.31	5.52	28.77
4/10/06 15.32	4.2	41.9

4/10/06 23.22	2.27	31.19
4/10/06 23.23	5.97	26.43
4/10/06 23.25	27.52	9.622
4/10/06 23.26	53.72	16.28
4/10/06 23.27	65.23	17.11
4/10/06 23.28	63.33	16.84
4/10/06 23.29	57.23	15.48
4/10/06 23.30	38	14.16
4/10/06 23.31	17.38	10.02
4/10/06 23.32	5.97	12.03
4/10/06 23.33	2.35	22.55

Fig. 10.17: Particle rate (blue curve) and relative counting differences (red curve) between (SDU1+SDU4) and (SDU3+SDU6) in ISS passages over SAA (4/10/2006 12.50-5/10/2006 0.50).

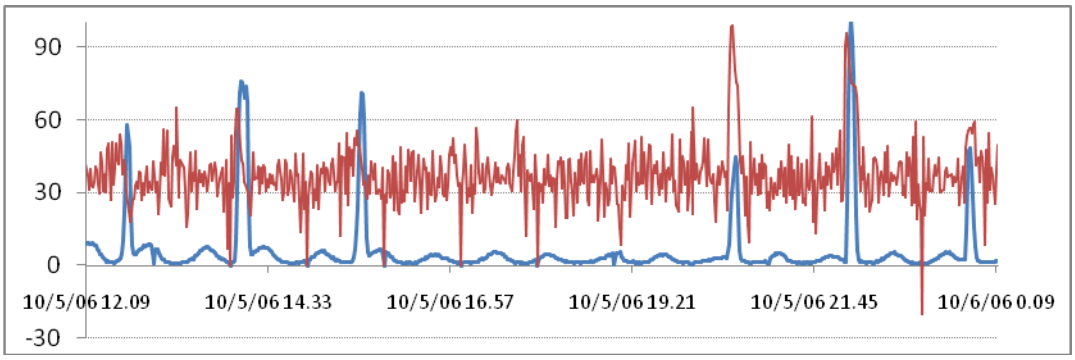

5/10/06 12.38	5.08	37.64
5/10/06 12.39	10.52	43.14
5/10/06 12.40	21.73	40.05
5/10/06 12.41	41.73	30.94
5/10/06 12.42	57.67	25.95
5/10/06 12.43	48.77	22.06
5/10/06 12.44	23.1	18.1
5/10/06 12.45	8.2	21.83
5/10/06 12.46	4.83	26.96

5/10/06 20.37	3.22	22.61
5/10/06 20.38	8.93	65.31
5/10/06 20.39	20.72	86.43
5/10/06 20.40	30	98.33
5/10/06 20.41	35.18	98.7
5/10/06 20.42	40.23	89.66
5/10/06 20.43	44.57	80.54
5/10/06 20.44	41.3	75.52
5/10/06 20.45	21.63	74.03
5/10/06 20.46	5.98	60.23
5/10/06 20.47	2.92	42.74

5/10/06 14.06	1.97	35.43
5/10/06 14.07	10.08	54.98
5/10/06 14.09	31.87	64.32
5/10/06 14.10	55.25	64.56
5/10/06 14.11	71.28	57.2
5/10/06 14.12	76.02	48.39
5/10/06 14.13	75.48	43.34
5/10/06 14.14	72	41.63
5/10/06 14.15	68.83	34.14
5/10/06 14.16	73.77	31.53
5/10/06 14.17	67.52	29.66
5/10/06 14.18	25.45	25.15
5/10/06 14.19	7.47	20.72
5/10/06 14.20	4.45	33.03

5/10/06 22.09	1.18	38.31
5/10/06 22.10	1.12	90.89
5/10/06 22.11	25.23	95.81
5/10/06 22.12	68.63	90.93
5/10/06 22.13	93.72	83.35
5/10/06 22.15	101.82	77.95
5/10/06 22.16	92.88	75.19
5/10/06 22.17	78.63	74.11
5/10/06 22.18	49.67	73.56
5/10/06 22.19	20.53	69.52
5/10/06 22.20	6.05	59.5
5/10/06 22.21	2.27	42.64

5/10/06 15.41	3.27	52.54
5/10/06 15.42	6.9	49.86
5/10/06 15.43	13.92	55.3
5/10/06 15.44	24.08	49.68
5/10/06 15.45	45.03	48.68
5/10/06 15.47	62.88	43.71
5/10/06 15.48	71.08	39.9
5/10/06 15.49	70.67	33.22
5/10/06 15.50	60.87	34.25
5/10/06 15.51	34.7	29.37
5/10/06 15.52	11.47	27.45
5/10/06 15.53	5.35	37.01

5/10/06 23.44	2.2	25.91
5/10/06 23.45	2.53	48.7
5/10/06 23.46	13.9	53.17
5/10/06 23.47	34.32	55.41
5/10/06 23.48	47.43	56.53
5/10/06 23.49	48.12	56.67
5/10/06 23.50	40.53	54.34
5/10/06 23.51	28.15	58.26
5/10/06 23.52	15.85	58.93
5/10/06 23.53	7.67	41.04
5/10/06 23.54	3.48	43.45

Fig. 10.18: Particle rate (blue curve) and relative counting differences (red curve) between (SDU1+SDU4) and (SDU3+SDU6) in ISS passages over SAA (5/10/2006 12.00-6/10/2006 0.10).

10.5 DOSI data analysis: filter setting

A big amount of data has been gathered since the start of DOSI data acquisition on August. The offline analysis is performed with the same tool used for receiving real-time data. In this paragraph details of data treatment will be discussed.

First step of analysis involves the pedestal subtraction: pedestals (zero signals) are periodically acquired in order to assess the detector baseline. Pedestals have to be subtracted to get the real particle signals. 100 Pedestals are usually acquired every hour for each SDU and their mean value and standard deviations are automatically calculated (pedestals are considered as Gaussian distributions); then this mean value is subtracted to the particle signal during data processing. Subtraction of the last previous pedestal mean value is usually considered. As discussed elsewhere (see chapter 7), it has to be noticed that the baseline found with pedestal is a little bit lower than the real baseline during scientific data acquisition. For this reason the strips not hit by particles often show a negative value. In order to compensate those negatives on energy value a correction was considered: the pedestal value to be subtracted is 'running'. Average of values read on the not hit strips in the last N events (usually 25-30 events are considered) is calculated and the obtained number is added to the standard pedestal. This procedure is called "negative correction".

After pedestal subtraction, particle signals have to be analyzed. In the first analysis it was chosen not to select any energy range, but this possibility is available by selecting the desired energy range on the analysis software panel. The first cut considered on particle events concerns the single track event. Also multiple events (showers) can be analyzed, but it will be done later in the analysis. For each event, the maximum energy released on the single silicon plane is considered; the alignment of the track is then evaluated checking if inclination of the line through the first silicon plane couple and inclination of the line trough the last couple are the same within a chosen error. The minimum number of hit strips in the single event should be 24, because the trigger signal considers the sum of four strip signals. Still the trigger only concerns the X silicon plane strips, so the minimum number of strip read in a triggered event is actually 12. In order not to lose all good events having an incomplete track on Y silicon planes, also events where a Y plane is missing are considered valid, obviously only if the track is aligned on the rest of the planes. In summary, only events having five or six non zero maximum energy values in strips that result aligned within a certain tolerance are analyzed. This method to recognize alignment is efficient, but a new more sophisticated algorithm for track reconstruction is under investigation (see further in the chapter).

Among selected events, only "relativistic" ones, satisfying the condition:

$$(\Delta E_0+\Delta E_1)- (\Delta E_4+\Delta E_5) / (\Delta E_4+\Delta E_5) \leq R$$

are analyzed. In this simple formula ΔE_n is the energy loss in the plane n; this formula has to be slightly changed if not all three Y planes are hit, however energy loss in the first two and in the last two silicon planes has always to be considered. R is a value selectable via software, usually it is chosen equal to 0.1. Selection on relativistic events is needed because only in this case the energy loss in all the silicon planes is quite constant and calculation of the mean energy loss for event, for example, is possible. Particles slowing down in the detector need a different treatment. In fig. 10.19 and 10.20 an example of cut effectiveness is showed; in both the plot same data are considered. In the first plot data are showed with no energy cut, so not only relativistic particles are included; in the second one only relativistic events were considered. The main difference between the two plots involves element peaks above 30 ADC channels: those peaks are more clear in the second plot, just because the non relativistic events enlarge the distributions. It has to be remembered that in the plots like the ones of fig. 10.19 and 10.29 the mean energy per event is considered.

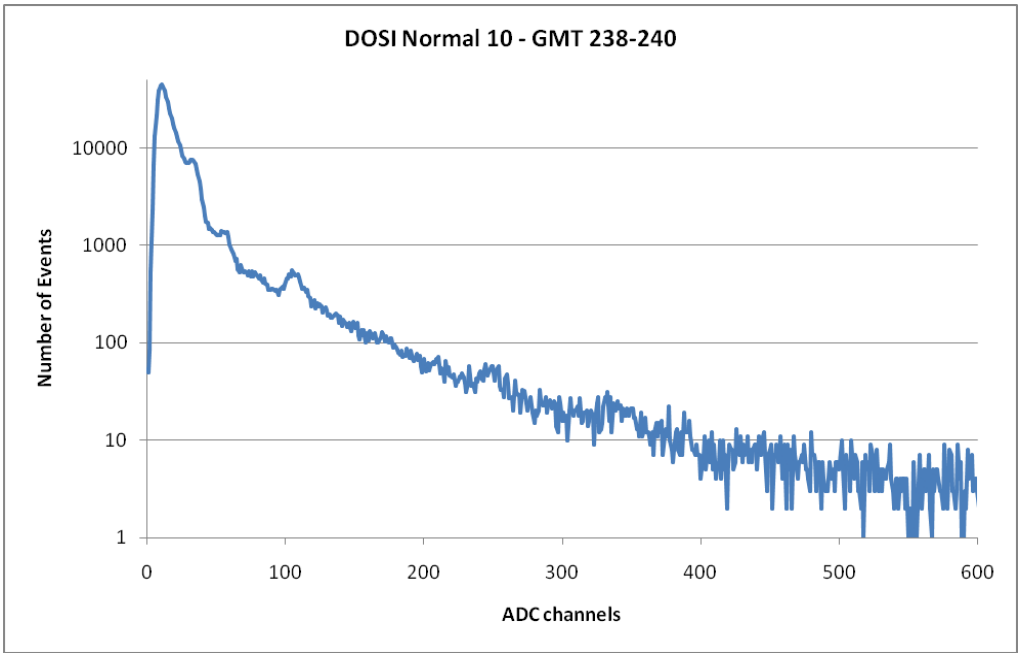

Fig. 10.19: Spectrum of data obtained with no energy cut.

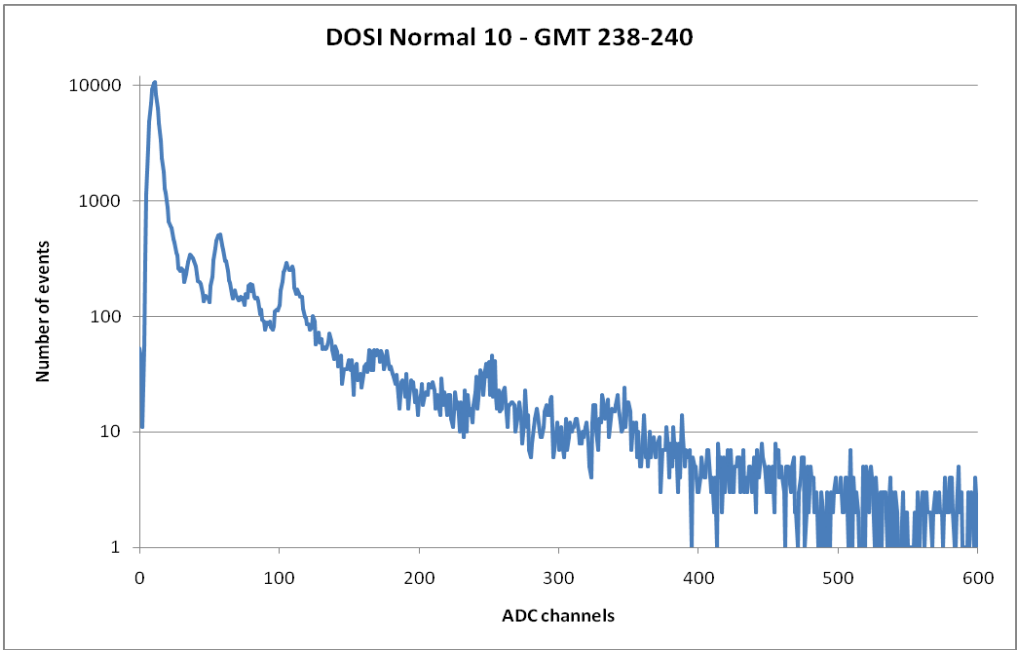

Fig. 10.20: Spectrum of data obtained selecting relativistic particle with R=0.1.

Once particles satisfying these cuts are selected, a further correction can be considered. In fact, if the tracks are aligned the angle between the track and the normal to the silicon plane can be found; this angle can be used, if desired, to correct the energy loss considering the real detector thickness travelled by the particles.

An angle is calculated for both the views so that the angle between the normal to the silicon planes and the particle incidence direction is given by:

$$\theta = arctg\left[\sqrt{tg^2\theta_x + tg^2\theta_y}\right]$$

where θ_x and θ_y are angles between particle trajectory and z axis on xz and yz planes respectively (see fig. 10.21).

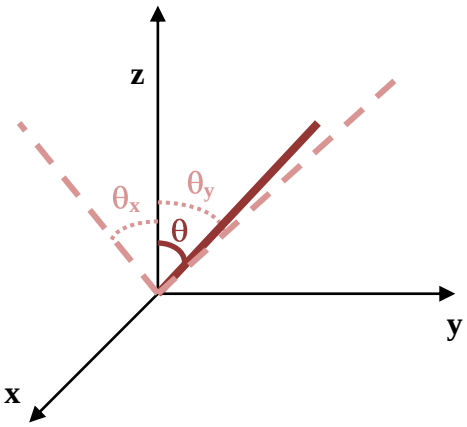

Fig. 10.20: The reference system used in angle definition. Silicon plane detectors lay on the xy plane.

In order to evaluate the number of events surviving the selection rules, an example of filter action is showed in table 10.2; data reported in the table are DOSI Normal 10, GMT 274-278. In the last column the ratio between the filtered and the unfiltered events is reported. It has to be noticed that the ratio between the relativistic aligned particles and all the aligned particles is about 0.16; then, the ratio between the energy filtered particles relativistic/non relativistic is quite similar, 0.13.

Number of Events	Filters			Ratio
	alignment	relativistic events	energy cut	
648218				1
510027	x			0.79
141833	x		E>35 ADC ch	0.22
79445	x	x		0.12
18253	x	x	E>35 ADC ch	0.03

Table 10.2: Events surviving after the selection rules application

.

10.6 Preliminary analysis results

As mentioned in the previous paragraph, first step of data analysis is pedestal subtraction, then data are processed applying some filters. Default conditions for this preliminary analysis include the selection of aligned events hitting at least 5 on the 6 silicon planes (the missing one being a Y plane); relativistic particles are also considered, with the R parameter equal to 0.1.

Angular correction and correction of negative values are always setted.

Maximum value of energy loss is found in each silicon plane triggering an event; if event overcomes all the selection rules, energies of the hit planes are averaged and a mean energy value for each SDU with a good event was considered. After processing the data, a text file with the histogram of the energy loss (in the ADC channels 0- 4095) is produced. This text file is processed again with an IDL script. Spectra generated by this processing are like the one showed in fig. 10.21 and 10.22.

The plot in fig. 10.21 refers to DOSI data acquired in Normal 5 mode (with 5 MIP threshold) in the period between the August ,18th and September, 11th for a total of about 20 days; in this plot data of all the six SDUs, consisting in 831318 filtered events, are reported..

In fig. 10.22 DOSI data acquired in Normal 10 mode (with 10 MIP threshold) are showed in the histogram; data were acquired between the August, 26th and the December, 2nd for about 65 days. Also in this case data of all the SDUs are showed; there are 1763135 filtered events.

In both the plots, histograms with single binning were considered. Peaks of elements with $Z \geq 5$ are distinguishable, also if the difference of statistics implies that not all nuclei between S and Ca and between Ca and Fe are clearly visible in the 5 MIP histogram. Fluorine and Phosphorus peaks are not visible in either spectra.

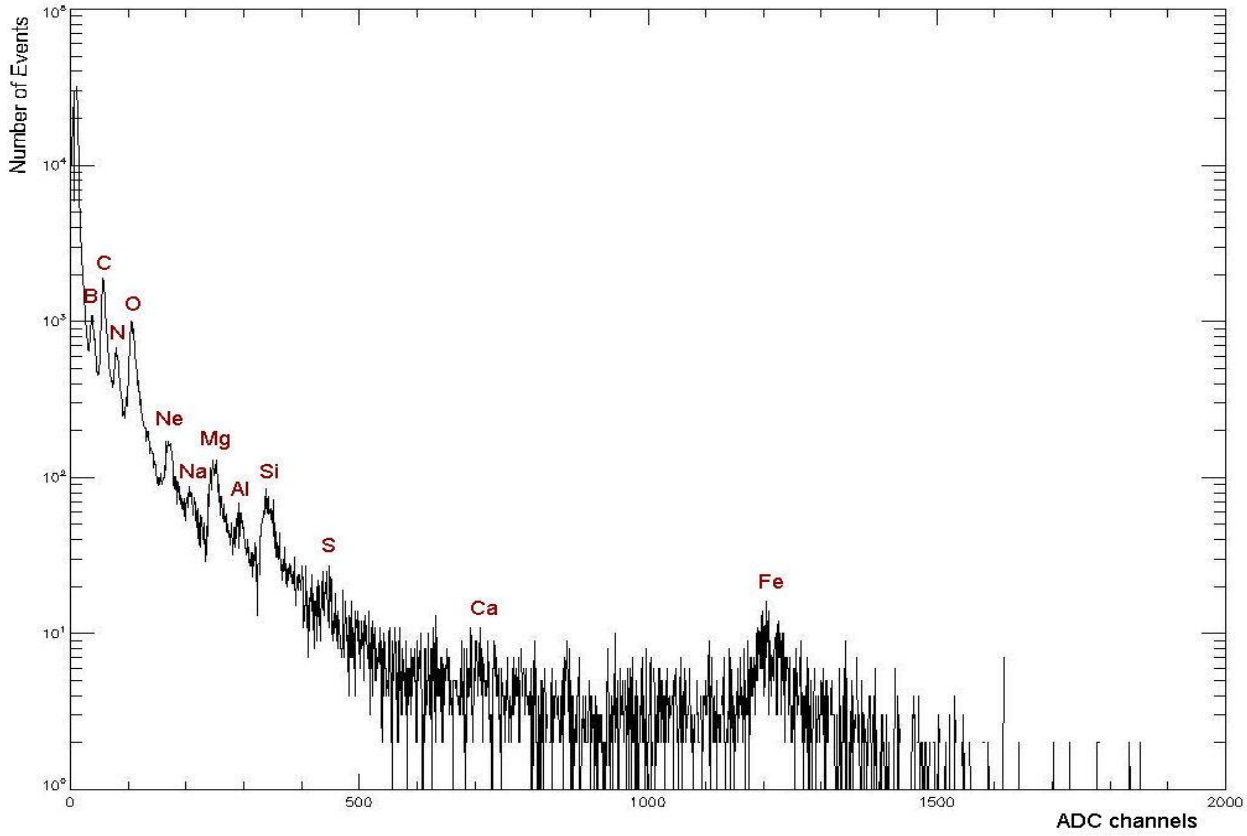

Fig. 10.21: Spectrum of about 830000 events acquired in Normal 5 mode.

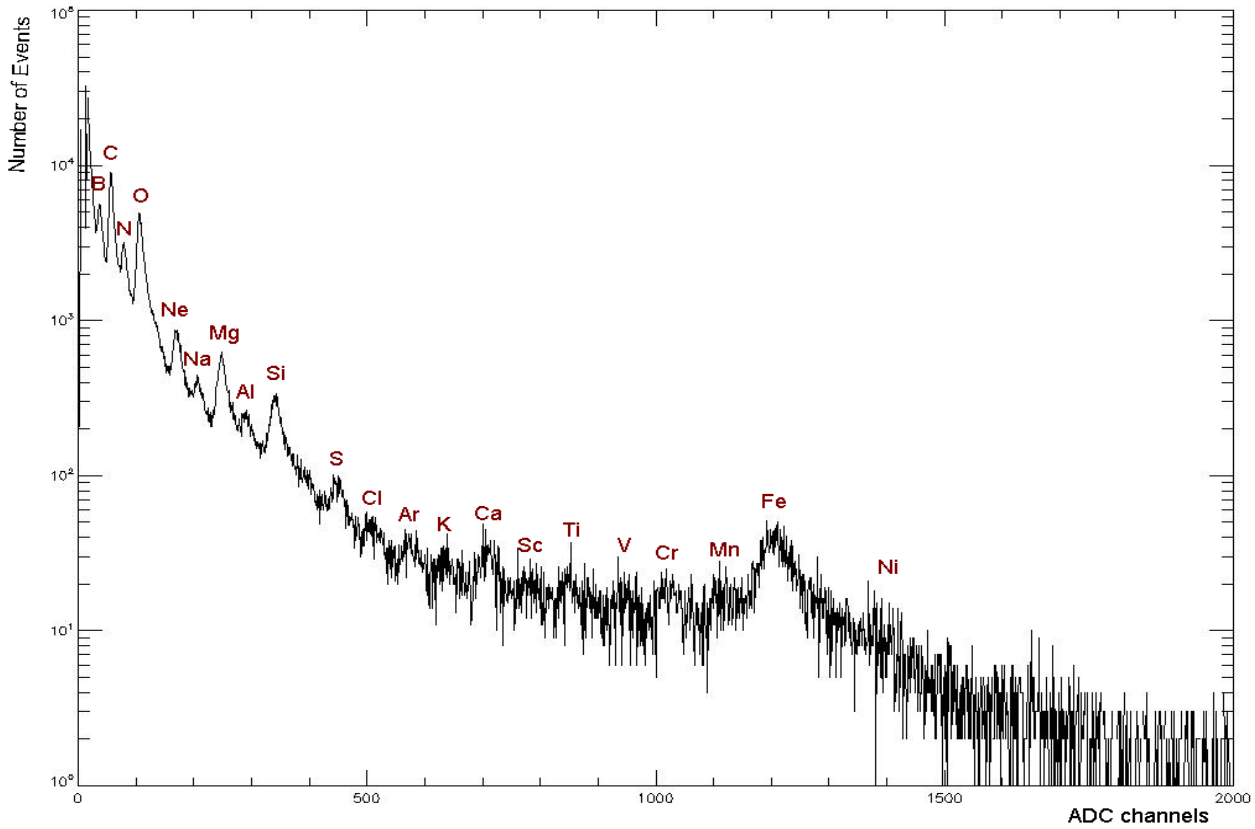

Fig. 10.22: Spectrum of about 1760000 events acquired in Normal 10 mode.

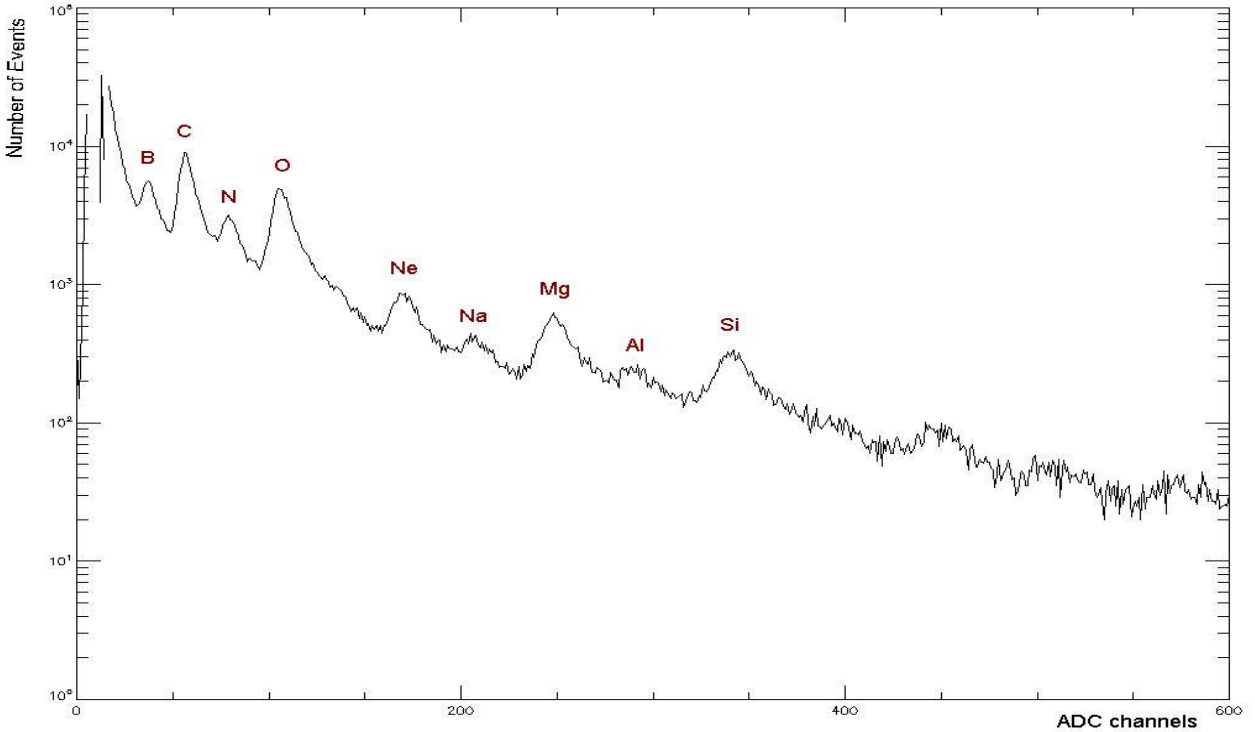

Fig. 10.23: Zoom on low Z peaks: as Z grows up, the peak appearance gets worse.

One of the first feature to note is the difference in the spectra appearance for nuclei from Boron to Silicon and above Silicon. In fact, while peaks related to nuclei from Boron to Silicon are quite clear (see fig. 10.23), peaks of nuclei above Silicon show a segmented distribution. It seems like the kind of distributions noted during beam calibration (see chapter 7). As explained in chapter 7, this problem should have been solved with a capacitor in order to decouple trigger from particle signals. This solution was applied and tested in laboratory and appeared successful; however, heavy nuclei lose high energy and the capacitor solution, efficient for lower energies, could be not enough for all the energy range. Heavier nuclei peaks are in any case distinguishable, if statistics is high enough, and this strange distribution should not invalidate the peak integrals.

In order to check the linearity of peak positions with Z^2, the statistical fits of the histograms were performed with IDL statistical tool. Peaks were fitted with a Gaussian distribution; actually, peaks are not completely symmetric and a Landau distribution could be more appropriate. A further analysis will be performed with the Landau distribution and results will be compared with the ones obtained with Gaussian distribution.

In fig. 10.24 and 10.25 Gaussian fits calculated on 5 MIP and 10 MIP spectra are showed. In the 5 MIP case, only peaks from Boron to Silicon (except Fluorine and Phosphorus) plus Sulfur, Calcium and Iron were fitted. In the 10 MIP case the greater statistics makes possible the fitting of Boron to Iron, still except Fluorine and Phosphorus; Nickel peak was fitted too, even if it is not so clear. Gaussian fit seems to be efficient to extrapolate the peaks also where the distribution is highly segmented (despite a not so low statistics); in fig.10.26 the fits of the peaks until Silicon are plotted, showing in details the fit good determination of the peak positions and widths.

In any case no peaks are resolved under the Boron peak.

In table 10.3 fit parameters are reported for DOSI Normal 10 data. The fits were performed considering the peak range as the only input parameter; output values are A_0, A_1 and A_2 as in the Gaussian formula:

$$G(x) = A_0 e^{-\frac{(x-A_1)^2}{2A_2^2}}$$

so A_0, A_1 and A_2 are estimations of the height, the center and the width of the Gaussian curves.

In the table errors of output fit parameters are also showed.

The first estimation of the peak positions were done by a comparison with the simulation previously performed, but an exhausted examination of the trend of peak positions with Z^2 was needed. In order to do this, the A_1 parameters were plotted versus Z^2; the expected trend is a line, according to the Bethe-Bloch formula (see Chapter 1).

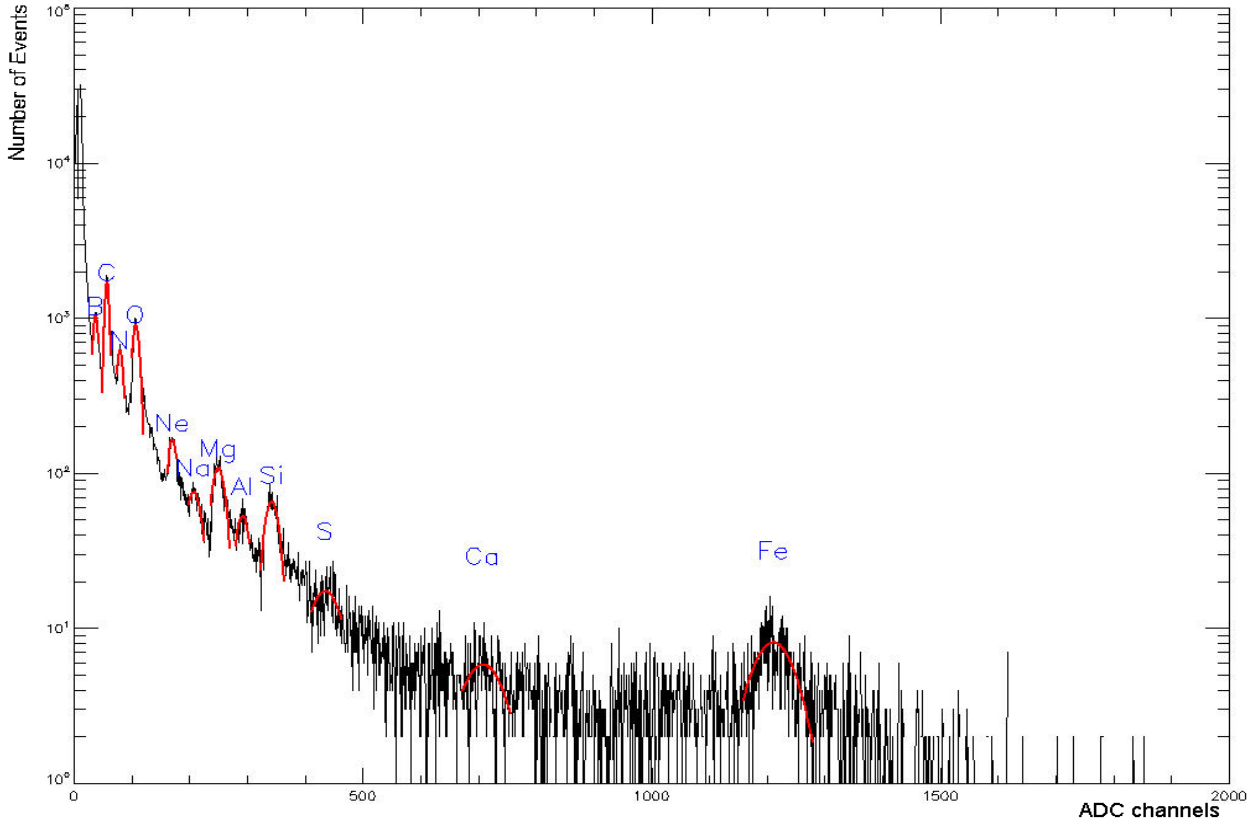

Fig. 10.24: 5 MIP spectrum with Gaussian fits superimposed.

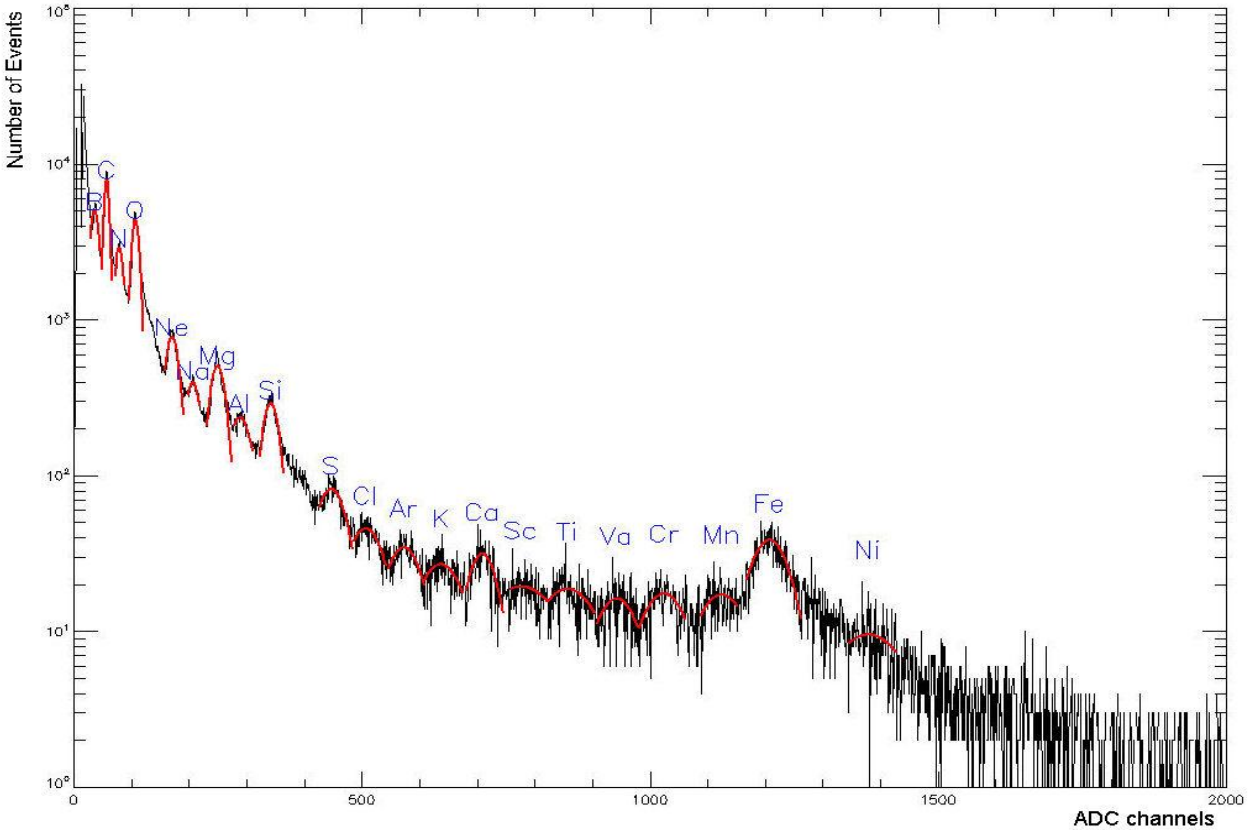

Fig. 10.25: 10 MIP spectrum with Gaussian fits superimposed

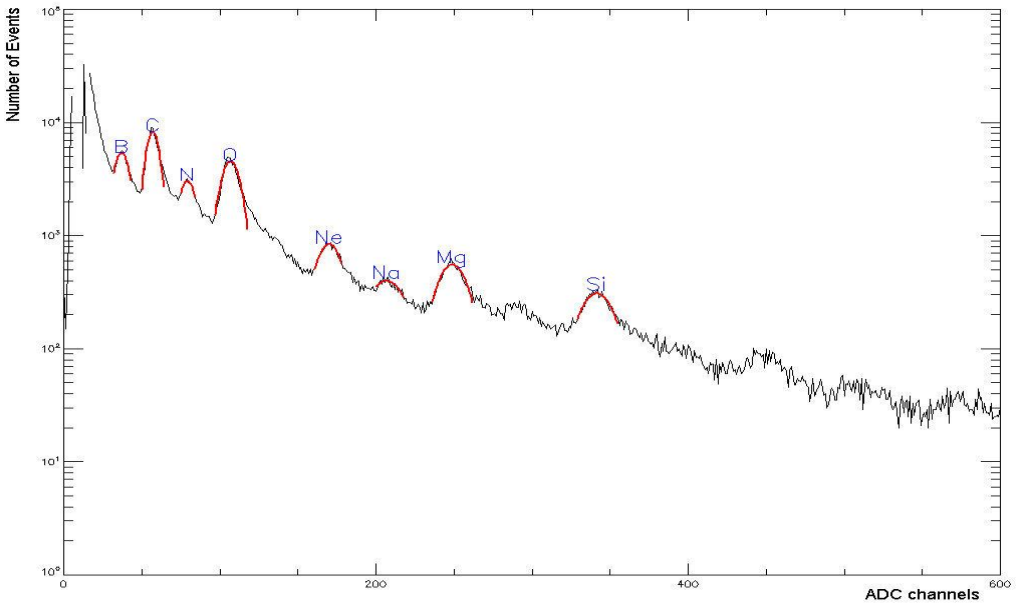

Fig. 10.26: 10 MIP spectrum of low Z peaks with Gaussian fits superimposed.

Elements	Z	Fit range		Fit parameters			Fit errors		
				A_0	A_1	A_2	ΔA_0	ΔA_1	ΔA_2
B	5	32.14	42.86	5452.75	37.01	5.26	100.48	0.13	0.25
C	6	49.29	66.44	8039.85	57.26	5.06	311.55	0.23	0.26
N	7	75.02	85.73	3033.93	79.23	6.12	31.82	0.11	0.21
O	8	98.60	117.89	4601.05	106.79	6.46	136.26	0.23	0.29
Ne	10	160.76	182.20	823.09	170.23	9.97	14.08	0.23	0.38
Na	11	199.35	216.49	401.16	206.72	12.37	9.39	0.54	1.37
Mg	12	235.79	265.80	544.67	249.19	11.30	11.50	0.30	0.42
Al	13	278.66	306.53	238.80	288.67	19.71	5.60	1.07	2.23
Si	14	325.82	364.40	293.40	342.12	15.12	6.25	0.42	0.60
S	16	433.00	482.30	83.31	447.81	25.29	2.05	1.46	1.93
Cl	17	488.74	542.33	45.87	507.48	32.63	1.31	2.10	3.65
Ar	18	548.76	604.49	34.54	574.62	33.49	1.10	1.72	3.81
K	19	608.78	679.52	26.60	637.21	46.81	1.01	3.54	7.64
Ca	20	681.66	739.54	32.25	708.55	25.00	1.42	1.45	2.34
Sc	21	748.11	812.42	19.92	776.20	48.21	0.96	4.78	12.62
Ti	22	821.00	906.74	18.80	853.56	58.32	0.80	5.36	10.98
V	23	911.03	979.62	16.32	942.60	39.14	0.90	3.46	7.31
Cr	24	983.91	1073.94	17.21	1025.59	48.30	0.67	2.80	5.58
Mn	25	1091.09	1148.97	16.91	1122.82	60.17	0.84	7.43	27.78
Fe	26	1170.41	1262.58	38.77	1207.49	35.68	1.02	1.31	1.81
Ni	28	1344.04	1427.64	9.55	1378.38	67.86	0.57	9.65	25.52

Table 10.3: Fit parameters for Normal 10 data.

In fig. 10.27 and 10.28 the plots for 5 and 10 MIP data are showed. Errors associated to the points are the ones coming from the fits (peak value within 2 sigma). In both the 5 and 10 MIP cases, a good linearity is found and parameters from line fits are perfectly in agreement, despite differences in statistics and in number of considered peaks. The meaning of the negative value of intercept is currently under investigation; it is probable due to a negative additive term arising in the pedestal subtraction.

Using parameters obtained by the Gaussian fits, the relative abundances of the fitted nuclei were calculated. The peak area can be estimated as product of A_0 and A_2 parameters and the normalization factor $\sqrt{2\pi}$. Results for SDU2 are showed in fig. 10.29: ALTEA data are compared with data from Alteino-Sileye3 [57] experiment and abundances at 1 Astronomic Unit [8,9].

Obtained results are not of simple interpretation at the level of this preliminary analysis; for most of the nuclei ALTEA values seem to be not consistent with Alteino or literature values. For some elements (Boron most of all, then Neon and Sodium) ALTEA finds abundances higher than expected, while abundances of Oxygen and Iron are lower. In particular, discrepancies between ALTEA and Alteino values have not a definite sign. Some difference can be due to nuclei spallation with the ISS shielding and with all the instrumentation inside the Station.

Alteino was also on board ISS (within the Russian PIRS module), so it could be important the study of different shielding between PIRS module and US Lab, where ALTEA is.

In table 10.4 results of relative abundances up to Silicon calculated for each of the six SDUs are showed; in fig. 10.30 those abundances are plotted. From the comparison between the SDUs, the most evident feature is that while abundances of Neon, Magnesium and Silicon are mostly compatible within errors, the bigger differences are found in lighter nuclei. Boron, in particular, is very different between SDU3, SDU4, SDU6 and SDU1, SDU2, SDU5. Those results are compatible with possibility of different shielding causing a diverse fragmentation in respect to the SDU position, but a further analysis is needed with a greater statistics and a more detailed error treatment.

10.7 Work in progress

Results presented in this chapter are very preliminary, both for the recent beginning of the space operations and for the time needed for troubleshooting. First of all analysis will go on with the

inclusion of ancillary data in order to study correlation between particle fluxes and characteristic areas (polar regions, equator, SAA). Then the study of the flux angular distribution will be also considered. An algorithm for track reconstruction is also being implemented.

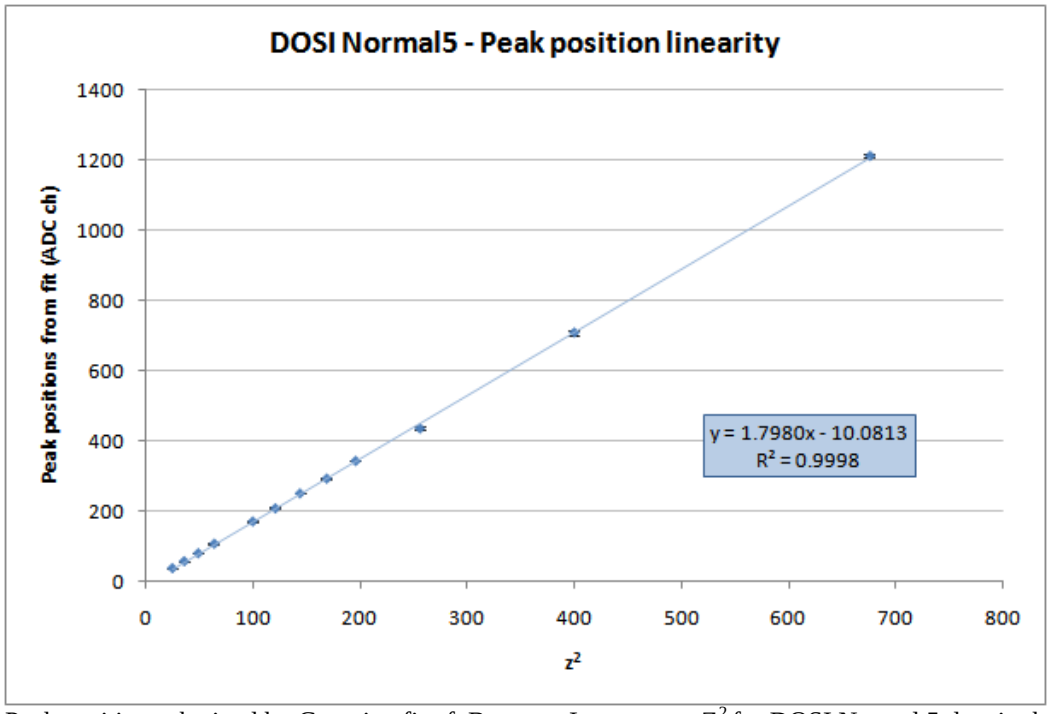

Fig. 10.27: Peak positions obtained by Gaussian fit of Boron to Iron versus Z^2 for DOSI Normal 5 data is showed. The trend line, together with fit line parameters, are also showed.

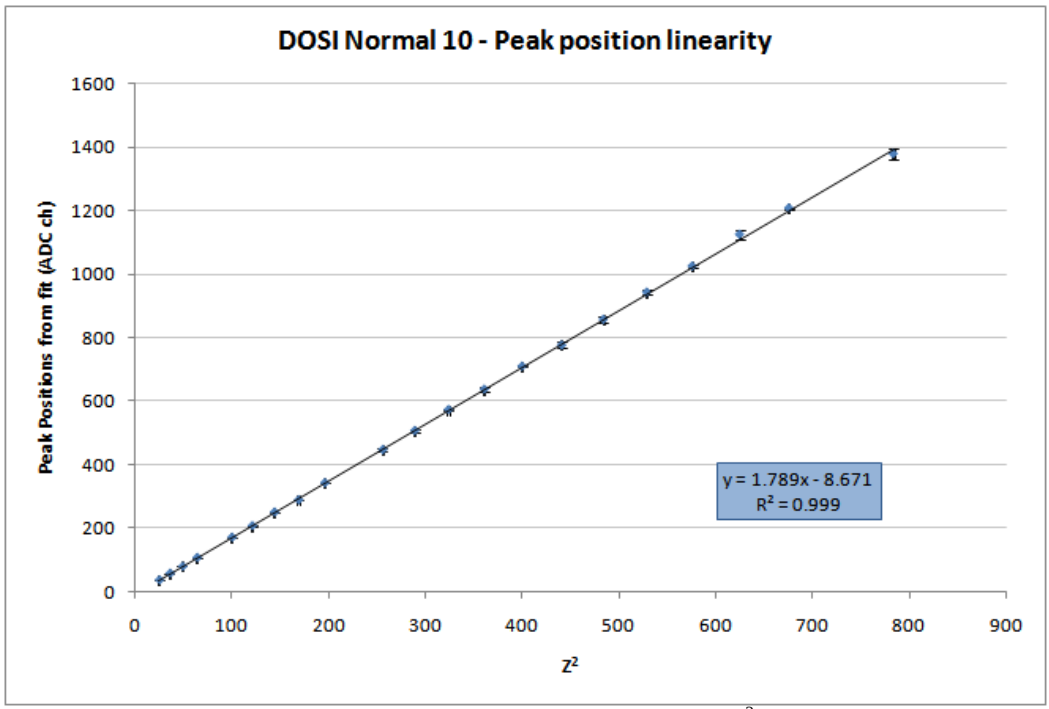

Fig. 10.28: Peak positions obtained by Gaussian fit of Boron to Nickel versus Z^2 for DOSI Normal 10 data is showed. The trend line, together with fit line parameters, are also showed.

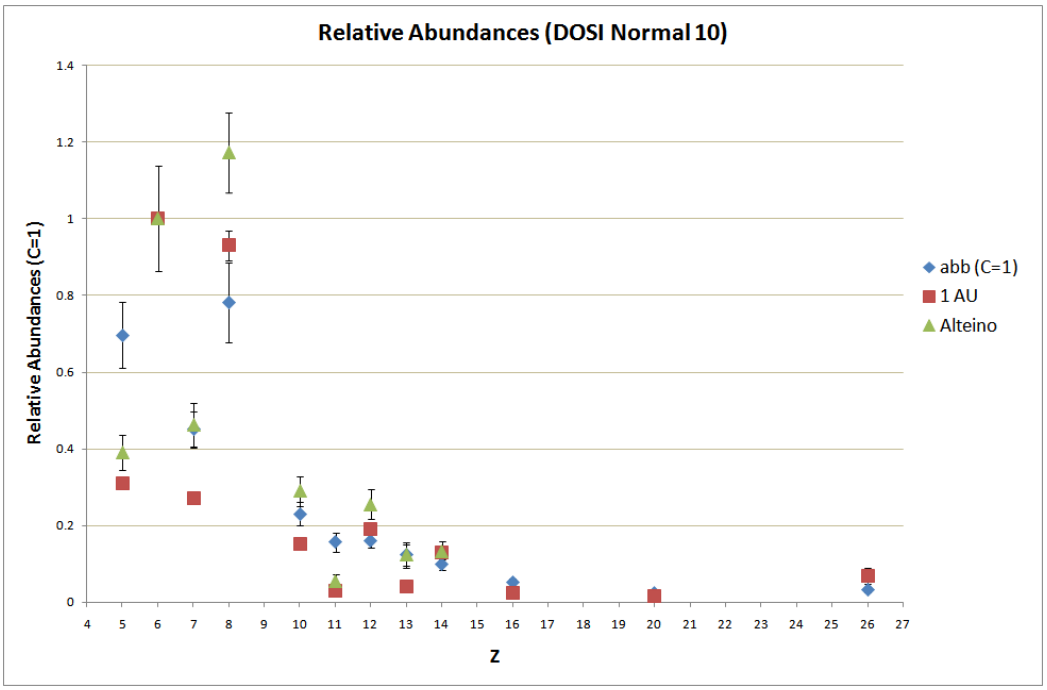

Fig. 10.29: Relative abundances normalized to Carbon (SDU2).

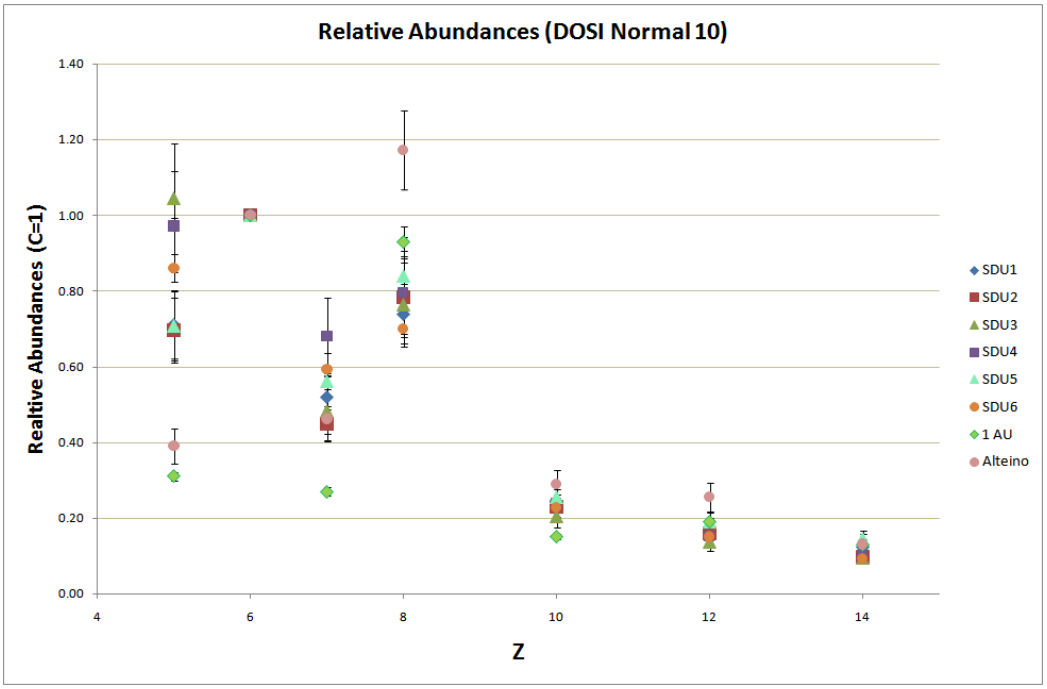

Fig. 10.30: Relative abundances normalized to Carbon for the six SDUs.

SDU1	SDU2	SDU3	SDU4	SDU5	SDU6	Simpson	Alteino
0.71±0.09	0.70±0.09	1.04±0.15	0.97±0.15	0.71±0.09	0.86±0.13	0.31±0.01	0.39±0.05
1.00	1.00	1.00	1.00	1.00	1.00	1.00	1.00
0.52±0.06	0.45±0.05	0.48±0.06	0.68±0.10	0.56±0.07	0.59±0.10	0.27±0.01	0.46±0.06
0.74±0.08	0.78±0.10	0.76±0.11	0.80±0.11	0.84±0.10	0.70±0.10	0.93±0.04	1.17±0.10
0.22±0.03	0.23±0.03	0.20±0.03	0.24±0.04	0.26±0.04	0.23±0.03	0.15±0.01	0.29±0.04
0.16±0.02	0.16±0.02	0.14±0.02	0.15±0.02	0.19±0.02	0.15±0.03	0.19±0.01	0.25±0.04
0.12±0.02	0.10±0.01	0.10±0.02	0.10±0.02	0.15±0.02	0.09±0.02	0.13±0.002	0.13±0.03

Table 10.4: Relative abundances for the six SDUs normalized to Carbon.

10.7.1 Track recognition: the Hough transform method

In order to establish an effective method to implement a track recognition algorithm, the Hough transform method was studied. The Hough transform is a method used in pattern recognition and it allows finding some particular geometrical structures inside given figures. Its simplest application consists in verifying the alignment of three or more points; in this case, each point (x,y) to check for alignment is transformed in the line q = - xm + y in the so called Hough space, as can be seen in fig. 10.31.

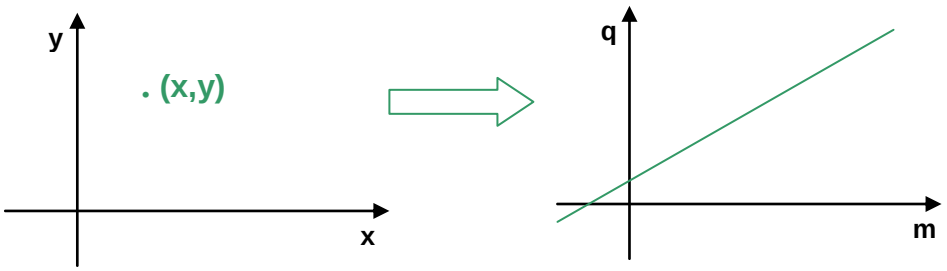

Fig. 10.31: Transformation of a point (x,y) from the Cartesian system to the Hough space.

Two points in the Cartesian plane are transformed in two lines in the Hough space intersecting in (m,q), correspondent to the inclination and the offset term of the line passing for the two given points. For three or more points a correspondent number of lines will be found in the Hough space; intersection between those lines will demonstrate the alignment level of the points. Example considering three points is showed in fig. 10.32.

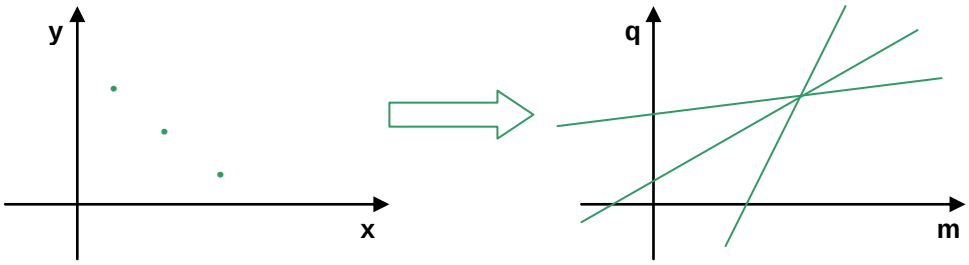

Fig. 10.32: Transformation of three aligned point from the Cartesian system to the Hough space.

In real cases, transformation of each single point is considered and a matrix with elements (m,q) is filled with it; intersections between lines will correspond to a maximum of m,q. For example, if we consider three points, the element correspondent to the values m and q of line passing per the given points will be populated with value 3.

This method theoretically allows to recognise segments as aligned and to give a 'statistical' estimation of the most probable trajectory passing through some points.

The choice of m and q steps (Δm and Δq) results is crucial: if the step is too fine it is possible not to find any intersection between the different lines in Hough space (then any element m,q populated as expected), while if the step is too large there can be more than one element m,q populated with the maximum value.

In order to test the possibility to use an algorithm based on the Hough transform for track recognition, a specific software was developed (fig. 10.33). The program has a simple interface in which the strips constituting a specific track can be entered. Then both the linear fit and the Hough transform can be calculated and the reconstructed strips are showed in both the cases. The physical space, segmented in strips, and the Hough space are showed; in particular, if the choice of Δm and Δq (selectable on the interface) permits to find only one element (m,q) with the maximum population, in the Hough space the lines corresponding to the particle passage points on the silicon planes are plotted.

This software was used to check the alignment recognition capability in several track configurations and varying the steps Δm and Δq. First of all, method capacity to recognize aligned tracks was tested as showed in tables 10.5 to 10.8.

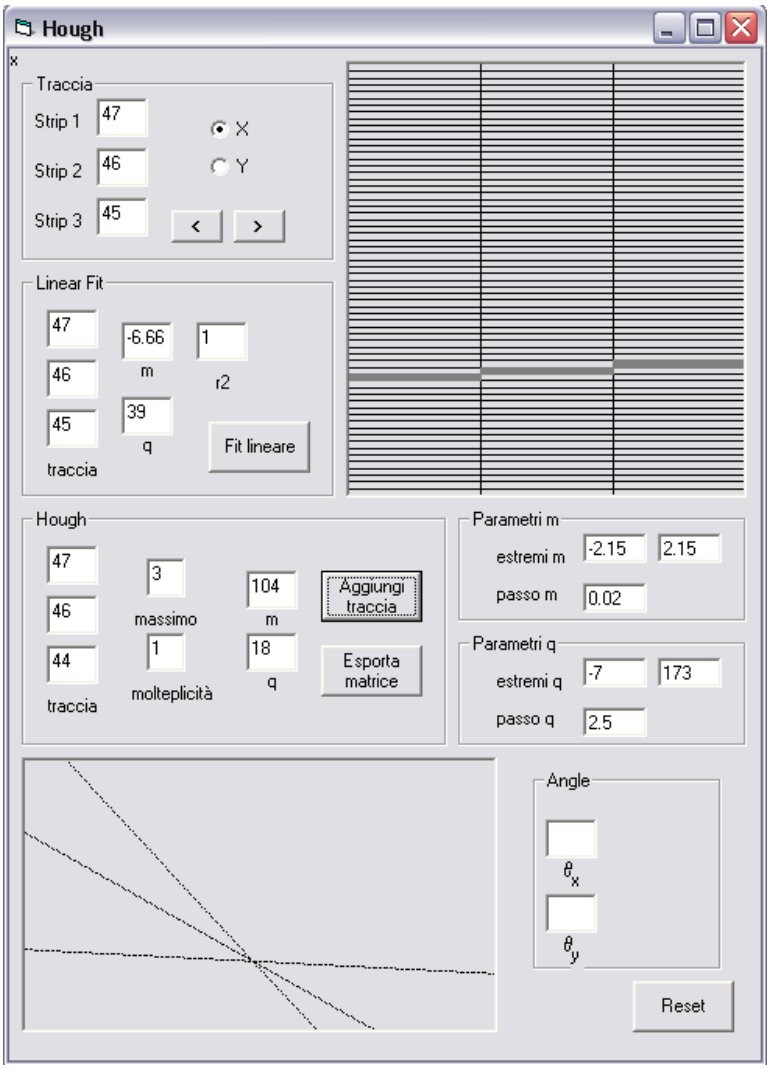

Fig.10.33: The interface of the script created to test track recognition capability of Hough transform.

Table 10.5

-2.15 ≤ m ≤ 2.15 , Δm=0.02

-7 ≤ q ≤ 173 , Δq=2.5

Δs	strip 0-31	strip 32-63	strip 0-63
0	2	1	
1			2
2	1	2	
3	4	2	
4	1	2	
5	3	2	
6	1	1	1
7	2	1	
8	2	1	
9			2
10	1	2	
11	1	2	
12			1
13	2	3	
14	2	1	
15	4	1	
16			2
17			2
18			1
19			1
20			1
21			2
22			2
23			4
24			2
25			2
26			1
27			1
28			1
29			2
30			2
31			2

Table 10.6

-2.15 ≤ m ≤ 2.15 , Δm=0.01

-7 ≤ q ≤ 173 , Δq=2.5

Δs	strip 0-31	strip 32-63	strip 0-63
0			3
1			3
2			3
3	3	6*	
4			3
5	6	3	
6			3
7			3
8			3
9			3
10			3
11			3
12			3
13	3	6	
14			3
15	7	3	
16			3
17			3
18			3
19			3
20			3
21			3
22			3
23			7
24			3
25			3
26			3
27			3
28			3
29			3
30			3
31			3

Table 10.7 -2.15 ≤ m ≤ 2.15 , Δm=0.025 -7 ≤ q ≤ 173 , Δq=2.5			
Δs	strip 0-31	strip 32-63	strip 0-63
0			1
1	2	1	
2			1
3			2#
4			1
5	2	1	
6	2	1	
7			1
8	2	1	
9			1
10	1	2	
11			1
12	1	2	
13	1	2	
14			1
15			2
16			1
17			1
18			1
19			1
20			1
21			1
22			1
23			2
24			1
25			1
26			1
27			2
28			1
29			2
30			1
31			2

Table 10.8 -2.15 ≤ m ≤ 2.15 , Δm=0.02 -7 ≤ q ≤ 173 , Δq=2			
Δs	strip 0-31	strip 32-63	strip 0-63
0			1
1			1,2,3
2			1
3			1,2
4			1
5			1,2,3
6			1
7			1,2,3
8			1
9			1,2
10			1
11			1,2,3
12			1
13			1,2,3
14			1
15			1,2
16			1,2
17			2
18			1
19			1-2
20			1
21			1,2,3
22			1,2
23			1,2
24			1
25			1,2
26			1
27			1,2,3
28			1,2
29			1,2
30			1
31			1

* the track 32-35-38 has a transform with 7 (m,q) couples with value 3

Then a comparison between tracks analyzed with Hough transform and linear fit was performed on the real tracks found in file DOSI_Normal5 (see chapter 8). Results are showed in table 10.9: the linear fit is certainly the most effective way to recognize tracks (it fails only in recognizing two strips), while the Hough transform results as very sensitive on the parameters Δm and Δq choice and it probably experiences the fragmentation of detector. However the Hough transform is a powerful tool on the multiple track analysis and the investigation and the test have to be continued.

Event	X0	X1	X2	Linear Fit			Hough transform		
				X0	X1	X2	X0	X1	X2
720	25	15	5	✓	✓	✓	-1	-1	-1
721	5	60	47	✓	-1	✓			
722	20	18	16	✓	✓	✓	-1	-1	-1
724	47	46	45	✓	✓	✓	✓	✓	-1
725	7	0	61	✓	+1	✓			
726	23	19	14	✓	✓	✓	-1	-1	✓
727	58	46	34	✓	✓	✓			
728	8	9	10	✓	✓	✓			
729	7	8	10	✓	✓	✓	✓	✓	-1
730	53	63	6	✓	✓	✓			
731	33	57	14	✓	✓	✓			
732	26	21	17	✓	✓	✓	-1	✓	-1

Table 10.9: Comparison between track recognition capability of linear fit and Hough transform on the real event of file DOSI_Normal5

Conclusions

The scientific goal of ALTEA experiment is the characterization of radiation environment on board the ISS and the investigation of effects of radiation interaction with human Central Nervous System.

In this thesis I described the work I went through during my three PhD years. I followed ALTEA experiment since first tests on Flight Model, both analyzing data taken in the laboratory and then performing calibration at GSI accelerator.

I had the privilege to follow the beginning of flight operations and to analyze first data collected by ALTEA on board the International Space Station. This first analysis presented in this thesis reflects the difficulties to carry out a complete and deep work on flight data during this first time acquisition. In fact a lot of time was needed to troubleshoot the problems found during space operations and to develop and test appropriate tools needed to manage, preprocess and analyze collected data. In addition to this some computational time is needed to achieve statistically significant results on the big amount of data collected until now (60 Gb up to December, 15th).

Preliminary data analysis provided some interesting results on particle rate and on energy distribution of particle events. Nuclei from Boron to Nickel were recognised and a first estimation of relative abundances were calculated. An appropriate strategy was established to continue the analysis, including the correlation with ancillary data of ISS in order to get also an angular distribution of particle events.

I want to thanks Livio Narici and all ALTEA-team.

Appendix A:

Pedestal and rms values with and without silicon bonded

Without silicon planes bonded:

FM1

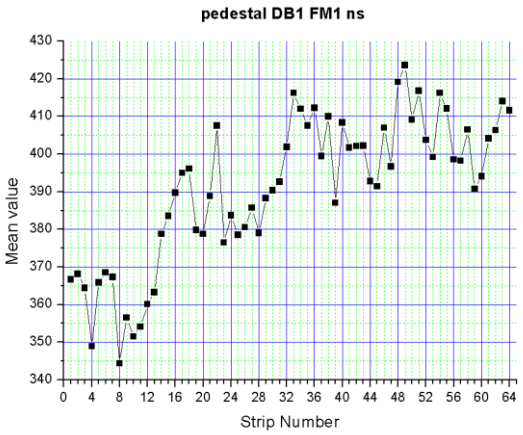

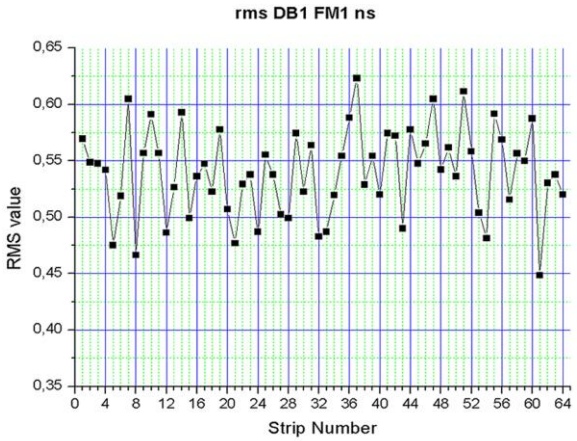

DB1: pedestals 0-99

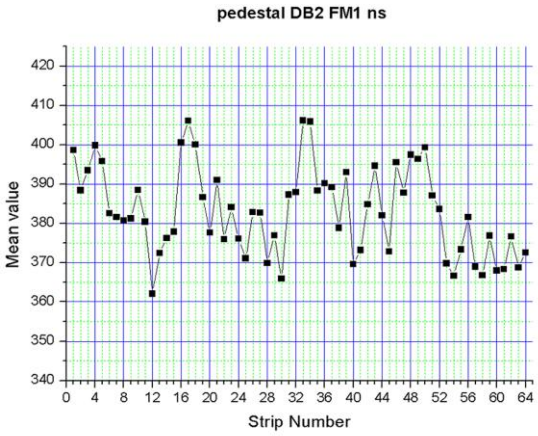

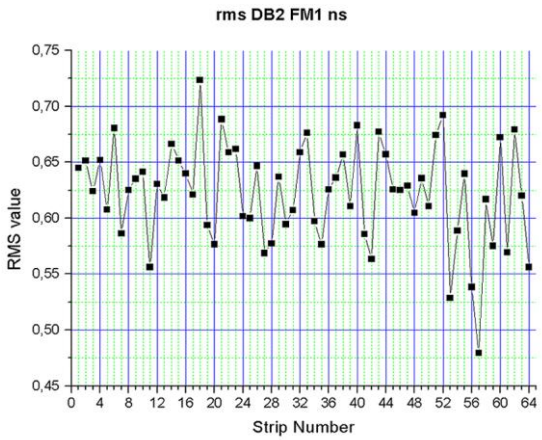

DB2: pedestals 1-99

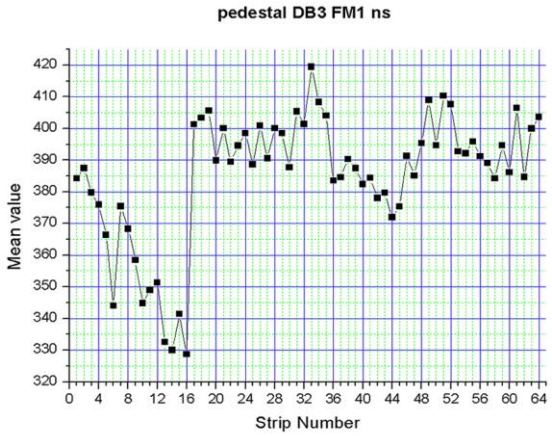

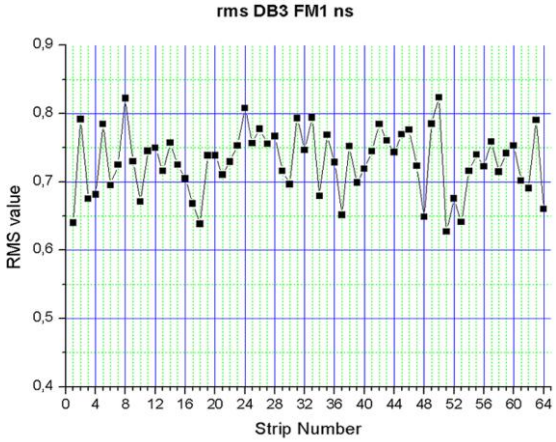

DB3: pedestals 1-99

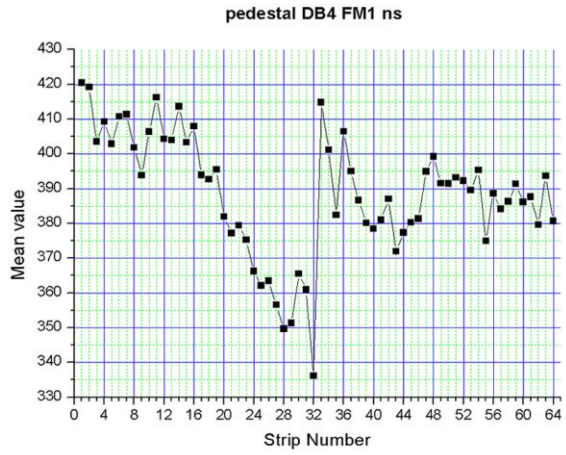

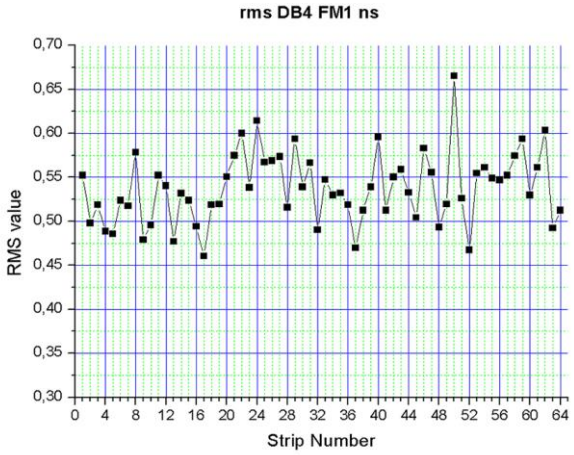

DB4: pedestals 1-99

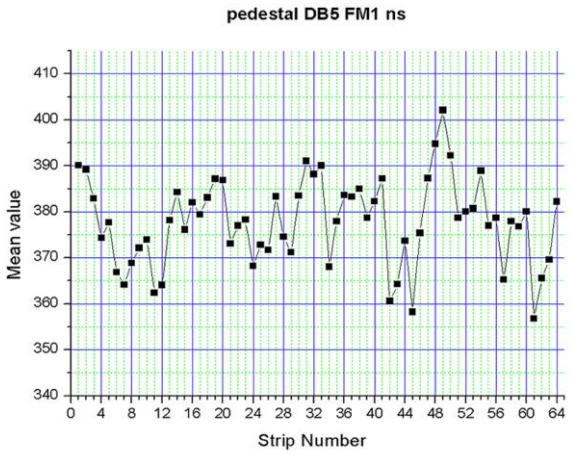

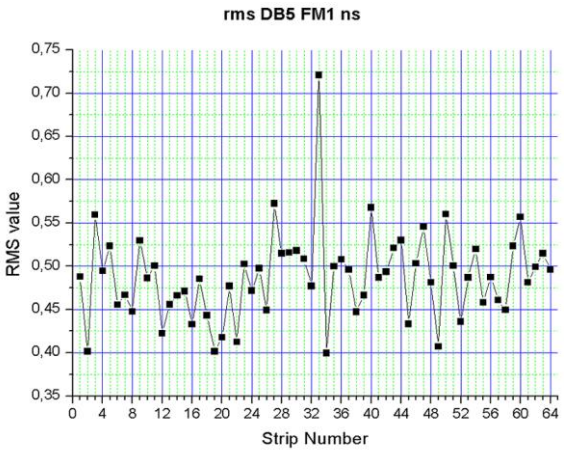

DB5: pedestals 0-99

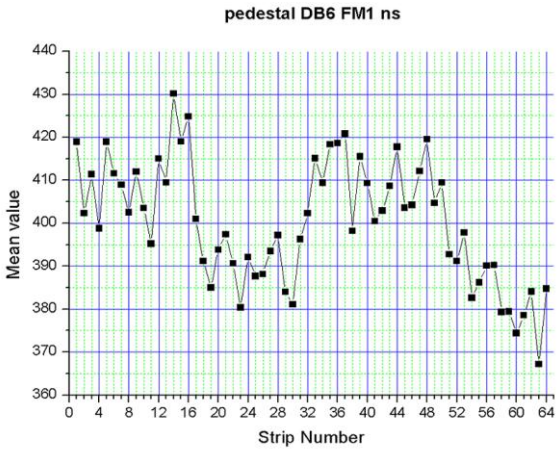

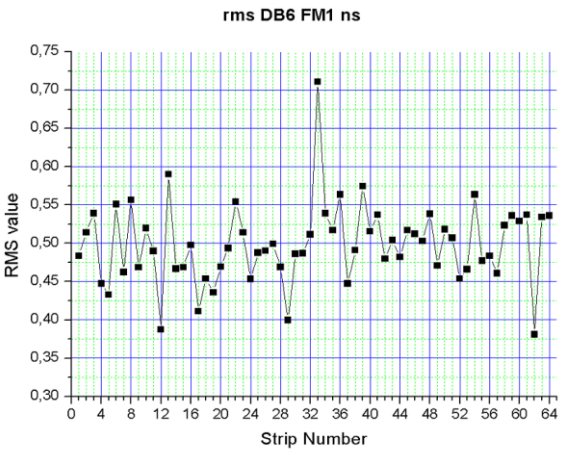

DB6: pedestals 0-99

FM2

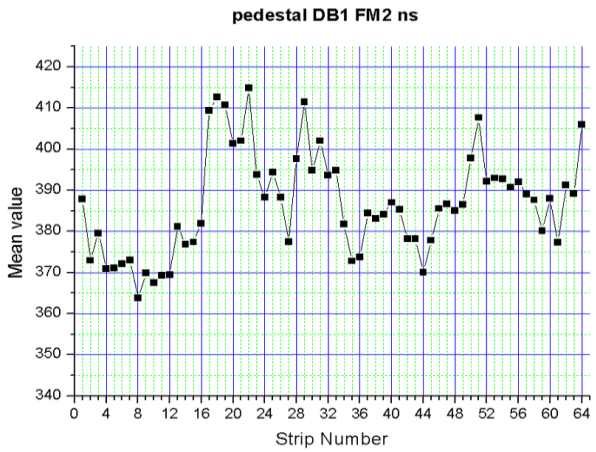

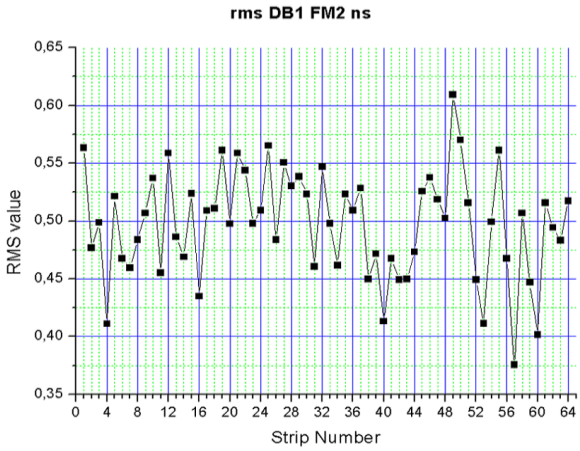

DB1: pedestals 1-99

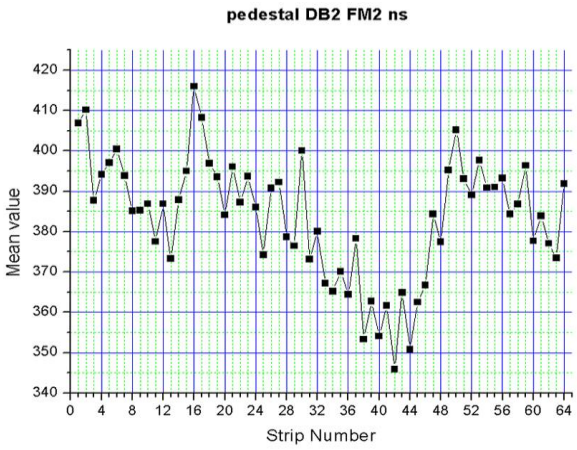

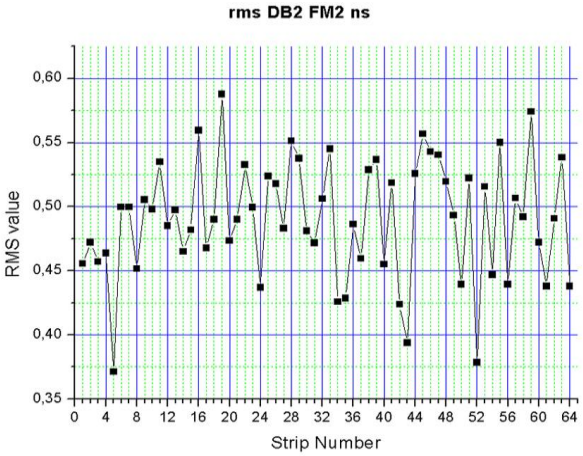

DB2. pedestals 1-99

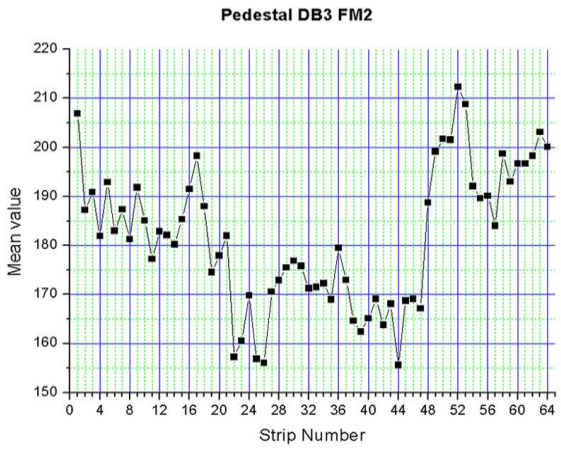

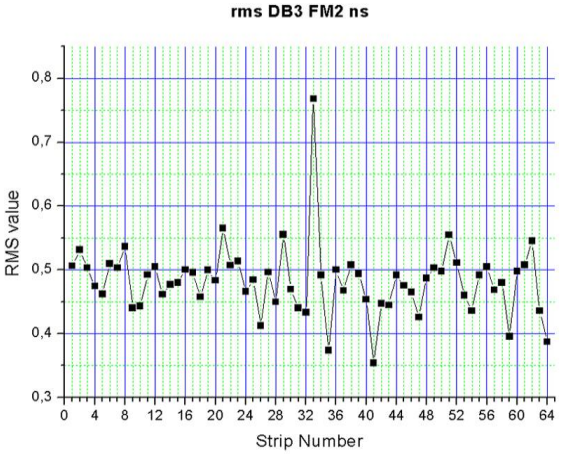

DB3: pedestals 0-99

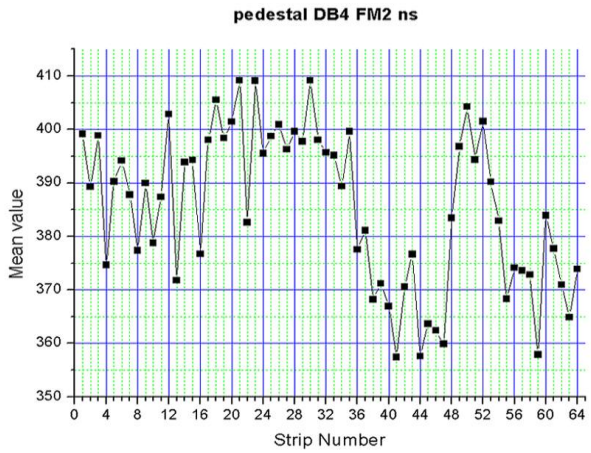

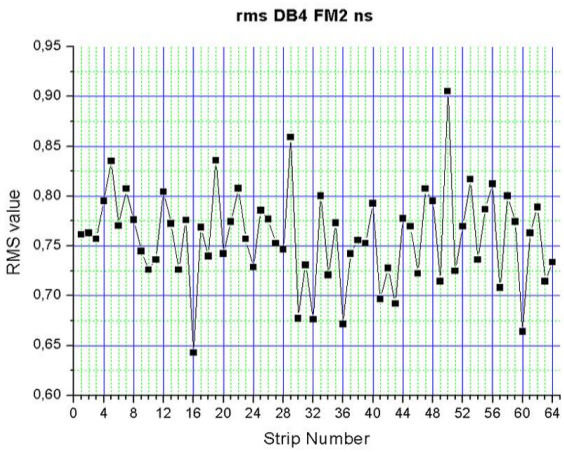

DB4: pedestals 1-99

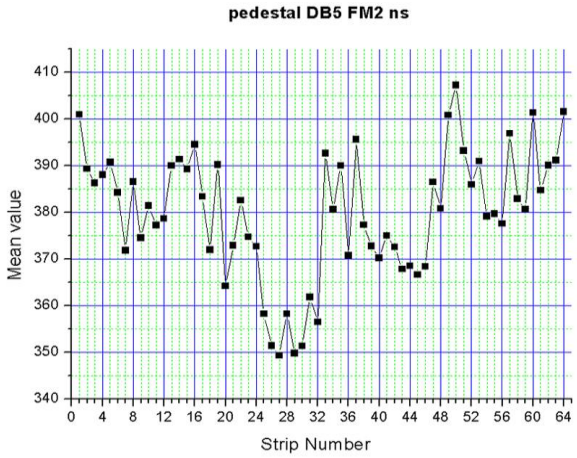

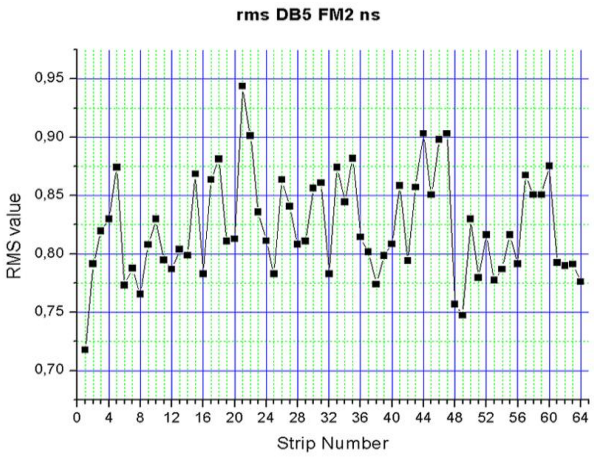

DB5: pedestals 1-99

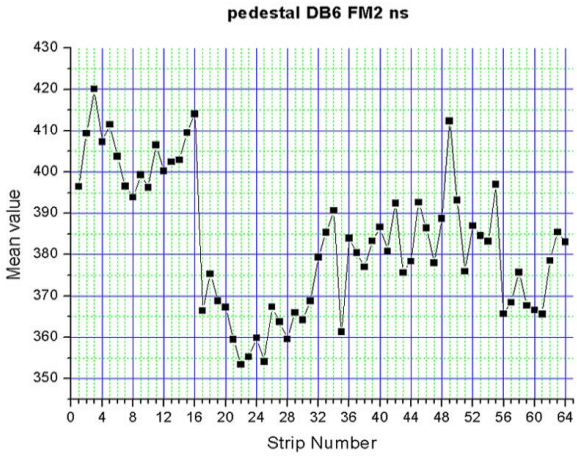

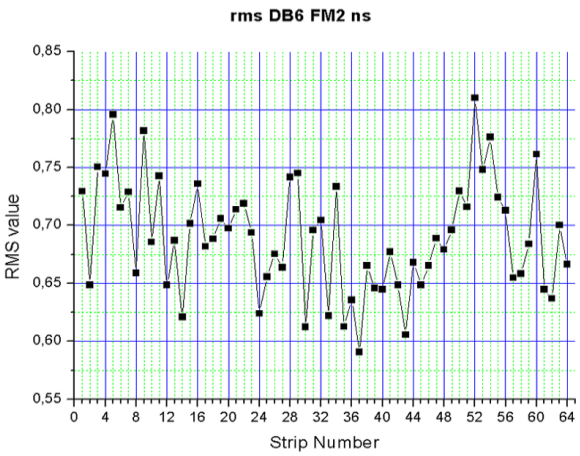

DB6: pedestals 1-99

FM3

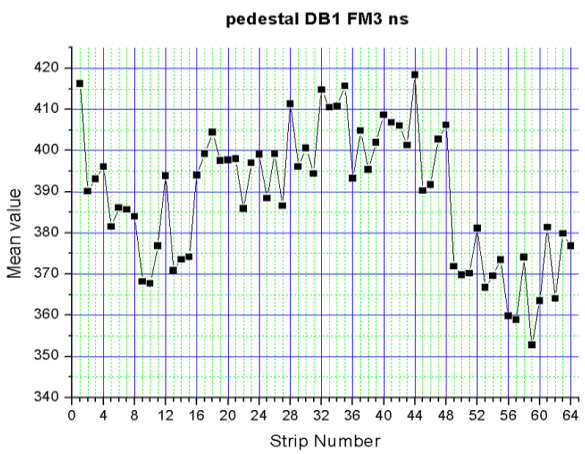

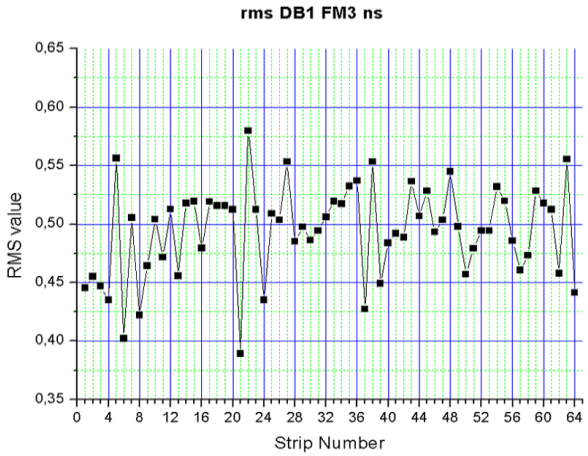

DB1: pedestals 1-99

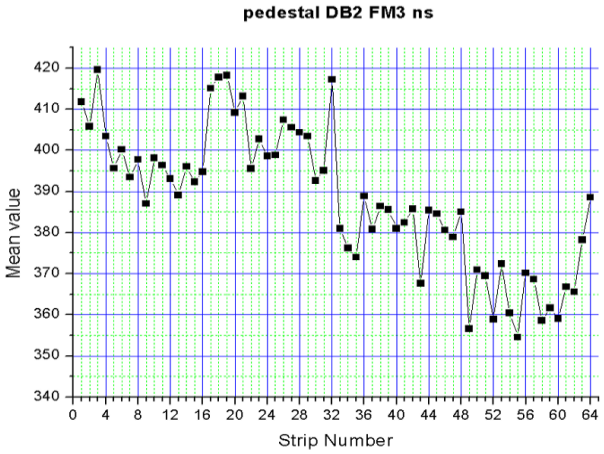

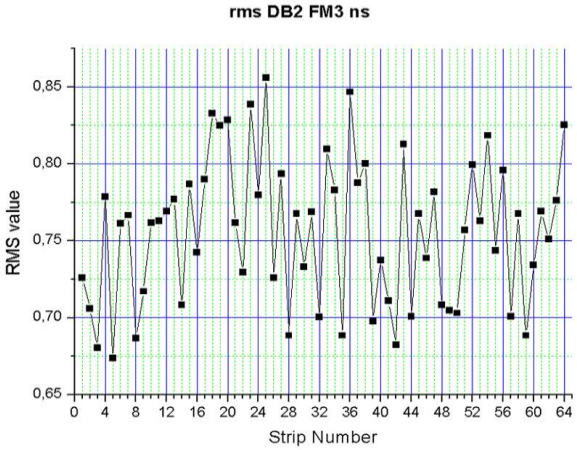

DB2 : pedestals 1-99

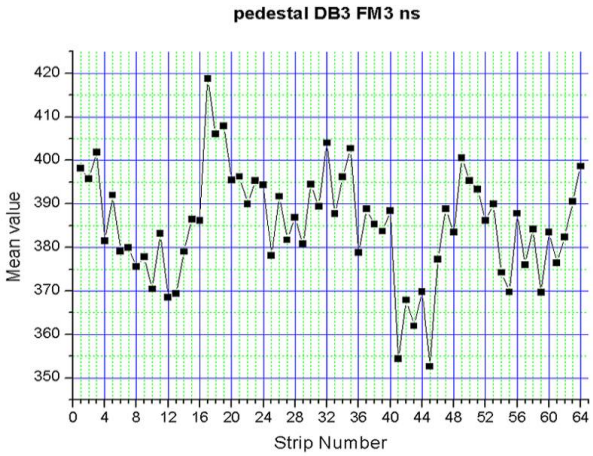

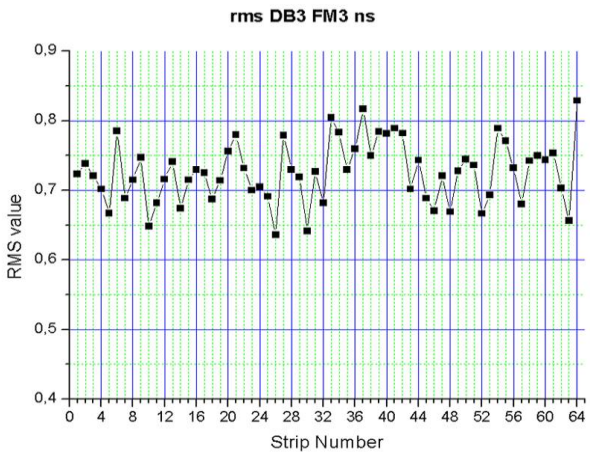

DB3: pedestals 1-99

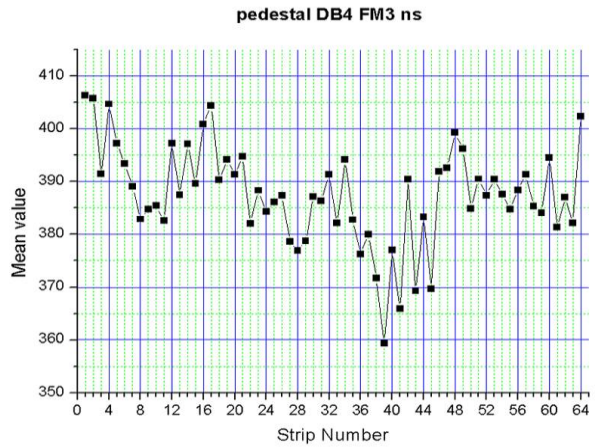

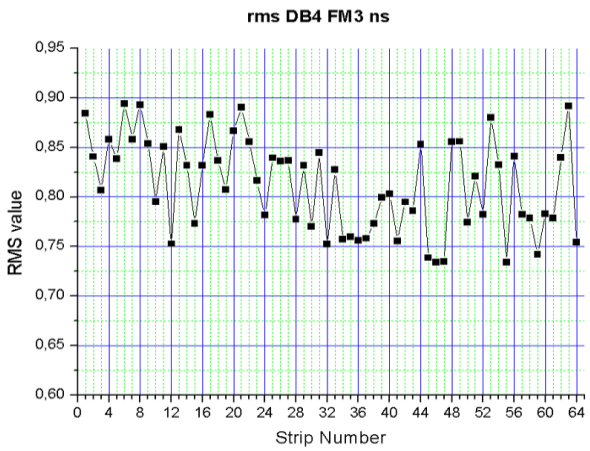

DB4: pedestals 1-99

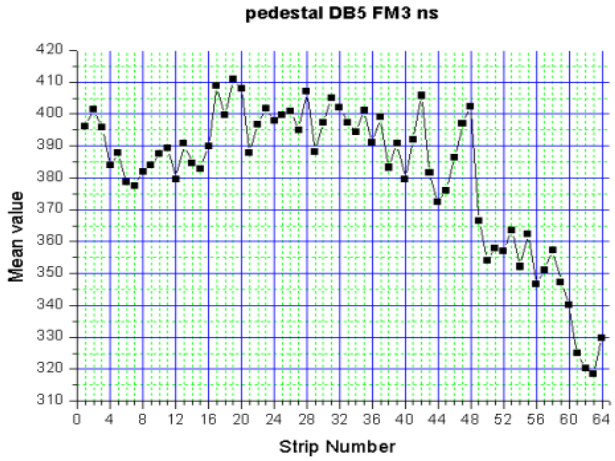

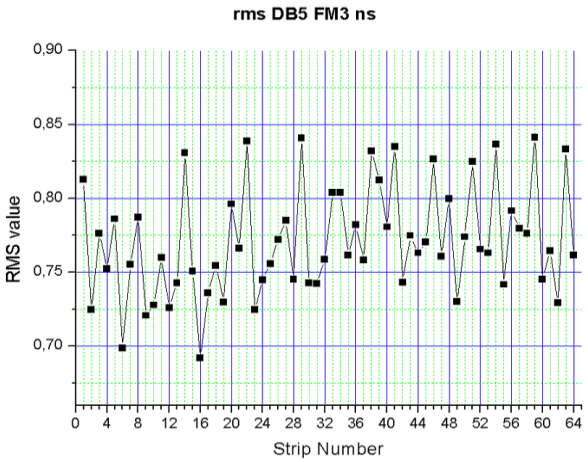

DB5: pedestals 1-99

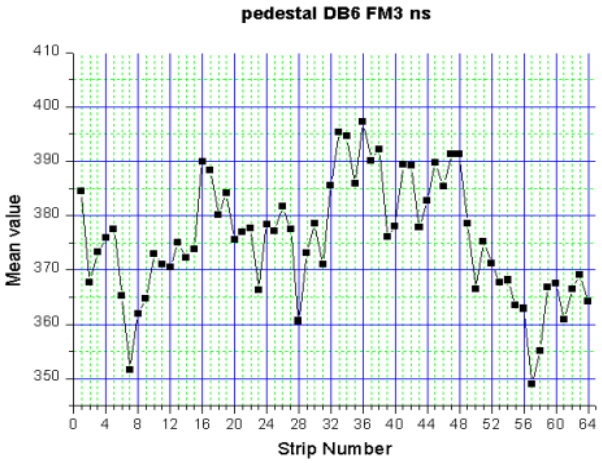

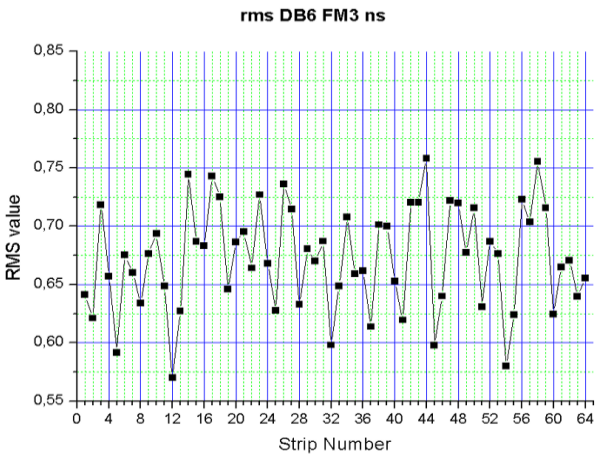

DB6: pedestals 1-99

FM4

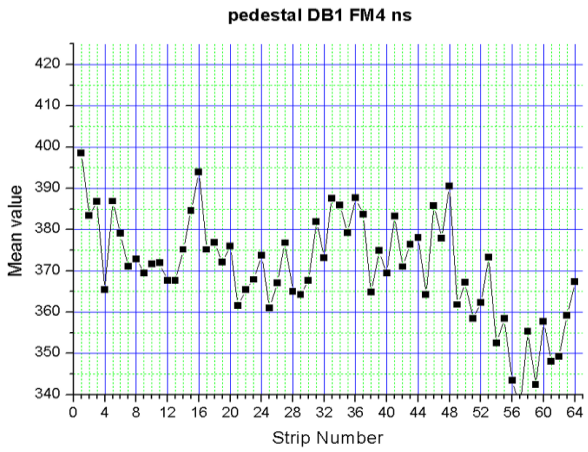

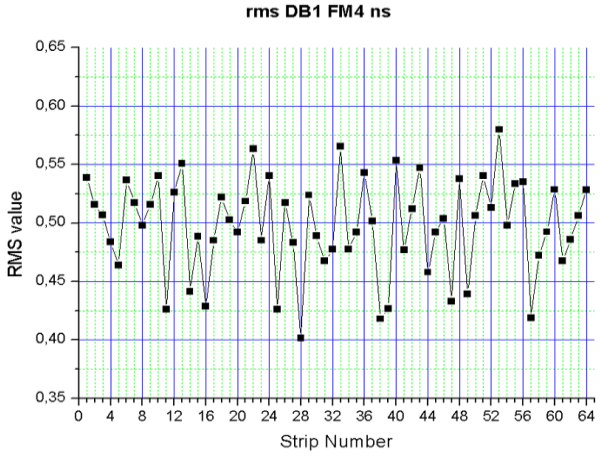

DB1: pedestals 1-99

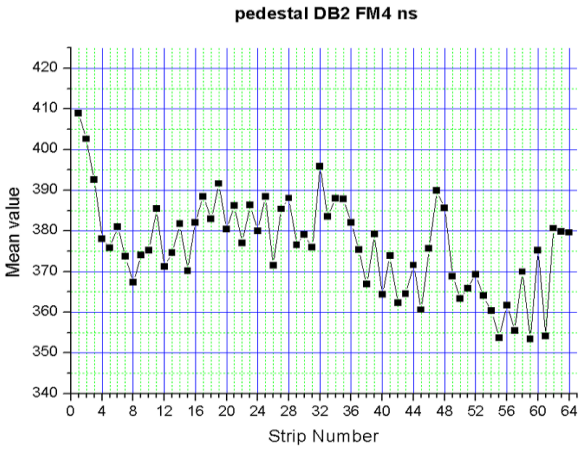

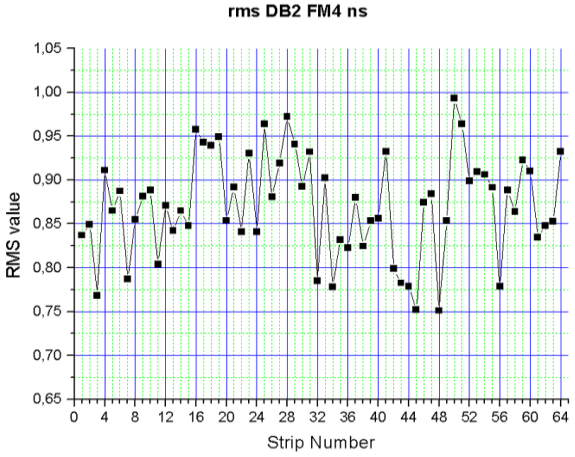

DB2: pedestals 1-99

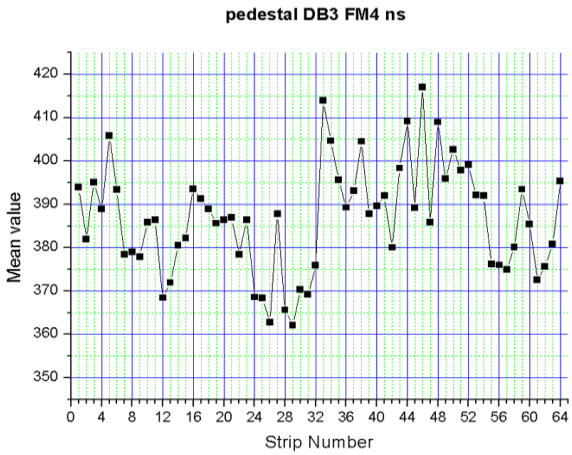

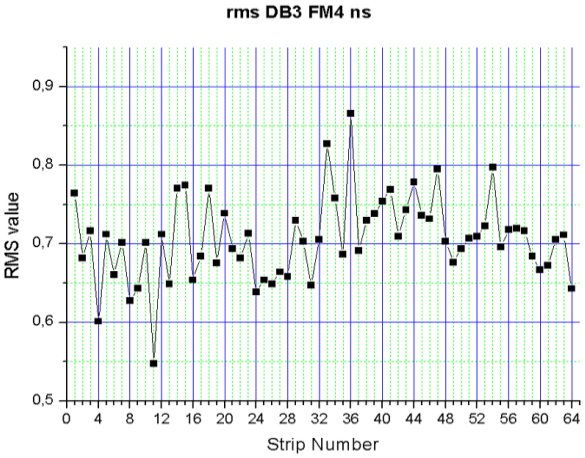

DB3: pedestals 1-99

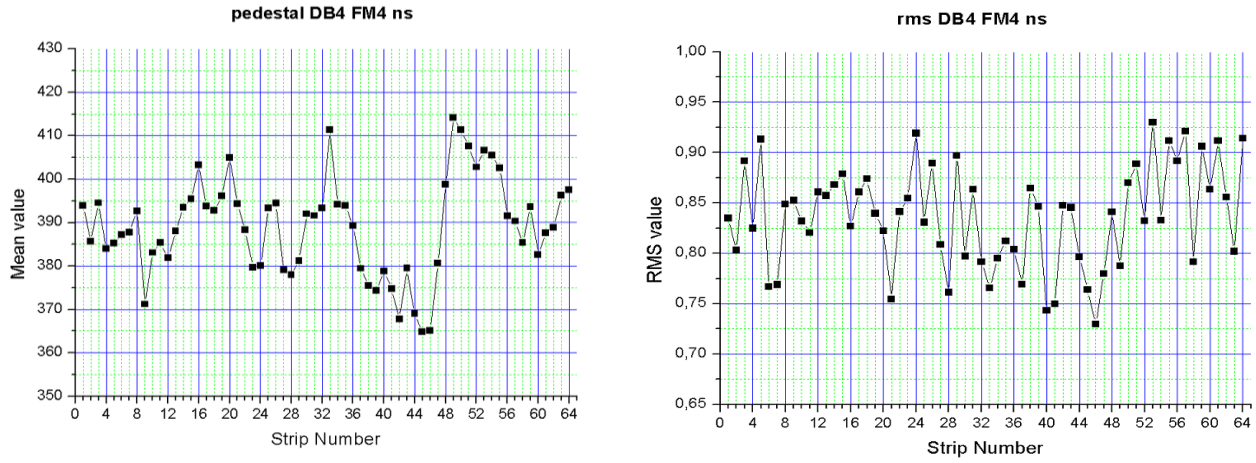

DB4: pedestals 1-99

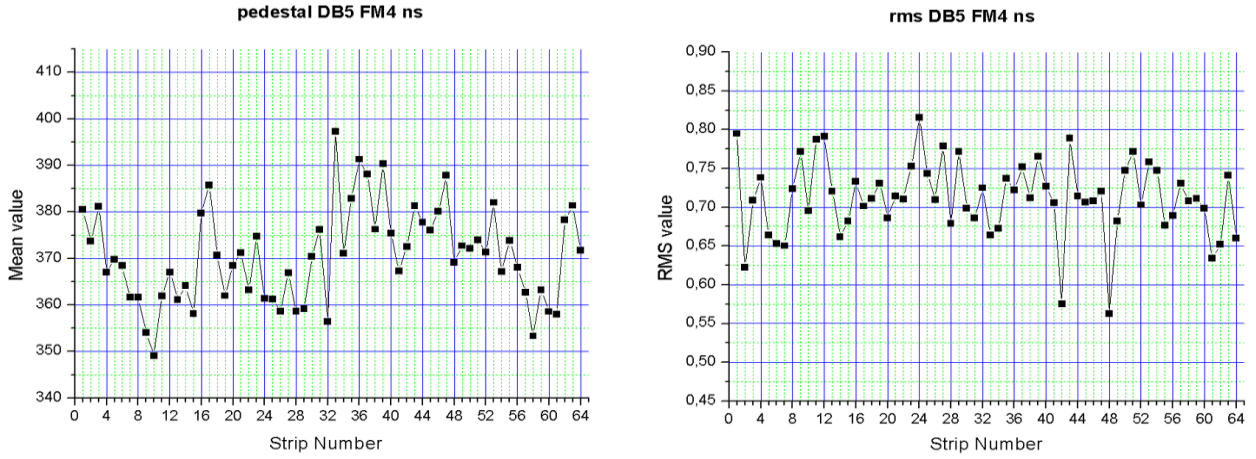

DB5: pedestals 1-99

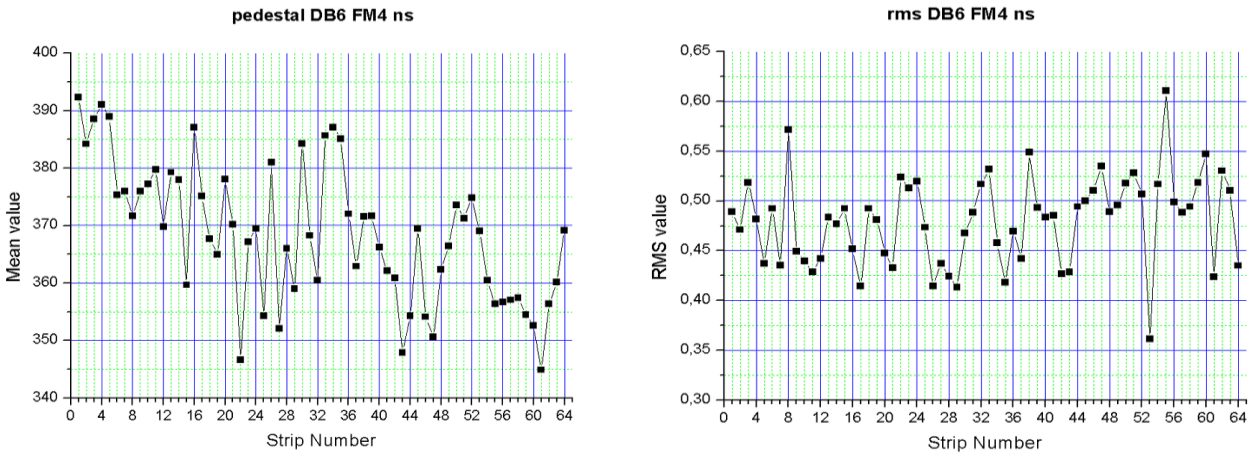

DB6: pedestals 1-99

FM5

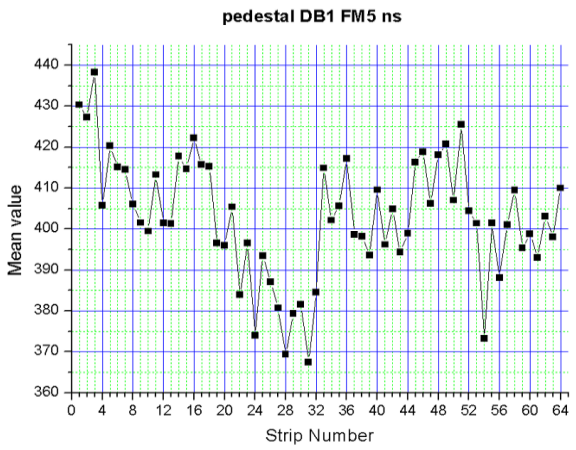

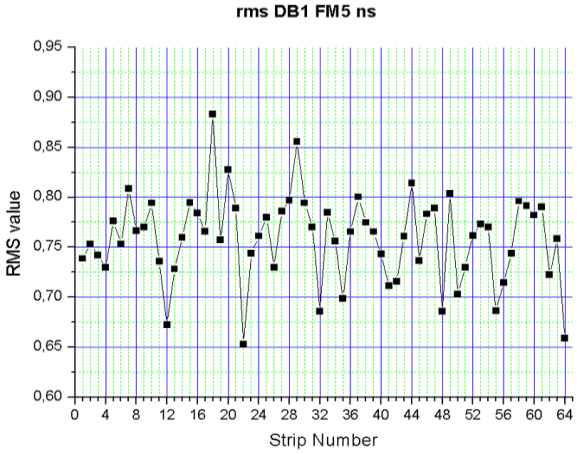

DB1: pedestals 1-99

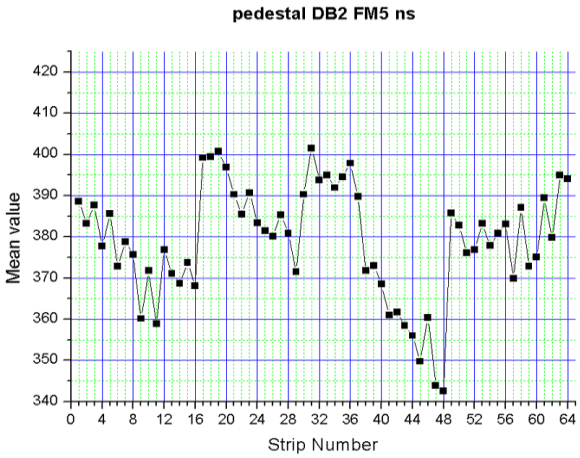

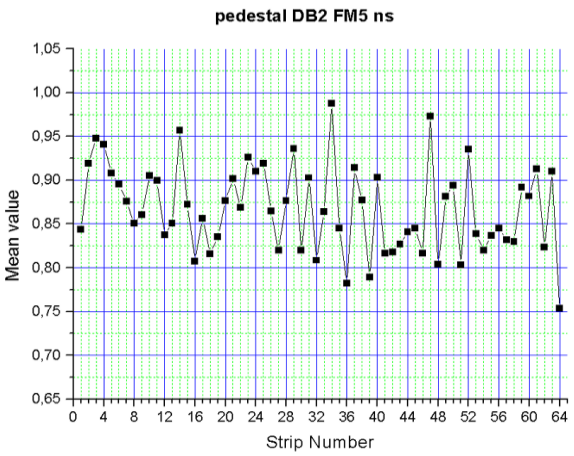

DB2: pedestals 1-99

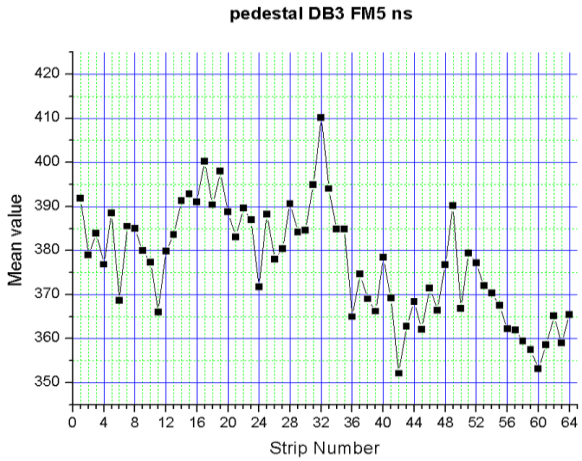

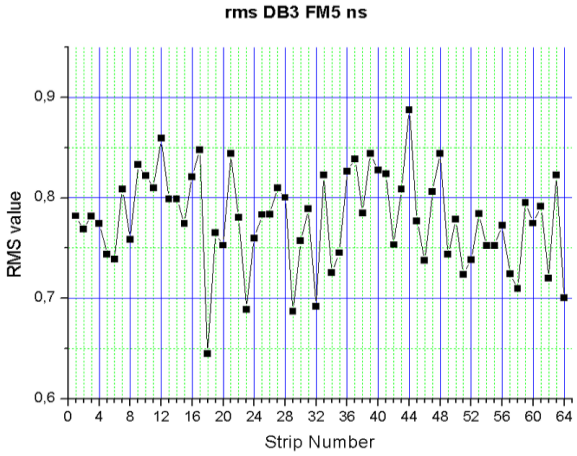

DB3: pedestals 1-99

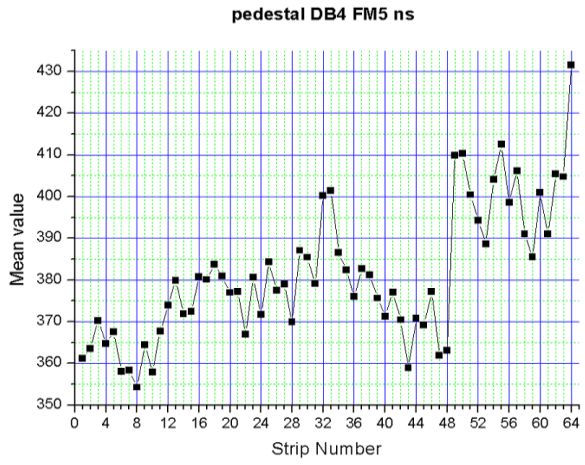

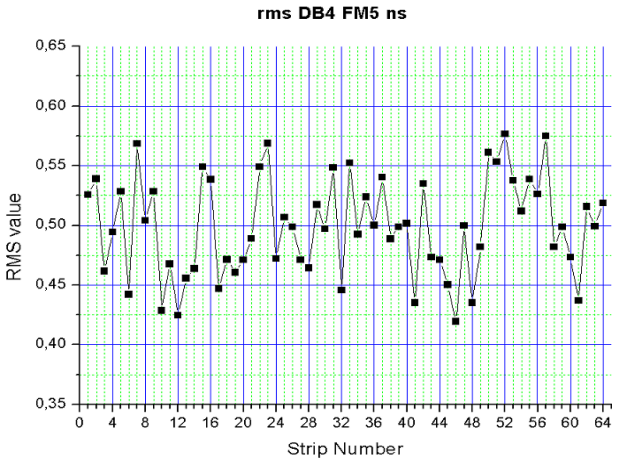

DB4: pedestals 1-99

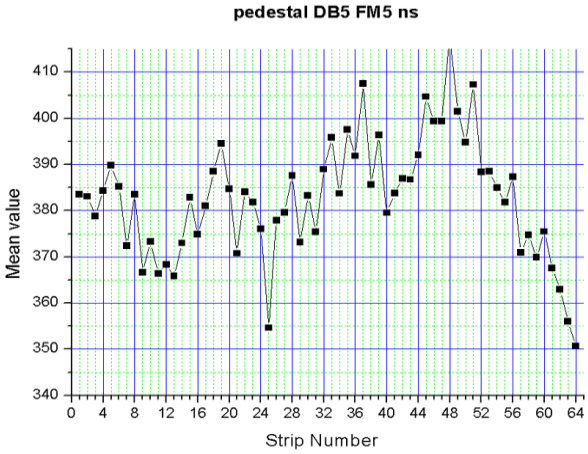

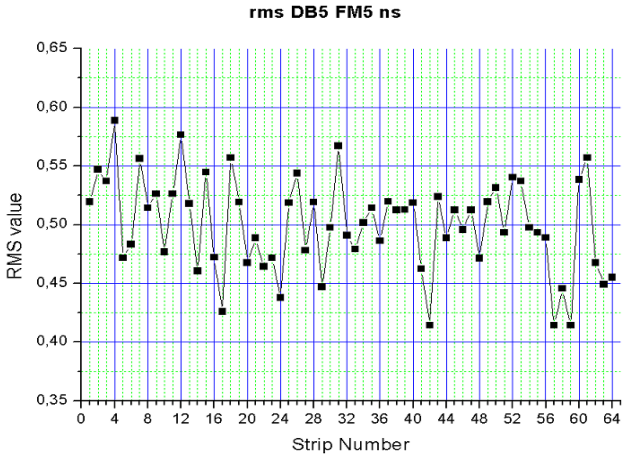

DB5: pedestals 1-99

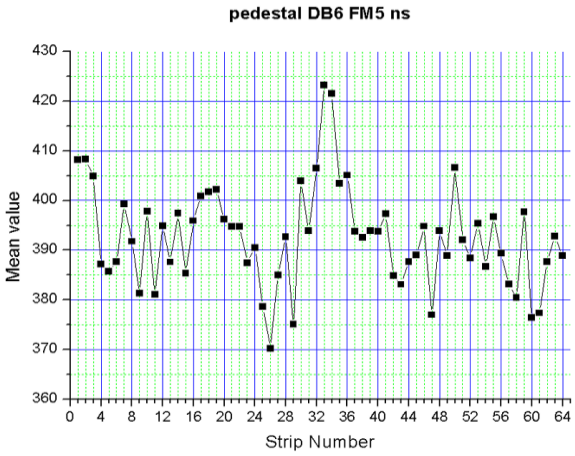

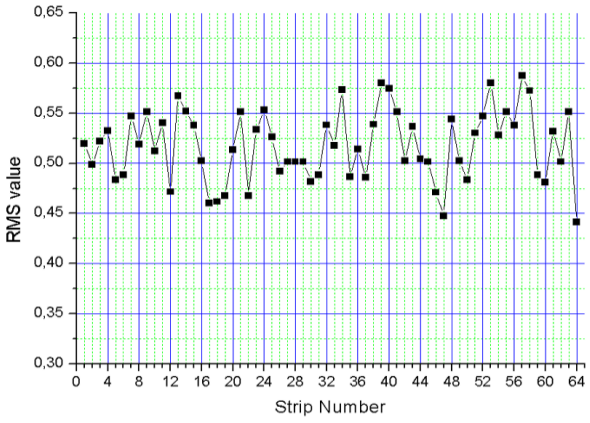

DB6: pedestals 1-99

FM6

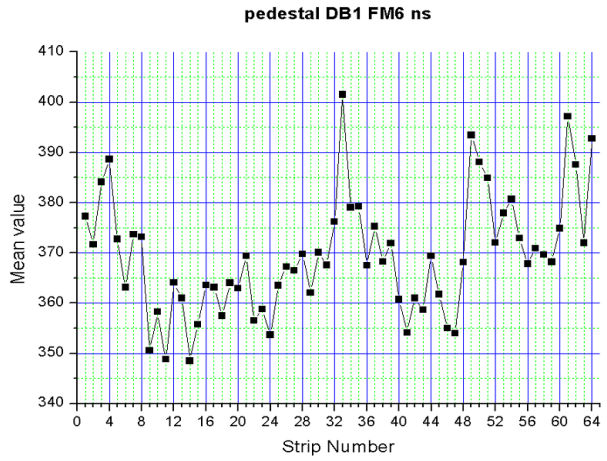

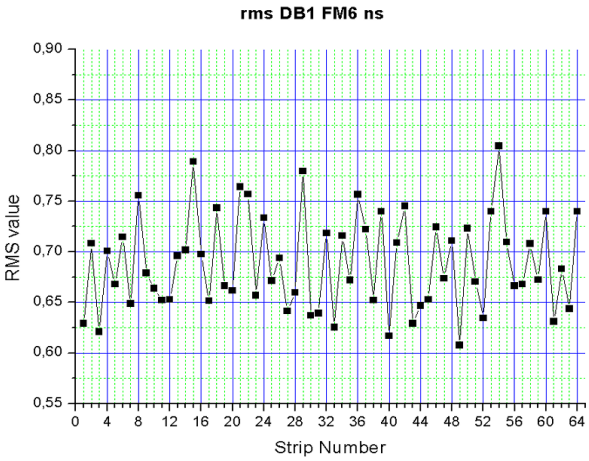

DB1: pedestals 1-99

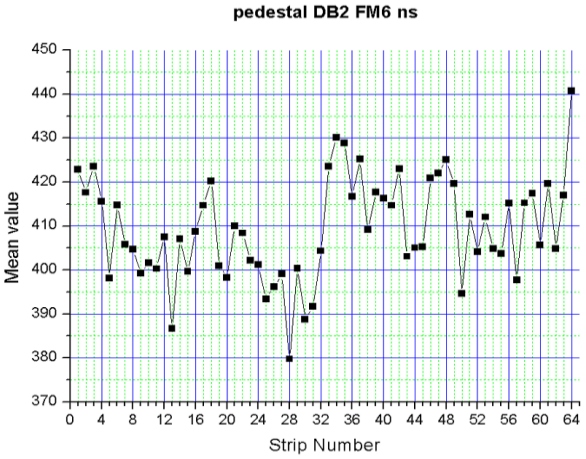

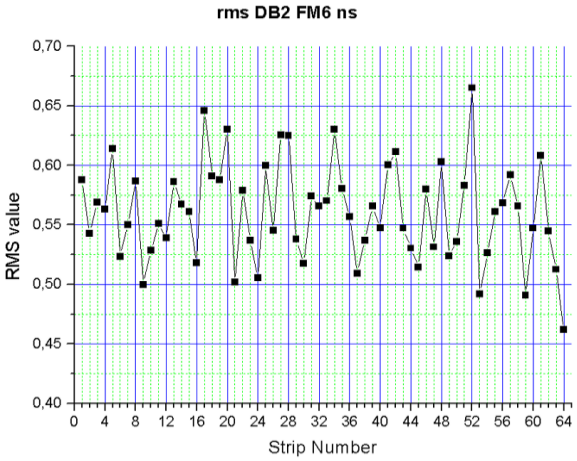

DB2: pedestals 1-99

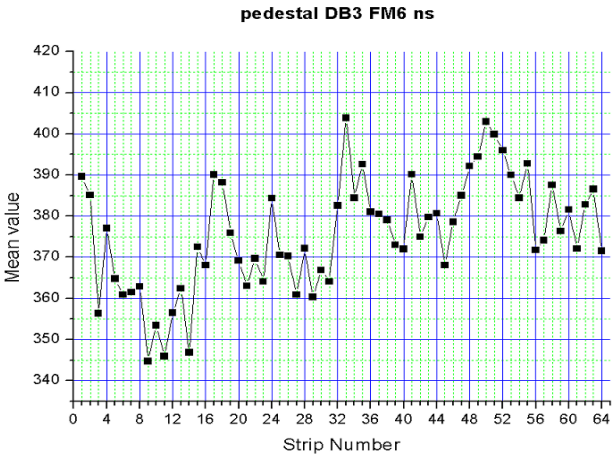

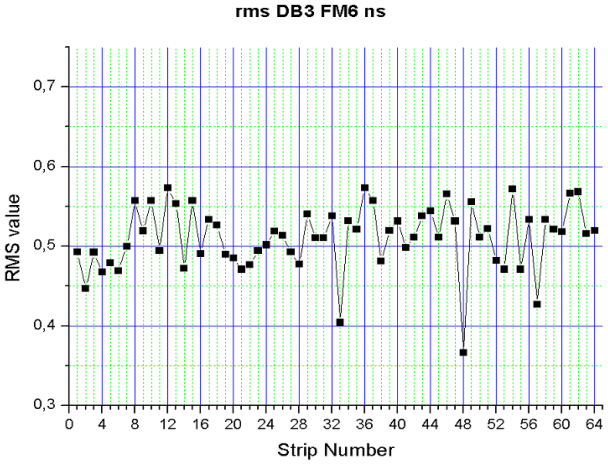

DB3: pedestals 1-99

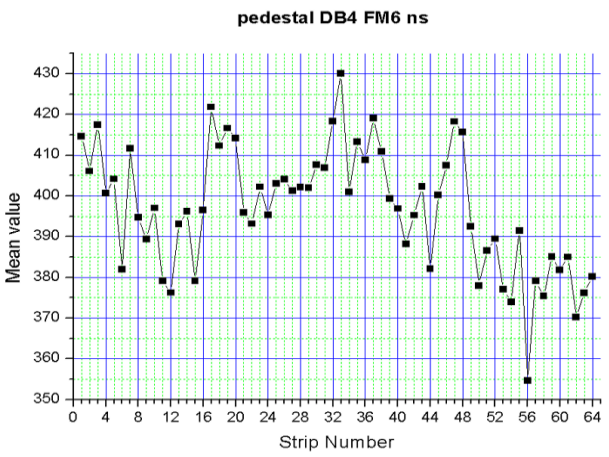

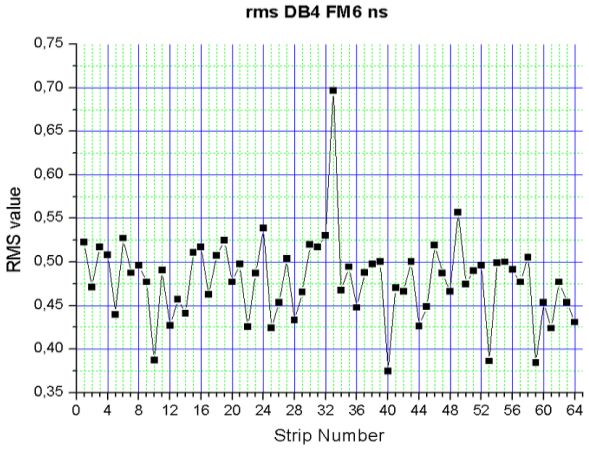

DB4: pedestals 0-99

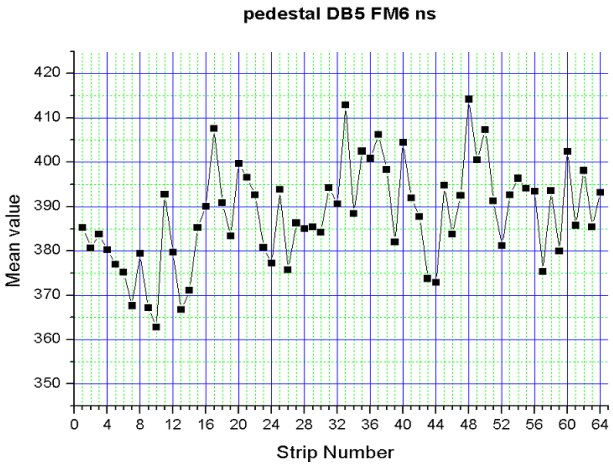

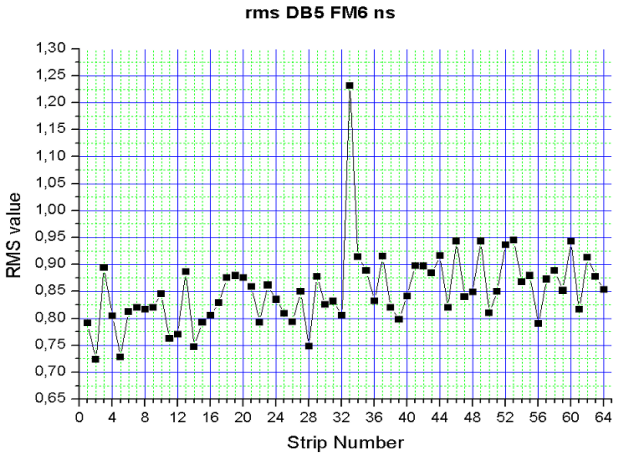

DB5: pedestals 0-99

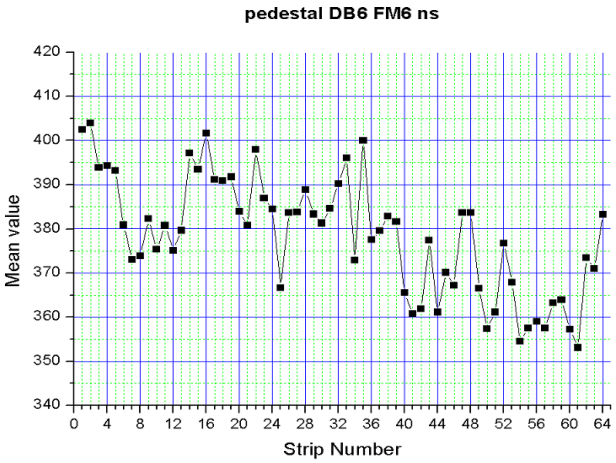

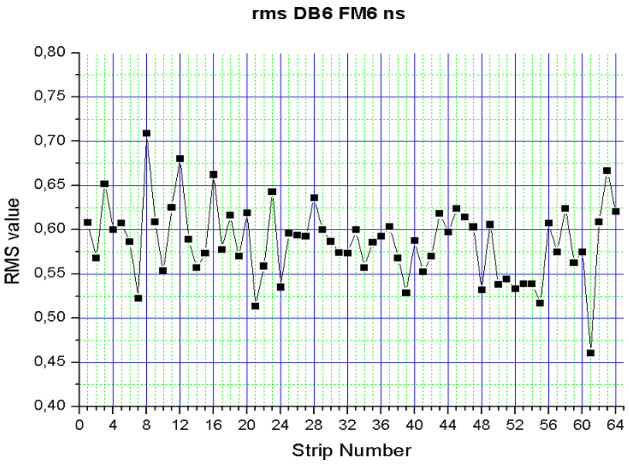

DB6: pedestals 1-99

With silicon planes bonded:

FM1

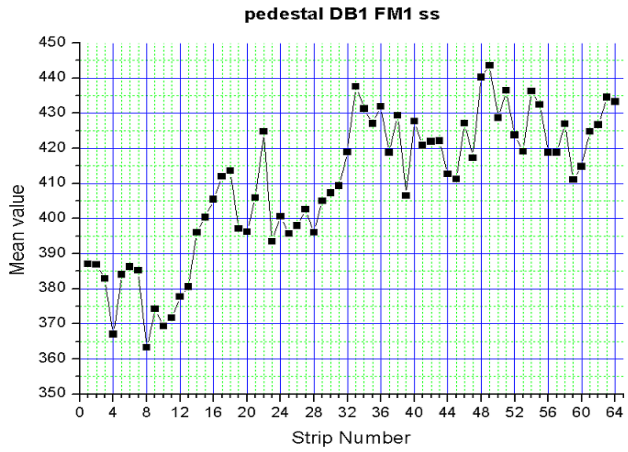

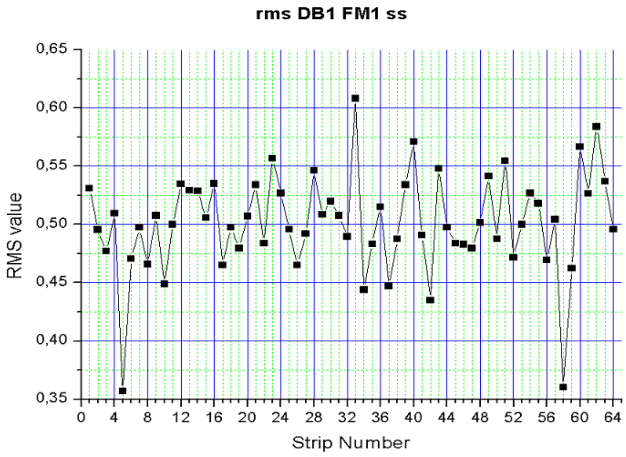

DB1: pedestals

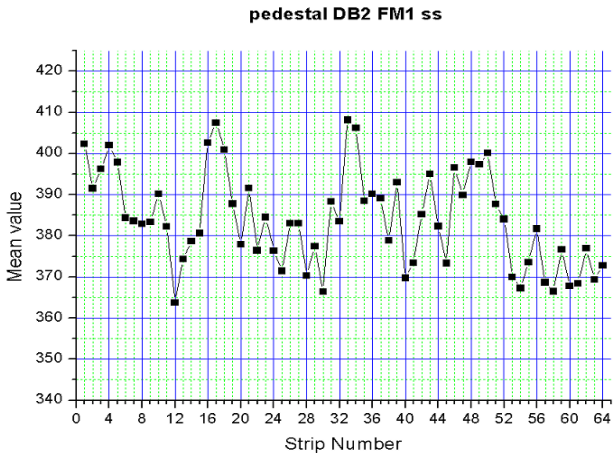

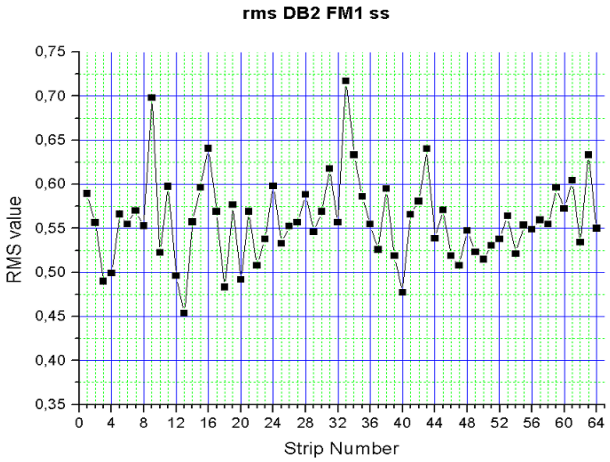

DB2: pedestals

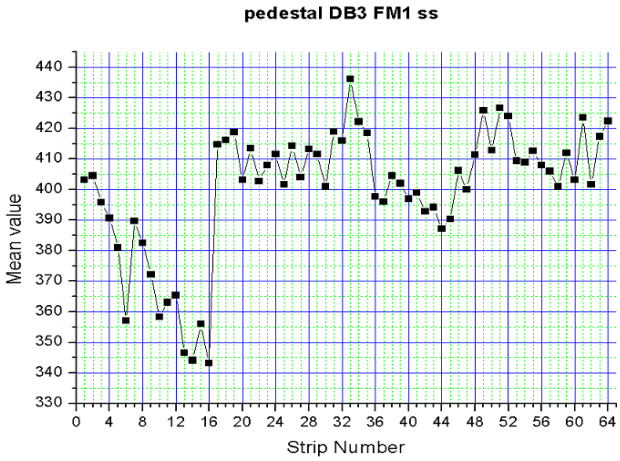

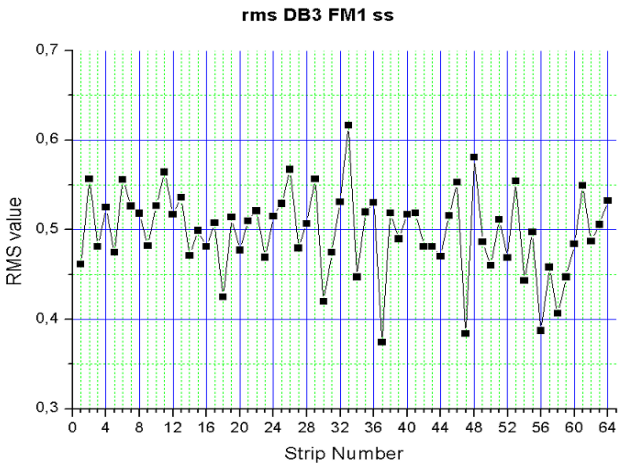

DB3: pedestals

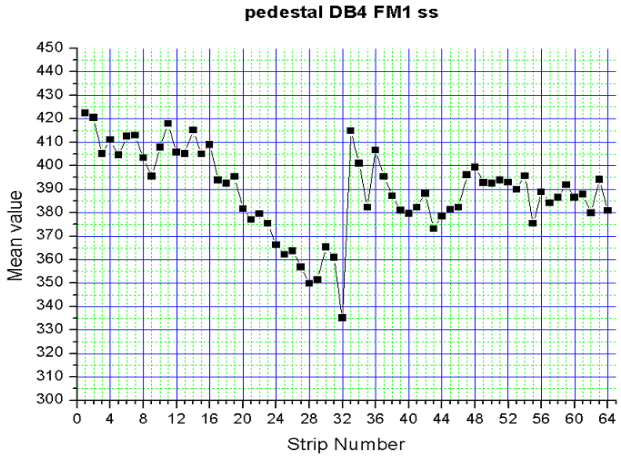

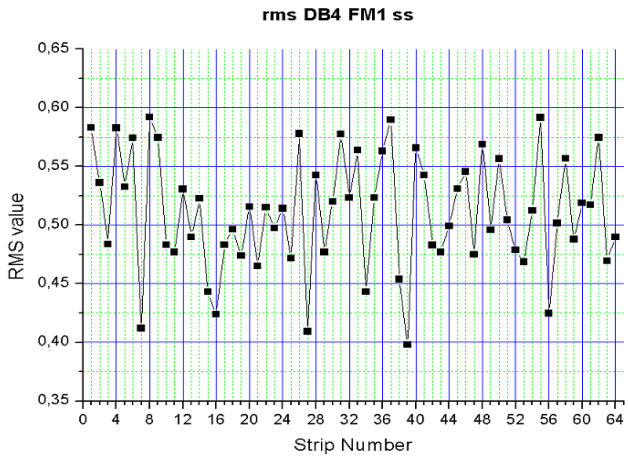

DB4: pedestals

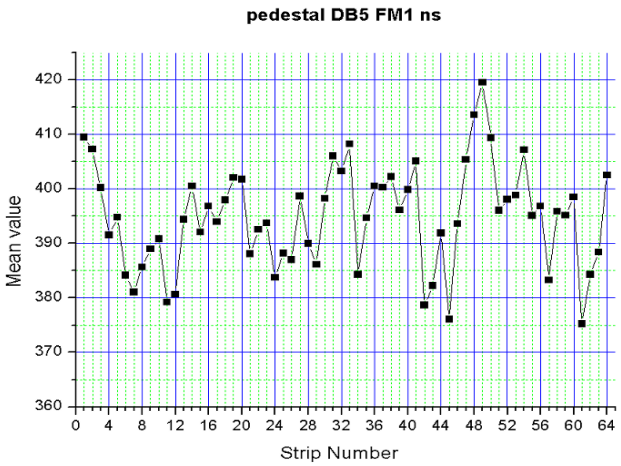

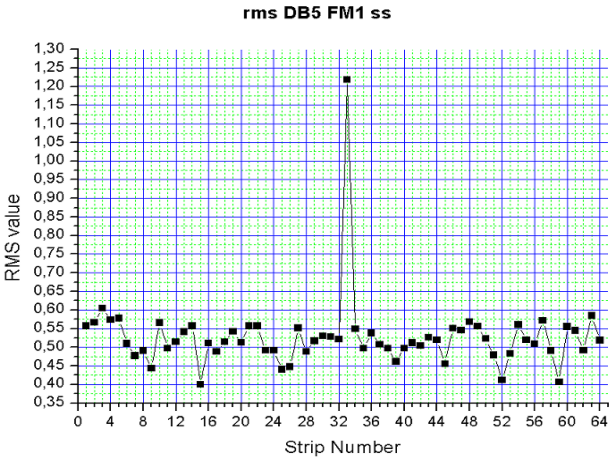

DB5: pedestals

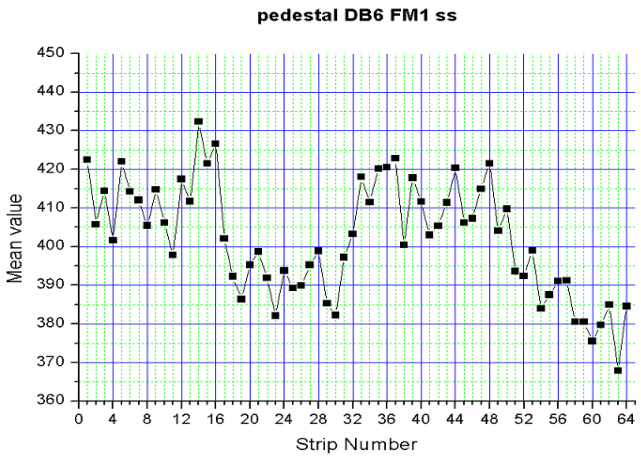

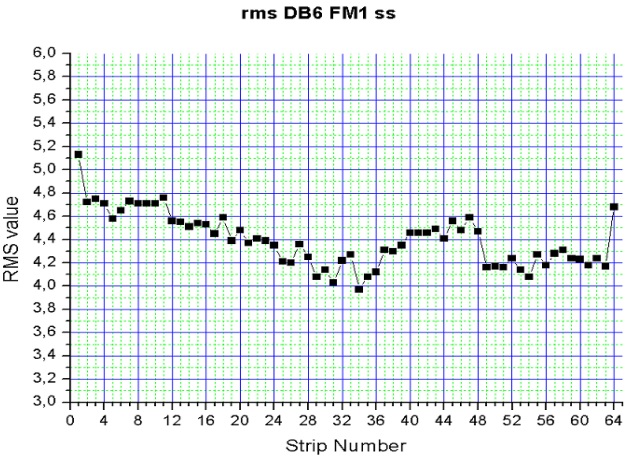

DB6: pedestals

Appendix B:
MIP definition

The particle energy loss varies with the target material like Z/A(≤ 0.5 for most elements).
The MIP, Minimum Ionizing Particle, is a physical quantity defining the minimum energy loss for a particle going through a medium. Minimum ionizing particles lose 1.94 MeV/(g/cm^2) in helium decreasing to 1.08 MeV/(g/cm^2) in uranium.
For our purpose is useful an operative definition of the MIP for particle going through silicon:

one particle at minimum produces in Silicon about 80e-h/μm (couple electron-hole per micron); then in 380 μm Silicon, as our silicon detector plane is thick, about 30400 electrons are produced. The extraction potential (potential needed to extract a couple electron-hole) in Silicon is 3.6 eV, so in 380 μm Silicon a particle at minimum loses 109 keV.

In table B.1 energy loss in silicon for different nuclei at minimum is showed (plane = 380 μm Silicon). The conversion used is:

1 MIP → 109 keV in 380 μm Silicon

Table B.1: energy loss of nuclei at minimum

Nuclei	eV/Å	MIP/plane
H	0,04	1,4
He	0,16	5,6
Li	0,35	12,2
Be	0,6	20,9
B	0,9	31,4

Appendix C:
MIP→mV conversion

In the following the calculation of conversion factor between charge injected in mV and MIP is reported.
The ADC range varies between -3.37 and 4.77 V, so the entire range is 8.14 V = 8140 mV.
The ADC used for ALTEA has 12 bit, then it has 4096 channels. It means that there is 1.99 mV (obtained dividing the mV ADC range for the number of channels).
In order to test amplification two charges are periodically injected in the silicon detector, a 4980 mV charge, called 'Big', and a 540 mV charge, called 'Small'.
Considering a 2 pF capacitor for ADC, there are the following results:

4980 mV corresponds to a charge $Q = 2 \cdot 10^{-12}$ pF $\cdot 4980 \cdot 10^{-3}$ mV =
$= 9.96 \cdot 10^{-12}$ C =
$= 6.225 \cdot 10^{7}$ e^- =
≈ 2048 MIP

540 mV corresponds to a charge $Q = 2 \cdot 10^{-12}$ pF $\cdot 540 \cdot 10^{-3}$ mV =
$= 1.08 \cdot 10^{-12}$ C =
$= 6.75 \cdot 10^{6}$ e^- =
≈ 222 MIP

In the conversion MIP→e^- the value reported in Appendix B was used.
Finally, the MIP→mV conversion factor is obtained:

(2048-222)/(4980-540) = 0.4113 MIP/mV

References

[1] P. Picozza, V. Bidoli, M. Casolino, R. Sparvoli, M. De Pascale, A. Morselli et al., *WiZard Si-W imaging calorimeter: a preliminary study on its particle identification capability during a ballon flight in 1993,* Nuc. Instr. Met., A 360, 1995, 17

[2] P. Picozza, V. Bidoli, M. Casolino, R. Sparvoli, M. De Pascale, A. Morselli et al., *The WiZard/CAPRICE Silicon-Tungsten Calorimeter,* Nuc. Inst. Meth., A 370, 1995, 403-412

[3] P. Picozza, V. Bidoli, M. Casolino, R. Sparvoli, M. De Pascale, A. Morselli et al., *Performance of the CAPRICE RICH detector during the 1994 ballon flight,* Nucl. Inst. Meth., A 371, 1996, 169-173

[4] P. Picozza, V. Bidoli, M. Casolino, R. Sparvoli, M. De Pascale, A. Morselli et al., *A fine grained silicon detector for high energy gamma-ray astrophysics,* ROM2F/94/61, Atti di "GIFCO94, Settimo Convegno Nazionale di Fisica Cosmica", Rimini 1994, 775-781

[5] P. Picozza, V. Bidoli, M. Casolino, R. Sparvoli, M. De Pascale, A. Morselli et al., *A wide aperture telescope for high energy gamma rays detection,* Nuc. Phys., B 43, 1996, 253-256

[6] T. K. Gaisser, *Cosmic Rays and Particles,* Cambridge University Press, Cambridge, 1990.

[7] M. S. Longair, *High Energy Astrophysics,* Volume 1, Cambridge University Press, 2000.

[8] J. A. Simpson, *Ann. Rev. Astr. Astrophy., 33 323,*1983.

[9] A. G. W. Cameron, *Space Sci. Rev.15, 121,* 1973

[10] M. D. Jones, E. C. Stone, C. J. Waddington, W. R. Binns, T.L.Garrard and M. H. Israel, *19th Intl. cosmic ray conference,* La Jolla, USA, 1985.

[11] N. Lund, *Cosmic radiation in contemporary astrophysics,* ed. M. M. Shapiro, D. Reidel Publishing Co., Dordrecht, 1984, p.1.

[12] W. R. Webber, *Composition and origin of cosmic rays,* ed. M.M.Shapiro, D. Reidel Publishing Co., Dordrecht, 1983, 83.

[13] N. U. Crooker, G. L. Siscoe, *The effect of the Solar Wind on the Terrestrial Environment,* Physics of the Sun, edited by P. A. Sturrock, pp. 193-- 249, D. Reidel, Norwell, Mass, 1986

[14] L.Golub, J.M. Pasachoff, *The Solar Corona,* Cambridge University Press, 1987, 219

[15] E.R. Priest, *Solar Flares Magnetodynamics,* Gordon and Breach Science Publisher, 1981

[16] D.L. Chenette, W.F. Dietnich, *The Solar Flares Heavy Ion Environment for Single-event Upsets: a Summary of Observations over the last cicle 1973,1983,* IEEE Trans. of Nucl. Sci., 1994

[17] J.H. Adams et al., *Energetic Ions in Cosmic Rays*, Nuc. Phys., 1985

[18] X.Y. Wang, Y.N. Huang, *The Particle Source Temperature in the Fe Rich and Fe Poor Events*, XXIV ICRC, Rome 1995

[19] R.P. Linn, *Solar Particle Acceleration and Propagation,* Rev. of Geophys., 1987

[20] M.Walt, *Introduction to Geomagnetically Trapped Radiation,* Cambridge University Press, 1994

[21] J.K. Hargreaves, *The Solar-Terrestrial Environment*, Cambridge University Press, 1968

[22] W.N. Hess, *The Radiation Belt and Magnetosphere,* Blaisdell Publishing Company, 1968

[23] W.N. Hess, *Introduction to Space Science,* edit. by Hess, W. N., 347, Gordon and Breach Science Publisher, 1965

[24] M.G. Kivelson, Ch.T. Russel, *Introduction to Space Physics*, Cambridge University Press, 1996

[25] W.R. Leo, *Techniques for Nuclear and Particle Physics Experiment*, Springer-Verlag, 1994

[26] P. Buhler, L. Desorgher, A. Zehnder, E. Daly, L. Adams, *Observations of the Low Earth Orbit Radiation Environment from MIR*, Rad. Meas. Vol. 26, No. 6, 1996

[27] V. M. Petrov, *Overview on experience to date on human exposure to space radiaztions,* Institute of Biomedical Problems, Moscow, Adv. Space Res., Vol. 14, No. 10, 1994

[28] G. Reitz, R. Beaujean, C. Heilmann, J. Kopp, M. Leicher, K. Strauch, *Dosimetry on the Spacelab missions IML1 and IML2, and D2 on MIR,* Radiat. Meas., Vol. 26, No. 6, 979-986, 1996

[29] G. Horneck, *Radiobiological experiments in space: a review*, DLR, Institute for Aerospace Medicine, Biophysics Division, Nucl. Tracks Radiat. Meas., Vol. 20, 1, 188, 1992

[30] J. D. Sullivan, *Geometrical factor and directional response of single and multi-element particle telescopes*, Nucl. Instr. Meth., 5-11, 1971

[31] N. Hasebe et al., *Improvement of mass resolution of cosmic ray nuclei using a ΔE* x *E Si detector telescope,* Nucl. Instr. and Meth. in Phys. Res., 335-342, 1992

[32] T. Doke et al., *A New Silicon Detector Telescope for Measuring the Linear Energy Transfer Distribution over the Range from 0.2 to 400 keV/μm in Space,* Jpn. J. Appl. Phys., Vol. 35, 6241-6247, 1996

[33] *ICRP Publication 60: 1990 Recommendations of the International Commission on Radiological Protection*. Elsevier Science Pub Co (1991)

[34] V. Bidoli et el., *In-flight performance of SilEye-2 experiment and cosmic ray abundances inside the Mir Space station,* J. Phys. G: Nucl. Part. Phys., 27, 2051-2064, 2001

[35] Sakaguchi T, Doke T, Hasebe N, Hayashi T, Kashiwagi T, Kikuchi, J, Kono S, Nagaoka S, Nakano T, Takagi T, Takahashi K and Takahashi S 1999 *NIM A* **437** 75

[36] Tobias, C. A., *J. Aviation Medicine, 23, 345, 1952*

[37] Pinsky L. S., Osborne W. Z., Bailey J. V., Benson R. E. And Thompson L. F., *Light flashes observed by astronauts on Apollo 11 through Apollo 17,* Science, 183, 957-959, 1974

[38] Fazio G. G., Jelly J. V. and Charman, W. N., *Generation of Cerenkov light flashes by cosmic radiation within the eyes of the Apollo astronauts,* Nature, 228-260, 1970

[39] Chapman P. L., Pinsky L. S., Benson R. E. and Budinger F. T., *Observations of Cosmic Ray Induced Phosphenes on Apollo 14,* Proc. Nat. Symp. Natural and Manmade Radiation in Space, p. 1002, NASA TM X-2440, 1972

[40] Biomedical Results from Skylab, NASA SP-377, 127-130, 1977

[41] Budinger T. F. *et al., Quantitative observation of light flash sensations experiment MA-106,* NASA TM X-58173, 13-1 13-17

[42] Budinger T. F., Hans Bichsel and Tobias C. A., *Visual phenomena noted by human subjects on exposure to neutrons of energies less than 25 MeV,* Science, 172, 868-870, 1971

[43] Charman W. N. and Rowlands C. M., *Visula sensations produced by cosmic ray muons,* Nature, 232, 574-575, 1971

[44] McNulty P. J., *Light flash produced in the human eye by extremely relativistic muons,* Nature, 234, 110, 1971

[45] Tobias C. A., Budinger T. F. and Lyman J. T., *Radiation induced light flashes observed by human subjects in fast neutron, X-ray and positive ion beams,* Nature, 230, 596, 1971

[46] Budinger T. F., Lyman J. T., and Tobias C. A., *Visual perception of accelerated nitrogen nuclei interacting with the human retina,* Nature, 239, 209-211, 1972

[47] Avdeev S. *et al., Eye light flashes on the Mir space station,* Acta Astronautica 50, 511-525, 2002.

[48] Casolino M. *et al., Space travel: dual origins of light flashes seen in space,* Nature 422, 680, 2003.

[49] Narici L. *et al., ALTEA: Anomalous long term effects on astronauts. A probe of the influence of cosmic radiation and microgravity on the central nervous system during long flights ,* Advances in Space Research 33, 1352-1357, 2004.

[50] Fuglesang C. *et al., Astronaut Light Flash Survey,* ESA Report MSM-AM-AHC-GNC-RP-001, 2004

[51] Casolino M. *et al., Detector Response and Calibration of the Cosmic-Ray Detector of the Sileye-3/Alteino Experiment,* Adv. Sp. Res. 37 (2006) 1691-1696

[52] Casolino M. *et al., The Sileye-3/Alteino experiment on board the International Space Station,* Nucl. Phys. 113B, 71-78, 2002.

[53] Sannita W.G. *et al., Effects of heavy ions on visual function and electrophysiology of rodents: the ALTEA-MICE project,* Advances in Space Research 33, 1347-1351, 2004.

[54] Schardt, D., & Krämer, M. (2003), *Particle induced visual sensations in heavy-ion tumor therapy*, GSI ScientiWc Report 2002, Biophysics and therapy, Gesellschaft für Schwerionenforschung mbH, Darmstadt, FRG, p. 167.

[55] Di Fino L. *et. al., ALTEA data handling,* Adv. Sp. Res. (2006) 1710-1715

[56] Zaconte V. *et. al, ALTEA: Flight Model calibration at GSI,* Adv. Sp. Res. (2006) 1704-1709

[57] Casolino M. *et al., Relative nuclear abundances inside ISS with Sileye-3/Alteino experiment,* Adv. Sp. Res. 37 (2006) 1686-1690

[58] Oganov VS , Rakhmanov AS, Novikov VE, Zatsepin ST, Rodionova SS, Cann C., The state of human bone tissue during space flight, Acta Astronaut. 1991;23:129-33

[59] Cucinotta FA, Manuel FK, Jones J, et al. Space radiation and cataracts in astronauts. *Radiat Res*. 2001;156:460-466.

[60]Cucinotta FA, Schimmerling W, Wilson JW, Peterson LE, Saganti PB, Dicello JF. Uncertaintie s in estimates of the risks of late effects from space radiation. *Adv Space Res*. 2004;34:1383-1389.